Universitat de València

DESIGN OF A GENERIC END-TO-END MISSION PERFORMANCE SIMULATOR AND APPLICATION TO THE PERFORMANCE ANALYSIS OF THE FLEX/SENTINEL-3 MISSION

By

Jorge Vicent Servera

PHD THESIS · TESIS DOCTORAL
Programa de Doctorado en Teledección

THESIS ADVISOR · DIRECTOR DE TESIS
José F. Moreno Méndez

Laboratorio de Procesado de Imágenes
Parque Científico
UNIVERSITAT DE VALÈNCIA - ESTUDI GENERAL
València, June 2016

Design of a generic end-to-end mission performance simulator and application
to the performance analysis of the FLEX/Sentinel-3 mission

Jorge Vicent Servera, 2016.

Book cover art by Cecilia Plaza, www.ceciliaplaza.com

Departamento de Física de la Tierra y Termodinámica
Facultat de Física

Laboratorio de Procesado de Imágenes
Parque Científico · Universitat de València

D. JOSÉ F. MORENO, Doctor en Ciencias Físicas, Profesor Titular del Departamento de Física de la Tierra y Termodinámica de la Facultad de Física de la Universitat de València

HACE CONSTAR QUE:

El M.Sc en Física Jorge Vicent Servera ha realizado bajo su dirección el trabajo titulado “*Design of a generic end-to-end mission performance simulator and application to the performance analysis of the FLEX/Sentinel-3 mission*”, que se presenta en esta memoria para optar al grado de Doctor en Teledetección por la Universidad de Valencia.

Y para que así conste a los efectos oportunos, firmo el presente certificado, en Valencia, a 24 de Junio de 2016.

José F. Moreno Méndez

Tesis Doctoral:
Design of a generic end-to-end mission performance simulator and application to the performance analysis of the FLEX/Sentinel-3 mission

Autor: D. JORGE VICENT SERVERA

Directores: Dr. JOSE F. MORENO MENDEZ

El tribunal nombrado para juzgar la citada Tesis Doctoral, compuesto por:

Presidente: ______________________________

Vocales:

____

____

____

Secretario: ______________________________

Acuerda otorgarle la calificación de ______________________

Y para que así conste a los efectos oportunos, firmamos el presente certificado.

Valencia, a

Agradecimientos

Quiero agradecer a mi director, el Prof. José F. Moreno Méndez, por ofrecerme la posibilidad de formar parte del Laboratorio para la Observación de la Tierra (LEO). Para mí, y para muchos, José es una referencia, tanto en el ámbito científico como personal, con la cual he tenido la suerte de empaparme de conocimiento. Durante estos últimos años he tenido el honor de formar parte de su equipo donde he podido participar en un proyecto tan interesante como es el desarrollo de la misión FLEX para la Agencia Espacial Europea.

Me gustaría también agradecer a mis compañeros/as y amigos/as del grupo LEO con los que hemos compartido tanto momentos de alegría y estrés. Muchas gracias a Luis Alonso por dejarme invadir su despacho durante estos años. Luis ha sido casi como mi tutor de Tesis, el cual nunca ha dudado en parar lo que estaba haciendo para resolver mis dudas y con el cual he podido compartir ideas que me han permitido avanzar tanto en esta Tesis como en los proyectos científicos en los que hemos trabajado. También muchas gracias a Neus Sabater, con la cual he ido mano a mano desde que comenzamos a trabajar en el grupo LEO. No puedo describir con palabras lo mucho que Neus me ha apoyado tanto profesional como personalmente. Sin duda, hay un buen pedazo de ella en el éxito de esta Tesis. Tampoco puedo olvidarme de agradecer a Jesús Delegido por su apoyo constante y su capacidad personal de mantener al grupo unido. A Carolina Tenjo, Juan Pablo Rivera, Jochem Verrelst, Antonio Verdú, Shari y María Vidal, por formar parte de esta familia que es el grupo LEO y enseñarme distintas formas de entender la teledetección así cómo el placer del trabajo en equipo.

Como parte del Laboratorio de Procesado de Imágenes, agradecer a Gustau Camps, Julia Amorós, Jordi Muñoz, Emma Izquierdo, Valero Laparra, Jesús Malo y Luis Gómez por hacer de mi lugar de trabajo un sitio donde disfruto venir cada día. Muchas gracias por esos fantásticos momentos que hemos compartido en los congresos en Milán y Lausanne así como por darme una amplia visión de como funciona la investigación científica.

También quisiera agradecer por su ayuda y contribución en la consecución de esta Tesis al personal de la Agencia Espacial Europea (R. Franco, M. Drusch, S. Kraft, P. Jurado, U. del Bello y muchos otros), GMV (F. Alemán, C. de Negueruela, M. Manzano) y Deimos Space (J.R. Acarreta), con los cuales he tenido el inmenso placer de trabajar. Así mismo, también agradecer a R. Colombo, U. Rascher, W. Verhoef, B. Middleton, A. Damm, Y. Goulas y sus

equipos por los conocimientos que he adquirido al participar en los diferentes proyectos científicos en torno a la misión FLEX.

Quisiera expresar mi gratitud a los co-autores y revisores anónimos que contribuyeron a la enriquecer las publicaciones que apoyan esta Tesis. Sus comentarios críticos contribuyeron enormemente a mejorar la Tesis como un todo. Además, la consecución de los objetivos propuestos en esta Tesis ha sido posible gracias a la financiación de los siguientes proyectos:

- FLEX End-to-End Mission Performance Simulator, ESA-ESTEC Contract No. 4000108364/13/NL/BJ [2013-2015].
- FLEX - Performance Analysis and Requirements Consolidation Study (PARCS), ESA-ESTEC Contract No. 4000105078/11/NL/AF [2012-2014].
- Estimación de parámetros biofísicos para la misión FLEX a partir de Sentinel-3, Plan Nacional de Investigación, Ref. AYA2010-21432-C02-01 [2011-2014].

A mis amigos, gracias por acompañarme todos estos años y compartir esos momentos que han hecho de mi la persona que soy hoy en día. Muchas gracias a Juampi por estar siempre presente desde que comenzamos juntos la carrera en Física, gracias de verdad por compartir tu sabiduría en nuestras inacabables conversaciones. Gracias a Javi por hacerme ver que salir un miércoles por la noche hasta las tantas es compatible con realizar proyectos científicos. A Alan, gracias por poner ese toque de creatividad, locura y caos y compensar mi mente cuadriculada. Gracias también a Luismi, Roberto, Cristina, Álvaro, Gloria, Paco y Juanda por permitirme desconectar de mi Tesis. A mis amigos Alexis, Asle, Astrid, Aurelie, Cybele, Elena, Emelie, Florian, Jérôme, Kitty, Luis, Matthias, Marco, Monika, Peter, Reidun, Sabrina, Weronika y Zohreh por enseñarme lo maravilloso de cada rincón de Europa además de su apoyo y amistad en diferentes momentos de mi vida. Os debo una birra.

A mi pequeña Ulita, por tu inmensa paciencia y apoyo en estos años que, aunque a veces largos y difíciles, también han sido apasionantes. Gracias por estar a mi lado y poder contar contigo. Gracias por darme amor y confianza para poder seguir cada día.

Por último, aunque para nada menos importante, doy las gracias a mi familia. A mi madre, mi padre y mi hermano por quererme, educarme y ayudarme cada uno de los días de mi vida. Vosotros habéis puesto sentido a lo que hago y sin vuestro constante apoyo no sé cómo habría podido llegado hasta aquí.

Jorge Vicent Servera

“*Fais que ton rêve soit plus long que la nuit.*”

Vangelis

Abstract

Earth observation by satellite optical remote sensing aims to monitor bio-geophysical processes happening in the Earth surface and the atmosphere by acquiring data at different wavelengths of the electromagnetic spectrum. In order to ensure sustained observations and capabilities to fill scientific gaps in our current understanding of the Earth system, new satellite missions are being developed by national and international space agencies and research organisations. In this context, End-to-End Mission Performance Simulator (E2ES) tools offer scientists and engineers a unique framework to understand the impact of instrument configuration in the final mission products and to accelerate the mission development from concept to deployment. At the same time, these cost-effective and flexible tools are capable of defining a methodology for the consolidation of requirements and performance assessment of these new satellite missions, setting the criteria for mission selection by the various space agencies' programme boards. While the concept of an E2ES is simple, the design of new E2ES and the evolution of existing ones lack from a standard methodology and guidelines, which translates into a complex and costly re-engineering process.

This Thesis covers two main objectives. On the one hand, it aims to harmonize the work done in the field of E2ES during the last decades and to propose a set of guidelines or methodology to develop E2ES for future remote sensing satellite passive optical missions. The first main objective, therefore, is: *'To design a generic end-to-end mission performance simulator that can be easily adapted to reproduce most present or future passive optical spaceborne instruments'*. On the other hand, the ESA's FLEX/Sentinel-3 tandem mission is used to validate, through the implementation of its E2ES, the designed generic E2ES architecture and to evaluate the performance of the FLEX mission for the retrieval of Sun-induced fluorescence. The FLEX/Sentinel-3 mission is optimally suitable for this validation task due to the complexity of the mission (e.g. tandem flight, multi-platform/-instrument mission, multiple spectral ranges and resolutions, multi-angular observations, synergy of products). The second main objective, therefore, is: *'To evaluate the FLEX mission for Sun-induced fluorescence retrievals using a newly developed E2ES in agreement with the designed generic E2ES architecture.'*. The rationale behind this Thesis is promoting the use of a common generic E2ES architecture that allows comparing missions in competitive selection process (e.g., ESA's Earth Explorers) and speeding-up the analysis of the mission technical requirements and scientific performances. Particularly, this is shown by implementing this generic E2ES architecture for the specific case of FLEX/Sentinel-3 mission demonstrating that: **(1)** the mission is capable of retrieving Sun-induced fluorescence within the required accuracy; and **(2)** the conceptual generic E2ES architecture is suitable to reproduce the complexity of the FLEX/Sentinel-3 tandem mission and thus it is expected to be also applicable for a wide range of passive optical missions. This rationale is achieved by categorising several satellite missions to identify and analyse the main elements that affect the mission performance and impact the simulator architecture. The proposed generic E2ES architecture is validated by implementing the ESA's FLEX/Sentinel-3 E2ES, both satellites and their instruments, and testing it through the performance assessment of the FLEX mission products.

In this Thesis, Chapters 1 and 2 introduce the main research questions and sets the background concepts. Then Chapters 3–5 describe the design of a generic E2ES architecture for passive optical missions. Finally, Chapter 6 summarizes the main results and conclusions derived in this Thesis.

Acronyms and Definitions

Acronyms

A/D	Analog-to-Digital
ACT	Across-Track
ALT	Along-Track
AOCS	Attitude and Orbit Control System
AOT	Aerosol Optical Thickness
BRDF	Bidirectional Reflectance Distribution Function
CCD	Charge-Coupled Devices
DEM	Digital Elevation Model
E2ES	End-to-End Mission Performance Simulator
EC	European Commission
ECEF	Earth Centered Earth Fixed
EO	Earth Observation
ESA	European Space Agency
FLEX	Fluorescence Explorer
FLEX-E	FLEX end-to-end mission performance simulator
FLORIS	Fluorescence Imaging Spectrometer
FOV	Field Of View
FTS	Fourier Transform Spectrometers
FWHM	Full-Width at Half-Maximum

GCOS	Global Climate Observing System
GPP	Ground Processor Prototype
IPCC	Intergovernmental Panel on Climate Change
ISS	International Space Station
ISRF	Instrument Spectral Response Function
L1	Level-1
L2	Level-2
L2R	Level-2 Retrieval Module
LAI	Leaf Area Index
LCC	Land Cover Class
LOS	Line-of-Sight
LUT	Look-Up Table
MIR	Midwave–InfraRed
MODTRAN	MODerate resolution TRANsmittance
MSI	Multi-Spectral Instrument
NIR	Near-InfraRed
OLCI	Ocean and Land Color Instrument
PARCS	Performance Analysis and Requirements Consolidation Study
PEM	Performance Evaluation Module
PSF	Point Spread Function
RMSE	Root Mean Squared Error
RTM	Radiation Transfer Model
RS	Remote Sensing
S3	Sentinel-3
SCOPE	Soil-Canopy-Observation of Photosynthesis and the Energy balance
SFM	Spectral Fitting Method
SGM	Scene Generator Module

SIF	Sun-Induced chlorophyll Fluorescence
SLSTR	Sea and Land Surface Temperature Radiometer
SNR	Signal-to-Noise Ratio
SSD	Spatial Sampling Distance
SSI	Spectral Sampling Interval
SWIR	ShortWave-InfraRed
SZA	Solar Zenith Angle
TIR	Thermal–infraRed
TOA	Top Of Atmosphere
TOC	Top Of Canopy
UV	Ultraviolet
VIS	Visible
VNIR	Visible and Near InfraRed

Definitions

Space Mission Phases

A space mission typically evolves in successive life cycle “Phases” (or “stages”, according to the standard ISO 15288[1]) of conception, development, production and testing, utilization and support, and retirement, as part of an iterative and recursive process, until the satellite is delivered and launched into orbit, and the data are exploited in the ground segment. Though the terminology and precise content of these Phases may vary across space agencies [1, 2], a generic definition might be used as follows:

- **Phase A:** It consists of a preliminary detailed analysis of the mission goals, proposing and validating a preliminary design for the platform, payload and ground segment and operational plan.
- **Phase B:** Proposes a baseline technical solution to meet specific requirements, schedules and specifications. These outcomes are formally evaluated to assess the validity of the requirements and the feasibility of the proposed design.
- **Phase C/D:** Concern the actual manufacturing, assembly and testing of the space hardware, typically including full or partial models to test all the systems and subsystems under environmental conditions relevant to prolonged operation in space.
- Subsequent phases involve the launch itself, the commissioning of the satellite, and the mission operations, followed by the de-commissioning and eventual de-orbiting of the satellite at the end of its useful lifetime.

Data Processing Levels

The following Data Processing Levels is based on ESA and NASA standard definition [3]:

- **Level-0:** Instrument raw data in digital counts together with platform and instrument attitude and orbit geometric data. This processing Level is achieved independently of the scientific mission objective and radiometric target.
- **Level-1 (L1):** Radiometrically and spectrally calibrated data in radiance units and instrument projection with appended geolocation (i.e. pixel coordinates). Additional ancillary data such as quality flags is attached to the L1 product for further analysis. This processing Level is achieved for all missions independently of their scientific objective and radiometric target.

---

[1] ISO/IEC/IEEE 15288:2015, 2015. Systems and software engineering & System life cycle processes. International Standard Organization. Available from http://www.iso.org/iso/catalogue_detail?csnumber=63711.

- **Level-2 (L2):** Retrieved bio-geophysical parameters (e.g., Leaf Area Index (LAI), Surface Temperature, fluorescence) from the L1 products or after the atmospheric correction of the L1 data (i.e., derivation of surface reflectance for Earth surface pointing instruments). This processing Level is specific of each mission according to their scientific goal and radiometric target, however some algorithms are common for a variety of satellite missions (e.g., retrieval of atmospheric gas concentration through differential absorption, atmospheric correction, spectral indices).

- **Level-3:** L1 and/or L2 data from different images resampled to create regional/global mosaics maps at different temporal scales (usually daily to yearly). This processing Level could be independent of the mission scientific goal and common tools might be used.

- **Level-4:** Analysis of the L2 products at different spatial and temporal scales to retrieve higher value scientific information (e.g., classification of plant species or crops based on phenologic cycle). This processing Level is mission-specific.

Calibration and Geolocation

A variety of methods are used for the calibration and geolocation of passive optical instruments and they depend on the mission design, spectral bands and instrument type. These methods are briefly described in the following items:

- Radiometric (absolute and relative) calibration: It consists in the characterization of a set of coefficients needed to convert Level-0 data in digital counts to L1 data in radiance units. These coefficients are provided by on-ground laboratory calibration procedures but might be updated during the mission lifetime. The radiometric calibration is achieved by comparing the signal acquired by the instrument with a reference radiometric target. Sun-calibration, through a solar diffuser, is commonly used for instruments acquiring in the UV-SWIR spectral range due to the well-known irradiance values. Some instruments use instead the Sun-light reflected on the Moon's surface, LEDs or spectral lamps with spectrally-characterized radiance. Thermal spectral channels are radiometrically calibrated using an on-board blackbody with known temperature or deep-space measurements (e.g., [4]). Additionally, radiometric calibration determines and substracts the zero-offset signal based on methods that depend on the instrument spectral bands. For instruments measuring in the UV-NIR spectral range, the instrument acquires measurements over the ocean surface on the dark part of the orbit assuming that the emitted and reflected light is negligible. For measurements in the SWIR-TIR spectral range, the instrument points towards the deep space. Alternatively, a shutter is placed in front of the telescope to close the entrance of light into the instrument. Vicarious calibration or instrument cross-calibration (e.g., [5–7]) are used as alternative or complementary methods for the radiometric calibration in all the optical range and rely on the image acquisition over a spectrally characterized surface target (e.g., desert, homogenous vegetation cover, snow/ice covered area) or the comparison between radiances acquired by similar instruments.

- Spectral calibration: Tags each instrument spectral channel by the barycenter wavelength of its spectral response function. Light sources with known spectral features (e.g., spectral lamps, LEDs) and/or Solar absorption lines are typically used for spectral calibration.
- Image geolocation: The geolocation of satellite data is based on the use of the platform attitude and orbit measurements and characterization of the instrument mounting in the platform. This is possible through the use of high-accuracy attitude and orbit control sensors such as Sun-sensors, star-trackers and GPS for determination of orbit position The geolocation can be refined or supported by the use of ground control points, i.e. ground target pixels with known geolocation.

Contents

1

Introduction

Contents

1.1 Context and overview

Earth observation (EO) by satellite remote sensing is an interdisciplinary field of Science and Engineering that aims to monitor bio-geophysical processes happening in the Earth surface and atmosphere using a wide range of passive and active instruments that cover the whole electromagnetic spectrum. With satellite-borne remote sensing instruments, a variety of Earth processes can be studied with a global coverage and temporal continuity, allowing scientists and policy makers having a wide understanding of our changing Earth environment, and thus leading to great impacts in scientific advances and societal benefits. Examples of remote sensing products and applications include characterization of land cover change, weather forecasting, atmospheric gas composition, estimation of biophysical parameters for quality assessment of surface vegetation and water bodies, among many others. EO with satellites has therefore provided strong evidence of the significant human impact in climate and environmental change.

In this context, and with the maturity of satellite technologies and recent advances in data processing, various national and international space agencies and research organizations are developing their own EO science strategy to carefully design new and complementary satellite missions that ensure sustained observations and capabilities to fill scientific gaps in our current understanding of the Earth system. The European Space Agency (ESA) is developing, within the Copernicus and Living Planet programmes, the Sentinel, Earth Watch and Earth Explorer missions, aiming to provide continuous monitoring of the Earth system, weather forecasting and foster scientific advances in EO remote sensing. These satellite missions are developed by a join effort of scientists and engineers in successive "phases" from conception to operations. The first phases consist of an analysis of the mission performance; consolidation of their technical requirements; and testing and optimizing implemented data processing algorithms. New end-to-end system engineering tools are therefore needed to understand the impact of instrument configuration in the final mission products and to accelerate the mission development from concept to deployment. At the same time, these cost-effective and flexible tools should be capable of defining a methodology for the consolidation of requirements and performance assessment of these new satellite missions, setting the criteria for mission selection by the various space agencies' programme boards.

For the last three decades, end-to-end mission performance simulator (E2ES) tools have been studied and developed for both specific satellite missions and generic mission concepts. These tools take advantage of recent advances in computer science and radiative transfer modeling to realistically simulate the proposed mission concept, their data and the data processing algorithms. Therefore, they offer a unique framework to determine the mission characteristics impacting the data quality and achievement of scientific goals, enabling the consolidation of mission requirements and to check the consistency of platform and payload specifications. E2ES support trade-off studies and are useful in preparation for system calibration tests. From a data processing perspective, these tools allow testing and optimizing retrieval schemes prior to mission operations [8, 9]. While the concept of an E2ES is simple, their implementation for each developed mission constitutes a major endeavor that requires complex and costly re-engineering activities. On the one hand, the efforts done in the development of generic E2ES concepts have had a limited applicability into real satellite E2ES due to **(1)** approximations on the implemented algorithms and simulations of radiative transfer and instruments; and **(2)** narrow scope of simulated scenarios and instrument types. On the other hand, some satellite remote sensing mission have implemented their own specific E2ES that can be hardly adapted to new developed missions. For these reasons, a rigorous and advanced generic E2ES tool that can be applied to most remote sensing satellite missions is definitely needed. The use of a common E2ES architecture would allow comparing missions in competitive selection processes (e.g., ESA's Earth Explorers), speeding-up the analysis of the mission technical requirements and, overall, the first phases of the mission design and development.

1.2 Motivation and objectives

This Thesis will investigate the recurrent problem in the design of remote sensing satellite missions, where every new EO mission develops its own E2ES tool with all the costly and complex engineering and scientific issues involved. On the one hand, this problem will be addressed by reviewing E2ES tools developed in the past decades with the goal of studying the common elements that were implemented and analysing whether the implemented solutions can be extended to any passive optical mission for first mission development phases. On the other hand, past, present and planned EO missions will be categorized to extract commonalities that affect the mission performance. The methodology adopted in this Thesis to tackle this problem firstly considers both approaches in order to design a generic E2ES architecture concept for passive optical instruments that can be applicable in various satellite mission applications, instrument types and mission designs. Secondly, and in order to validate the proposed generic E2ES concept, the designed tool will be implemented in a real satellite mission scenario (i.e., ESA's FLuorescence EXplorer (FLEX)/Sentinel-3 tandem mission) and tested through the performance assessment of its mission products. This approach will deliver two main results: **(1)** a generic E2ES architecture concept for passive optical missions will be defined, with the posibility of being implemented in wide range new satellite remote sensing missions; and **(2)** by implementing this E2ES concept for the FLEX/Sentinel-3 mission, the mission performance will be analyzed, deriving conclusions with respect to the accuracy of the FLEX mission products.

Thus, this Thesis aims to support the scientific and technological interest in the field of E2ES for EO missions, particularly for passive optical instruments. Two major points motivate the design and development of a generic E2ES architecture for passive optical instruments. On the one hand, designing a generic E2ES architecture would speed-up the conceptual design of new satellite missions through the consolidation of their technical requirements, trade-off evaluation and development of data processing algorithms. On the other hand, the use of a common generic E2ES architecture for various satellite remote sensing missions would allow to intercompare their performance and establish whether the required accuracy can be met, maximizing measurement synergies between satellite missions.

The Thesis in a nutshell

- **What are the main goals? (1)** To design a generic E2ES architecture than can be easily adapted to reproduce most present and near future passive optical spaceborne instrument and, **(2)** to evaluate the FLEX mission for Sun-induced fluorescence retrievals using a newly developed E2ES in agreement with the designed generic E2ES architecure.
- **Why is the topic important?** Setting a generic E2ES architecture concept for passive remote sensing missions is important in the frame of the EO science strategy for ESA and other national and international space agencies and organizations. Providing such a tool would have a large impact in the planning, development and analysis of new satellite missions. In addition, it will offer a framework where to implement new data processing algorithms. The goals of this Thesis are also challenging in the field of EO science and technology as it demands extracting commonalities from a wide range of remote sensing passive optical instruments and applications while, at the same time, be applicable to specific satellite mission such as the one analyzed here (i.e., ESA's FLEX/Sentinel-3).

- **How is the topic addressed?** A review and categorization of past, current and planned satellite passive optical missions will first determine the main characteristics that impact the mission performance and will identify the required elements needed to develop a generic E2ES architecture. The designed conceptual E2ES architecture will then be implemented for the specific case of ESA's FLEX/Sentinel-3 tandem mission, which will be exploited to analyze the performance of the FLEX mission in terms of its mission products, showing the suitability of this generic E2ES concept in a real case scenario.

1.3 Research questions

This Thesis contributes to advance the field of E2ES with respect to the design and development of robust tools that can be implemented for a wide range of passive optical missions. The implementation of these advances into an operational software tool would lead to the possibility of assessing the performance of passive optical missions as is the case of the implemented FLEX/Sentinel-3 E2ES. The main objectives, therefore, are: **(1)** *'To design a generic E2ES that can be easily adapted to reproduce most present and future passive optical spaceborne instruments'* and **(2)** *'to justify the FLEX mission for Sun-induced fluorescence retrievals using a newly developed E2ES in agreement with a generic E2ES architecure concept.'*. These objectives will be guided by the following research questions:

1. *What are the main mission and instrument characteristics that should be modeled in an E2ES for EO passive optical missions?* A wide range of EO passive optical missions have been launched in the last decades. These missions focus on various scientific applications such as ocean, atmosphere, land surface or ice/snow cover through the combination of data acquired by one or more instruments. These instruments acquire the received electromagnetic signal in specific parts of optical spectrum (from ultraviolet (UV) to thermal infrared (TIR)) with a large variety of instrument types that use different sensor technology, pointing mechanisms and optics. The problem is therefore to identify, among this wide range of instruments and satellite missions, the main characteristics that have an impact in the performance of a satellite remote sensing mission.

2. *What are the common elements that are required to develop a generic E2ES architecture for EO passive optical instruments?* As it will be seen, proposing a generic E2ES architecture for EO passive optical missions requires to identify the basic elements that conform this architecture. Various E2ES architectures will be proposed to cover a wide range of satellite remote sensing missions. In addition, each common basic element will be defined so that they can tackle different instrument types and scientific applications while still be applicable within the same generic E2ES architecture.

3. *How should be implemented a specific E2ES for ESA's FLEX/Sentinel-3 tandem mission based on a generic E2ES architecture concept?* As part of the ESA's 8th Earth Explorer

mission selection process, an E2ES for the FLEX/Sentinel-3 tandem mission must be implemented in order to evaluate the FLEX mission performance and help to consolidate its technical requirements. This question will address whether or not the proposed generic E2ES architecture can be considered as baseline for the implementation of FLEX E2ES. By answering this question, the generic E2ES architecture will be validated as a concept that can be applied to other passive optical remote sensing missions.

4. *What is the accuracy of the FLEX Level-1b mission products in terms of spectral, geometric and radiometric performance?* The performance evaluation of any satellite remote sensing mission should be done based on the accuracy of its main mission products. The Level-1b products (i.e., geolocated and radiometrically calibrated instrument data) are directly related with the performance of the satellite orbit and attitude determination, instrument optical and sensor performance, instrument calibration and data processing algorithms for correction of systematic effects. This question will tackle the issue of the accuracy of these FLEX Level-1b products.

5. *What is the impact of the current FLEX instrument design and implemented data processing algorithms to retrieve FLEX Level-2 products?* From an end-user perspective, the mission performance is, in essence, evaluated through the accuracy of its Level-2 products (i.e., bio-geophysical parameters objective of the mission). This Thesis will evaluate the accuracy of the retrieved sun-induced fluorescence through the FLEX/Sentinel-3 tandem mission data processing algorithms.

1.4 Thesis outline

This Thesis is organized in six chapter covering an introduction to development of satellite missions, an overview of ESA's FLEX/Sentinel-3 tandem mission, a conceptual design of a generic EO mission simulator for passive optical instruments, a description of the implemented FLEX E2ES and mission performance assessment results, and a discussion and conclusions obtained from the work. The outline is summarized as follows:

- CHAPTER 2 presents a general background regarding the development of EO satellite missions and, in particular, introduce the concept of E2ES for passive optical instruments. This chapter will review previous E2ES and will set the need to design a generic E2ES architecture. Next, this chapter will focus on ESA's FLEX/Sentinel-3 tandem mission as the specific case for the implementation of an E2ES.

- CHAPTER 3 describes, based on a review and classification of EO satellite missions, the proposed design of a generic E2ES architecture and interfaces for passive optical instruments.

- CHAPTER 4 describes how the proposed generic E2ES architecture concept was implemented for the specific case of ESA's FLEX/Sentinel-3 tandem mission.

- CHAPTER 5 analyzes the results of the simulations carried out to evaluate the FLEX mission performance in terms of its Level-1b (radiometry, geolocation, spectral configuration) and Level-2 (retrieval of Sun-induced fluorescence) products.
- CHAPTER 6 summarizes the accomplished objectives and the main scientific achievements, discusses the main conclusions, and proposes future research lines.

Particularly, the three thematic chapters (Chapters 3-5) represent an answer to the research questions presented in Section 1.3.

2

Background

Contents

2.1 Preparation of future Earth Observation missions

Since the successful launch and deployment of the first experimental satellite, Sputnik, in 1957, satellites have been used for applications such as surveillance, navigation, communication and EO. Notable applications of remote sensing include those relating to meteorology, agriculture, mining, geology, mapping, ecological monitoring and disaster monitoring. The conceiving of a satellite EO mission comes from end-users, particularly civil national and international administrations and scientific community, which set the requirements of a satellite mission in terms of its final mission products and services. In this respect, a solid scientific research programme sustains basic research projects as e.g., field measurements and flight campaigns, modeling of the bio-geophysical processes, development of retrieval algorithms. Through these projects, scientists conduct detailed analysis of the science behind an EO satellite mission, defining the main objectives and key measurements in order to meet the user requirements and analyzing the capabilities to perform observations and processing satellite data. Notwithstanding, the preparation and development of future satellite EO missions involve a joint effort from both scientists and engineers in order to translate user requirements into scientific measurement and technical specifications with respect satellite/instrument configuration and data processing chain [10] (see Fig. 2.1). From this perspective, space agencies organize and give support to industrial projects that perform specific mission studies (e.g., instrument design and modelization, stray-light analysis, spectral calibration) that are needed to analyze the main engineering issues of the platform and instruments to produce data with the quality needed by the end-users. Each of these scientific and industrial projects focuses on specific aspects of the mission performance and introduce assumptions on other mission characteristics. However, the translation between final mission goals (e.g., maps of bio-geophysical variables such as leaf area index (LAI) or CO_2 concentrations in the atmosphere) and technical mission requirements needs specific tools that integrate both scientific aspects of the mission (i.e., modeling of the bio-geophysical processes and retrieval algorithms) and technical characteristics of platform and instruments (e.g., modeling of instrument design, platform orbit and attitude, data calibration and geolocation). Within this frame, E2ES emerge as suitable tools to accelerate the mission development from concept to deployment and integrate, within a common framework, the advances from independent mission scientific and industrial studies.

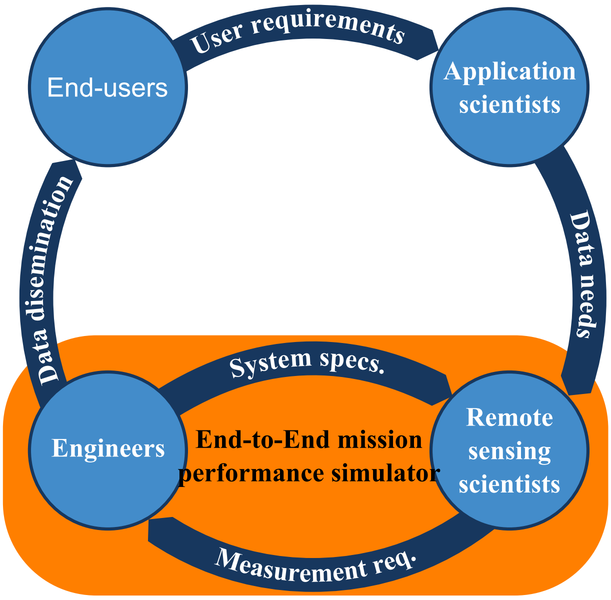

Figure 2.1: Schematic representation of the processes involved in converting users' requirements into measurement requirements that can be used by engineers to design the payload as well as the implied ground segment and processing system that need to be developed and implemented. The E2ES tool is used by both engineers and remote sensing scientists to translate measurement requirements into system specifications and optimize mission design. Based on Verstraete et al. (2015) [10].

Whereas these complex E2ES tools have traditionally been used by few users within the engineering and remote sensing teams in order to consolidate the technical aspects of the satellite mission, more simplified simulation tools based on Radiative Transfer Models (RTM) such as the Automated Radiative Transfer Models Operator (ARTMO) toolbox [11, 12] are used by end-users and application scientists to study new applications and scientific research lines as well as testing new retrieval algorithms. Therefore, one of the purposes of this Thesis is to define an E2ES robust enough so that it can be used by **(1)** engineers and remote sensing scientists to translate measurement requirements into consolidated system specifications; and **(2)** scientific community and end-users to study the user requirements and data needs of future EO missions.

2.2 End-to-End Mission Performance Simulators

The research field of E2ES started in the late 80s with the advent of EO satellite data and of configurable sensors. Users faced the problem of specifying data acquisition parameters and sensor configuration while, at the same time, being able to understand and extract the desired information from an increasing amount of satellite data. Kerekes et al. (1989) [13] proposed to use remote-sensing system models (i.e., E2ES) to better understand the remote-sensing process and the interrelations between final data and satellite-acquired data. In their work (see Fig. 2.2), an E2ES was divided in three main parts (scene, sensor and processing algorithms) that, as proof of concept, were implemented for the specific case of High-resolution Imaging Spectrometer (HIRIS)/Landsat instrument.

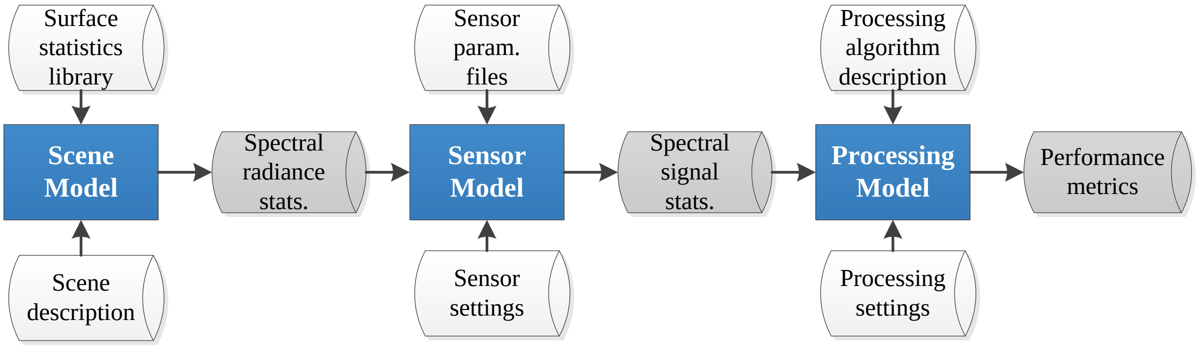

Figure 2.2: Block diagram of spectral imaging system analytical model. Source: Adapted from Kerekes et al. (2005) [14].

The *scene model* was determined by the illumination/observation geometry and surface reflectance (from a field-reflectance database). The reflected light was then propagated upwards through the atmosphere to generate the Top-of-Atmosphere (TOA) radiance scene seen by the sensor. In this propagation, the atmosphere was considered to be constant across the scene in order to speed-up the calculations performed by the Low resolution atmospheric Transmission radiative transfer model (RTM). The *sensor model* was divided into four main elements, two of which performed the spectral and spatial resampling of the input high-resolution scene through the use of the instrument response functions. After that, a random Gaussian number generation and a calibration error simulated the noise model that accounts for instrument noises and radiometric calibration errors. Finally, the sensor model simulated the analog-to-digital (A/D) conversion and quantization of the digital data. The E2ES chain was completed with the *processing* *model*, implementing an algorithm to classify the input data. These simplified models and algorithms were further developed and implemented in the work done by Kerekes et al. (2002) [15] keeping the same high-level architecture (i.e., scene, sensor and processing models). The updated scene model introduced Moderate resolution atmospheric Transmission (MODTRAN) [16] as the atmospheric RTM with more flexibility with respect the user-configuration of the scene atmospheric parameters. In addition, the scene modeled the shadow effects due to topography. Also, the sensor model improved parameterization and modelling of photon noise, thermal noise, readout noise, relative radiometric calibration error and quantization noise in the A/D conversion. The processing algorithms included an atmospheric correction algorithm based on the contrast between bright and dark surfaces. In 2005, Kerekes et al. [14] further extended their work with the simulation of scenes in the thermal domain and introducing adjacency effects. The sensor model was further enhanced for dispersive spectrometers and Fourier transform spectrometers.

Börner et al. (2001) [17] also developed an E2ES, called *SENSOR*, for the simulation of hyperspectral instruments, and implemented for the Airborne Prism Experiment. As in the works of Kerekes et al., *SENSOR* was divided into three main parts (or modules) as shown in Fig. 2.3.

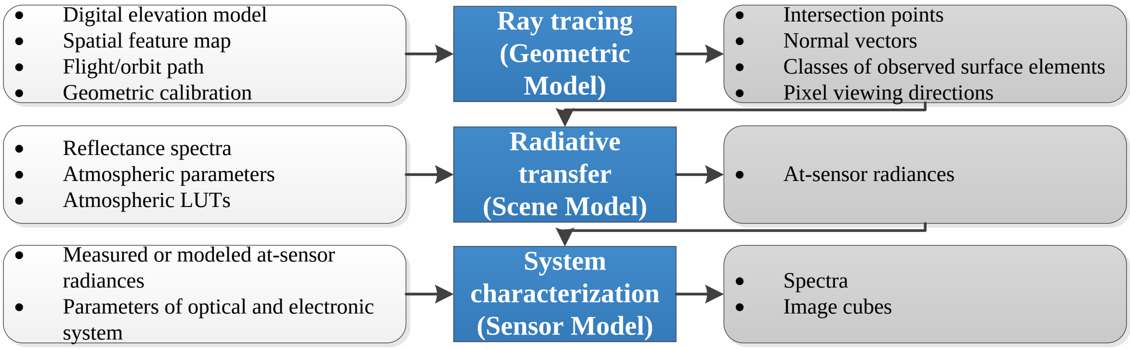

Figure 2.3: Scheme of *SENSOR* simulator for optical remote sensing systems. Modules (**blue**), input (white) and output (gray). The nomenclature used by Kerekes et al. is applied for cross-reference. Source: Adapted from Börner et al. (2001) [17].

The *ray tracing* module determined the geometric relation between the scene as observed by the instrument and illuminated by the Sun through a ray tracing algorithm. This geometry model considered the surface topography and intersected the instrument line of sight and solar illumination vector, determining the observation and illumination geometry of each instrument pixel. Each surface element was associated with a land cover map that linked with a spectral library of simulated or measured surface reflectance. After the scene is defined and the observation/illumination geometry is calculated, the *radiative transfer* module propagated the reflected light through the atmosphere based on a pixel-wise interpolation of pre-computed MODTRAN look-up tables (LUT) taking into account topographic effects on the reflected signal (e.g., sky-view factor, shadow). The E2ES chain ended with the execution of the *system characterization* module, which simulated the behavior of the instrument considering effects such as spectral response function, optical transmission, photon noise, quantum efficiency, non-uniformities in the detector, dark signal, white noise of the electronics, A/D conversion, modulation transfer function and blurring by flight motion.

The *PICASSO* software tool was developed by Cota et. al (2010, 2011) [18, 19]. Like other E2ES, *PICASSO* starts with a description of the remote sensing system to be modeled through a set of user-defined instrument configuration parameters. The scene model was based on an external input image with higher spatial and spectral resolution than the instrument resolution that was converted into a reflectance map (through the use of reflectance spectral libraries) and propagated with MODTRAN to TOA radiance (considering an homogeneous atmosphere). As for *SENSOR*, the instrument was executed after the generated scene to perform the spatial/spectral image degradation and to introduce instrument noises and non-uniformity effects from various sources (e.g., smearing, A/D Conversion and quantization, quantum efficiency, detector noise, near-field noise).

Similar work was carried out by Coppo et al. (2013) [20] with emphasis on the description of equations applied to optical imaging instruments. They implemented an E2ES software tool (*SG_SIM*) for the simulation of synthetic airborne/spaceborne visible and infrared instruments. This E2ES tool was divided in six main modules (see Fig. 2.4) that perform similar tasks as those modules defined by Kerekes, Börner and Cota.

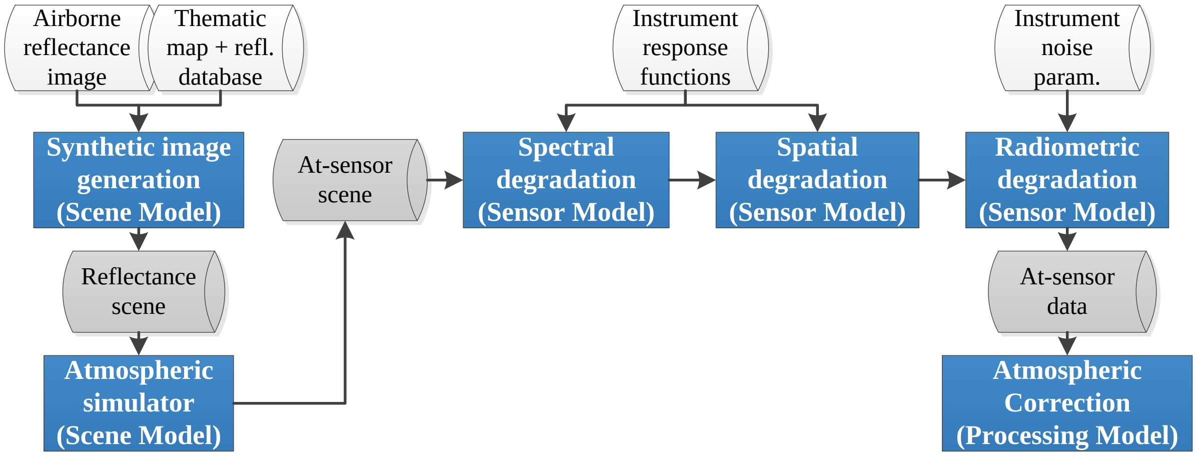

Figure 2.4: Scheme of *SG_SIM* simulator for airborne/space-borne optical sensor data simulation. The nomenclature used by Kerekes et al. is applied for cross-reference. Source: Adapted from Coppo et al. (2013) [20].

SG_SIM starts with the *synthetic image generation* module that generates a high spatial and spectral resolution scene based on input airborne images. Alternatively, this module can generate a synthetic scene based on the use of thematic maps where each scene pixel is associated with a combination of end-members from a surface reflectance database. Once the surface reflectance scene is defined, the *atmospheric simulator* module propagates (using MODTRAN) the reflected light through an atmosphere characterized by the atmosphere and aerosol types while neglecting 3D topography effects. The atmospheric propagation considers lambertian surface scattering, near-nadir observation, flat Earth surface and no-adjacency effects. The third and fourth steps consist respectively on the spectral and spatial degradation of the input high-resolution scene by the instrument response functions. These response functions are obtained on an inverse Fourier transform of a parameterized modulation transfer function. The next module performs the *radiometric degradation* of the at-sensor resampled signal based on random values from a Gaussian distribution of a parameterized noise-equivalent difference-radiance. This module includes the effects of noise variance of the detector (dark current, read-out and Johnson noises), front-end electronics and A/D converter, and photon noise. Finally, the *atmospheric correction* module implements an atmospheric correction algorithm for the characterization of aerosols, water vapor and inversion of surface reflectance from instrument radiances.

Other commercial software such as *MCScene* [21] are used for the TOA radiance scene generation based on a direct simulation Monte Carlo approach to model the 3D atmospheric radiative transfer using MODTRAN-generated scattering and absorption optical properties.

These simplified E2ES tools, among others, were conceived as generic Phase[1] 0/A tools for the dimensioning of new optical instruments and for tracing the link between user and instrument requirements through the flexibility of the parameterizations of geometry, scene and sensor models. In parallel, several scientific research activities and industrial projects have developed mission-specific E2ES tools as part of satellite mission development Phases 0/A and C/D. The following paragraphs give an overview of these remote-sensing system models.

The architecture of the Environmental Mapping and Analysis Program (EnMAP) end-to-end simulator (*EeteS*) [22, 23] follows the concepts introduced in *SENSOR* and the works of Kerekes by dividing the E2ES into four main modules. First, the *EnMAP Scene Simulator* module uses an external input reflectance image at high spatial resolution that is propagated through the atmosphere to generate TOA radiance at high spectral resolution. This first module integrates the sensor model by **(1)** simulating the scene spatial and spectral resampling caused by the instrument response functions, introducing non-uniformity effects such as spectral smile, keystone and spatial aberrations and **(2)** converting the resampled image into digital counts. The radiometric part of the sensor adds effects of read-out noise, shot noise, dark current, A/D conversion, quantization noises and variable offsets and gains from the detector elements. Second, the *Onboard Calibration* module simulates the process of the onboard characterization of the absolute calibration coefficients, dark current and correction of detector non-linearity. Third, the *L1 Processor* integrates the calibration coefficients and characterization of non-linearity effects to recover the radiometric information from the sensor data in digital counts. Finally, the *L2 Processor* module performs the spatial co-registration of the two EnMAP spectrometers,

---

[1] See *Acronyms and Definitions* section at page xv for a brief description of space mission Phases.

corrects atmospherically the data and orthorectifies the image. The same architecture concept as EeteS was applied to the Copernicus' Sentinel-2 mission in the *S2eteS* software tool [24]. *S2eteS* implements a tailored model of Sentinel-2 radiometric noises, detector non-linearity and A/D conversion. Both *EeteS* and *S2eteS* generate synthetic EnMAP and MultiSpectral Instrument (MSI)/Sentinel-2 data from an input reflectance scene. Therefore, these software tools allow doing performance assessment of the at-sensor TOA radiances and the atmospherically corrected surface reflectance without the possibility, a priori, of validating algorithms for the retrieval of bio-geophysical variables due to the absence of input maps of bio-geophysical variables in the generation of the scene. In addition, these tools define the input scene in sensor focal plane coordinates, therefore not being fully representative of the 3D interaction of the instrument observation geometry with the scene.

Similar to EnMAP, the Italian hyperspectral mission PRecursore IperSpettrale della Missione Applicativa (PRISMA) developed its own E2ES [25]. The PRISMA E2ES was divided into three main modules, the first of them being the *scenario builder* that simulates a ground map of surface Lambertian reflectance based on a classified remote sensing image associated with a surface reflectance spectral library, adding textures and mixing of end-members to add realism to the input scene. The simulation of the atmospheric effects is carried out in the *atmospheric propagation calculator* module, which assumes an homogeneous atmosphere modeled by MODTRAN without including adjacency effects. The last module (*sensor simulator*) implements the spatial/spectral degradation of the input scene based on the modeling of straylight, fore-optics, detector sampling, and noise. Some of the implemented features included in the simulator are: platform vibration and orientation, fore-optics and spectrometer modulation transfer function, smile and keystone, pixel integration, spatial and spectral sampling, chage coupled devices (CCD) pixels inhomogeneity, photonic noise, detector thermal noise, change transfer noise, smearing and quantization.

Parente et al. (2010) [26] developed an E2ES for the Compact Reconnaissance Imaging Spectrometer on board of the Mars Reconnaissance Orbiter. The system is divided into three main parts that cover the scene generation (Surface and Atmosphere models), instrument behavior (spatial/spectral resampling and instrument noise generation) and Level-2 data processing. The scene model generates a fractal digital elevation model (DEM) that is used to distribute a discrete land cover map over the high spatial resolution scene. Each land cover class is associated with a mixture of two surface reflectance end-members. Once the surface reflectance map is generated, the reflected light is propagated through the atmosphere using the Discrete Ordinates Radiative Transfer Program for a Multi-Layered Plane-Parallel Medium (DISORT) assuming that the atmosphere is homogeneous over the scene and the light propagation is not affected by the pixel-to-pixel difference in surface altitude. The instrument model simulates the spatial and spectral resampling of the high-resolution input scene by convolution with a parametric representation of the instrument spatial and spectral response functions. The resampling includes distortions such a spectral smile. Then, the instrument model introduces a noise model (burst, elevated and spike noises) that takes into account the time-dependent behavior of the infrared detectors. Finally, the data processing model reproduce the atmospheric correction and denoising of the instrument data and the algorithms for image classification.

As part of the ESA's mission selection process for 6th Earth Explorer, Voors et al. (2997) [27] developed the E2ES for the Earth Clouds, Aerosols and Radiation Explorer (EarthCARE) mission. Similarly, during the 7th Earth Explorer selection process, Scagliola et al. (2012) [28] and Lopez-Dekker et al. (2012) [29] developed respectively the E2ES for the ESA's Cold Regions Hydrology high-resolution Observatory (CoReH2O) and BIOMASS missions during the Phase A/B1 of the mission development. Despite of being radar missions, the architecture of the developed E2ES were also divided into five main modules that includes Geometry, Scene Generator, Instrument Simulator, (Level-1) Product Generator and Level-2 Retrieval. In addition, they implement an additional module for the mission performance evaluation by comparing reference data from the scene generation with retrieved Level-1 and Level-2 data. Also, E2ES were developed for Soil Moisture and Ocean Salinity (SMOS) [30], Surface Processes and Ecosystem Changes Through Response Analysis (SPECTRA) [31], PREMIER [32] and CarbonSat [33], candidate or selected missions for the 2nd, 6th, 7th and 8th Earth Explorer. All these E2ES were used to evaluate each mission performance with a set of guidelines that allow the intercomparison of the performance results and the selection of one candidate mission to be finally implemented.

Also as part of ESA's Sentinel-2 and Sentinel-3 activities in Phase C/D, the E2ES for Sentinel-2 images [34] and for Sentinel-3 optical instruments (Ocean and Land Color Instrument (OLCI) and Sea and Land Surface Temperature Radiometer (SLSTR)) [35] were developed. These tools were used for the technical definition of their Groung Processor Prototypes (GPP) as well as the follow-up of the Ground Segment implementation and validation, data processing during mission commissioning phases and verification of the correct functioning of the operational processors implemented within the Payload Data Ground Segment.

Most of these E2ES project activities and research studies have been developed without harmonization between them. This implied that for each EO mission in Phase 0/A, a new mission simulator was designed and developed from scratch without reusing codes and simulator frameworks developed in other similar activities. In addition, the evolution of the design and processing algorithms of an E2ES between early phases of a satellite mission to advanced implementation phases involved costly reengineering work. For this reason, ESA has promoted several activities in order to reduce this reengineering process and setting guidelines for the harmonization and development of future E2ES. A brief description of these projects is given below:

- The *ARCHEO-E2E* [36] and *SS-E2E* [37] projects aimed to define a reference architecture for EO and Space Science end-to-end mission simulators. The rationale behind these projects is promoting reuse in the development of mission performance simulators by describing architecture elements that can be generalized for the various mission categories, payloads and planetary bodies.

- The *EOMODEL* [38] project builds upon the *ARCHEO-E2E* project to consolidate its results and implement a selection of some of the identified modules. Thus, the project aims to identify all the generic models needed for an EO E2ES and define, develop and validate a subset of these models.

- *OpenSF* [39] is a software that provides a framework to support standardized E2ES capabilities. The OpenSF tool allows to plug in scientific models and product exploitation tools with ease using a well-defined integration process.

As presented in this Section, the field of E2ES has increased in the last years and have gained more importance for the design of new EO mission and consolidation their payloads and data processing algorithms. Though the E2ES concept is applicable to any type of EO remote sensing mission and instrument type, this Thesis will focus on the design and development of E2ES for passive optical instruments.

2.3 Specificities for passive optical missions

Remote sensing instruments can be categorized in terms of the spectral region at which data is acquired (optical versus microwave) and in terms of the way instruments acquire the data (active versus passive). These two criteria have an impact on the definition and design of an E2ES for EO satellite missions. This Thesis focuses on the study of passive optical instruments.

Passive optical instruments measure energy levels from natural light sources (Sun, Moon or stars) as it is absorbed, scattered and energy which is emitted (thermal and/or fluorescence) from the Earth surface and atmosphere. The entire region of electromagnetic energy distinguished by wavelength is called the electromagnetic spectrum (see Fig. 2.5), from which optical instruments acquire data in from UV-TIR spectral regions.

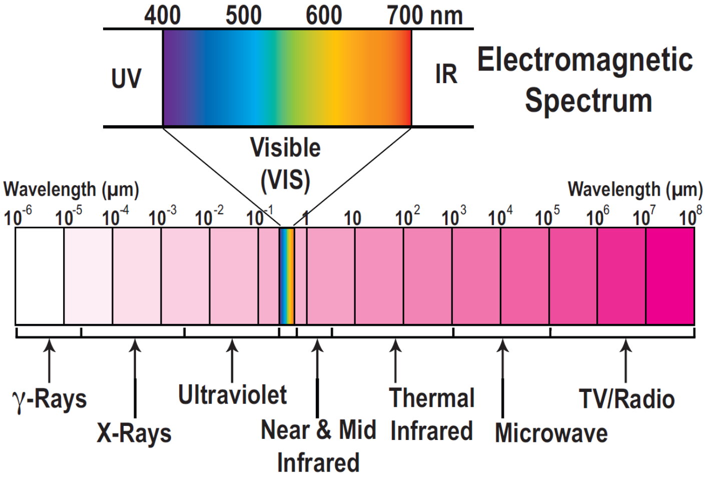

Figure 2.5: Electromagnetic spectrum classification based on wavelength range (in logarithmic scale).

The information provided by passive optical instruments has opened new fields of applications with direct impact on Earth and space science and civil applications such as meteorology and weather forecasting, forestal and agriculture applications, surface topography or water quality among other environmental aspects of the Earth system and their interactions. These instruments reach spatial resolutions from 1 m to 5 km, imaging the Earth with swath widths in the order of tens to hundreds of kilometers. Spectral, radiometric or polarimetric information can be obtained from nadir-viewing or pointable instruments/platforms allowing a global coverage of the Earth.

2.4 The FLEX mission: retrieving sun-induced fluorescence from space

Although the design of a generic E2ES architecture concept is the main goal of this Thesis, its implementation to ESA's FLEX/Sentinel-3 tandem mission will be considered as a proof of concept of the proposed E2ES architecture. This Section will give an overview of the scientific user requirements, data needs and system specifications behind the FLEX mission.

2.4.1 The role of Sun-induced fluorescence signal from vegetation

Photosynthesis is the process by which vegetation converts the absorbed Sun-light energy into chemical energy leading to vegetation growth through conversion of CO_2 and H_2O into carbohydrates and O_2. In this process, light is absorbed by photosynthetic pigments, mainly chlorophyll and carotenoids. By photon absorption, the chlorophyll molecule reaches an unstable excited energetic state (see Fig. 2.6 left) that returns to its base energetic level (ground state) by four means of dissipation mechanisms (see Fig.2.6 right): part of it is used to perform photosynthesis; another part is dissipated through Sun-induced fluorescence (SIF) spectral emission; the remaining energy is dissipated in terms of heat through two mechanisms regulated by the vegetation.

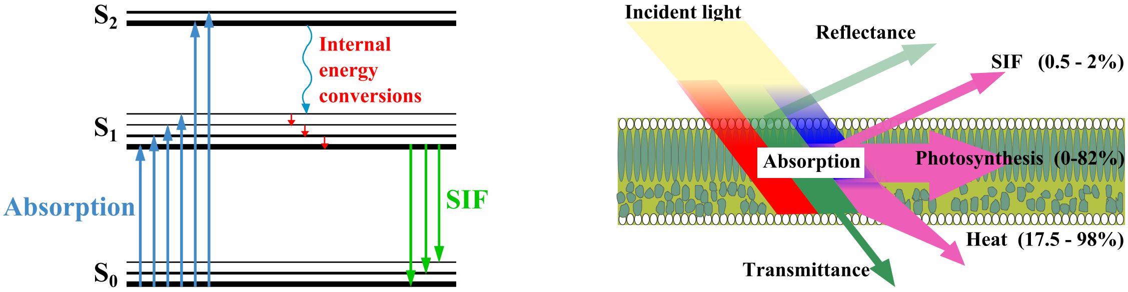

Figure 2.6: Left: Scheme of energetic levels S of the chlorophyll molecule as consequence of light absorption and SIF emission. S_0 is the ground level. S_1 and S_2 are excited energetic levels. Right: Scheme of the light absorption by the leaf and energy dissipation mechanisms.

Thus, by measuring SIF one can have a sensitive indicator of the actual photosynthetic activity in vegetation and the changes on photochemical efficiency [40], providing a novel tool for the early detection of stress in vegetation before damages are visible in reflected light (e.g., [41, 42]). In addition, SIF is a good indicator of environmental perturbations such as ozone excess, presence of contaminants, lack of nutrients or water stress, which are interesting for environmental studies and precision farming. The observation of SIF is also of particular interest to refine the predictive capability of global carbon cycle models through improved parameterizations of canopy photosynthetic activity and surface-atmosphere water and energy exchange processes [43, 44].

The SIF spectrum (see Fig. 2.7) is characterized by two peaks with maxima at 685-690 nm and 735-745 nm respectively. The low SIF signal is superimposed with the high signal reflected by vegetation, thus making necessary the use of state-of-the-art data processing algorithms to disentangle both signals from EO satellite radiance measurements. The recent advances in remote sensing offer scientists new tools for measuring SIF from space [45]. Several techniques have been proposed in the past based on hyperspectral measurements [46, 47]. These methods use atmospheric absorption bands (see Fig. 2.8) to uncouple the Sun-reflected light from the SIF emission, particularly the O_2-B and O_2-A absorption bands in the red (687 nm) and near-infrared (760.4 nm) spectral regions. Given the strong absorption of these bands, the solar reflected light gets importantly reduced making it comparable with the SIF emission. Given the narrow width of these bands, SIF retrieval methods require of a very high spectral resolution, on the order of 0.1 nm [45]. In addition, these techniques are based on measurements at the top of the canopy, requiring an accurate atmospheric correction of the satellite data.

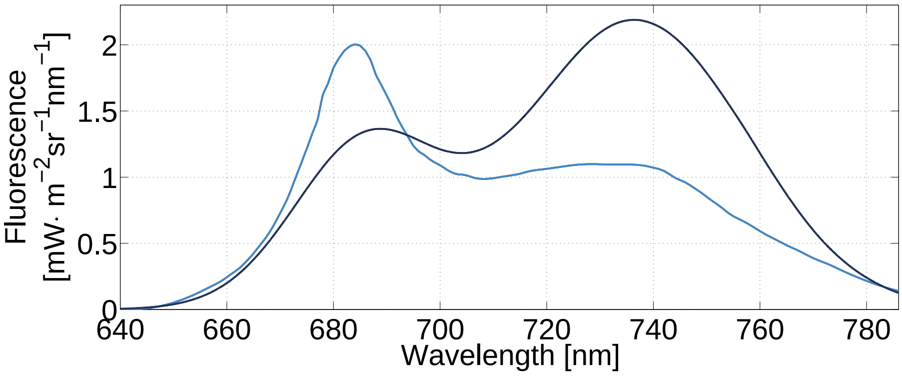

Figure 2.7: Example of two SIF spectra for different species and/or stress conditions.

Although satellite remote sensing SIF measurements have been performed in the past [48–50], the future ESA's 8th Earth Explorer mission FLEX [51] has been specifically designed and optimized to globally measure SIF emission from terrestrial vegetation.

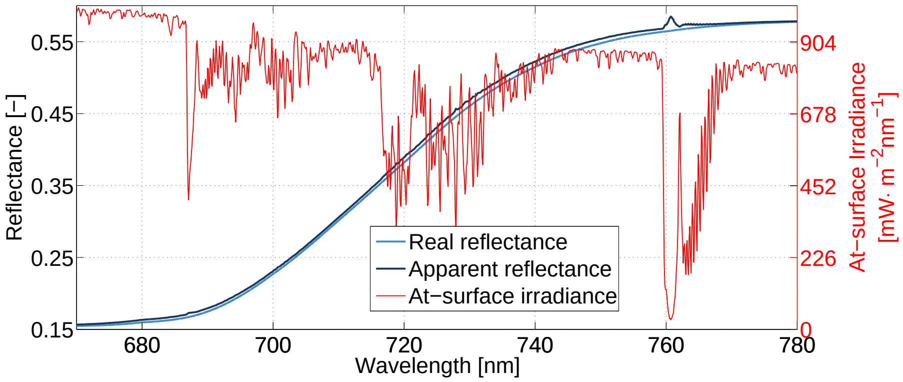

Figure 2.8: O_2 absorption bands allow uncoupling the SIF emission from the real reflectance (**light blue**) based on the peaks in the apparent reflectance (dark blue).

2.4.2 Summary of FLEX mission observational requirements

In this Section, a brief summary of the FLEX mission observational requirements is presented. A detailed description of these requirements is available in *FLEX Report for Mission Selection* (Chapter 4) [51].

Land vegetation SIF is a highly dynamic variable both spatially and temporally. For a successful understanding of this variability, FLEX should be able to monitor changes in SIF at spatial resolutions that allow to identify changes at level of land management units and, at the same time, with monthly observations to analyze seasonal temporal dynamics in vegetation. For this reason, FLEX will acquire images over land, major islands ($>$100 km^2) and coastal waters (within 50 km distance from land) in latitudes from 56°S and 75°N at a spatial sampling of 300 m and spatial resolution of 330–350 m/pixel. Regarding the temporal sampling, the FLEX mission should capture seasonal changes in SIF, thus a revisit time of 1 month at the equator (higher revisit over high latitudes) is required. In addition, the monitoring of SIF interannual changes due to climate variability requires a mission duration of 3 to 5 years.

In order to have a compromise between maximum SIF and maximum solar illumination so that the SIF signal can be better captured by a remote sensing instrument, the optimal observation time should be around 9:30-10:00 local time. Given that the satellite orbit constrains the illumination conditions around the Earth, selecting 10:00 as the time to cross the equator guarantees that observations will be taken around the globe between 9:00 and 11:30 local time at various latitudes and seasons.

The retrieval of SIF cannot be done directly from satellite measurements as this signal is superimposed on the background signal from reflected light. However, retrieving SIF from space is possible due to the different atmospheric path of the photons coming from reflected (Sun-Target-Sensor) and from SIF emission (Target-Sensor). In regions with important solar and atmospheric absorptions, the SIF signal is comparable to the reflected signal and thus it is possible to decouple both signals. The oxygen absorption bands in the red (687 nm) and near-infrared (760.4 nm) spectral regions are suitable candidates for the measurement of SIF from space due to their well-characterized absorption spectrum, its low variability in space and time and its vertical homogeneity. The TOA radiance measurements should be compensated for the atmospheric scattering and absorption effects, thus atmospheric water vapor and aerosol characteristics should be determined as mission measurements. Water vapor retrieval is possible through differential absorption techniques in deep water absorption bands (e.g., at 940 nm). The aerosol characterization needs full-spectrum measurements from the visible to the short-wave infrared, preferably with dual-angle observations of the same target.

SIF per se does not provide a complete understanding of the photosynthetic activity of vegetation and its relation with the global carbon balance and stress conditions in vegetation. Further information is therefore needed to interpret vegetation SIF dynamics. For instance, SIF can be higher due to growth in vegetation (higher LAI) or increase of fractional soil cover, thus not implying differences in photosynthesis levels or plant stress conditions. Another element that is particularly important for understanding the relationship between SIF and photosynthesis is the heat dissipation mechanisms in vegetation, also called non-photochemical quenching. This mechanicsm can be measured through reflectance changes in the spectral region of the Photochemical Reflectance Index (530–570 nm). Lastly, temperature measurements are required as it regulates the biophysical and physiological processes in vegetation. Therefore, FLEX should be able to measure the following information in addition to SIF:

- Non-photochemical quenching through changes in reflectance at 500–600 nm.
- Total light absorbed by the vegetation, which depends on key biophysical variables such as chlorophyll concentration, LAI and fractional coverage.
- Canopy temperature.

The measurements needed for an accurate SIF retrieval and interpretation of its values and dynamic requires a number of instruments. A tandem mission concept with Copernicus' Sentinel-3 (S3) [52] is proposed in order to re-use existing capabilities while ensuring proper spatial and temporal co-registration of the measurements taken by the various instruments within the mission. S3 is specifically designed for monitoring the color and temperature of vegetation and water bodies, with several applications in environmental studies and climate change. S3 host two passive optical instruments: OLCI and SLSTR. OLCI is a pushbroom imaging spectrometer acquiring large swath (1270 km) images with a spatial resolution of 300 m in 21 spectral channels in the 400–1020 nm spectral range. Its main purpose is to study vegetation and water quality. SLSTR is a whiskbroom radiometer with a conical scanning designed to measure land and water surface temperatures with an accuracy of 0.3 K. It counts with 9 spectral channels in the visible and thermal infrared spectral range with a resolution between 500 m and 1 km. S3 instruments can provide valuable information for the characterization of the atmosphere (clouds, aerosols, water vapor) and land (land-cover type, biophysical parameters and surface temperature). These parameters can be directly obtained from the Level-2 data or through the processing of Level-1b/c data in synergy with FLEX data. Also, the spatial resolution of OLCI (300 m) and SLSTR (500 m to 1 km) are similar to the requirement imposed to FLEX. In addition, Sentinel-3 orbit is in agreement with the FLEX orbit requirement of a descending node at 10:00 local time.

In order to limit the temporal misregistration effects between FLEX and S3 instruments (e.g., cloud motion, surface temperature), FLEX should fly with a time delay of 6–15 seconds with respect to S3. At the same time, in order to limit surface bidirectional reflectance effects, Fluorescence Imaging Spectrometer (FLORIS) should point to nadir with a tolerable off-zenith angle about 5°. With respect to the effect of spatial misregistration, for the given FLEX-S3 orbit conditions, a FLORIS-OLCI geometric misregistration about 0.2 pixels is tolerable. This spatial misregistration can be increased a factor 3–5 with respect FLORIS-SLSTR due to the lower spatial variability of surface temperature and the larger spatial sampling distance of SLSTR.

The S3 orbit altitude drives the FLORIS swath requirement to satisfy a global coverage in one orbit cycle of 27 days. A swath width of 104 km at equator would achieve this requirement but a wider swath of 150 km is preferred to increase the revisit time at higher latitudes and limit the impact of cloudiness.

FLORIS instrument observational requirements are constrained by the capabilities of measuring SIF, determination of the energy dissipation mechanisms and measuring the absorbed light by vegetation.

SIF is emitted in the range between 650 nm and 800 nm but, in order to limit the effect of the atmospheric water vapor band at 800 nm, the upper end of the spectral range should be limited to 780 nm. In this range (650–780 nm) the requirement with respect the spectral resolution and sampling is dictated by the ability of decoupling SIF from reflectance by using the O_2 absorption bands. The optimal separability between SIF and reflectance signals is achieved with a spectral resolution around 0.3 nm. At this resolution, a spectral sampling of 0.1 nm is needed to avoid aliasing in the measured signal. These requirements are only needed within the O_2 absorption regions, elsewhere the resolution and sampling can be degraded up to 2 nm. The Signal-to-Noise Ratio (SNR) requirement is derived by setting an accuracy of 10% in the retrieved total SIF (integrated value) for typical SIF values. This 10% accuracy is sufficient to discriminate several different values of photosynthesis from minimum to maximum values and, in addition, is within the expected natural SIF variability due to the individual behavior of each leaf in the canopy. An error of 10% in the total SIF implies that the SIF errors in the O_2 absorption bands cannot be larger than 9% (at 687 nm) and 17 % (at 760 nm).

With respect to the determination of energy dissipation, these mechanisms are associated with changes of vegetation reflectance spectrum in the spectral range of 500–600 nm. Since atmospheric absorptions are not to be resolved in this range, FLORIS spectral configuration can be reduced to a resolution of 3 nm with 2 nm sampling. The measures in this spectral range should be temporally and spatially co-registered with those acquired in the O_2 spectral regions for having a simultaneous observation of SIF and the non-photochemical quenching.

The measurement of absorbed light by vegetation is necessary as SIF directly depends on the intensity of the incident light and, in particular, of the absorbed light by the chlorophyll molecules, which is dominant in the 600–650 nm range.

Since FLEX SIF retrieval algorithm is based on a spectral fitting technique [53], the relative radiometric accuracy is determined by an acceptable error on the least-squares spectral fitting. The absolute radiometric accuracy for all instrument spectral channels should be limited within 5% threshold (3% absolute error + 1% polarization sensitivity + 1% straylight effects) and temporal stability of 0.5% along one orbit. The cross-calibration between FLORIS and OLCI should be within 2% difference for all FLORIS-OLCI overlapping spectral channels.

The main mission observational requirements driving FLEX design are summarized in Tab. 2.1 and Tab. 2.2:

Table 2.1: Level-1b observational requirements that drive the FLORIS design.

Observational requirement	Specification
Pointing	5° off-nadir
Dynamic range	Dark (L_{min}) to bright (L_{max}) soil/vegetation
Swath width	150 km
Spatial Sampling Distance (SSD)	300 m
Spectral stability	1 nm
Knowledge of instrument response function	1%
Spectral coregistration	<0.1 SSD
Spatial coregistration (intra/interband)	<0.15/0.3 SSD
Interchannel temporal coregistration	2 seconds
Absolute radiometric accuracy	5%
Relative radiometric accuracy	1%
Polarization sensitivity	2%
Calibration	Sun-based

Table 2.2: FLORIS spectral and SNR requirements at Level-1b.

Band	Band I	O_2-B		Band II			O_2-A		
λ [nm]	500	677	686	697	740	755	759	762	769-780
FWHM [nm]	3.0	0.7	0.3	2.0	0.7		0.3		0.7
SSI [nm]	2.0	0.5	0.1	1.0	0.5		0.1		0.5
SNR	245	340	175	425	Linear from 510 to 1015	1015	115	Linear from 115 to 455	1015

2.4.3 ESA's FLEX/Sentinel-3 tandem mission

In this Section, a brief description of the FLEX mission elements is presented. Further information is available in *FLEX Report for Mission Selection* (Chapter 5) [51].

Based on the observational requirements for the observation of SIF from space, the FLEX mission (see Fig. 2.9) concept consists of a single platform with two imaging pushbroom spectrometers (FLORIS-HR and -LR) [54]. FLORIS-HR, through a focal plane separator, will acquire in the O_2-B (677-697 nm) and O_2-A (759-780 nm) spectral absorption bands at 0.3 nm (0.1 nm) spectral resolution (sampling) for the non-binned spectral channels within the absorptions and at 0.7 nm (0.5 nm) spectral resolution (sampling) for the binned channels around the O_2 absorptions. FLORIS-HR is designed to provide the measurement capabilities that will allow decoupling SIF and reflectance within these O_2 bands. The FLORIS-LR spectrometer will cover the spectral range used to obtain information about the absorbed light by vegetation and understand the non-photochemical energy dissipation mechanisms. Therefore, FLORIS-LR is designed to cover the spectral range between 500 nm and 780 nm with 2 nm spectral resolution and sampling.

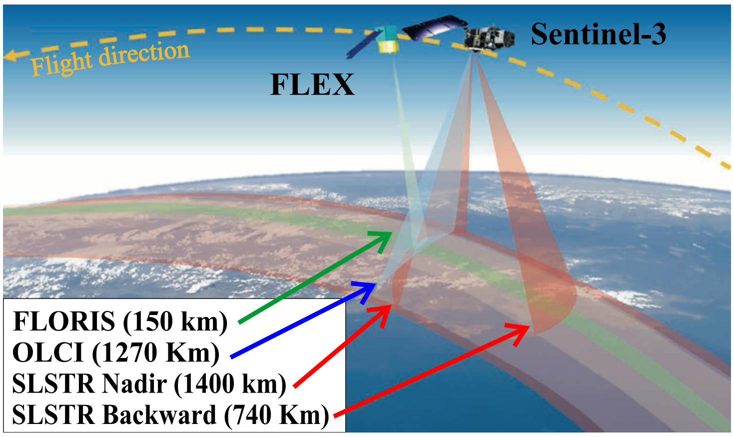

Figure 2.9: Artist concept of FLEX/Sentinel-3 mission with FLORIS, OLCI and SLSTR swath coverage.

FLEX will operate in tandem with S3 satellite in a Sun-synchronous polar orbit at 10:00 local time of the descending node and acquiring data over the same target with 6–15 s time delay. The flight operations with S3 imposes a specific FLORIS optical design so that the instrument fulfills the spatial mission requirements (e.g., coverage, spatial resolution/sampling, revisit time). The focal plane will be divided in 500 pixels in the across-track direction, each with a spatial resolution and sampling of nearly 300 m, and thus with a swath width of 150 km. With this swath width and orbit, the revisit time over the equator will be 27 days.

The FLEX/Sentinel-3 mission key sensor characteristics are summarized in Table 2.3.

Table 2.3: FLORIS, OLCI and SLSTR sensor characteristics as per [51, 55].

	FLEX		**Sentinel-3**	
	FLORIS-HR	FLORIS-LR	OLCI	SLSTR
Imaging principle	Pushbroom-grating			Scanning radiometer
# pixels×bands[2]	~500×292	~500×245	21	9
Spectral range [nm]	677–697 (O_2-B) 740–780 (O_2-A)	500–780	400–1020	555–12000
Spectral resolution[3]	0.3 nm	2 nm	2.5–40 nm	20–1000 nm
Spectral sampling	0.1 nm	0.7 nm	–	–
Spectral coregistration	0.01 nm		–	–
Swath width	150 km		1270	1420 (nadir) 740 (oblique)
Spatial sampling	300 m		300 m	0.5–1 km
Spatial coregistration	45–90 m		–	–
Geolocation accuracy	120 m		–	–
SNR @L_{ref}	115–1015 (See Fig. 5.11)		150–2200	25–900
NeΔT	–	–	–	20–80 mK (TIR)
Radiometric accuracy	5% abs, 1% rel		2% abs, 1% rel	2% (VIS-SWIR) 0.1 K (TIR)
Radiometric resolution	16 bit		14 bit	
Coverage	Land, coast, major islands		Global	
Revisit time	<27 days		<2.2 days	<1.8 days

The main FLEX Level-2 products consist on georeferenced atmospherically-corrected surface reflectance and emitted SIF. Additionally, Level-2 products include biophysical parameters of vegetation associated with the photosynthetic activity such as canopy chlorophyll content, LAI and fraction of Absorbed Photosynthetically Active Radiation. The main application of FLEX mission products will be in carbon assimilation and climate change studies, early stress detection in vegetation, and studies of vegetation productivity and food production. SIF detection will give an insight of the photosynthetic process, offering an important knowledge on the productivity of terrestrial vegetation and global carbon balance, fundamental for climate change studies as vegetation is one of the main sinks of atmospheric CO_2. In the context of food production and sustainable bioeconomy, a rising problem is the propagation of plagues and illness in vegetation, for which global maps of SIF would provide a useful tool for the monitoring of the first signs of vegetation stress, orienting end-users in the management of agricultural and forestal resources.

In the context of E2ES, ESA requested to develop an E2ES for the FLEX/S3 tandem mission in order to evaluate the maturity and feasibility of the mission concept in view of the selection of ESA's 8th Earth Explorer. In addition, FLEX is considered as a suitable candidate to implement the concept of a generic E2ES architecture given the complexity of the mission (i.e., tandem flight, two platforms, multiple instrument types, visible (VIS) to TIR spectral range, fluorescence, high spectral resolution).

3

Design of a generic end-to-end mission performance simulator

Contents

As part of satellite mission development, E2ES have been studied, developed and applied for more than three decades [13, 15, 17, 22, 23, 28, 29]. These software tools reproduce all aspects of satellite missions including platform orbit/attitude, synthetic scene radiative transfer generation, sensor behavior, ground image processing and product evaluation. E2ES are unique frameworks to determine the mission characteristics impacting data quality and achievement of scientific goals, to enable the consolidation of mission requirements, and to check the consistency of platform and payload specifications. These tools support trade-off studies and are useful in preparation for system calibration tests. From an image processing perspective, E2ES help in the development, testing and optimization of retrieval schemes prior to mission operations [8, 9]. The simulated data should allow analyzing the impact of individual error sources on the output of an ideal system, both separately and simultaneously, and to assess the performance of retrieval algorithms and of their associated assumptions.

ESA is currently developing these E2ES to study and intercompare the performance of EO satellite missions in competition (e.g., ESA open calls for Earth Explorers[1]). If the mission is approved, these E2ES can evolve into a supporting tool for the detailed design definition, preparation of ground processing implementation and testing of Calibration/Validation (Cal/Val) procedures. However, the design and evolution of an E2ES architecture and interfaces, and the implemented processing algorithms involve a costly engineering process that require modifications and replacements of the components of previous versions of a simulator. In order to reduce this engineering process and to facilitate the design, implementation and evolution of future E2ES tools, a generic architecture promoting reuse of these tools was studied. Thus, this Chapter tackles the two first **main objectives** of this Thesis i.e.:

- To review and categorize past, present and planned EO passive optical missions, determining the main characteristics that impact the mission performance.
- To identify and design the common elements required to develop a generic E2ES architecture for EO passive optical missions in Phases A/B1.

The rationale of this generic E2ES concept is presented in the following Sections:

- A review of past, current and future EO passive optical missions is presented in Section 3.1 with the goal of finding commonalities and specificities of passive optical satellites and instruments.
- Section 3.2 gives an overview of the proposed mission and instrument classification, identifying common elements that define a high-level E2ES architecture for EO passive optical missions and how the particularities of passive optical instruments affect at a lower-level of the E2ES architecture.
- Based on this classification, a generic E2ES architecture is described in Section 3.3, showing how it adapts to different passive optical mission and instrument concepts.

This chapter is partly based on:

- C. de Negueruela, M. Scagliola, D. Guidici, J. Moreno, **J. Vicent**, A. Camps, H. Park, P. Flamant, R. Franco, (2012). ARCHEO-E2E: A Reference Architecture for Earth Observation End-to-End Mission Performance Simulators. In: SESP, Simulation and EGSE facilities 2012, 25-27 September, Noordwijk, The Netherlands.
- Reference Architecture for Earth Observation End-to-End Mission Performance Simulators (ARCHEO-E2E), ESA-ESTEC Contract No. 4000104547/11/NL/AF [2012]

---

[1] ESA's 8th Earth Explorer User Consultation Meeting.

3.1 Review of passive optical space missions

Since 1969, several space agencies and private companies have designed, independently or in cooperation, more than 450 EO missions [56, 57]. These satellite missions have a wide range of instruments that can be classified in four main groups: passive/active optical or microwave missions. Among them, passive optical instruments are one of the most common types of satellite payloads for EO. With a swath width in the order of tens to hundreds kilometers, these instruments acquire global and continuous information of the processes occurring in the Earth's atmosphere and surface at a spatial resolution from 1 m to 5 km. The spectral, radiometric, multiangular and polarimetric information from the reflected and emitted light in the UV to TIR wavelength range is obtained with limb sounders, nadir-viewing or pointable instruments and platforms. The information provided by passive optical instruments has opened new study areas and fields of applications with direct impact on Earth and space science and civil applications [58, 59]. Some these studye areas are atmosphere, meteorological prediction, vegetation, ocean color or land topography among other environmental aspects of the Earth's surface, atmosphere and their interaction [60, 61].

In order to define a generic architecture for E2ES suitable for passive optical missions, past, current and planned EO missions were reviewed and categorized. This review focused, at a first level, on the different mission options and their implications on the definition of this generic E2ES architecture, such as the possibility of using common elements or defining independent processing chains. At second level, this review analyzed the commonalities between various passive optical instruments in order to determine the most important characteristics that would define a generic E2ES architecture.

The overview and categorization of passive optical missions was based on the information available in Committee on Earth Observation Satellites (CEOS) *Missions, Instruments, and Measurements Database* [56] regarding applications, spectral range and spatial resolution of satellite missions. CEOS classification was complemented with technical information based on a review of ESA's Satellite Mission Database (*eoPortal*) [57] and the work done by Kramer (2002) [62]. All this information about satellite, instrument and algorithms allowed extracting commonalities between EO missions and design a generic architecture for E2ES. The following sections 3.1.1 to 3.1.3 give an overview of the characteristics of a few selected ESA and non-ESA missions, both satellites or on board of the International Space Station (ISS) (see Annex A.1 for the list of analyzed instruments).

3.1.1 ESA EO passive optical instruments

European Remote Sensing satellites (ERS-1 and ERS-2 [63]) were ESA's first Earth-observing satellites. These pioneer missions were launched in 1991 and 1995 respectively into Sun synchronous polar orbits. The ERS-1 and -2 passive optical instrument was Along Track Scanning infrared Radiometer (ATSR), specifically designed with three spectral bands in the VIS spectral range for the study of the chlorophyll in vegetation. Envisat (launched in 2002), successor ERS satellites, had improved versions of the instruments onboard ERS-2. Envisat was designed to cover a wide range of applications such as land surface (e.g., temperature, vegetation monitoring, land use), ocean (e.g., temperature, water quality), atmosphere (e.g., aerosols, trace gases, O_3 profiles, clouds, water vapor, troposphere and stratosphere transport processes) and cryosphere (e.g., snow/ice cover). This wide range of applications was possible with a set of multispectral and hyperspectral instruments (Advanced Along Track Scanning Radiometer (AATSR) [64], Global Ozone Monitoring by Occultation of Stars (GOMOS) [65], MEdium Resolution Imaging Spectrometer (MERIS) [66, 67], Michelson Interferometer for Passive Atmospheric Sounding (MIPAS) [68], SCanning Imaging Absorption spectroMeter for Atmospheric CHartographY (SCIAMACHY) [69]) acquiring single and multi-angular measures in the VIS-TIR spectral range with the spatial resolutions between 300 m and several km in various pointing modes (limb-pointing, near nadir, star/moon occultation).

To ensure Europe's capability for monitoring the Earth, European Commission (EC) signed a contract with ESA to build the Copernicus Sentinel satellite constellation [70, 71]. The Copernicus space segment comprises six space missions with a continuity of 20-years. Among them, Sentinel-2, -3, -4 and -5 host optical instruments.

- The **Sentinel-2** [72] (Sentinel-2A launched in 2015), with its MSI instrument intents to replace the old generation optical satellites such as Landsat 7 and Satellite Pour l'Observation de la Terre (SPOT). MSI acquires 12 spectral channels in the VIS to ShortWave InfraRed (SWIR) spectral region with a spatial resolution between 10 m and 60 m (depending on the spectral channel) and a swath of 290 km.

- Launched in 2016, the first **Sentinel-3** satellite hosts two passive optical remote sensing instruments (OLCI and SLSTR [55]), with improved capabilities compared to Envisat's MERIS and AATRS. OLCI is a pushbroom spectrometer acquiring 21 spectral channels in the VNIR spectral range with a spatial resolution of 300 m and a swath width of 1270 km thanks to its multicamera arrangement. SLSTR is a whiskbroom conical scanner taking multi-angular measurements on 9 broadband spectral channels in the VIS-TIR spectral region.

- The **Sentinel-4** mission [73] consists on the Ultra-violet/Visible/Near-Infrared (UVN) sounder instrument on-board of the meteorological Meteosat Third Generation (MTG) satellites. UVN is an ultraspectral pushbroom sounder in the UV to Near InfraRed (NIR) spectral range with a spatial resolution of 8 km with a scanning motion covering 75 degrees.

- The **Sentinel-5** mission [74], on-board of the meteorological MetOp-SG satellites, consists on a payload called Ultraviolet Visible Near-infrared Shortwave (UVNS), an ultraspectral pushbroom sounder consisting of several cameras (spectrometers) acquiring in the UV-SWIR spectral range with a spatial resolution of 7 km and a swath width of 2715 km. To fill the time gap between SCHIAMACHY/Envisat and Sentinel-5, the Sentinel-5 precursor (Sentinel-5P [75]) consists on a satellite with an instrument called TROPOspheric Monitoring Instrument (TROPOMI). TROPOMI is a multicamera ultraspectral instrument acquiring in the UV, VIS and SWIR spectral regions with a spatial resolution of 7 km.

Whereas the first satellites of each Sentinel mission are already designed and soon in orbit, the continuity satellites are still being in their design phase and therefore would benefit of an E2ES to optimize e.g. spectral band configuration or radiometric data quality. Moreover, the EC foresees to extend the capabilities of the Copernicus programme beyond the current six missions with the design and development of new Sentinels. In this frame, E2ES offer possibilities to study these future mission concepts and accelerate the process between mission concept to design and implementation.

ESA also has a long tradition in missions dedicated to meteorology, designing and developing the geostationary Meteosat satellite series. Three pre-operational spacecraft were launched in 1977, 1981, and 1988, before the Meteosat Operational Program was initiated with Meteosat 4 in 1989. ESA was responsible for designing and developing the Meteosat Second (and Third) Generation (MSG, MTG) satellites [76, 77], and procuring them on behalf of the European Organisation for the Exploitation of Meteorological Satellites (EUMETSAT). At the same time, launched in 2006, MetOp-A is Europe's first polar-orbiting satellite dedicated to operational meteorology, followed by MetOp-B (2012) and MetOp-C (2016) [78]. These three satellites guarantee a continuous delivery of high-quality data for medium- and long-term weather forecasting and for climate monitoring until at least 2020.

Within its Living Planet Programme, ESA also carries out specific scientific studies with the so-called Earth Explorer missions. One of these missions, the Earth Clouds, Aerosols and Radiation Explorer (EarthCARE), developed in collaboration with the Japanese space agency JAXA, will study the interaction between clouds and aerosols with a lidar and a radar instruments together with two optical multiband radiometers (MSI [79] and Broadband Radiometer (BBR) [80]), providing radiative balance information. In addition, the future 8th Earth Explorer, the FLEX/Sentinel-3 tandem mission, is specifically designed and optimized to retrieve sun-induced chlorophyll fluorescence emission from vegetation over land. The FLEX [51] satellite will host an imaging spectrometer (FLORIS [54]) acquiring reflected and emitted light in the visible and nearinfrared (VNIR) spectral range at a spectral resolution of 0.3 nm and a spatial resolution of 300 m. The process for selecting future Earth Explorers missions is based on the intercomparison the performance of these mission. Here, E2ES are suitable for the mission performance evaluation, setting a frame with common guidelines and rules for the mission simulation and evaluation. Additionally, a generic E2ES could benefit to better define missions in calls[2] for new Earth Explorers during preliminary conceptual design phases.

ESA also fostered advances in Space science by initiating technology demonstrators with

---

[2] www.esa.int/Our_Activities/Observing_the_Earth/ESA_issues_call_for_new_Earth_Explorer_proposals.

the launch, in 2001, of Proba-1 satellite [81]. This micro-satellite allowed multiangular observations due to the platform pointing capabilities. It hosted two passive optical instruments dubbed Compact High Resolution Imaging Spectrometer (CHRIS) and High Resolution Camera (HRC). CHRIS was a VNIR hyperspectral sensor with a ground resolution up to 18 m. Within this program, Proba-V satellite (launched in 2014) is a medium resolution multispectral imager that provides continuity of the data from SPOT-4 and SPOT-5 (vegetation sensor) [82] satellites.

3.1.2 Non-ESA EO passive optical instruments

In addition to ESA, other space agencies and organizations have developed their own EO passive optical missions. These non-ESA EO missions have been mostly developed by the American National Aeronautics and Space Administration (NASA) since 1969 with nearly 25 currently flying or approved/planned missions with passive optical payloads. Among them, the Terra [83] mission, developed in partnership with JAXA and the Canadian Space Agency (CSA), is considered to be NASA's flagship for EO. With five passive optical instruments on board, Terra provides a general monitoring of the Earth with applications in atmosphere, land surface, ocean and cryosphere. Terra's satellite measurements are complemented with those from the satellite Aqua. Terra's orbit descending node crosses the equator in the morning while Aqua ascending node crosses the equator in the afternoon.

- Specific of the Aqua satellite, the Atmospheric Infrared Sounder (AIRS) [84] aims to study the atmosphere, land and sea temperatures and the land-atmosphere radiation budget. AIRS is composed of: **(1)** a grating spectrometer acquiring more than 2000 spectral channels in the SWIR-TIR spectral range; and **(2)** a 4-bands spectrometer in the VNIR spectral region.

- Advanced Spaceborne Thermal Emission and Reflection Radiometer (ASTER) [85] has 12 spectral channels in the VIS-TIR spectral regions. The VIS-SWIR spectral range is acquired with two pushbroom spectrometers (VNIR and SWIR) while the TIR subsystem performs whiskbroom imaging. ASTER provides pointing capabilities in the across-track (ACT) direction in order to increase the revisit time.

- The Clouds and the Earth's Radiant Energy System (CERES) [86] is specifically designed to measure the Earth's and atmosphere radiation budget. The instrument consist of a pair of identical scanning radiometers acquiring three broadband spectral channels in the VIS-TIR spectral range at a low spatial resolution (20 km)

- Multi-angle Imaging SpectroRadiometer (MISR) [87] acquires 4 spectral bands in the VNIR spectral region. The multiangularity is achieved by a set of 9 cameras, imaging the Earth with a total swath of 360 km at a spatial resolution of 275-1100 m. MISR has multiple applications given its multiangular capabilities, particularly the study of the surface albedo, vegetation and aerosol properties.

- Moderate Resolution Imaging Spectroradiometer (MODIS) [88] is a whiskbroom instrument with an ACT mirror scanning, imaging the Earth with swath of 2330 m and a spatial resolution that varies between 250 m (for the VIS channels) and 1 km (for the TIR channels). The instrument acquires a total of 36 spectral channels in the VIS-TIR spectral range. A revisit time of 1-2 days is achieved with the combination of Terra and Aqua. MODIS is heritage of Advanced Very High Resolution Radiometer (AVHRR/POES), High Resolution Infrared Sounder (HIRS/POES), Thematic Mapper (TM/Landsat) and Costal Zone Color Scanner (CZCS/Nimbus-7) instruments. Given the spectral channel configuration and spatial resolution, MODIS has multiple applications in atmosphere, ocean, land surface and vegetation.

- Measurements of Pollution in the Troposphere (MOPITT) [89] is a scanning instrument based on the technique of gas correlation spectroscopy, which measures in 8 spectral channels in the SWIR part of the spectrum.

Since 1969, NASA and USGS have developed the Landsat project with the launch of series of 8 satellites (one failed). The Multispectral Scanner (MSS), TM and the enhanced versions ETM+ (Landsat-7) and Operational Land Imager (OLI)/Thermal Infrared Sensor (TIRS) (Landsat-8) are Landsat's main payloads, which are high spatial resolution multispectral (7 to 11 bands) whiskbroom and pushbroom spectrometers covering the VIS-TIR spectral range. Landsat mission has a wide range of applications such as the land surface resources, agriculture, forestry, snow, ice cover, and water quality. NASA is currently designing the future Landsat-9 [90] with upgraded capabilities with respect Landsat-8. Through Landsat-9 Phases A and B, an E2ES would be useful to optimize band configuration and instrument design.

Similar to Meteosat and MetOp satellites, NASA-NOAA have launched the geostationary GOES [91] and polar-orbiting POES [92] satellite series. The main goal of these missions is to carry out meteorological and atmospheric studies as well as oceanographic research and applications. This is achieved by a set of multispectral radiometers covering the VIS-TIR spectral range with different scanning geometry (conical, ACT and full Earth disk). Among them, the most relevant instruments are the AVHRR-series (whiskbroom, 1.1 km spatial resolution at nadir), the HIRS infrared sounder (20 spectral bands with 20 km spatial resolution) and the multispectral Advanced Baseline Imager (ABI) (16 spectral channels with 0.5-2 km spatial resolution).

As part of its Earth System Science Pathfinder program [93], NASA has launched a set of 3 satellites with passive optical instruments on board as main or secondary payloads:

- The Aquarius/SAC-D mission [94] was developed in collaboration with Argentina's space agency. It aims to study the sea surface salinity from space with a set of 7 instruments from which 2 are passive optical: **(1)** a panchromatic VNIR camera (High Sensitivity Camera, HSC) of 300 m spatial resolution with the objective of detecting electric storms, urban lighting, fires and aurora events at night; and **(2)** an imaging pushbroom spectrometer (New Infrared Sensor Technology, NIRST) with ACT pointing capabilities acquiring three spectral channels in the Midwave InfraRed (MIR) and TIR spectral regions.

- The Calipso mission [95] was designed to monitor the cloud and aerosol vertical profiles with lidar instrument and two complementary passive optical instruments: **(1)** an imaging infrared radiometer (IIR) developed by CNES with three spectral channels in the TIR spectral regions; and **(2)** a wide field camera (WFC) with one spectral channel in the VIS spectral and a spatial resolution of 125 m matching MODIS band #1.

- The Orbiting Carbon Observatory (OCO)-2 satellite [96] aims to study the CO_2 cycle in the atmosphere with a set of three high spectral resolution grating spectrometers measuring in the spectral regions of the O_2-A (765 nm) and CO_2 (1.61 μm and 2.06 μm) absorptions. The instrument acquires 8 ACT punctual measurements with a footprint of 1.29×2.25 km^2 at nadir and a total swath of 10.6 km.

NASA and its international partners put in operations a set of satellites following the same orbit in close formation. This constellation is known as the A-Train [97] and it is form of 8 satellites. Among them, Aqua, Calipso, OCO-2, Aura and Parasol host passive optical instruments on board:

- Aura [98, 99] is a large platform with 3 (out of 4) passive optical instruments on board: **(1)** the High Resolution Dynamics Limb Sounder (HIRDLS) in the MIR-TIR spectral range to determine temperature and gas profiles in the upper atmosphere; **(2)** the Ozone Monitoring Instrument (OMI) a pushbroom image spectrometer measuring in three spectral ranges in the UV and VIS; and **(3)** a pointable (limb and nadir) Tropospheric Emission Fourier transform Spectrometer (TES), measuring in the SWIR-TIR spectral range for understanding of long-term variations in the quantity, distribution, and mixing of minor gases in the troposphere.

- Parasol [100], designed by French space agency CNES and launched in 2004. The POLarization and Directionality of the Earth's Reflectances (POLDER-P) instrument is a wheel-filter multispectral imager (9-bands in the VNIR spectral range) sensitive to polarized reflected light. Together with the light polarization, the image-overlap multiangularity caused by the wide field of view (FOV) ($\pm43^\circ$ along-track (ALT); $\pm51^\circ$ ACT) allows Parasol to study the role of clouds and aerosols in climate mechanisms.

Future convoy and constellation mission concepts[3] can be supported with the use of a generic E2ES tool.

NASA, within the New Millennium Program for testing new satellite technologies, developed the EO-1 mission [101], a high spatial resolution satellite (10 m) with a panchromatic camera (Advanced Land Imager, ALI) and a hyperspectral imager (Hyperion) acquiring in the VIS-SWIR spectral range. Based on experience of Hyperion, NASA, as part of its Earth Science Decadal Survey program, is developing the HyspIRI mission [102]. HyspIRI will host two complementary instruments on board to provide with hyperspectral measurements in the

---

[3] See reports and key messages from ESA's 1st International EO Convoy and Constellation Concepts Workshop http://congrexprojects.com/2013-events/13m12/home.

VIS-TIR spectral range.

In addition to NASA and ESA, countries such as Brazil, Canada, China, France, Germany, India, Japan, Korea, Russia, Sweden or Taiwan have also launched several EO missions for their own research programs and civil applications. A few relevant cases are:

- Due to its particular geographic location, the Brazilian space agency has designed the Amazonia-1 mission (sun-synchronous 0° inclination orbit at 753 km altitude). It has a multispectral radiometer (Advanced Wide Field Image, AWFI) in the VNIR and infrared spectral range with a ground resolution or 40 m scanning the equatorial region from 5° north to 15° south in nadir pointing.

- Canada's SciSat-1 mission [103] studies the ozone layer and atmospheric profiles of pressure and temperature, particularly over Canada and the Artic region. The mission has an inclined non sun-synchronous orbit at 650 km altitude and host two spectrometers in the VIS-TIR region. A limb-pointing Fourier transform spectrometer (Atmospheric Chemistry Experiment, ACE) studies, by occultation method, the depletion of the ozone layer with measurements in the SWIR-TIR spectral range.

- The Russian non-sun-synchronous satellite Resurs-P [104] operates three passive optical instruments: **(1)** a 8-band pushbroom imaging spectrometer (Geoton-L1) in the VNIR spectral range with ACT pointing and high spatial resolution (1-4 m) capabilities; **(2)** a hyperspectral imager (GSA) in the VNIR spectral range with 25-30 m spatial resolution and a swath of 30 km; and **(3)** a multispectral spectrometer (ShMSA) with 5 bands in the VNIR spectral range to study land surfaces.

- The French SPOT satellite series have been in operation since 1986. SPOT-4/-5 [105] and SPOT-6/-7 [106] carry high resolution optical imagers (High-Resolution Visible and Infrared sensor (HRVIR), High Resolution Geometrical (HRG) and New AstroSat Optical Modular Instrument (NAOMI)) well suited for land and coastal applications. The SPOT family has a high-resolution multispectral imager in the VNIR spectral range onboard. SPOT-4 and-5 also have a band in the SWIR.

- Similar to SPOT, Spain is developing its own high-spatial resolution imager. The Spanish EO Satellite (SEOSat) mission [107] is a contribution to ESA, and consists of a sun-synchronous polar orbiting satellite carrying a panchromatic and multispectral camera with 2.5-10 m of spatial resolution.

- The German EnMAP mission [108, 109] is an EO satellite hosting a hyperspectral multicamera instrument measuring the whole spectrum from the VIS to SWIR wavelengths. The EnMAP instrument will acquire images with 30 m spatial resolution and a swath of 30 km. The instrument has pointing capabilities to increase revisit time on selected targets on demand.

- Similar to EnMAP, the Italian PRISMA mission [110] consists on a hyperspectral instrument with a multicamera arrangement acquiring in the VNIR and SWIR spectral regions. PRISMA also includes a panchromatic camera with a spatial resolution of 5 m.
- The Swedish-led satellite mission Odin [111] carries the Optical Spectrograph and InfraRed Imaging System (OSIRIS). OSIRIS is a multiband pushbroom grating spectrometer in the UV-VNIR spectral range together with an imager in the NIR spectral range. It is designed to retrieve vertical profiles of chemical species in the atmosphere.
- Private companies have developed their own EO satellites for commercial applications with multispectral and panchromatic instruments in the VNIR spectral region at very high spatial resolutions (e.g., SeaWiFI/OrbView-2, Ikonos-2 [112], DMC [113, 114] or Deimos-2 [115]).

3.1.3 ISS passive optical missions

With an altitude of 350-450 km and an inclination of 51.6°, the ISS covers nearly 85% of the Earth surface. The ISS can accommodate remote sensing instruments for nadir and limb pointing, offering the possibility of observing the Earth with different conditions from those of satellite missions. Given the particularities of its orbit, the ISS passive optical missions were analyzed separately. Some of the passive optical missions are briefly described below:

- ESA's Atmosphere-Space Interaction Monitor (ASIM) instrument [116] (planned for 2017) aims to quantify and analyze the transient luminous events and the terrestrial Gamma-ray flashes. One of the two ASIM modules consists into a nadir-pointing camera with 2-bands in the UV and NIR spectral range. The orbit altitude is close enough to track these events and covers most latitudes with thunderstorms activity at all local times.
- NASA's Ecosystem Spaceborne Thermal Radiometer Experiment on Space Station (ECOSTRESS) [117] aims to measure vegetation temperature in order to analyse how much water plants need and their response to stress conditions. ECOSTRESS consists on the Prototype HyspIRI Thermal Infrared Radiometer (PHyTIR) instrument, with 5 spectral channels in the 8-12 μm spectral range and one additional band at 1.6μm for geolocation and cloud masking.
- NASA's Hyperspectral Imager for the Coastal Ocean (HICO) [118] (ended in 2014) consisted in a hyperspectral VNIR pushbroom spectrometer specifically designed to quantify coastal and bio-geophysical features with a spatial resolution of 90 m.
- NASA's International Space Station Agricultural Camera (ISSAC) [119] is a frame multicamera acquiring three spectral bands in the VNIR spectral regions. ISSAC has a slide mechanism for a 30° ACT pointing.
- Rusalka is a Russian experiment measuring the CO_2 and CH_4 content in Earth atmosphere with an infrared high-resolution spectrometer in limb view at sunset.

- Stratospheric Aerosol and Gas Experiment (SAGE)-III [120] is a NASA's instrument (planned for 2016). This limb pointing instrument retrieves aerosol and gas properties based on measures in nine spectral bands in the UV-SWIR spectral range.

3.2 Classification of passive optical missions and instruments

In order to design a generic E2ES architecture that can accommodate any type of passive optical instrument, the reviewed missions were analyzed and classified according to a set of criteria that impacts E2ES architectures. The following Sections 3.2.1 and 3.2.2 describe the proposed mission and instrument categories and analyze how these categories have an impact in an E2ES in terms of its architecture and implemented algorithms.

3.2.1 Criteria for mission categorization

The following criteria were considered for the classification of EO passive optical missions:

- **Number of satellites composing the mission:** It was considered that a mission consisting of a constellation of two or more satellites instead of a single spacecraft would have an impact on the E2ES architecture, particularly in the simulation of the observation geometry from multiple platforms. Moreover, in the case of multiple platform, other sub-criteria were taken into account:
  - Formation flying: The various satellites fly in formation (loose or strict) or have completely decoupled dynamics.
  - Combined/separate measurements: The instrument measurements taken from the two spacecraft are covering the same area at certain temporal co-registration, which impacts the E2ES architecture at the Level-1b (L1b) or Level-2 (L2) processing chains with respect to data synergy from more than one simulation chain (e.g., radiometric cross-calibration, spatial co-registration).
  - Identical/different instruments on-board: Each spacecraft could have different instruments on board, which would require completely different instrument simulation modules in the E2ES, but the data coming from the several spacecraft may have to be integrated for the retrievals.
- **Number of instruments on-board the spacecraft:** The architecture of the E2ES is affected by the number of instruments on-board each satellite of the mission. There are some elements of the E2ES architecture that are unique (e.g., common geometry of the platform) and others are specific of each instrument.
- **Scientific objective of the mission:** This criterion was also linked to the instrument categorization (see Section 3.2.2). The scientific objective of the mission could not be

unique, and it is also independent from the number of instruments. This criterion has an implication in the E2ES architecture at a lower level, depending on how the radiative transfer of the signal acquired by the instrument(s) shall be modelled and how the retrieval of the final mission products is implemented (e.g., synergy between instruments, multi-temporal analysis).

- **Links with other missions:** There are missions with requirements asking for loose formation flying configuration with respect to an existing mission (e.g., FLEX/Sentinel-3 [51]). The final objective of these missions is to obtain measurements that are temporally and spatially co-registered with those from the existing mission, in order to exploit the synergy of their data at some point in the retrieval. This criterion is similar to the case of having two spacecraft of the same mission combining measurements.
- **Orbit characteristics:** The orbit of an EO mission could have an impact to the simulation of the observation geometry within the E2ES.
- **Observation geometry/scanning method:** Depending on the instruments on board, but not exclusively, it will be defined for the mission a determined observation strategy or satellite pointing method. This criteria intends to address only the characteristics of the satellite platform. Scanning methods provided directly by the instrument, like scanning mirrors (e.g., SLSTR [121]), were not considered in this categorization.

Based on the proposed criteria, the following mission classifications were envisaged:

- Based on the number of spacecraft and instruments (see Fig. 3.1), passive optical remote sensing missions were divided, at a first level, into single platform (e.g., Envisat [122], MTG [123]), if there is only one spacecraft in the mission, or multiple platform (e.g., Sentinel-3/FLEX [51, 52]) if there is more than one. For the single platform category, the missions were further classified into: **(1)** single instrument (e.g., OCO-2 [124], EnMAP [108]); or **(2)** multiple instruments (e.g., Envisat, Terra [83]). For multiple platform missions, these were further classified into **(1)** those making use of formation flying technologies; and **(2)** those not making use of them. Examples of multiple platform missions not making use of formation flying are Sentinel-2 [125] (single instrument) or Sentinel-3 (multiple instruments). An example of multiple platform mission flying in formation is FLEX (single instrument), which is flying in tandem with Sentinel-3.
- The categorization based on the number of spacecraft and possible co-registration of measurements (see Fig. 3.2) came up with two main options:
  - For single-platform missions, the most straightforward option is that the observation data taken from one instrument is not combined with any other data. Nevertheless, it might be cases where the observation data from one instrument is used in synergy with the data coming from other instrument of the same mission at certain point of the retrieval process (e.g., cloud screening and atmospheric correction using Envisat's MERIS and AATSR instruments [126]). Another option is where the synergy

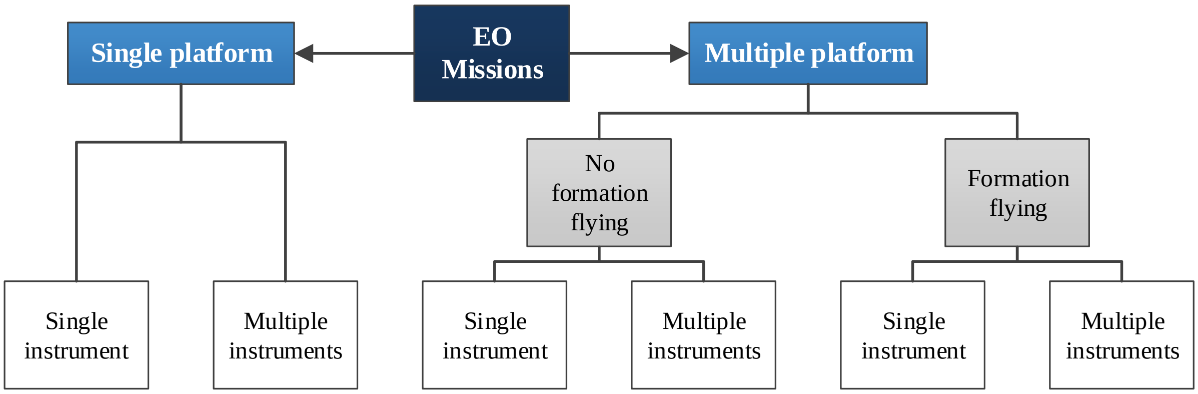

Figure 3.1: Categorization of EO missions by number of satellites and number of instruments.

is with data coming from other mission (e.g., retrieval of bio-geophysical parameters using FLORIS/FLEX and OLCI/Sentinel-3 instruments [127]).

- Similar options were considered in the case of multi-platform missions. The most straightforward option would be not to combine the data from instruments in the mission. Nevertheless the observation data taken from one instrument can be used in synergy with the data coming from the same instrument in other spacecraft of the mission at certain point of the retrieval process. Another option is that the data from one instrument in the multi-platform mission is used in synergy with the data coming from other instrument of the same mission (e.g., synergy between OLCI and SLSTR on board of Sentinel-3A and Sentinel-3B). Finally, the data can be also used in synergy with data coming from other mission (e.g., multitemporal data fusion between Sentinel-2 and Landsat 8 following techniques such as [128]).

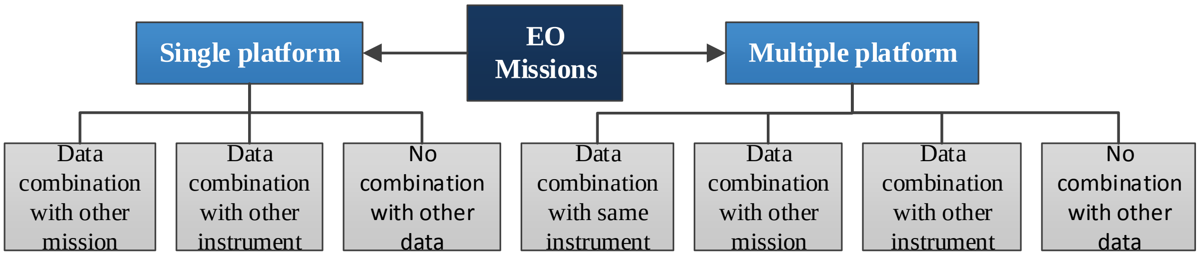

Figure 3.2: Categorization of EO missions by number of satellites and possible co-registration of measurements.

- Using the criterion of scientific objective of the mission, the following main scientific areas of interest were identified based on ESA's Climate Change Initiative [129] and ESA's Earth Observation science strategy [58]:
  - Land applications: aiming at studying forests, urban development, land use. . .

  - Ocean and in-land water applications: analyzing ocean and in-land water characteristics (temperature, salinity, suspended matter. . .).
  - Atmospheric applications: in charge of studying atmospheric processes and characteristics (composition, aerosols, cloud formation, CO_2. . .).
  - Ice/Snow applications: monitoring evolution of ice and snow areas, determining width of ice layer.
  - Other applications: altimetry, gravity field or magnetic field determination.

  One mission could have different scientific applications at the same time, independently of the number of instruments. The scientific objective of the mission has implications on the E2ES architecture in terms of how the scenes should be generated, e.g., through the use of specific RMT, external satellite/airborne images or spectral databases.

- Based on the orbit characteristics, a few categories were identified: Geostationary, polar Sun-synchronous, Near equatorial, Inclined (non-Sun-synchronous), Highly elliptical. Other non-standard keplerian orbits (e.g., [130, 131]) were reviewed but not included in the analysis given that these are few cases with one or none current/planned EO missions.

The mission categories were selected based on the review of satellite missions (see Section 3.1) after looking at the defined criteria and analyzing how they are combined, always from the point of view of the impact on the E2ES architecture. Sometimes different criteria were combined in one categorization (e.g., number of platform and number of instruments) and in other cases only one criterion was used for the categorization (e.g., application type). In addition, it is worth noticing that the type of instrument was not used as one of the criteria to classify the missions given that the mission categories will have an impact at the higher-level architecture (e.g., multiple instrument vs a single instrument per mission). Instead, it was considered that the type of instrument has impact on the second layer. E.g., for a single-platform, single-instrument mission, the high-level architecture and main interfaces will be common for all types of instruments (i.e., active and passive optical/microwave). The instrument classification criteria and categorization is described in Section 3.2.2.

The EO missions included in the survey were analyzed according to the proposed classification criteria in Fig. 3.1 and Fig. 3.2 with the goal of extracting conclusions that may drive the architecture of the E2ES.

Fig. 3.3 shows the analysis of the number of spacecrafts in the mission (left) and the number of missions in formation flying (right). The concept of fomation flying includes tight formation flying, loose formation flying (e.g., the FLEX/Sentinel-3 tandem mission) and also constellations (e.g., Sentinel and RapidEye [132] constellations). With respect to the number of spacecraft, it was included as multiple-spacecraft those missions that have several spacecraft even if they do not fly at the same time (e.g., the NOAA series), since they allow exploiting commonalities in the instruments and products.

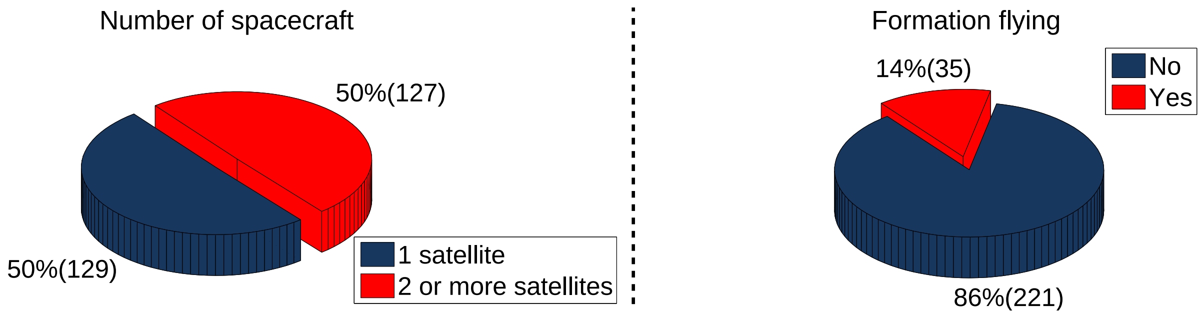

Figure 3.3: Statistical analysis of the surveyed missions in terms of the number of spacecraft (left) and their formation flying (right).

As shown in Fig. 3.3 (left) half of the missions have one single spacecraft, while the other half has two or more spacecraft. However, according to Fig. 3.3 (right) only 14% of the surveyed missions exhibit some kind of formation flying. This means that for most of the multi-platform missions there is no link in the scene, orbit or attitude. This implies that these multi-platform missions might require different simulators with a high level of reuse. For most of these missions the goal is to have an increased coverage or improved revisit time.

The formation flying missions include both formation flying with another satellite in the same missions (e.g., Sentinel-2 and -3 constellations), or with a satellite in another mission. An example of the later is the FLEX mission, designed to operate in tandem with Sentinel-3 and to exploit their data in synergy. In this case each mission should have its own individual simulator, but the FLEX mission simulator should be able to ingest the simulated data from the Sentinel-3 simulator. Alternatively, within the FLEX mission simulator, customized Sentinel-3 modules could be developed with a lower level of detail and complexity with respect the Sentinel-3 simulator. When products are to be combined it is important that the observed target is defined in the same coordinates for both acquisitions so that the observation geometries from each platform are consistent. In summary, if the spacecraft belong to two missions there will be two simulators that need to be able to ingest the data generated from each other simulator, with a common defined scene and synergy between their products (if applicable). If the spacecraft belong to the same mission, the best approach would be, in principle, to have one single simulator with two different processing chains with the same instrument model and able to simulate different platform conditions (possibly by different configuration of the same module).

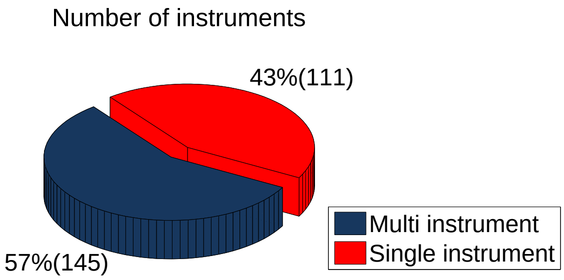

Figure 3.4: Statistical analysis of the surveyed missions in terms of the number of instruments.

As shown in Fig. 3.4, slightly more than half (57%) of the missions are multi-instrument. For these type of missions, the E2ES architecture should simulate the commonalities in orbit, attitude and platform, but having parallel chains simulating each instrument (e.g., PREMIER E2ES [32], Sentinel-3 Optical System Performance Simulator [35]). In this case, if the instruments are observing the same radiometric target, one single scene generator could be used to simulate the scenes observed by the various instruments.

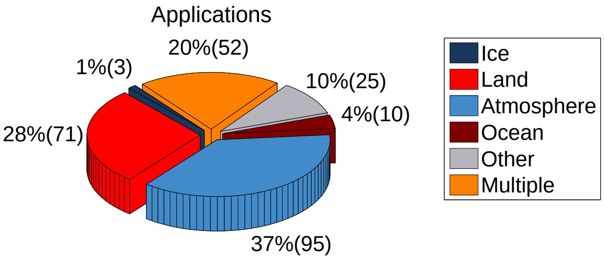

Figure 3.5: Statistical analysis of the surveyed missions in terms of the area of application.

As shown in Fig. 3.5 most missions (80%) are aimed at one single application, while only 20% are aimed at multiple applications. This means that, in general, for single-application missions there are commonalities to be exploited such as the same scene generator or the same L2 processing chain. In the case of a mission with various applications, these applications could be merged in the same simulator in order to exploit commonalities in the orbit, attitude and platform at expenses of more complete scene generator (e.g., capable of generating scenes for land and ocean applications) and L2 processing chain (e.g., with parallel processing chains depending on the application).

As for the platform orbit type, Fig. 3.6 shows that most of the instruments are onboard of platforms in Sun-synchronous orbits. This is due to the possibilities to perform observations at every latitude and longitude and keep the same illumination conditions. Geostationary and inclined orbit types are the second most used orbits. Geostationary are particularly interesting as it offers a continuous temporal acquisition over the same location of the Earth at expenses of, in most cases, lower spatial resolutions. Highly elliptical orbits (e.g., Molniya orbit) are configured on very special cases to maximize the viewing time over high latitudes. Finally, instruments in near equatorial orbit have been found only on board the ISS. The different orbit types do not imply different E2ES architecture at high level but rather at lower level with the simulation and propagation of the orbital elements.

3.2.2 Criteria for passive optical instruments categorization

As with the mission categorization presented in Section 3.2.1, passive optical instruments were classified in order to identify the commonalities and specificities that impact the definition of a generic E2ES architecture. It was considered that this classification criteria affects E2ES architectures at a lower level, i.e., at the details of how satellite mission has to be modeled. As an example, a single-satellite mission with one instrument will have the same high-level

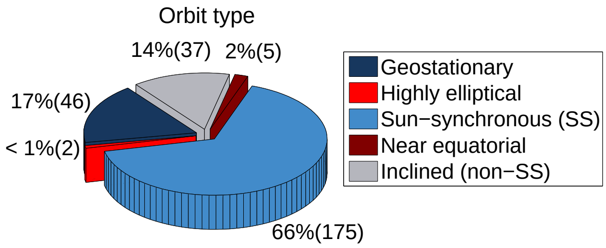

Figure 3.6: Number of instruments according to the orbit of the platform.

architecture regardless the spectral range covered by a passive optical instrument. The spectral range will therefore have an impact at lower level with respect to e.g. how the instrument noises are modeled or how scenes are generated through specific RTMs.

The following items give a brief description of the main classification criteria (see summary tables in Annex A.2):

- **Acquisition mode:** It refers to the temporal mode in which data is acquired. Two options were considered: **(1)** continuous (global) mode, in which an instrument obtains information along all its orbit; **(2)** and a localized (target) mode, in which a satellite operates its payload on single targets around the Earth. The acquisition mode constrained the E2ES capability to simulate small (target) or long (global) scenes in order to simulate e.g., temporal stability of the instrument within the continuous acquisition. Nevertheless, it was considered that both acquisition modes can be achieved with the same E2ES architecture based on the selection of a scene size and location, ranging from relatively small target scenes to large scenes from a continuous acquisition. Also, global acquisition mode might require global data to configure a scene (e.g., DEM, land cover map, atmospheric parameters map) whereas local acquisition might only require definition of the targeted areas, reducing the amount of auxiliary data needed to generate the observed scenes.

- **Pointing:** This feature indicates the instrument/platform attitude change to perform measurements over a target area. The proposed pointing modes were: **(1)** fixed (commonly near-nadir pointing); **(2)** angular (ACT, ALT or bi-directional); **(3)** limb-pointing; and **(4)** slow down. It was considered this criterion impacts the E2ES architecture in terms of the simulation of the acquisition geometry, the generated scenes (limb or Earth surface), and the retrieval algorithms (atmospheric limb or Earth surface retrieved parameters). By associating an acquisition time-tag and a line-of-sight (LOS) to each image pixel, all the pointing modes can be simulated with the same E2ES architecture.

- **Multiangularity:** Defined for instruments observing the same target area with different viewing angles. These observations can be achieved **(1)** by steering the instrument or platform and changing its attitude; **(2)** by using different cameras; **(3)** overlapping two consecutive images of the same target; or **(4)** using rotating or flipping mirrors (conical scanning), alternating between several viewing angles. In terms of the E2ES architecture, multiangular observations imply: Firstly, the same target scene shall be generated with multiangular configuration (e.g., effect of topography, variations due to bi-directional reflectance). Secondly, the observation geometry should be simulated to include multiangularity (e.g., instrument scanning motion, multiple cameras acquiring images at different times and observation angles). Thirdly, the simulator should generate the images acquired by the instrument at the various observation angles. Finally, multiangular data should be eventually ingested in a single L2 processing retrieving L2 products.

- **Spatial resolution:** The spatial resolution ranges from low (>500 m) to very high (<10 m). This criterion is related with the mission application (e.g., atmospheric missions normally have low spatial resolution) and implied trade-offs with other instrument criteria (e.g., very high spatial resolutions are achieved at expenses of smaller spectral range and resolution, using panchromatic cameras). Notwithstanding, with the evolution of technology, one could in principle decouple the criteria of spatial resolution from spectral range/mode (i.e., instruments with the same spectral range/mode can achieve very different spatial resolutions). With respect to the E2ES architecture, the spatial resolution has an impact in the scene generation as these scenes should have higher spatial resolution than the instrument resolution e.g., very high resolution scenes generated from external airborne images. The very high spatial resolution also requires that the simulator is highly representative of the vibrational and attitude modes in the platform and instrument.

- **Polarization:** In some cases the scientific goal of the mission can be achieved by measuring how light is polarized (e.g., POLDER/PARASOL measures the polarization to extract information about cloud properties and aerosols). For other missions, light polarization affects the acquired signal and the scientific goal of the mission, and thus polarization measurement is avoided. This criterion influences on how the scene are generated (e.g., specific RTM that simulate light polarization in the atmosphere) and how the information from polarized light is extracted at L2. Regarding the scene generation, the E2ES should include a variable that represents the polarized scattering matrix for each spectral channel at each scene ground point.

- **Spectral mode:** Five spectral modes were distinguished according to the number of bands and their bandwidths: **(1)** monochromatic instruments, measuring at one single spectral channel (traditionally panchromatic cameras with large bandwidth); **(2)** multispectral instruments, with a few spectral channels (3-5) of large bandwidths. Some multispectral instruments also include a panchromatic band with very high spatial resolution; **(3)** superspectral instruments, acquiring a few (5-30) narrow bands (1-10 nm); **(4)** hyperspectral instruments, measuring a continuum spectral range with narrow bandwidths (e.g., HICO); **(5)** ultraspectral, increases the spectral resolution with bandwidths below 1 nm (traditionally used in atmospheric sounders). This classification criteria impacts the E2ES architecture in terms of the spectral resampling of a high resolution scene into the instrument resolution. The scene generation shall also be able to simulate TOA radiance scenes with a resolution at least a factor 3 to 10 higher than the instrument resolution, which might constrain the RTM to be used. Whereas for monochromatic, multispectral and superspectral instruments might not be an issue, the simulation of very high spectral resolution scenes (hyperspectral and ultraspectral) might impact the E2ES in terms of data memory and computation speed (particularly at high spectral resolution and large spectral ranges).

- **Spectral range:** Specifies the wavelength range (VIS, NIR, SWIR, MIR and TIR) measured by a passive optical instrument, which is related to the mission goal. The spectral range has an impact in the E2ES architecture with respect to how a scene is generated (e.g., use of specific RTM for different spectral ranges) and with respect to the type of detector, thus with the noises and instrument effects that should be simulated.

- **Scanning geometry:** It refers to the way the Earth surface is scanned by an instrument. Two possibilities were identified: **(1)** linear; and **(2)** conical/circular. Similar to the pointing and multiangularity criteria, this criterion influences how the viewing geometry is simulated, and can be simulated with the same E2ES architecture by considering the acquisition times and LOS for each instrument pixel.

- **Swath:** In combination with the scanning geometry, the swath defines how the data is acquired by an instrument. Three swath types were identified: **(1)** Full Earth disk, where the entire Earth is imaged after a whole scanning of the instrument; **(2)** Carpet mode, where the instrument FOV sweeps the ground target through the orbital path; **(3)** Scene mode, where instantaneous images of the Earth are taken. As the previous criterion, the swath type influences how the instrument viewing geometry is simulated, and can be simulated with the same E2ES architecture by considering the acquisition times and LOS for each instrument pixel.

- **Number of cameras:** Some instruments are composed by more than one unit (e.g., to separate different spectral regions or to increase the total FOV of the instrument). In this case, the different cameras could be placed with different (independent) or same (solidarity) optics. This criterion affects how the acquisition geometry is simulated, particularly the viewing conditions and time co-registration between various cameras. Eventually, the number of cameras could be considered as different instruments to be simulated in the same instrument simulator.

- **Instrument type:** This parameter accounts for the way in which data is acquired by an instrument. The data can be taken with a linear pushbroom, pixel by pixel with a whiskbroom or by a whole frame (see Fig. 3.7). This criterion has implications on how data is acquired in terms of geometry. Whereas frame instruments acquire all the ALT and ACT pixels in an image at the same time, pushbrooms acquire each line at different times and whiskbrooms acquire each single pixel at different times. Therefore, as proposed for the pointing criterion, each instrument pixel should be associated with a time tag in order to reuse the same E2ES architecture for all these instrument types. In addition, each instrument type might add different noises and systematic effects that should be included in the simulator.

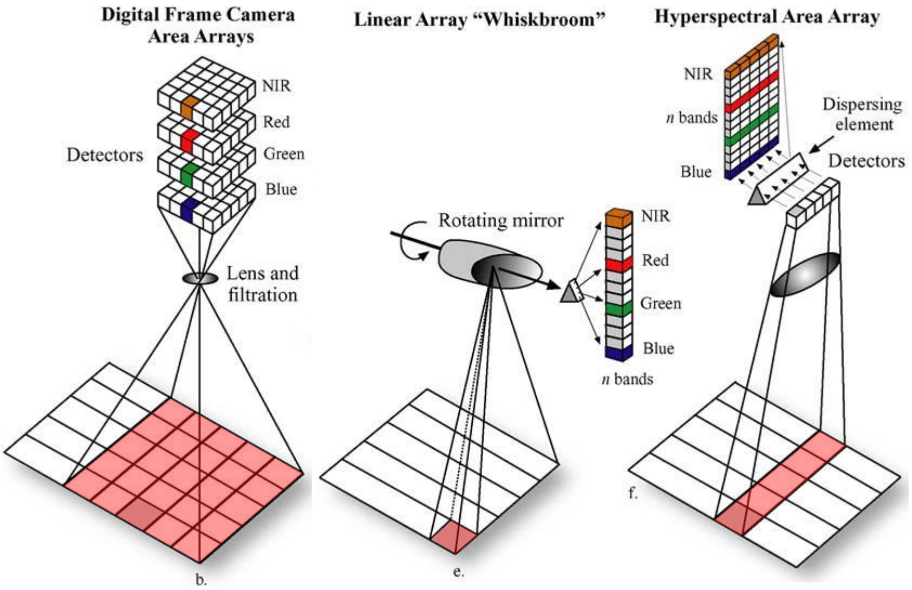

Figure 3.7: Schematic operations of a frame (left), whiskbroom (mid) and pushbroom (right) instrument types. The red-shaded areas are acquired at the same time. Source: Jensen (2007) [133].

- **Spectroradiometer type:** Passive optical instruments were divided in two main classes: radiometers and spectrometers. Radiometers integrate the amount of power received by the sensor at a given spectral range through the use of detector filter arrays or a multicamera arrangement. Spectrometers measure light intensity at several wavelengths specified by the spectral mode and range, separating the light spectrum through different sub-types: Grating, Fabry-Perot, Variable filters, Fourier transform, Prism and other. Spectroradiometer (sub-)types have implications in terms of how the image is acquired (e.g., observation geometry in the multicamera arrangement, acquisition times in Fabry-Perot and other modes, light diffraction through prism or grating) and in terms of specific noises and systematic effects that should be considered in the instrument simulator.

The surveyed passive optical instruments were analyzed according to the proposed classification criteria with the goal of extracting conclusions that may drive an E2ES architecture.

According to the results shown in Fig. 3.8 (left), most of the analyzed instruments operate in continuous mode covering the whole Earth surface. These kind of instruments typically retrieve global maps of atmospheric parameters or have multiple scientific applications (e.g., OLCI/Sentinel-3 studying both ocean and land). Given the continuous data acquisition, these instruments are limited to small FOV and/or low-mid spatial resolutions. Localized instruments are mostly used for specific applications (e.g., FLORIS/FLEX retrieving sun-induced fluorescence of vegetation over land, CHRIS/Proba-1 acquiring multiangular images through platform steering). The localized acquisition mode can also be due to lower data storage capabilities (e.g., demonstrator instruments such as HICO/ISS) or due to the very high spatial resolution of the data (typically multispectral imagers). As for the pointing modes shown in Fig. 3.8 (right), fixed near-nadir pointing is the most common mode followed by bi-directional and

ACT pointing. Fixed poiting is commonly used for pushbroom and frame instruments while the poiting capability is used for instruments in localized acquisition mode to increase the revisit time. Limb pointing is specific for instruments studying the atmospheric composition and are normally associated with hyperspectral or ultraspectral whiskbroom sounders.

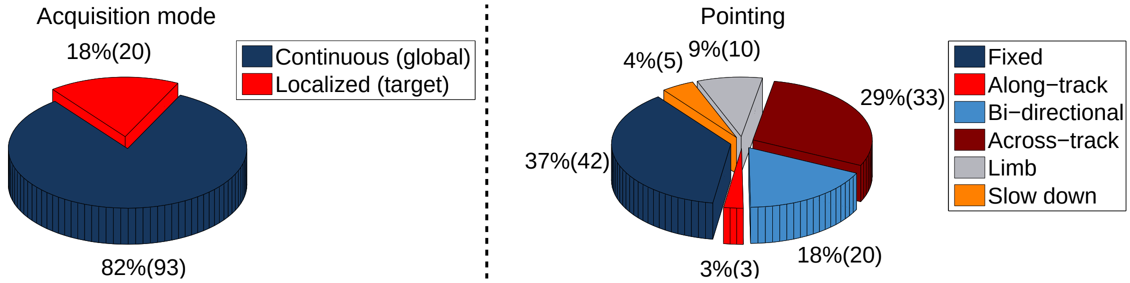

Figure 3.8: Number of instruments according to their acquisition mode (left) and pointing (right).

Regarding the multiangularity criterion (see Fig. 3.9), most analyzed instruments (78%) acquire images with a fixed or variable single viewing angle. Multiangularity (22% of analyzed instruments), mostly achieved by steering maneuvers (e.g., CHRIS/Proba-1) or by means of multi-camera instruments, is commonly used to determine surface bi-directional reflectance effects or retrieval of aerosol properties (e.g., characterization of the aerosol phase function). The multiangularity by steering limits the capability of the instrument to perform continuous data acquisition, thus it is used for specific applications that require multiple angular measurements over a localized target. To overcome this limitation, multiangularity and continuous acquisition can be achieved with scanning instruments (e.g., SLSTR/Sentinel-3 conical whiskbroom radiometer), by using a multiple camera instrument (e.g., MISR/Terra) or by image overlap (e.g., POLDER/PARASOL, 3MI/MetOp-SG). The L2 processing of multiangular measurements require an intermediate step (Level-1c or within the L2 processing) that co-registers, resamples and merges the data over a common grid.

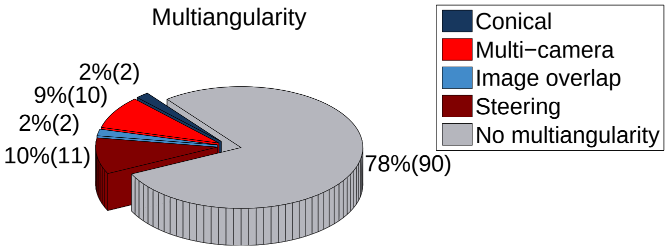

Figure 3.9: Number of instruments according to their multiangularity capability.

As for the spectroradiometer type and covered spectral range (see Fig. 3.10) it is observed that nearly 70% of the instruments acquire a few spectral bands (panchromatic and multispectral). This large proportion is due to the maturity and availability of the technology, largely used in disaster monitoring and commercial applications by private companies. These multispectral and panchromatic instruments normally use an arrangement of several cameras or filter wheels so each spectral channel image frame is acquired at different observation times. Superspectral and hyperspectral instruments have also been largely used for scientific and operational EO missions (e.g., OLCI/Sentinel-3, MODIS/Terra, FLORIS/FLEX, EnMap) and they traditionally use prisms and grating spectrometers. These instruments normally have a medium spatial resolution and operate in pushbroom linear scanning mode. However, whiskbroom hyperspectral radiometers can also be found operating in linear and conical scanning modes. For the superspectral and ultraspectral instruments, their higher spectral resolution is achieved with state-of-the-art prism and grating spectrometers. Fourier transform spectrometers are also common for very high spectral resolution instruments, particularly for infrared sounders both in near-nadir and limb pointing. The EO mission analysis indicated that the proposed classification of spectroradiometer types does not fully cover all the cases. For instance, some spectrometers combine both gratings and prism (e.g., GOME-2/MetOp) or even filters for bands rejection (e.g., AIRS/Aqua). In addition, some instruments (e.g., GOMOS/Envisat) combine spectrometers and radiometers.

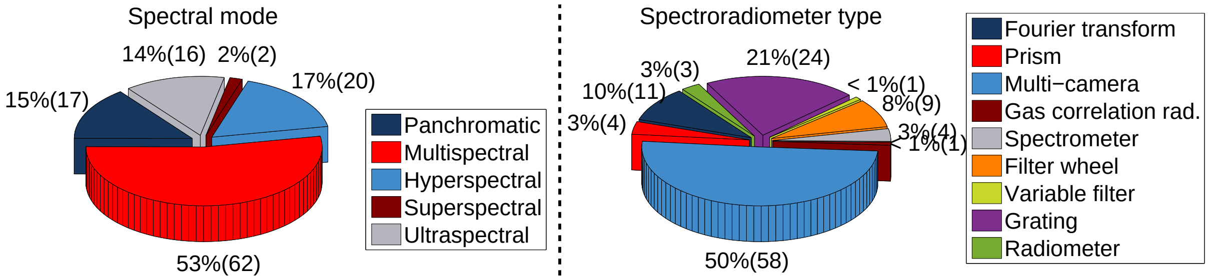

Figure 3.10: Number of instruments according to their spectral mode (left) and spectroradiometer type (right).

The results shown in Fig. 3.11 (left) indicate that more than two thirds of the analyzed instruments have several cameras working independently[4] while 31% work with several solidary cameras. As for the polarization measurement, Fig. 3.11 (right) indicates that most instruments acquire de-polarized images. This means that for most of these missions, an E2ES does not need necessarily to deal with light polarization in the scene generation. However, light polarization could still be considered in a generic E2ES architecture by including a variable representing, for each spectral channel, the scaterring matrix for polarized light.

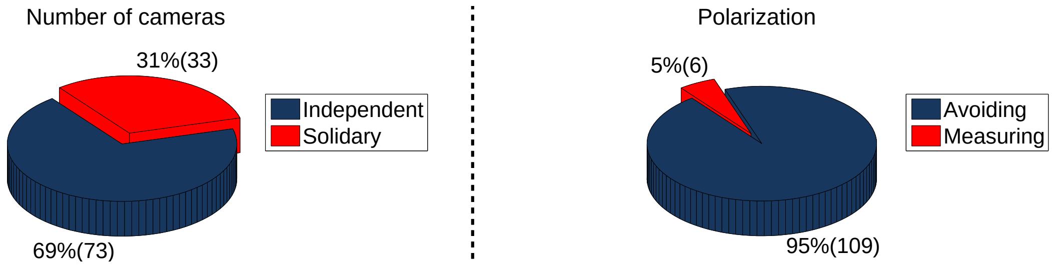

Figure 3.11: Number of instruments according to the number of cameras (left) and their polarization measurement capabilities (right).

---

[4] Single camera instruments were considered in this category

Regarding how data is acquired through the instrument and swath types, Fig. 3.12 firstly indicates that pushbroom instruments are one of the most common types, particularly for hyperspectral, superspectral and ultraspectral. These instruments scan the Earth surface in a carpet mode given the operation as image spectrometers (i.e., one dimension of the CCD is in the ACT spatial direction while the other is in the wavelength domain). Secondly, frame instruments are commonly acquiring multispectral images in scene mode and through the use of multi-cameras and wheel-filters. Finally, whiskbroom instruments, generally associated with hyperspectral-ultraspectral sounders or scanning radiometers, have carpet swath modes.

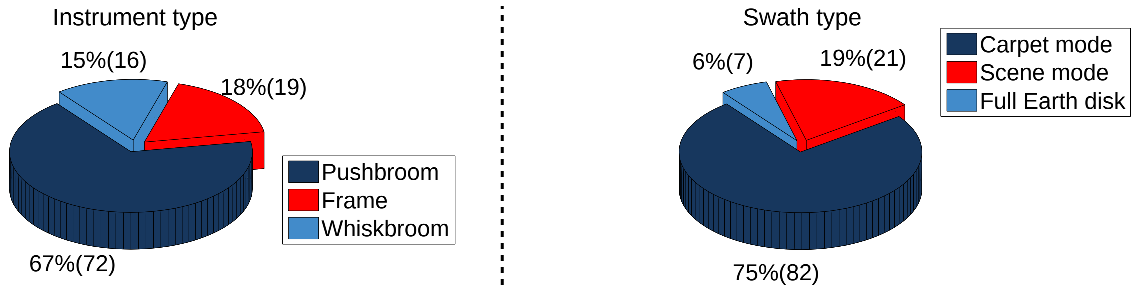

Figure 3.12: Number of instruments according to their type (left) and swath type (right).

With respect to the spectral range (see Fig. 3.13-left) it should be noted that some passive optical instrument are measuring in more than one spectral range. Most of the analyzed instruments acquire in the VNIR spectral range being lower in the SWIR-TIR spectral range. Instruments in the UV spectral range are a minority for passive optical missions as they are related with very specific applications (e.g., study the transient luminous events). As for the spatial resolution (see Fig. 3.13-right), most of the instruments acquire in low spatial resolution at all spectral ranges, particularly at UV and MIR-TIR spectral ranges. Also, atmospheric chemistry missions with high spectral resolution in the SWIR-TIR ranges do not require very high spatial resolution data given the low spatial variability of the atmospheric composition. High and very high spatial resolution instruments are mainly acquiring in the VNIR spectral range, especially using panchromatic cameras. In terms of E2ES architecture, it is important to generate scenes at a spatial sampling higher than the instrument resolution, which has an impact on how these scenes are generated (e.g., very-high spatial resolution scenes may use airborne data while mid-low spatial resolution scenes may use satellite images or RTMs).

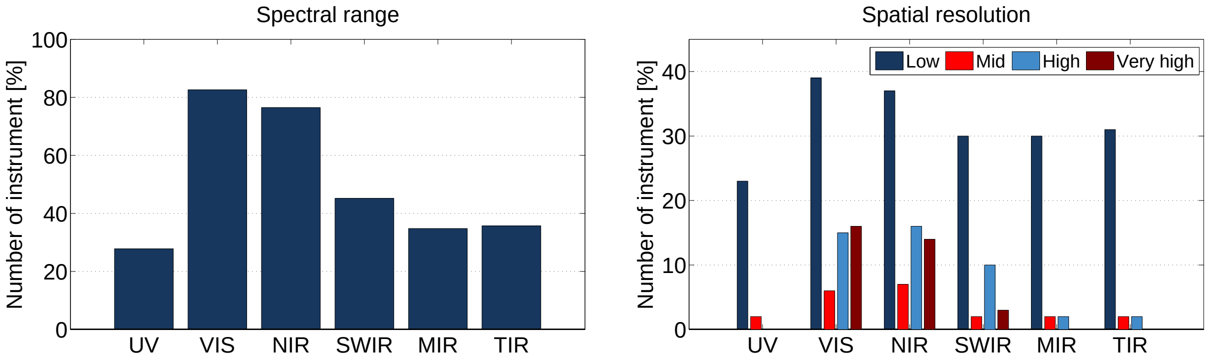

Figure 3.13: Number of instruments according to their spectral range (left) and spatial resolution (right).

The **detector type** was also considered in the analysis as it affects on how the instrument noises, systematic effects, readout times and wavelength sensitivity is simulated. Detector types are related with the spectral range acquired by an instrument, therefore an instrument could eventually have various detector types (e.g., if acquiring data in VIS and TIR spectral regions).

EO missions were also analyzed according to the **data processing Level** (see Acronyms and Definitions Section, page xv). The following conclusions were obtained with respect to the impact in E2ES architecture[5]:

- L1: Most EO mission carry out two steps for the generation of L1 data: **(1)** L1a is firstly produced from instrument Level-0 data, which includes among other information raw data in digital counts and ancillary data (e.g., orbit parameters, calibration parameters, correction factors and, in some cases, DEM). Calibration and geolocation coefficients are appended but not applied. **(2)** L1a data are processed to L1b, generating radiometrically-calibrated and noise-corrected TOA radiance with geolocated coordinates corrected from the effects of satellite attitude motion and Earth rotation. Preliminary pixel classification (e.g., land/water, bright pixel masks) are appended together with image quality identifiers for further processing at L2. The L1 processing implies the calculation and/or application of radiometric/spectral calibration coefficients and geolocation. Several methods were identified (see Acronyms and Definitions Section, page xvi). These methods depend on the mission design, spectral bands and instrument type and they should be considered within the E2ES as part of the instrument simulator and the scene generation.
- L2: Whereas L1 data processing and products are very similar for every passive optical mission, the algorithms for the retrieval of bio-geophysical L2 products depend on each mission. Notwithstanding, L2 products are related with the radiometric target:
  - Atmospheric measures retrieve content and spatial/vertical distribution of atmospheric gases (e.g., CH_4, CO_2, H_2O, O_3, trace gases), temperature vertical profile,

---

[5] Only L1 and L2 products were included for the analysis of a generic E2ES architecture.

cloud properties (e.g., coverage, top temperature, pressure), aerosol properties (e.g., optical thickness, scattering coefficients, phase function), also including volcanic ash properties or smoke plumes, and lightning detection.

- Surface imagery is used to retrieve information about vegetation (e.g., chlorophyll content, LAI, fluorescence), land/ocean surface temperature, water quality parameters (e.g., type and content of suspended matter), characterization of snow & ice coverage or fire spots detection. The retrieval of surface properties require that an E2ES implements an atmospheric correction algorithm to retrieve Top Of Canopy (TOC) reflectance and emissivity/temperature from the L1 TOA radiances.

3.3 E2ES architecture for passive optical missions

The initial steps in the definition of a generic E2ES architecture was carried out and presented in Section 3.2, by categorizing past, current and planned EO missions and instruments; identifying the main elements that affect the mission performance and impact the simulator architecture. This section defines the architecture elements required to model an EO passive optical mission and proposes a generic E2ES architecture that could be adapted for the different mission particularities. A bottom-up methodology was followed for deriving this generic E2ES architecture: For each identified mission category in Section 3.2.1, a baseline architecture was proposed. Then, the proposed architectures were analyzed with the goal of exploiting the commonalities among different instrument categories in Section 3.2.2.

In order to support the detailed mission design along various mission Phases, the E2ES architecture was designed to allow **(1)** an *extensive* growth, in order to include more effects, and **(2)** an *evolutionary* growth, in order to achieve more accuracy in the simulator. Thus, one of the main ideas of this Thesis was to define a modular generic architecture that contains the basic elements for the E2ES and that provides the required flexibility to the architecture to grow both in extensive and evolutionary sense. It is important noticing that the feasibility of the *evolutionary* growth of the E2ES is possible assuming that different modules use the same interfaces so that they can be plugged in the simulator without affecting the other modules. Similarly, the *extensive* growth of the E2ES has to be supported by assuming that additional modules will not modify the interfaces between basic modules even if they are inserted in the chain modifying the data passed from a module to another one. The concept of the proposed generic E2ES architecture aimed at minimizing the tasks related to the architectural design of the simulator by promoting reuse in the development.

3.3.1 Generic considerations for the high-level architecture

This section describes the methodology used to define a generic E2ES architecture and the specificities to be considered for special mission types. In order to be generic, the proposed

E2ES architecture should cope with all EO mission and instrument categories identified in Section 3.2. This requirement defined a set of high-level elements (called **modules**) that would be present in all simulators, independently of the category of mission and instrument. Regarding the definition of the high-level generic architecture, one of the premises was to keep it as simple as possible, defining very few variations with respect to the nominal solution. This allowed various E2ES to have more coherence between them so that they are implemented based on this generic architecture, even if they are quite different. Thus, the approach was to define few high-level architectures, depending on the type of mission (multi-instrument, multi-platform, synergies between products...). Then, the type of instrument would have an impact on the second layer i.e., the internal architecture of the high-level modules.

Five main premises, illustrated in Fig. 3.14, were set to define a generic E2ES architecture:

1. The generic architecture is defined with a set of high-level modules. The interfaces between them are common to all type of missions and instruments.
2. Although generic, the E2ES should be flexible to be adapted for the particularities of each mission.
3. Depending on the type of instrument to be simulated, each of the six high-level modules will have an internal architecture broken down in **building blocks**.
4. Different implementations of the same building blocks account for mission parameters and evolution of algorithms throughout different mission phases.
5. Some high-level modules and lower-level building blocks will be generic across missions and instruments (e.g., platform orbit/attitude simulator).

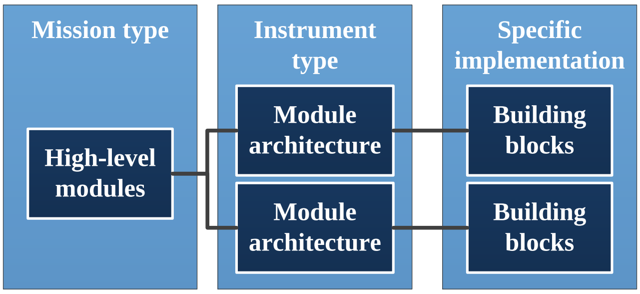

Figure 3.14: The generic E2ES architecture design concept.

The generic E2ES architecture was decomposed in three main elements:

- **Modules** and **Building Blocks**: software objects that implement specific models and algorithms. The modules were defined as the higher-level elements in the E2ES architecture and were associated to a specific functionality. Each high-level Module was divided into lower-level Building Blocks, which implement specific models and algorithms.

- Input/output **data files**, exchanging information between the different Modules.
- **Configuration files**, defined by the user according to the instrument type and the simulation to be run. They were divided into: **(1)** *configuration parameters*, setting the desired conditions of each module (e.g., instrument characteristics, target location and acquisition epoch, key atmospheric parameters); and **(2)** *activation flags*, which are used to enable/disable the execution of a subset of models or to select the algorithm to be adopted when the E2ES is run. These activation flags can also be used to select a particular implementation of the building blocks when it is shared by different types of instruments.

From the categorization of missions and analysis of commonalities performed in Section 3.2.1, and based on the design and implementation of previous E2ES (see review in Section 2.2), the entire EO mission simulation chain was divided into six high-level modules that allows to build a generic E2ES architecture. These modules simulate independently all the relevant parts of the mission and, in combination with the other modules, they allow to estimate the sensitivity of the final mission products to different input parameters and disturbing factors.

- **Geometry Module:** Simulates the platform orbit/attitude and generates the observation geometry of each instrument.
- **Scene Generator Module (SGM):** Simulates the scene to be observed (surface and/or atmosphere), at fine spatial and spectral resolution, taking into account all environmental effects (surface and atmosphere, illumination conditions, topography...) for the correct generation of the TOA radiance to be acquired by an instrument.
- **Instrument Module:** Simulates the instrument behavior, both in spatial and spectral domains, according to the instrument type. It includes the resampling of the input scene to the instrument resolution, the generation of instrument noises and systematic effects by simulation of the sensor electronics and optics and the analog-to-digital conversion through the simulation of the on-board processing.
- **L1 Processing Module (L1P):** Process the instrument Level-0 data, particularly raw data, together with the estimated geometry data and generates the L1 products (i.e., L1a to L1c).
- **L2 Retrieval Module (L2R):** Retrieves bio-geophysical parameters that are objective of the mission/instrument based on implemented scientific algorithms.
- **Performance Evaluation Module (PEM):** Evaluates the performance of the simulated L1 and L2 outputs by comparison against the reference data from the geometry and scene.

Although the data flows between these high-level modules and their order of execution may vary depending on the type of mission and instrument, Fig. 3.15 shows the typical generic data flow that was considered as the main generic E2ES architecture. In addition, Tab. 3.1 shows the high-level interfaces between these high-level modules.

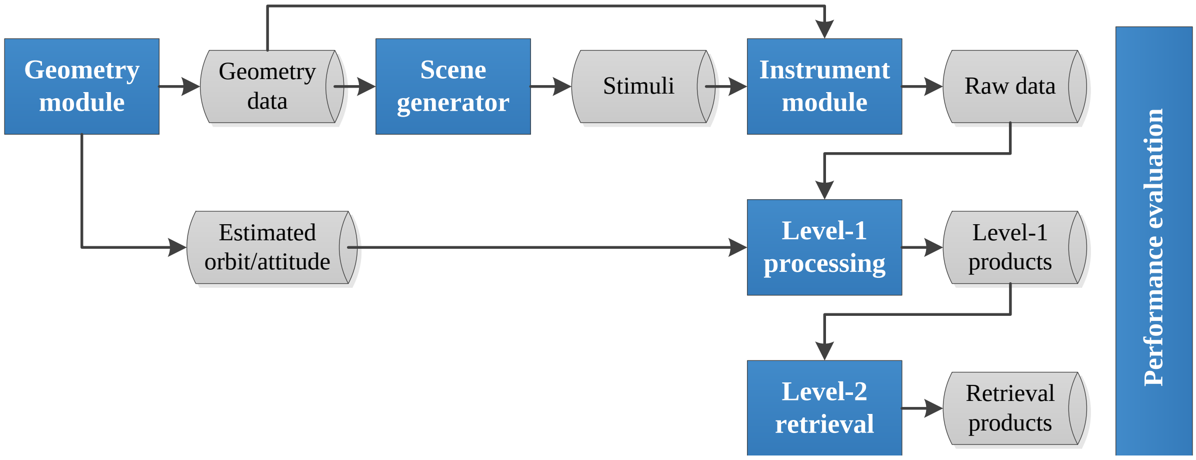

Figure 3.15: Generic E2ES data flow with **modules** and **i/o data**. For shake of simplicity, configuration files and links between PEM and the rest of the modules have not been represented.

Table 3.1: High-level interfaces in the generic E2ES architecture.

Module & Purpose	Configuration, Inputs and Outputs
Geometry: Simulates SC orbit & attitude & observation geometry of each instrument.	■ Configuration: Orbit & AOCS ■ Inputs: Target location and acquisition epoch ■ Outputs: Geometry data, Estimated orbit/attitude
Scene Generator: Simulates target scene and environmental effects needed for generation of stimuli entering the instrument.	■ Configuration: Scene parameters ■ Inputs: Geometry data ■ Outputs: TOA radiance
Instrument: Simulates sensor behavior, having different outputs depending on type of instrument.	■ Configuration: Instrument ■ Inputs: TOA radiance, Geometry data ■ Outputs: Raw (Level-0) data
L1 Processing: Generates L1 products, from L1a to L1c.	■ Configuration: Processing ■ Inputs: Raw (Level-0) data, Estimated orbit/attitude ■ Outputs: L1 products
L2 Retrieval: Performs retrieval of bio-geophysical parameters objective of the mission/instrument.	■ Configuration: Retrieval ■ Inputs: L1 products ■ Outputs: L2 products
Performance Evaluation: analyzes the simulator outputs to evaluate mission performances.	■ Configuration: Orbit & AOCS, Scene ■ Inputs: TOA radiance, Raw (Level-0) data, L1 and L2 products ■ Outputs: Performance reports

The most relevant mission categories identified in Section 3.2.1 indicated that the E2ES architecture was driven by the number of satellites and instruments in the mission as well as the combination of measurements (data synergy) from different instruments/platforms. From these categorization, some important aspects were addressed in the definition of the E2ES architecture. Firstly, the E2ES architecture should be able to simulate one or more satellites with one or more instruments on-board. Secondly, multiplatforms missions had implications in the simulator with respect of formation flying. Finally, the E2ES architecture should take into account the possibility of simulating a mission/instrument whose products are combined with other products from the same mission or from a different mission.

For a single spacecraft carrying several instruments, it is necessary to evaluate if secondary instruments shall be simulated. In that case, the E2ES architecture shall be tailored with the aim of including several instrument simulation chains taking into account the following remarks: **(1)** all chains will share most of the Geometry Module functionalities, apart from what refers to the specific instrument observation geometry; **(2)** the SGM is common for all instruments at least in what refers to the scene definition, so that the scenes observed by each instrument are consistent.; **(3)** there will be as many Instrument and L1P modules as instruments simulated in the E2ES; **(4)** it could be possible to have commonalities in the L2R (e.g., same atmospheric correction).

Two examples of data flows for the E2ES of these types of missions are shown in Fig. 3.16 and Fig. 3.17. Fig. 3.16 assumes that a common SGM generates the stimuli for both Instrument Modules. Then, a common L2R module will process in synergy the L1 products generated by the two instruments, retrieving the final L2 products. By sharing the same SGM, the two instruments are observing at the same radiometric target. Therefore, the L2 products would be also similar when closing the E2ES loop. Missions like FLEX/Sentinel-3 would fall in this category, were data from OLCI/Sentinel-3 and FLORIS/FLEX are processed in parallel up to L1b and then ingested in a common L2 retrieval to exploit their synergies.

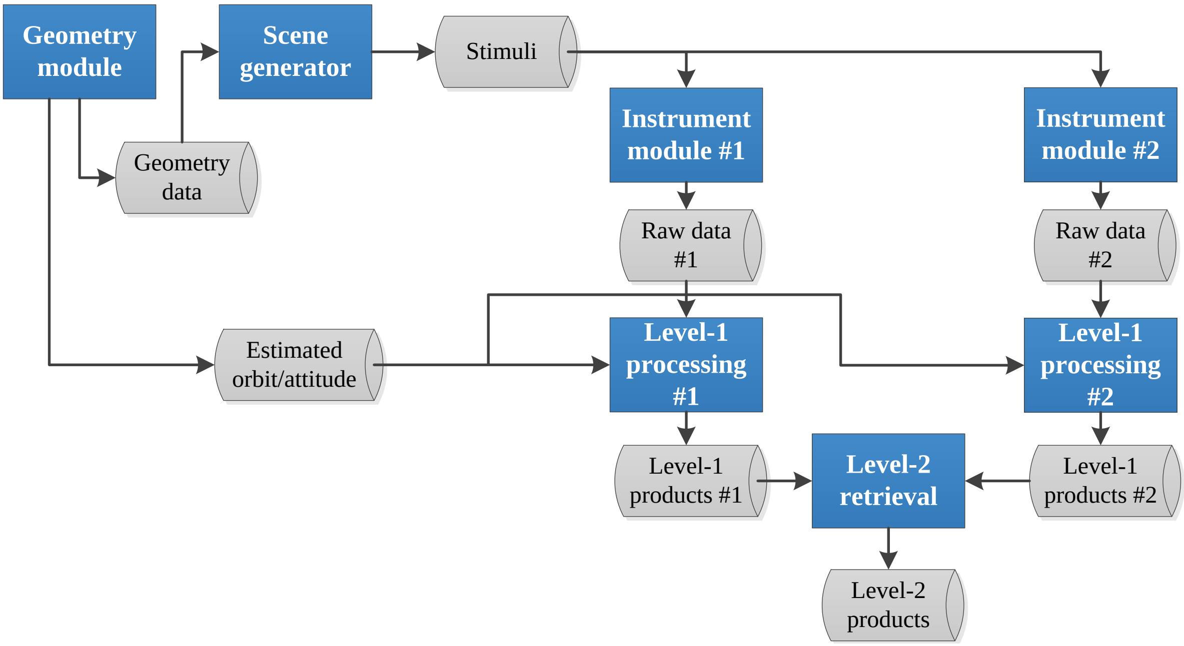

Figure 3.16: Example of generic E2ES data flow for a single platform with multiple instruments sharing scene generation and retrieval.

Fig. 3.17 shows the opposite behavior, where the two instruments are not sharing a common SGM, which indicates that they are designed to retrieve different bio-geophysical parameters (maybe also different scientific area of application). In this case, the L2R module would be necessarily different. Given that the only common module is the Geometry Module, it should be considered the option of defining two different E2ES for the mission, one for each instrument, replicating the common parts of the Geometry Module except the parts depending on the each instrument pointing. The reference architecture shown in Fig. 3.15 would then be applicable to each separate E2ES.

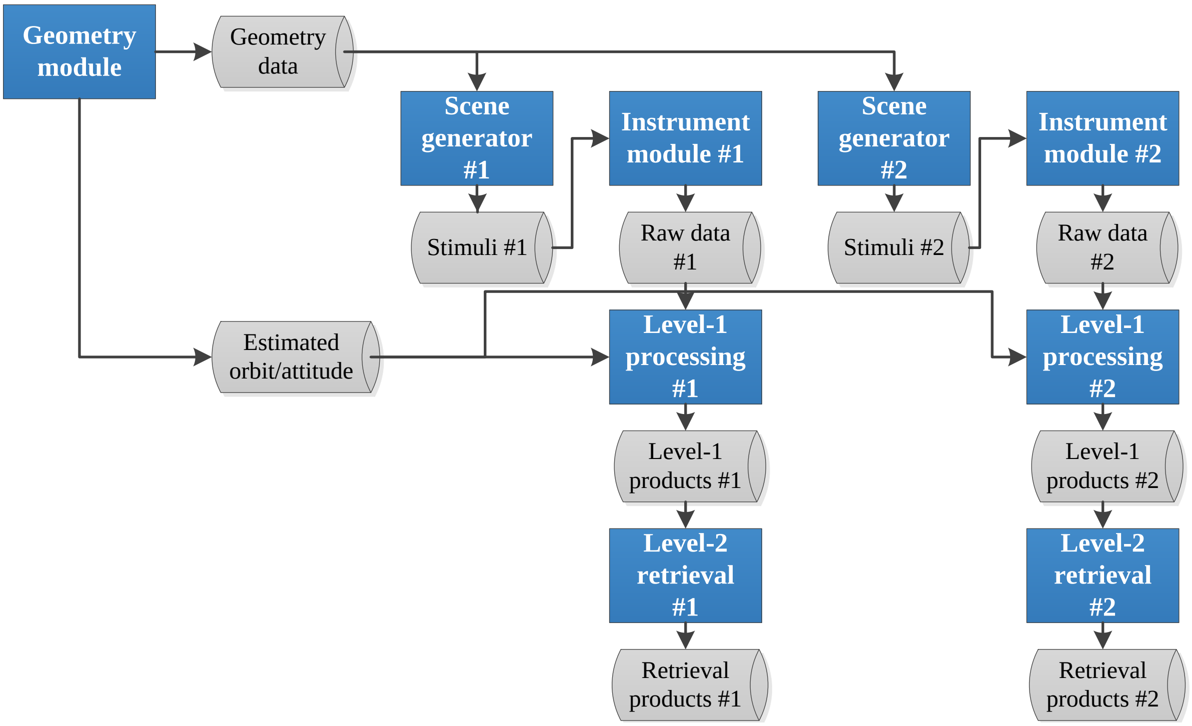

Figure 3.17: Example of generic E2ES data flow for a single platform with multiple instruments sharing only geometry simulation.

Missions like Sentinel-2 or Sentinel-3 (considering one instrument), would fall in this category, being two identical spacecraft placed at the same orbit phased 180 degrees. For this type of mission, in what respects to its E2ES, it can be considered as the simple case of single platform / single instrument (Fig. 3.15). Here, it was assumed that no combination of the instrument data from the two satellites is performed at any point of the processing or retrieval chain (at least for simulation purposes). In case of having strict formation flying requirements, the Geometry Module will deal with the generation of two satellite orbits and attitude profiles, most likely involving specific implementation of the building blocks to simulate the formation flying. Depending on the characteristics of each formation flying mission, the high-level E2ES architecture would present very different simulation chains. Some options were considered:

- Both instruments are identical, but fed with slightly different geometry and/or target scene. In this case, the nominal E2ES architecture in Fig. 3.15 can be applicable. Only the interfaces with the L2R module would slightly vary as it should ingest the data coming from two or more spacecraft instead of from only one.

- Different instruments in each spacecraft, but pointing to the same area with different geometry (e.g., MetOp or Sentinel-3). It may happen that the formation is performed with a spacecraft from a different mission. In that case, as the instrument simulation from the other mission will not be incorporated to the E2ES, the major issue is how to combine the products from it. If the formation is performed with a spacecraft of the same mission, it shall be evaluated at which point of the processing the data coming from the two spacecraft is put together. This would be probably the most complicated case to be handled from an architectural point of view.

This specific question was already raised in Section 3.2.1. Independently of the formation flying condition, the problem can be simplified in two scenarios: **(1)** Combination of products coming from a different instrument of the same mission; or **(2)** combination of products coming from a different instrument of a different ("secondary") mission. It was assumed that, up to L1, the data coming from other instruments is processed independently. Therefore, the L2R module would be the one responsible to deal with this data combination and produce integrated retrieval products. Based on this assumption, if this data is provided by another instrument from the same mission, the architecture proposed in Fig. 3.15 would be valid. If the data come from a "secondary" mission, two options were considered:

On the one hand, data from "secondary" missions can be considered as external outputs not produced in the frame of the E2ES. In this case, the E2ES architecture is not affected and the architecture shown in Fig. 3.15 would be valid. However, the use of this real data from other mission affects at two stages of the E2ES in terms of interfaces: **(1)** the SGM should produce a scene that is consistent with the external data, probably through its processing; and **(2)** the L2R module will internally process the external data and combine it in synergy with the L1 data produced in the E2ES in order to generate the final L2 products. The use of real scenes as input to the SGM may add some inconsistencies in the E2ES chain. Real images would be typically defined at L1c or L2, so they will be biased by the geometrical conditions and real bio-geophysical parameters of the areas observed in the image acquisition. Reproducing in the E2ES exactly the same conditions will be almost impossible, so part of the E2ES evaluations could then be invalid (retrieval products compared to bio-geophysical parameters or even the L1c products compared to the corresponding instrument TOA radiance). In order to minimize the inconsistencies, one approach would be to retrieve a map of bio-geophysical parameters from these external images so that the SGM generates consistent scenes for the main mission.

On the other hand, the "secondary" mission can still be simulated in the E2ES with the development of custom-made modules that include all the relevant mission characteristics while introducing simplifications with respect a detailed E2ES for that other mission. Following this approach, the same SGM can be used to generate consistent scenes for all the instruments in the main and "secondary" mission. In this case, the architecture would be similar to the one in Fig.

3.16 with two Geometry Modules (for the main and "secondary" mission).

Based on the objective of reducing as much as possible the number of high-level reference architectures, only three variations of high-level architecture were selected:

- Nominal E2ES architecture. It is proposed that the Geometry module will be always run in first place within the simulation chain. It would be valid for **(1)** single instrument missions, independently of the number of spacecraft and formation flying conditions, and **(2)** multiple instrument missions, if each instrument is simulated in a different E2ES.
- Multiple instrument, identical bio-geophysical parameter to be analyzed. The SGM and L2R modules are identical for both instruments.
- Multiple instrument, different bio-geophysical parameter to be analyzed. In this case, only the Geometry Module is shared between the two instruments.

The E2ES architecture should also allow the use of external files (e.g., in the form of LUTs) to be used instead of actual computations. This does not have a big impact over the general architecture, and it affects only at Module or Building Block level.

3.3.2 Specificities in the E2ES architecture for passive optical instruments

As analyzed in Section 3.2.2, passive optical instruments share some commonalities that can be represented using the same generic E2ES architecture proposed in Section 3.3.1. These commonalities have an impact at a lower level of the E2ES architecture with respect to the internal architecture of the six high-level modules. This section describes this internal architecture and analyzes the specificities introduced by different passive optical missions.

It was considered that any full E2ES chain for passive optical missions can be described by seven sequential steps:

1. The E2ES user sets the configuration parameters and selects the external data files needed to run a simulation. Among the possible configuration parameters, it was considered that the acquisition epoch and/or target location (or alternatively, duration of acquisition) were of common use for all types of passive optical instrument. These two configuration parameters are needed, through the Geometry Module, to define the size of the scene observed by the instrument(s) and constrain the observation and illumination geometry.
2. The Geometry Module is firstly run, computing platform orbit and attitude profiles for the observation of the selected target. This module computes the observation geometry (i.e., instrument LOS) for each instrument in the platform as one of its main ouputs.

3. The SGM generates the scene(s) to be observed by the instrument(s) based on the input geometry, configuration files and external data. Scene are defined as a TOA radiance hypercubes (i.e., spatial-spectral) at a spatial/spectral resolution higher than the instrument. For Earth-surface pointing instruments, scenes are characterized by their surface reflectance, emissivity, temperature and/or fluorescence together with key surface and atmospheric bio-geophysical parameters and surface topography. For limb-pointing instruments, scenes are characterized by vertical distributions of atmospheric parameters.

4. Next, the instrument acquires the TOA radiance scene and generates raw (Level-0) data based on the instrument type and configuration parameters.

5. The generated raw (Level-0) data is processed by the L1P module. This module generates L1 TOA radiance, geolocated, calibrated and free from systematic errors.

6. Finally, the L2R module processes L1 data and generates final L2 products. The first step in the L2R is to pre-process the L1 data (e.g., radiometric/spectral re-calibration, spatial co-registration). Next, the L2R will, for surface-pointing instruments, atmospherically correct the image producing surface reflectance, emissivity, temperature and/or fluorescence. The atmospherically corrected data can then be processed to retrieve bio-geophysical parameters, land-cover classification or other relevant products. For atmospheric missions (surface- or limb-pointing), the L2R will retrieve the atmospheric parameters describing the atmosphere (e.g., concentration and vertical distribution of trace gases, aerosol properties, water vapor).

7. As the L1 and L2 products are generated, the PEM will compare them against the reference (“truth”) data from the Geometry and SGM modules. The PEM evaluates the quality of the radiometric calibration, analyzes the instrument error budget and determines the accuracy of the retrieved L2 products.

Geometry Module

The main purpose of the Geometry Module (see Fig. 3.18) is to provide the instrument(s) observation geometry based on satellite orbital position, platform attitude and instrument(s) attitude (e.g., scanning motion, instrument mounting on platform). The Geometry Module therefore projects the detector array over the surface or atmospheric limb, calculating the LOS for each instrument pixel at each acquisition time.

The proposed architecture for the Geometry Module is applicable to all EO missions categorized according to their orbit types. The *Orbit Simulator* building block should generate the platform orbit (nominal, real and estimated) according to the Attitude and Orbit Control System (AOCS). By providing orbit coordinates in the Earth Centered Earth Fixed (ECEF) system, the rotation of the Earth is accounted within the platform orbit and allows the Geometry Module to generate all type of orbits. For instance, a geostationary orbit will have fixed orbit coordinates (except perturbations or AOCS errors) while a sun-synchronous orbit will have orbit coordinates such as the solar illumination remains almost the same over the Earth’s surface.

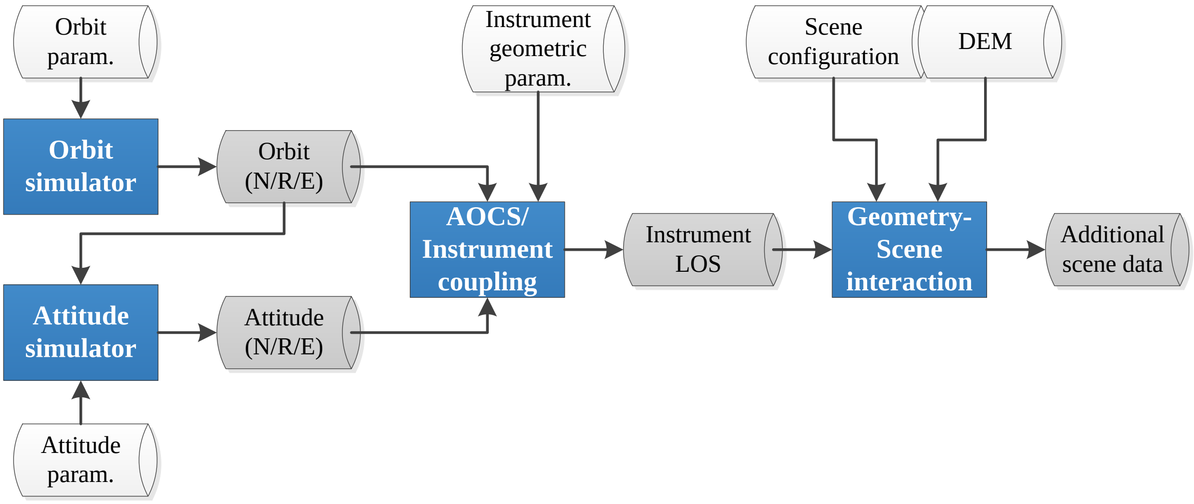

Figure 3.18: Architecture and building blocks of the Geometry Module (N/R/E= Nominal / Real / Estimated).

Also, the combination of the *Attitude Simulator* and *AOCS/Instrument coupling* building blocks account for all types of instrument/platform pointing maneuvers and instrument scanning geometries analyzed in Section 3.2.2. The *Attitude Simulator* building block should be capable of implementing different attitude profiles (i.e., temporal evolution of the platform attitude) including platform-pointing maneuvers for angular, limb, fixed (near-nadir) and slow down acquisitions. This block needs to know the relative orientation of the platform with respect to the ECEF frame and position of the Sun, Moon or stars (in case of limb-pointing in occultation mode). The scanning geometry is dealt within the *AOCS/Instrument coupling* building block, which simulates the instrument's mechanical features (e.g., scanning mirrors, multiple cameras, wheel-filters) and the LOS for each instrument pixel as function of the acquisition time.

With respect to multiangularity and multiple cameras, the proposed architecture accounts for the different identified types. Multiangular observations with multiple cameras (e.g., MISR/Terra), conical scanning (e.g., SLSTR/Sentinel-3) or platform attitude maneuvers (e.g., CHRIS/Proba-1) can be simulated by calculating the time and observation geometry of each angular acquisition of the same ground target. Considering this approach, each multiangular observation modifies the geometry of the scene being acquired, therefore there will be as many scenes (from the SGM) to be processed in the instrument module as multiangular observations.

Regarding the swath type, the Geometry Module can simulate all the proposed types (scene mode, carpet mode and full-Earth disk) by considering the time frame in which the images are acquired. In the first case (scene mode), the image is acquired at a single acquisition time (e.g., through a frame instrument or punctual acquisition by a sounder) and the orbit position and attitude are determined by this acquisition time. In the second case (carpet mode), the instrument acquires images during a time frame between t_0 and $t_0+\Delta t$ in which the platform follows an orbit segment and has changes in attitude (due to e.g., perturbations and AOCS maneuvers) and, eventually, instrument scanning motion (e.g., scanning mirrors or angular pointing). The last case (full-Earth disk) is similar to carpet mode but in this case the full-Earth disk is scanned in a time frame between t_0 and $t_0+\Delta t$ through the scanning motion of platform and/or instrument (e.g., Spinning Enhanced Visible and Infrared Imager (SEVIRI/MSG) or Flexible Combined Imager (FCI/MTG)). All these cases are different implementations of a time-dependent change in the platform attitude and instrument LOS scanning.

For instruments pointing towards the Earth surface, the *Geometry-Scene Interaction* building block, should consider the surface topography (particularly for high spatial resolution instruments over land) in order to determine which scene elements are seen by which instrument pixels and with which local observation and illumination conditions (see Fig. 3.19). Therefore, this block generates additional data needed by the SGM such as visual/solar zenith and azimuth angles, mask of scene elements not seen by the instrument and illumination-topography related parameters as e.g., described by Sandmeier et al. (1997) [134].

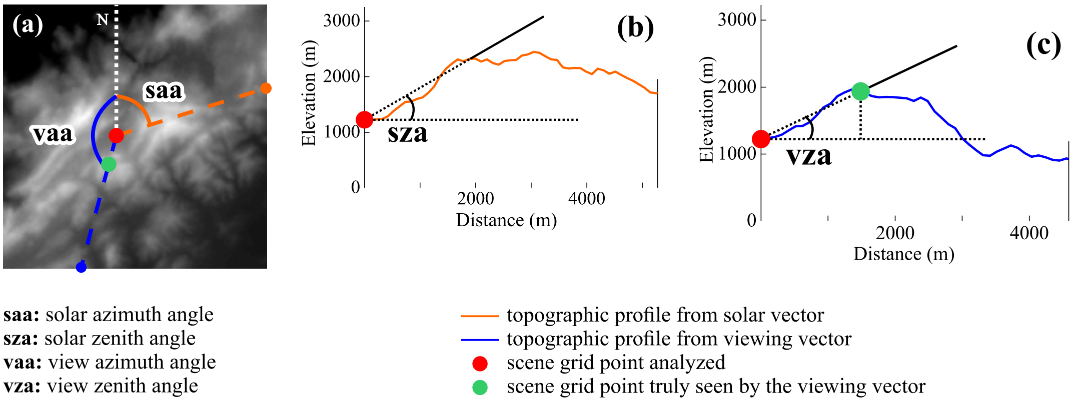

Figure 3.19: Schematic representation of the viewing/illumination vectors intersecting with a DEM for a selected scene grid point (●). (a) Nadir view of viewing/illumination vectors. Intersection of the illumination (b) and viewing (c) vectors with the topographic profile.

In addition, the Geometry Module provides estimated orbit and attitude profiles that are attached to the instrument raw data and are used at L1P module to perform the geolocation.

Scene Generator Module (SGM)

The SGM propagates the radiation through surface and/or atmosphere generating scenes that are observed by an instrument (e.g., [135, 136]). These scenes consist on a hypercube of high-spectral resolution TOA radiance spectra distributed over a high-spatial resolution grid. In order to be generic, the SGM architecture was designed (see Fig. 3.20) so that it generates scenes that are: **(1)** relevant for the mission goal/application (i.e., atmosphere, land, ocean…) according to spatially distributed key input bio-geophysical parameters for an end-to-end quality assessment of the L2 mission products; **(2)** compatible with the illumination and instrument observation geometry as input from the Geometry module; and **(3)** compatible with the instrument categorization in Section 3.2.2, particularly with respect to the spectral range and mode, spatial resolution and sensitivity to polarization. Based on these requirements, the SGM architecture was designed to be compatible with the instrument pointing types analyzed in Section

3.2.2, particularly the possibility of performing atmospheric limb measurements (in scattering and occulation modes) or Earth-surface pointing. In both cases the scene must be defined by key atmospheric and surface input parameters (*Scene Definition* building block). Also, radiative transfer models and equations should include contributions from atmospheric scattering, absorption and surface reflected/emitted light, generating TOA radiance scenes based on key input parameters and observation/illumination geometry (*Forward Model* building block).

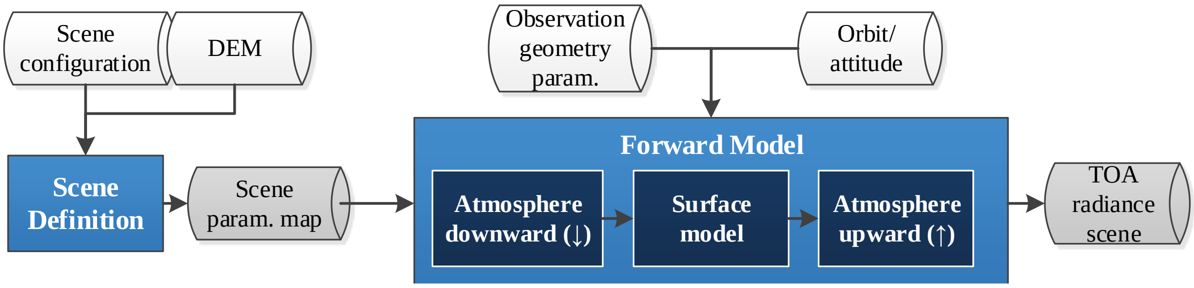

Figure 3.20: Architecture and building blocks of the SGM. Limb-pointing instruments only require the simulation of a forward atmospheric model for the fluxes from target to the instrument.

The *Scene Definition* building block aims to distribute key atmospheric and surface bio-geophysical input parameters over the target scene seen by the sensor:

- The distribution of key **surface** bio-geophysical parameters is based on a generated land-cover class (LCC) map of the target scene. The LCC distribution over the scene can be obtained from the analysis of external EO images (e.g., [22]), based on the topography (e.g., [26]), or directly provided through external LCC maps (e.g., [137, 138]). Each LCC is associated with a set of key input bio-geophysical parameters e.g., Essential Climate Variables [139]) with their statistical and spatial distributions (adding natural variability to the distributed values) and temporal evolution (adding phenologic temporal variability and land use changes). The set of parameters depend on the application domain. For instance, a mission studying vegetation will use parameters such as LAI or leaf chlorophyll content, whereas a mission retrieving atmospheric composition might not assign any bio-geophysical parameters to each LCC.
- The distribution of key **atmospheric** parameters (e.g., vertical profiles of atmospheric gases, aerosols and temperature; aerosol parameters; cloud cover and parameters) is based on external databases of images of geolocated atmospheric profiles and parameters (e.g., [140–142]).

The *Forward Model* building block is in charge of generating TOA radiance scenes. The proposed internal architecture (see Fig. 3.20) was considered to be suitable for limb- (see Fig. 3.21) and surface-pointing (see Fig. 3.22) instruments. In both cases, this building block calculates the TOA radiance scenes based on radiative transfer propagation through surface (within the *Surface Model* block) and atmosphere (downward and upward fluxes within the *Atmosphere* blocks). The implemented radiative transfer propagation (e.g., through RTMs or external images/databases) should consider the set of key input bio-geophysical parameters, surface topography and illumination/observation conditions. However, certain particularities of limb- and surface-pointing instruments should be considered:

- **Limb-pointing:** After the analysis of EO passive optical mission in Section 3.2.2, two limb-pointing modes (see Fig. 3.21) have an impact in the SGM architecture: **(1)** the *scattering* mode, where the output scene is generated from reflected, scattered and absorbed Sun-light in the atmosphere; and **(2)** the *occultation* mode, where a light source spectrum (Sun, Moon or star) is directly absorbed and scattered through the Earth's atmosphere. In both cases, the atmospheric RTM implemented in the *Atmosphere* blocks should have a spherical geometry to account for the Earth curvature and variations of atmospheric composition in the instrument's LOS. In addition, the *Atmosphere upward (↑)* block should include, in *occultation* mode, the contribution of absorbed and scattered light from an external light source. With respect to the *Surface model* block, and considering that a limb-pointing mission aims to study the atmospheric composition, the surface can be modeled with a set of geolocated surface reflectance associated with the LCC map from the *Scene Definition* building block.

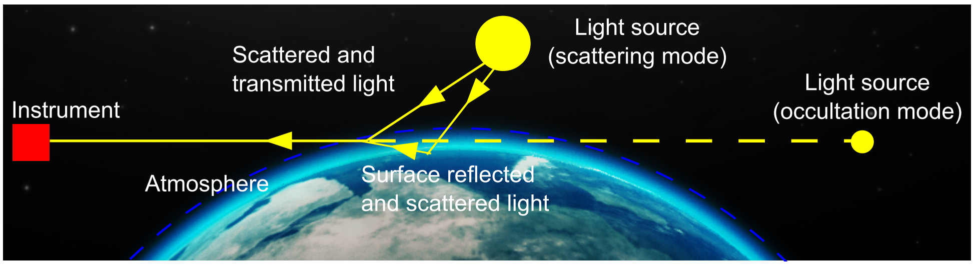

Figure 3.21: Conceptual representation of the *Forward Model* block for a simulation of a limb-pointing instrument in the scattering mode (solid line) and occultation mode (dashed line).

- **Surface-pointing**: These scenes are acquired when the instrument points towards the Earth's surface. They cover all type of applications: land (e.g., vegetation, land use, urban growing, fire detection), snow/ice cover, ocean (e.g., temperature, chlorophyll concentration) and atmosphere (e.g., aerosol parameters, concentration of atmospheric gases, cloud cover). Surface-pointing scenes are based on surface reflected and emitted[6] light generated in the *Surface model* block from specific RTMs and/or (reflectance, fluorescence and emissivity) spectral databases. In addition, these scenes might include topographic effects (e.g., terrain cast shadows, variation of target-to-sensor atmospheric path length) based on illumination-topography parameters derived in the Geometry Module.

---

[6] Fluorescence, emissivity and temperature, last two only for measurements in the MIR-TIR spectral range.

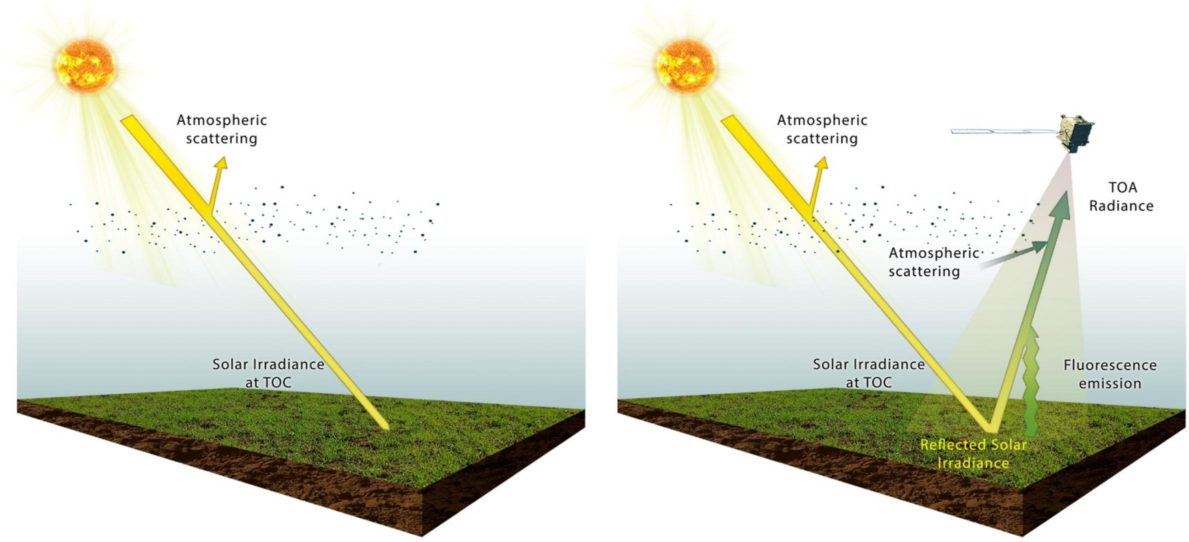

Figure 3.22: Conceptual representation of the *Forward Model* block for a simulation of a surface-pointing instrument in the UV-SWIR spectral range. Atmospheric downward propagation (left) and surface model simulation and atmospheric upward propagation (right).

Both surface- and limb-pointing scenes might also be affected by cloud cover (e.g., shadow projection on the surface, masks out surface areas covered by clouds, adjacency effects on neighboring areas). The cloud cover is defined by its position in the scene, height, thickness and geophysical properties. The radiometric simulation of clouds is carried out within the *Atmosphere* blocks and its required realism depends on the scientific mission objective. A realistic radiative transfer simulation of the cloud cover is computationally very demanding and most probably should not be considered in this general E2ES architecture. Alternatively, synthetic cloud covers can be generated using an atmospheric RTM such as MODTRAN [16].

The proposed architecture fulfills the requirements set in order to develop a generic SGM. Firstly, the generation of a TOA radiance scene based on distributed key input bio-geophysical parameters related to specific mission application allows evaluating these retrieved parameters at L2. Secondly, the *Forward Model* block calculates the TOA radiance scenes based on input illumination and observation geometry from the Geometry module. Finally, the use of specific RTMs and/or spectral databases generate scenes that are compatible with the instrument categories (i.e., spectral range, resolution and polarization) and mission application/goal [60].

A list of surface and atmosphere RTMs is included in Annex B.1 based on initiatives such as the Radiation transfer Model Intercomparison project [143–146] for evaluation of vegetation RTMs or the work by Kotchenova et al. (2008) [147] and ESA's project *ESAS-Light* [148] on the comparison of atmospheric RTMs.

In addition to limb- and surface-pointing scenes, calibration scenes are an additional case that can be generated with the described SGM. Calibration scenes are characterized by homogeneous radiance with a well-known spectrum. If the simulator is configured to generate a calibration measurement, the *Forward Model* block will output an homogeneous scene with a radiance spectra at the required spectral range and resolution from an external database of spectrum (e.g., solar irradiance, deep space background, lunar radiance/irradiance models [149], internal blackbody irradiance). An alternative case would be use vicarious calibration scenes, generated following the same approach as surface-pointing scenes.

Instrument Module

The Instrument Module aims to acquire the TOA radiance signal generated in the SGM, resampling an input scene to the instrument spatial and spectral resolution, and reproducing the effects of sensor electronics and optics in terms of radiometric noises, non-uniformity effects and analog-to-digital conversion, in addition to the data pre-processing (e.g., binning, data compression). According to the instrument categorization in Section 3.2.2, and with respect to the impact on a generic Instrument Module, instruments were defined by their geometric characteristics (i.e., spatial resolution, number of spatial pixels, instrument type), spectral characteristics (i.e., number of spectral bands, spectral sampling and resolution, smile) and radiometric characteristics (e.g., dead pixels, cross-talk, vertical striping, stray-light) driven by the spectroradiometer type and detector type. The instrument image acquisition requires that these geometric, spectral and radiometric features are applied sequentially in the simulation process. Based on this requirement, and considering analyzed instrument categories, a generic architecture for the Instrument module in Phase A/B1 (see Fig. 3.23) was designed following the work done in [14, 15, 20, 23, 26, 150].

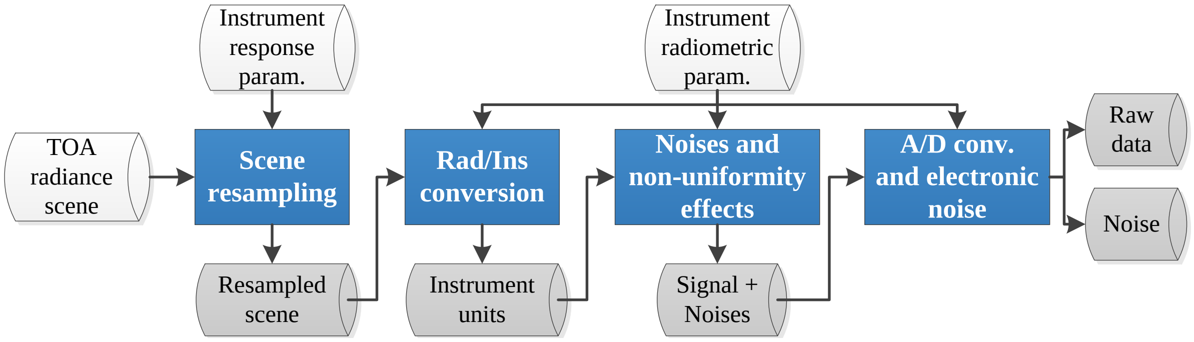

Figure 3.23: Architecture and building blocks of the Instrument Module.

The *Scene resampling* building block accounts for the spatial and spectral resampling of the input high-resolution scene to the final instrument resolution. For an E2ES in Phase A/B1, it was considered that the spatial-spectral resampling of the image can be done in two sequential steps. Firstly, the instrument Point Spread Function (PSF) is calculated (e.g., [150, 151]) at each spatial pixel of the detector, using it to convolve the input high-resolution scene to the lower instrument spatial resolution. Secondly, this block calculates the Instrument Spectral Response Function (ISRF) at each spectral channel, using it to convolve the spatially-resampled input scene to the lower instrument spectral resolution. By separating the spatial-spectral resampling into two steps, all instrument types (whiskbroom, pushbroom and frame) can be simulated using the same approach. Conceptually, the proposed architecture considers the spatial resampling in pushbroom and frame instruments as a particular case of whiskbroom instruments in which the acquisition time of a group of pixels (line in pushbrooms; 2D-arrays in frames) is simultaneous (see Fig. 3.24). The temporal and spatial coordinates where each PSF is applied is calculated in the Geometry module and it might be wavelength dependent (e.g., in spectrometers, all spectral channels are acquired at the same time, whereas in wheel-filter and multicamera radiometers, they are acquired at different times).

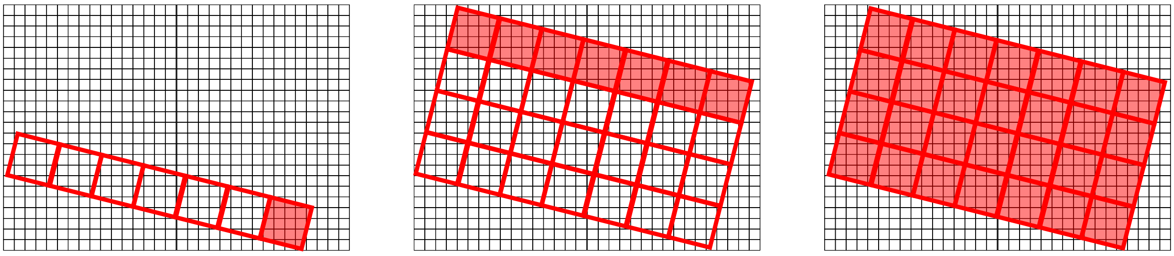

Figure 3.24: Conceptual representation of the instrument spatial grid (red) projected over the higher spatial resolution scene grid (**black**) for whiskbroom (left), pushbroom (mid) and frame (right) instruments. Every acquisition time, thus PSF projection, is represented by the red-filled square, non-filled squares corresponding to previous acquisitions.

After the spatial resampling, each ACT and ALT high-spectral resolution pixel is spectrally resampled. In terms of architecture, the spectral resampling can be implemented with a similar approach for spectrometers (prism, grating and variable filter) and radiometers (filter wheel and multicamera). For these cases, the high-spectral resolution image (one for spectrometers; several for multispectral radiometers) is convolved with the calculated ISRF (see Fig. 3.25), which might vary for different spectral channels. In addition, for pushbroom imaging spectrometers, the wavelength center of each spectral channel might vary ACT, an effect known as smile [152].

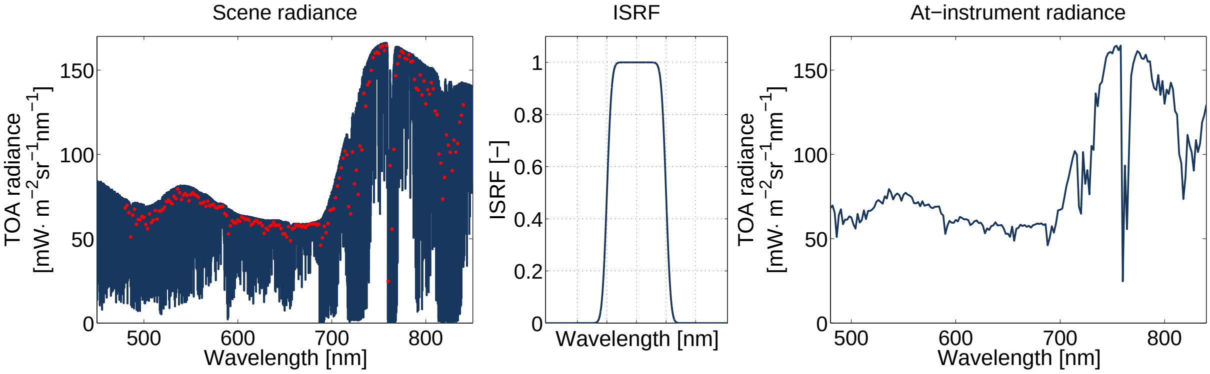

Figure 3.25: Conceptual representation of the instrument spectral resampling for superspectral and ultraspectral instruments. The high-spectral resolution scene TOA radiance (left) is resampled by the computed ISRF (mid) at various spectral channels (red dots) producing a resampled radiance (right).

The spectral resampling in Fourier Transform Spectrometers (FTS) is implemented differently than grating/prism/variable-filter spectrometer and radiometers. Instead of working in the wavelength domain, FTS acquires an interferogram of the SGM input scene based on the difference of optical path between the two FTS arms, and performs the spectral resampling based on the FTS line shape function in the wavenumber domain [153, 154].

Gas correlation spectrometers (e.g., MOPITT/Terra [155]) were not considered within a generic E2ES architecture given the particularity of these type of instruments.

The *Scene resampling* block calculates the shapes of the PSF and ISRF for every spatial pixel, spectral channel and acquisition time taking into account the instrument optics (e.g., spectral filters), spatial/spectral non-linearity effects (e.g., smile, keystone) and thermal stability depending on the spectroradiometer type (e.g., [107, 152, 156–158].

After the spatial-spectral resampling of the input scene, the Instrument Module applies radiometric effects from the acquisition chain. Firstly, within the *Rad/Ins conversion* building block, the radiance units are converted to instrument units (i.e., electrons) based mainly on quantum efficiency of the detectors and integration time. Secondly, the radiometric noises and non-uniformity effects are applied, adding shot noise, random dark signal [159], memory effects [160], detector variable non-linear responses and systematic pixel-to-pixel non-uniformities (e.g., vertical stripping, dead/bad pixels) [161–163]. In terms of architecture, this block is the same for every sensor and instrument type but the effects applied here will be adapted according to the characteristics of the detectors and instrument types. Finally, the *A/D conversion and electronic noise* building block converts the instrument signal in digital counts including variable high/low gains, adding the quantization effect of the input signal and simulating the generation of electronic noise. The generation of on-board data packages is not included in the generic E2ES architecture for missions in Phase A/B1, but should be added for Phases C/D.

L1 Processing (L1P) Module

The L1P module processes the raw (Level-0) data from the Instrument module, together with the estimated attitude and orbit data from the Geometry module, to produce radiometrically calibrated and geolocated L1 data with recovered pixel uniformity. In addition, the L1 processing includes image quality identifiers and preliminary classification (i.e., land/water/bright pixels) for each image pixel. A generic architecture was considered for the L1 data processing chain (see Fig. 3.26) for all passive optical missions based on the analysis of commonalities in Section 3.2.2. The proposed architecture is similar to the one adapted in missions such as ASTER/Terra [164], EnMap [22] or the Sentinel product definitions [71].

The *Calibration* building block, executed when the simulator is configured to run in calibration mode, determines the calibration coefficients needed for the instrument calibration, which are stored for their later use in an operational scientific acquisition mode. In this case, the input scenes (from SGM) and raw data (from the Instrument Module) are generated to reproduce

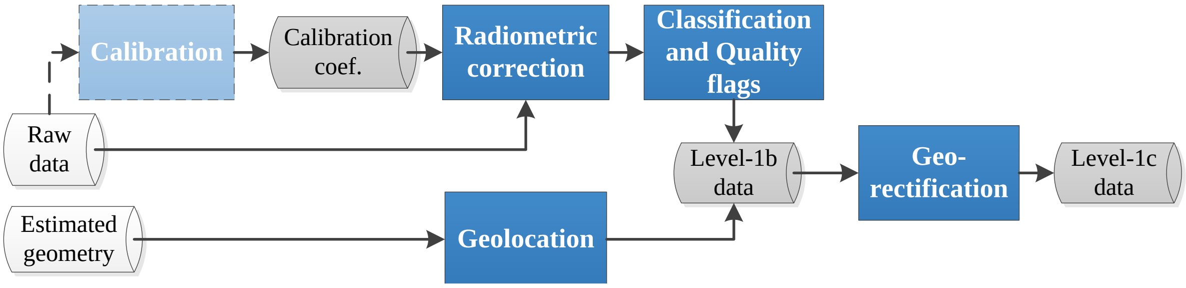

Figure 3.26: Architecture and building blocks of the L1 Processing Module. The light-blue *Calibration* building block is only executed in calibration acquisition mode to determine the calibration coefficients.

the calibration data used to determine the coefficients for the radiometric calibration, dark current correction and spectral characterization: Sun irradiance, Moon-reflected Sun irradiance, spectral lamps or LEDs, vicarious calibration target, blackbody or deep space (see Acronyms and Definitions at page xvi for further description). Alternatively, this block could imitate the application of ground-based calibration coefficients (e.g., [4, 165]), adding errors over the real coefficients used in the Instrument Module so that the conversion of the raw data into radiance units is performed with errors associated to the real calibration process.

If the simulator is configured to run in operational scientific acquisition mode, the calculated calibration coefficients are used in the *Radiometric correction* building block to convert the raw data from digital units to radiance units[7]. In addition, this block aims to reduce the effects of systematic instrumental spectral and spatial noises that were detected in the *Calibration* building block. The implemented algorithms depend on the mission Phase, instrument type and detector type:

- Bad/dead and dropout pixel detection and correction (e.g., [163]).
- Spectral and spatial non-linearity characterization and correction.
- Offset detection and subtraction.
- Dark Current characterization and subtraction. The dark current depends on instrument and sensor characteristics (e.g., analog offset independent of the integration time, leakage current, growth of an ice layer on the detector or background thermal signal for infrared channels [160]).
- Detection and correction of detector non-uniformities in the spatial and spectral directions (e.g., [162, 163]).
- Spectral and spatial stray-light correction (e.g., [166]).
- Smile and keystone characterization (only for pushbroom sensors) (e.g., [167]).

---

[7] E.g., MSI/Sentinel-2 Level-1 Algorithm Overview

- Memory effect, where previous readouts deviates the signal from a linear response (e.g., [160, 168]).
- Determination and correction of instrument polarization sensitivity (e.g., [160, 169]).

In the specific case of FTS, the *Radiometric correction* building block implements the algorithms to recover the spectra from the measured interferogram (e.g., [4, 170]).

The *Classification and Quality Flags* building block associates a preliminary classification tag (only for Earth pointing instruments) to each image pixel, identifying land, water, coast, bright and sun-glint pixel. This classification, based on TOA radiance or reflectance thresholds and instrument ancillary data, is mostly done for archiving purposes. In addition, it adds a set of quality flags in order to track the goodness of calibration, radiometric corrections and saturated pixel detection (e.g., [171]).

In parallel to the radiometric calibration/correction chain, the instrument raw (Level-0) data is geolocated in the *Geolocation* building block assigning a pair of latitude/longitude coordinates to each image pixel. This block uses the estimated attitude, orbit and LOS vectors data from the Geometry module together with instrument configuration parameters such as instrument mounting on platform (e.g., [164, 172]). The combination of geolocation and radiometric calibration generates L1b data.

The *Georectification* building block is finally run in the chain only for missions that require the generation of L1c data. This block uses a DEM to project the images through a coordinate transformation to an Earth coordinate system such as WSG85 (e.g., [4, 22, 173]).

L2 Retrieval (L2R) Module

The L2R module is in charge of retrieving the bio-geophysical parameters specific of each satellite/instrument mission. The implemented retrieval algorithms are normally tailored to instrument design (e.g., spectral channels, multiangularity, polarization sensitivity) and mission (e.g., synergy between instruments). Notwithstanding, the analysis carried out in Section 3.2.2 showed that L2 products can be classified into two main groups of bio-geophysical parameters: surface and atmospheric. Thus, a generic L2R module architecture was designed (see Fig. 3.27). It considered the difference between Earth limb- and surface-pointing instrument and the possibilities to perform synergy with external (i.e., from “secondary” instruments and/or satellites) L1 and L2 products. For surface-pointing instrument the *Atmospheric block* and *Target classification* building blocks will be executed sequentially before the *Retrieval algorithms* building block whereas for limb-pointing instruments, this block will be executed after the *Data pre-processing* building block.

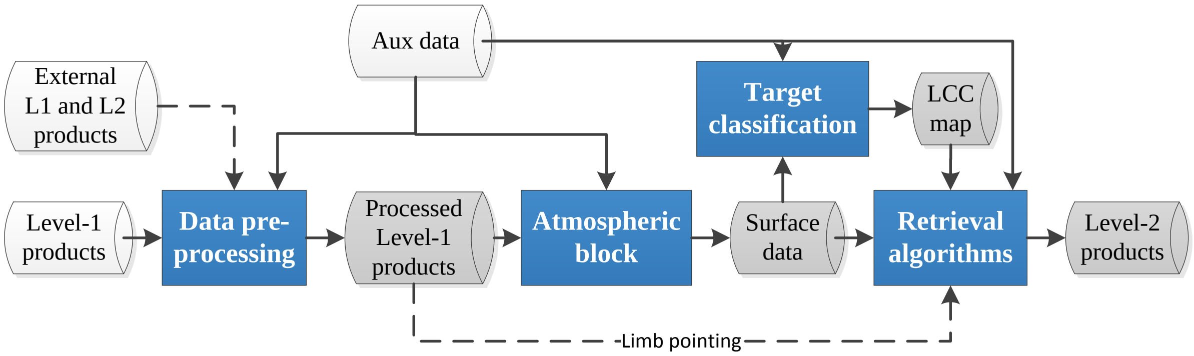

Figure 3.27: Architecture and building blocks of the L2R module. Limb-pointing instruments do not perform target classification and atmospheric correction of the data.

The *Data pre-processing* building block is in charge of processing the L1 data from the L1P module, refining the geolocation, spectral calibration (e.g., based on matching of atmospheric absorptions [174]) and correction of systematic errors. In case of synergy with external L1 and L2 data from other instruments and satellites, this block co-registers the L1 and L2 datasets (e.g., [175]). This step might also co-register various spectral channels in filter wheel or multicamera frame radiometers, multicamera instruments with different LOS or instruments performing multiangular measurements. The co-registration resamples the data to a common spatial grid and resolution. In addition, also in case of synergy between several L1 products, this block radiometrically cross-calibrates the L1 data (e.g., [6]) so that the measured radiances are compatible among the instruments in synergy.

For surface-pointing instruments, the *Atmospheric block* runs after the data pre-processing. This block is sub-divided in two lower-level blocks that are sequentially executed:

- A **cloud screening** algorithm is firstly executed in order to detect those pixels affected by clouds. Cloud screening algorithms can be of two types: **(1)** binary, indicating whether a given pixel is affected or not by clouds; and **(2)** probabilistic, indicating the abundance (0-100%) of cloud cover within a pixel. Binary methods rely on radiance thresholds associated with clouds properties (e.g., [176, 177]) or on change detection for image time-series (e.g., [178]). Probabilistic methods use L1 TOA radiance data together with external data (e.g., DEM) to do features extraction and clustering, spectral unmixing and cloud labeling (e.g., [179, 180]). The implemented cloud screening algorithm depends on the instrument spectral configuration (e.g., cirrus band detection at 1375 nm, atmospheric pressure based on the O_2 filling at 760 nm, whiteness of the spectra in the VNIR spectral region). Depending on the implemented cloud screening method, and in terms of the E2ES architecture, the SGM might be required to simulate realistic cloud cover and temporal variations of the cloud pattern and properties (e.g., in case of multi-temporal cloud screening algorithms).
- The **atmospheric characterization and correction** block is in charge of determining the

atmospheric characteristics (mainly aerosol properties and water vapor content) and/or retrieve the surface reflectance, temperature and emissivity. Several methods can be applied depending on the instrument characteristics (i.e., spectral, spatial, polarization, multiangularity): **(1)** complex atmospheric model inversion algorithms (see comparison done by de Leeuw et al. (2015) [181]) typically applied on hyperspectral data (e.g., [182, 183]) and multi-instrument and multiangular images (e.g., [184]); **(2)** based on external in-situ measurements (e.g., [185, 186] or AERONET [142]); **(3)** image-based (semi)empirical methods (e.g., [187–190]); and **(4)** image contrast reduction algorithms, mostly used in multispectral and high-spatial resolution instruments (e.g., [191, 192]). The atmospheric correction might use external data (e.g., DEM, meteorological data[140]) to constrain the inversion of atmospheric key parameters (e.g., concentration of water vapor, aerosol properties, ozone concentration) or to correct for topographic effects [134].

The *Atmospheric block* generates surface data (i.e., reflectance, emissivity, temperature and at-surface solar irradiance) in addition to retrieved key atmospheric parameters. The surface data are then used for target classification and retrieval of final L2 products. In case the instrument goal is to study the atmosphere (e.g., OCO-2, TANSO-FTS/GOSAT, FCI/MTG), the execution of the *Atmospheric block* might be skipped so that the *Retrieval algorithms* building block retrieves the atmospheric L2 products directly from the processed L1 products (e.g., ACOS CO_2 retrieval algorithm [193]).

The *Target classification* building block might also be executed for surface-pointing instruments when **(1)** the mission goal is to produce a LCC map [137, 138], or **(2)** the retrieval algorithm is applied over a specific set of pixels that need to be preselected (e.g., retrieval of Chlorophyll content in inland waters). In the first case, the LCC map is the final L2 product and thus the *Retrieval algorithm* building block is not executed. In the second case, the generated LCC map is a intermediate step to run the retrieval algorithms over surface data.

The *Retrieval algorithms* building block implements algorithms for the retrieval of final mission products. These algorithms are specific of each mission and thus it is not possible to develop a generic *Retrieval algorithms* building block. Nevertheless, the quantification of bio-geophysical variables relies on RTMs or a large database of in-situ measurements. Therefore, many retrieval algorithms are reduced to a regression problem based the measured surface data and thus they are classified based on the analysis carried by Odermatt et al. (2012) [194] and Verrelst et al. (2015) [12] as follows:

- **Parametric regression:** explicit relationships are set between retrieved bio-geophysical parameters and surface data, typically through spectral indexes (i.e., simple mathematical relations between two or more spectral bands). These parametrized equations have been implemented in multi- and super-spectral instruments. Differential absorption ratios for the retrieval of concentrations of atmospheric gases is an example of parametric regressions (e.g., [195]).

- **Non-parametric regression:** based on machine-learning algorithms that determine statistical relationships between observations (i.e., surface data) and retrieved parameters. These statistical relationships do not establish explicit transformations or fitting functions between observations and retrieved data, but use non-parametric approaches.
- **Physically-based algorithms:** based on the inversion of a RTM through the minimization of a cost function i.e., difference between observations and simulated RTM data. An example of these algorithms is the retrieval of aerosol optical thickness in [182].
- **Spectral (curve) fitting methods:** consist in the optimization of the fit between modeled and measured spectra (e.g., [53]). The parameters of the modeled spectra are then related to final mission bio-geophysical products. Curve fitting methods are related to physically-based algorithms when the modeled spectra is based on physical models.
- **Hybrid methods:** combine the generic properties of physically-based algorithms and the flexibility and computational efficiency of non-parametric regressions.

Performance Evaluation Module (PEM)

The PEM is the last module executed in an E2ES simulation chain. It evaluates the quality of every retrieved L1 and L2 product in terms of their accuracy against reference data from the SGM and Geometry modules. These evaluations allows performing sensitivity analysis, assessing the design process of the instrument and mission and evaluating error budgets in the instrument, Level-1 processing and Level-2 retrieval algorithms. The rationale behind the PEM is to answer the following questions:

- Are the retrieved bio-geophysical parameters representative of the ground and atmospheric “truth”?
- Which are the bias and accuracies of the retrieved products with respect to the “truth”?
- How well the image processing and retrieval algorithms resolve spatial structures?
- To what extent error sources, corrections, calibrations and algorithms have an impact on the retrieved products?

Thus, the PEM was designed following the approach described in CEOS Cal/Val portal [196] for the evaluation of land, ocean and atmosphere product and it is based on three main steps: **(1)** The E2ES simulation chain is firstly verified by checking that the generated products are internally consistent and physically meaningful; **(2)** the data products are then compared with external datasets (e.g., field measurements or test simulated scenes) in order to validate whether the simulated products fulfill the mission requirements (e.g., signal-to-noise, geolocation accuracy, L2 products accuracy); **(3)** through the evaluations in the PEM, the E2ES is used to assess the quality of the instrument and data processing algorithms and to perform trade-off studies in the mission and instrument or to identify improvements in the implemented algorithms. The PEM assess the performance of the following datasets:

- Estimated observation geometry, given by the platform orbit/attitude and instrument LOS, is evaluated by comparison against the real geometry, both generated in the Geometry module. The quality of the L1 geolocation is evaluated through comparison with the real geolocated pixel coordinates.
- The accuracy of the L1 calibration and assessment of instrument noises is evaluated by comparison of the L1 TOA radiances images against the output TOA radiance scenes from the SGM.
- The cloud screening algorithm is evaluated by the comparison of the retrieved cloud mask in the L2R module against the input cloud distribution in the SGM.
- The atmospheric correction can be evaluated through the analysis of the surface data (i.e., reflectance, emissivity, temperature and/or fluorescence) from the L2R module, compared against the equivalent data from the SGM. Also, the atmospheric correction can be evaluated by analyzing the accuracy of the L2 retrieved key atmospheric parameters against those defined in the generation of the scene in the SGM.
- L2 bio-geophysical products retrieved in the L2R module are compared against the reference maps of key bio-geophysical parameters in the SGM.
- The auxiliary input DEM data used in the SGM is used as reference for the evaluation of the derived surface altimetry (e.g., through stereoscopic images) in the L2R module.

The internal architecture of the PEM module and its building blocks is shown in Fig. 3.28.

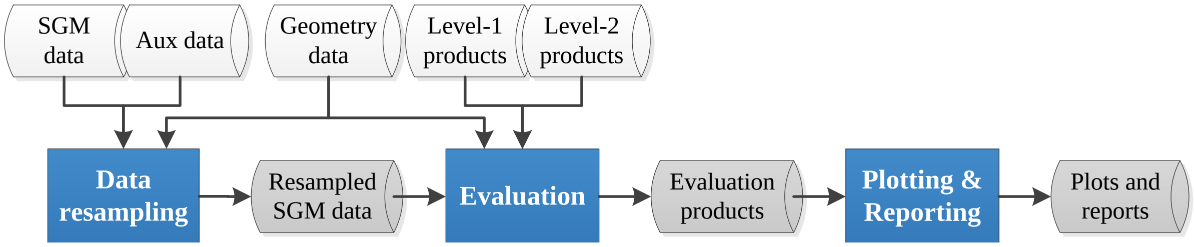

Figure 3.28: Architecture and building blocks of the PEM.

First, the *Data resampling* building block is in charge of resampling the high-resolution reference data from the SGM (e.g., reflectance map, bio-geophysical parameters map) to the same spatial and spectral resolution of the final L1 and L2 products. This resampling is done in a similar manner as implemented in the *Scene resampling* building block of the Instrument module by applying the instrument's PSF and ISRF. Secondly, the *Evaluation* building block compares the reference (from Geometry and SGM modules) and retrieved (L1 and L2 products) datasets by applying pixel-per-pixel error metrics and image error statistics. A few examples are:

- For spectral and/or scalar variables, pixel-wise and band-wise error metrics such absolute error, relative error. Image statistics can be provided for each spectral channel such as average absolute/relative error and its standard deviation, RMSE, R^2 and error percentiles.

- For spectral variables, pixel-wise error metrics such as the spectral angle mapper, spectral information divergence, or a mix of them [197].

- For non-continuous scalar variables (e.g., land cover classification), image statistics can be used determine the error in the classification. Commonly used metrics are the Kappa index, the overall accuracy or the McNemar's test [198].

Several other methods can be applied to compare images and evaluate the quality of the retrieval. Avcbas et al (2002) [199] list some of the methods that can be used in this block.

Finally, the *Plotting & Reporting* building block produces the figures and reports based on the input reference and retrieved data and calculated error metrics. This block produces figures such as error maps, histograms and scatter plots.

3.4 Summary

In this Chapter, a generic End-to-End Mission Performance Simulator (E2ES) architecture for EO passive optical missions was designed. Firstly, a review of past, present and planned EO missions was carried out with the goal of extracting commonalities among them. Secondly, these surveyed missions were classified in terms of their design (i.e., number of satellites and instruments, synergy between products, orbit types, mission goal and application) and in terms of specific aspects of the instruments onboard them (e.g., spectral range, spatial resolution, pointing, spectroradiometer type...). It was taken special attention to those characteristics that impact the mission performance and thus that should be considered to design the E2ES architecture. Thirdly, six high-level modules were identified as common elements needed to develop any type of EO mission (i.e., Geometry, Scene Generator, Instrument, L1 Processing, L2 Retrieval, and Performance Evaluation). Based on these six high-level modules, it was proposed a conceptual design for a generic E2ES architecture based on the commonalities found between EO passive optical missions and their instrument classification. Each of these high-level modules was then further described in terms of their internal architecture and interfaces with other high-level modules. In summary, the conceptual E2ES architecture design was found to be suitable to reproduce most passive optical instrument mission as it can be adapted to different EO missions by implementing specific algorithms that account for specific characteristics of each instrument and mission. In the following Chapter, the proposed generic E2ES architecture will be implemented for the ESA's FLEX/Sentinel-3 mission.

4

FLEX/Sentinel-3 End-to-End Mission Performance Simulator

Contents

After introducing conceptual design for a generic E2ES architecture in Chapter 3, this Chapter describes how this generic E2ES architecture was adapted and implemented for the ESA's FLEX/Sentinel-3 (S3) E2ES.

ESA's FLEX mission performance was analyzed in several interdependent industrial and scientific studies. Projects such as [200–202] consolidated FLEX mission requirements, developed a SIF retrieval algorithm, and investigated the linkage between SIF and photosynthesis. The industrial studies analyzed and developed engineering issues of FLEX platform and instrument. Each of these projects focused on specific aspects of the mission performance and introduced assumptions on other mission characteristics. Nevertheless, the competitive ESA mission selection process relied on the analysis of E2ES simulations that combine all different mission aspects following the guidelines in [36, 39]. For this reason, a FLEX E2ES (called FLEX-E) was developed in order to test the accuracy of the retrieved SIF and overall mission performance. FLEX-E was designed following the generic architecture proposed in Chapter 3 and it is considered as a suitable candidate to evaluate this generic architecture given that:

- ESA's request to develop an E2ES for the evaluation of the FLEX/S3 mission implied that the generic E2ES architecture concept would be demonstrated in a real case scenario for the ESA's 8th Earth Explorer mission selection process[1].

- FLEX is a **muliplatform** (FLEX and S3) and **multi-instrument** (FLORIS, OLCI and SLSTR) mission in **tandem flying formation** with **product synergy at L2**, which allows to test the generic E2ES architecture concept in this complex scenario.

- The instruments involved in the FLEX mission span several categories, which allows to test how the generic E2ES architecture copes with differences between them:
    - While FLORIS and OLCI are **fixed** near-nadir **pointing linear scanners**, SLSTR has a **bi-directional conical scanning** capability that provides **multiangular** images at near-nadir and 55° oblique views.
    - The instruments' **spatial resolution** ranges from 300 m (FLORIS and OLCI) up to 1-5 km (SLSTR nadir-oblique view).
    - The simulated **spectral modes** include superspectral (OLCI and SLSTR), hyperspectral (FLORIS-LR) and ultraspectral (FLORIS-HR). FLEX/S3 instruments cover the **VIS-TIR spectral range**.
    - All instruments within FLEX/S3 tandem mission are **multicamera** instruments: FLORIS **pushbroom** is splitted into two cameras (-LR and -HR for the low and high resolution spectrometers) and SLSTR **radiometer** is divided into three cameras (each one covering a different spectral range: VIS/SWIR/TIR), and OLCI pushbroom is splitted into five cameras (each one with a different ACT pointing angle).

Thus, this Chapter tackles the third **main objective** of this Thesis i.e.:

- To describe how the generic E2ES architecture concept was adapted and implemented in the FLEX-E tool, showing its suitability to reproduce a real case scenario and to assess the performance of the mission concept and the implemented processing algorithms.

This chapter is partly based on:

- **J. Vicent**, N. Sabater, C. Tenjo, J. R. Acarreta, M. Manzano, J.P. Rivera, P. Jurado, R. Franco, L. Alonso, J. Verrelst, J. Moreno, (2016). FLEX End-to-End Mission Performance Simulator. *IEEE Transactions on Geoscience and Remote Sensing*, Vol. 54, No. 7, pp. 4215-4223

- FLEX End-to-End Mission Performance Simulator, ESA-ESTEC Contract No. 4000108364/13/NL/BJ [2013-2015]

---

[1] ESA's 8th Earth Explorer User Consultation Meeting: www.esa.int/spaceinvideos/Sets/Earth_Explorer_8

4.1 FLEX-E architecture design

The FLEX-E design was based on the generic architecture concept described in Chapter 3 and outlined in [36] where the entire remote-sensing system was divided into multiple parts so-called *high-level modules*. These modules encompass different areas of the platform, instrument and signal modelling and were integrated and streamlined within the openSF [39] simulator framework. Following these guidelines, FLEX/S3 tandem mission was classified as a multiplatform mission (i.e., FLEX and S3) with a loose formation flying in Sun-synchronous orbit that performs synergy of L1b data from the different instruments. S3 is an external existing mission. The FLEX/S3 tandem mission is multi-instrument given that FLORIS (on FLEX), OLCI and SLSTR (on S3) are used to retrieve SIF of vegetation over land. Based on this classification, the E2ES architecture (see Fig. 4.1) was based on the generic architecture concept in Fig. 3.16 considering the following particularities:

- Two geometry modules were included for the simulation of FLEX and Sentinel-3 satellites. These two modules reproduce independently the platform attitude and orbit as well as the observation geometry for FLORIS, OLCI and SLSTR instruments.
- Given that all the instruments observe the same target scene, a single Scene Generator Module (SGM) was implemented. This SGM generates consistent and compatible input scenes for each instrument taking into account their observation geometry.
- Two parallel chains of instrument and L1 processing modules were envisaged. The implementation of FLORIS required a detailed modeling of the instrument and its L1 processing in two independent modules whereas OLCI and SLSTR instruments are “secondary” instruments within the mission. It was considered that the integration of (part of) S3 E2ES [35] within FLEX-E was not possible due to the constraints with respect to the generation of radiometric scenes compatible with S3 E2ES and FLORIS within FLEX-E. Thus, S3 instruments were simulated within FLEX-E in one single module that includes a tailored modeling of OLCI, SLSTR and their L1 processing chains.
- The mission uses OLCI and SLSTR L1b data in synergy with FLORIS L1b data within a common L2 Retrieval (L2R) module.

The following sections describe how the generic architecture concept was adapted and implemented in the FLEX-E tool for each high-level module and streamlined within the openSF simulator framework.

4.1.1 Geometry modules

The geometry modules are in charge of simulating the satellite orbit and attitude, as well as the generation of the observation geometry of each instrument. They are constrained by the simulation of the FLEX/S3 tandem flight configuration. This implies that each sensor, given

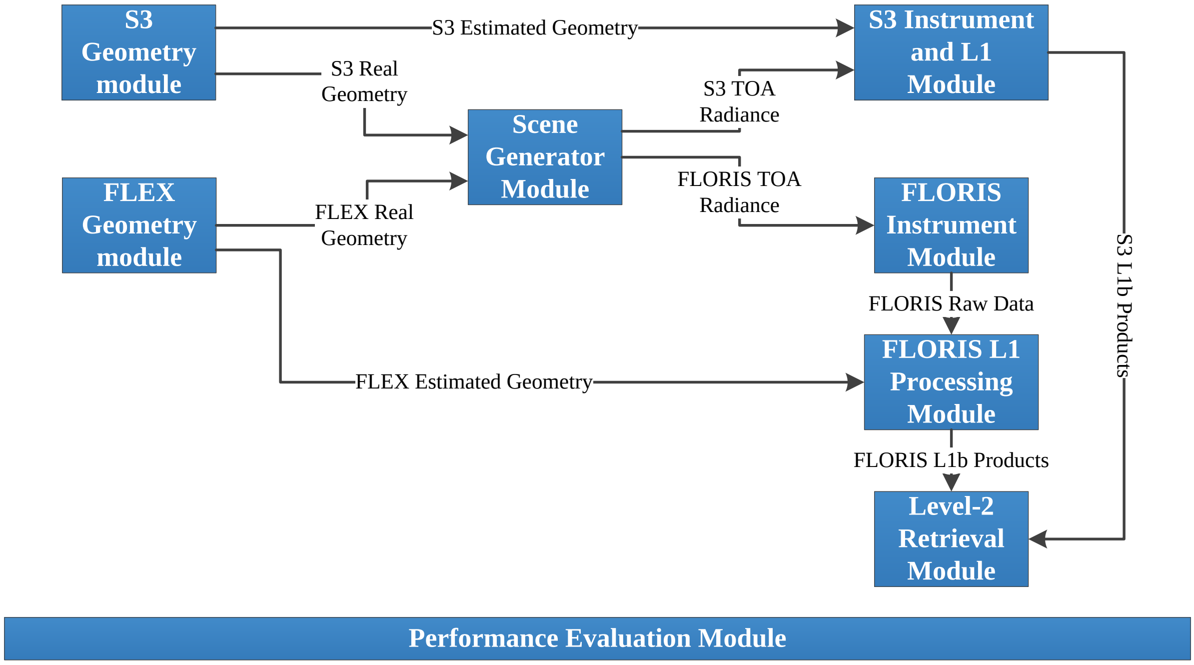

Figure 4.1: FLEX-E high-level modular architecture and data flow. For clarity, the links between all the modules and the PEM have been omitted.

the specific illumination and observation geometry, acquires different radiance from the same target area. The usage of the full 3D geometry along the processing chain guarantees the consistent geometrical treatment when projecting focal plane of each instrument on ground and the explicit accounting for all topographic effects. For this reason, the FLEX and S3 geometry modules are run in first place following the approach in [17]. Accounting for the illumination and observation geometry in the forward modeling of the scene generation offers an advantage with respect to conventional E2ES where the scene is generated prior and independently of the observation and illumination geometry (e.g., [13, 23]).

After the user selection of the geographical coordinates of the ground target area and the acquisition epoch, the geometry modules calculate the real geometry through the orbit segment and line-of-sight (LOS) for each acquisition time and pixel in the satellite focal plane [203]. The tandem configuration is ensured by the use of FLEX and S3 full orbit cycles with a configurable time-delay between them (see Fig. 4.2).

Based on the orbit cycles, each module calculates the orbit segment corresponding to the overpass time of the satellite over the target area closest to nadir observation and for the selected acquisition time through the following sequence:

1. Find the minimum distance between the sub-satellite points along the satellite orbit cycle, and the center of the target scene (user input). This step determines the satellite orbit point closest to the scene acquisition, $\vec{r}_0$, and the acquisition epoch within the 27-days orbit cycle data file, t_0.

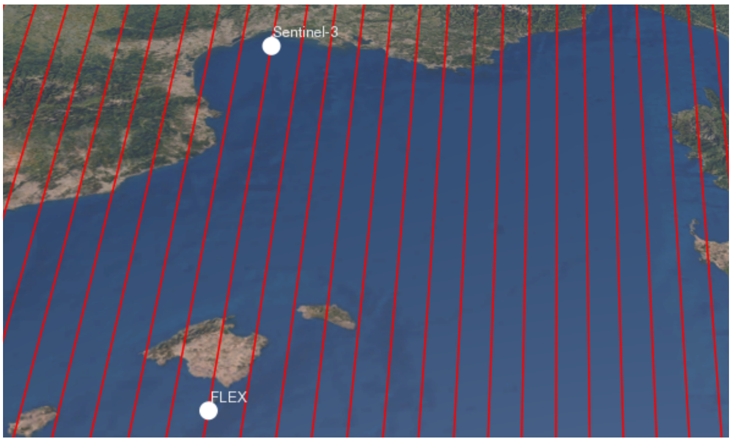

Figure 4.2: Representation of FLEX and S3 orbits based on the used external orbit data files. FLEX flies 6 s ahead of S3 in a descending Sun-synchronous orbit of 27-days repeat cycle.

2. The time-delay, t_{delay}, between acquisitions of the SLSTR nadir and oblique view (viewing zenith angle θ_v=55°), thus determining S3 orbit point for the acquisition of the SLSTR oblique image, is given by the velocity of sub-satellite point, v_{ground}, on ground at at the geodetic altitude of S3 at the selected epoch, h, given the following equation:

$$t_{delay} = \frac{\tan\theta_v \cdot h}{v_{ground}} \tag{4.1}$$

3. Given that the reference orbit (initial epoch of the reference orbit, t_i, is repeated every 27 days, it is possible to find the epoch t_x closer to the user-input epoch t_{input} as it follows:

$$t_x = t_0 + n \cdot rem(\frac{t_x - t_i}{27}) \tag{4.2}$$

   where rem is the remainder of the division and the integer number n is set so that t_x is the closest to t_{input}.

4. The final step determines the time interval of the satellite orbit segment, given by the length of the target scene in the ALT direction.

The LOS is calculated for each instrument at each acquisition time taking into account the instrument scanning motion as well as the instrument mounting, platform attitude and all the geometrical distortions and colocation issues. The LOS is divided into the multiple cameras of FLORIS instrument (-HR and -LR for the high and low spectral resolution respectively) and SLSTR (S1-S3, S4-S6 and S7-S9 for the VIS, SWIR and TIR spectral channels). Regarding OLCI, only the near-nadir pointing camera (#4) is simulated as is the only coincident with the FLORIS swath. Finally, the dual view of SLSTR is defined by its own LOS, orbit segment and acquisition times. A brief description of the main geometry outputs is given in Tab. 4.1. Notice that while all the ACT pixels are acquired at the same time in FLORIS and OLCI pushbroom spectrometers, SLSTR acquisition times is different for each acquired pixel given that it is a whiskbroom scanner.

Table 4.1: Main geometry modules' outputs and dimensions. N_{cam}, N_l and N_c refers respectively to the number of cameras (2 for FLORIS; 3 for SLSTR), number of acquisition lines and number of ACT pixels. F=FLORIS; O=OLCI; S=SLSTR. *Applies both to nadir and oblique views with different number of acquired pixels.

Variable	**Dimensions**		
	FLORIS	OLCI	SLSTR*
LOS	$N^F_{cam} \times N^F_l \times N^F_c \times 3$	$N^O_l \times N^O_c \times 3$	$N^S_{cam} \times N^S_l \times N^S_c \times 3$
Acquisition times	$N^F_{cam} \times N^F_l$	N^O_l	$N^S_{cam} \times N^S_l \times N^S_c$
Orbit state vector	$N^F_{cam} \times N^F_l \times 3$	$N^O_l \times 3$	$N^S_{cam} \times N^S_l \times N^S_c \times 3$

Both geometry modules also calculate the estimated geometry, including the platform orbit/attitude and instrument mounting errors, necessary for the simulation of the L1b geolocation.

4.1.2 Scene generator module (SGM)

The Scene Generator Module [204] propagates solar radiation through the canopy and atmosphere, simulating on a pixel-by-pixel basis the target scenes for FLEX and S3 sensors. The scenes are defined according to key biophysical, atmospheric and topographic input parameters, and consist of high spectral resolution Top-Of-Atmosphere (TOA) radiance spectra $L_{scn}(\lambda_{scn})$ distributed over a high spatial resolution grid. Their resolution is at least an order of magnitude finer than the instrument resolution in order to simulate the instrument acquisition through its spatial/spectral response functions. A common scene grid is set for the FLEX and S3 instruments, which enables the SGM to generate intrinsically different but consistent scenes for each sensor. This is possible by considering the specific instrument observation geometry and spectral configuration, while keeping the same definition of the canopy, atmosphere and topographic properties. The SGM is sub-divided in three blocks:

- The *scene definition* block distributes key biophysical (LAI, Chlorophyll content) and atmospheric (aerosol type/content, water vapor content) input parameters over the scene grid (see sample maps in Fig. 4.3). This is achieved based on global or user-defined LCC maps [137], atmospheric data [140], and surface topography [205]. Each LCC is associated with a database that defines the surface reflectance or alternatively the range and statistical/spatial distribution of the key biophysical parameters[2] as input to a radiative transfer model (RTM).
- Implemented within the SGM instead of the Geometry modules (see Fig. 3.18), the *geometry-scene interaction* block determines the viewing and illumination conditions over each scene grid point considering the surface topography, platform orbit position and sensor LOS at each acquisition time [206]. In order to properly convolve the reference high resolution scene with an accurate instrument response function that accounts

---

[2] See Annex B.2 for further information.

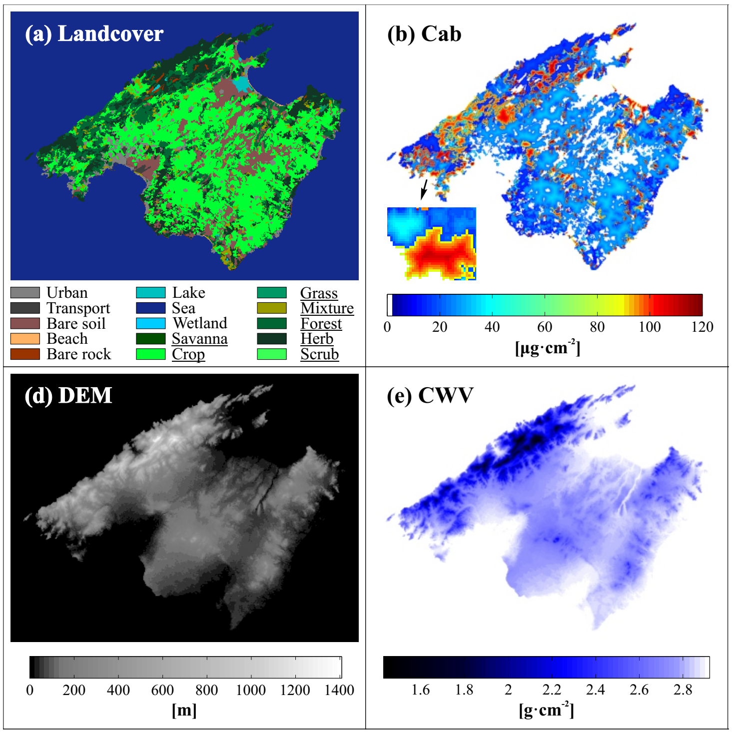

Figure 4.3: Sample maps of generated data in the *scene definition* block. From top-left to bottom-right: LCC, chlorophyll concentration, DEM and columnar water vapor.

for technical aspects in the optics and detectors, the Instrument Module requires the focal plane coordinates corresponding to each surface grid point. This is achieved by the *geometry-scene interaction* block, firstly projecting the sensor pixel center onto the 3D surface (using DEM), and secondly resampling these pixel coordinates for each scene grid point.

- The *forward model* block must simulate TOA radiance spectra, including SIF, at very high spectral resolution. Accordingly, the SGM relies on two RTMs. At the canopy scale, the SCOPE model [207] is implemented in the SGM due to its capability to simulate surface bi-directional reflectance and SIF. These simulations are then coupled with the atmospheric MODTRAN5 model [16], which is used for the simulation of atmospheric effects to properly account for narrow atmospheric absorption bands. These models use biophysical and atmospheric input parameters, together with the observation/illumination geometry and surface topography to propagate the light through the canopy and atmosphere. Thus, the *forward model* block generates, according to [208][3], the surface reflectance, SIF and TOA radiance spectra that are also used as reference for the evaluation of the L1b and L2 products.

  The *forward model* building block is implemented according to the generic architecture in Fig. 3.20 and Fig. 3.22. Firstly, the *Atmosphere downward (↓)* block implements an atmospheric MODTRAN5 LUT [136] interpolation generating, at each scene grid point,

---

[3] See Annex B.3 for further details.

the at-surface direct and diffuse solar irradiance according to the distributed key atmospheric parameters, DEM and illumination conditions. Then, the *Surface model* block runs SCOPE (for vegetation targets), or reads a surface reflectance database (for non-fluorescent targets), determining the reflectance and fluorescence over each scene grid point according to the input key bio-geophysical parameters, illumination and observation conditions. Finally, the *Atmosphere upward (↑)* block interpolates an atmospheric MODTRAN5 LUT to provide the atmospheric transfer functions (i.e., path radiance, transmittance, spherical albedo) and propagating the surface data (reflectance and fluorescence) to generate the high-resolution TOA radiance scenes.

The use of land cover class maps and atmospheric data in combination with the running of RTMs offers important advantages as opposed to the use of external reflectance maps or airborne images [8, 21]. Firstly, the RTM-generated scenes are noise-free while the use of external images introduce their instrumental characteristics (e.g., noise, calibration). Secondly, the RTM-generated scenes are unconstrained by the observation/illumination geometry of the external images. Finally, the scene definition according to key biophysical and atmospheric parameters allows to evaluate the quality of the L2 retrieval algorithms in a wider range of cases. Moreover, the spectral and/or spatial resolution of currently available airborne/spaceborne imaging spectrometers is insufficient for the simulation of the very high spectral resolution scenes required for FLEX [209].

In order to evaluate the accuracy of the L1b and L2 products, the SGM (instead of the PEM module) implements the *Data resampling* building block, resampling the high-resolution data to the instrument resolution for a pixel-to-pixel comparison against the instrument output. This resampling is achieved by the convolution of the high-resolution data with the instrument spatial and spectral response functions based on the input instrument line-of-sight and spectral configuration.

4.1.3 Instrument and Level-1 processing modules

Two parallel chains of Instrument and L1P modules are executed to simulate the scene signal acquisition by FLEX and S3. Regarding FLEX, the simulation of FLORIS instrument and its L1b processing is carried out in two independent modules following the generic architecture[4] described in Chapter 3 (see Fig. 3.23 and Fig. 3.26), i.e., **(1)** the FLORIS instrument module; and **(2)** the FLORIS L1P module. These two modules implement a detailed representation of the actual instrument design and data processing [51]. The FLORIS instrument module simulates the FLORIS spatial-spectral behavior by resampling the high resolution scene to the lower instrument resolution for each spectral band λ_{sen} and instrument focal plane pixel coordinates (l, c) according to the following two steps:

---

[4] The *Geo-rectification* building blocks were not included as the L2R module only uses L1b data for the synergic data processing.

1. The first step aims to spatially resample, at each high resolution spectral channel, the input high spatial resolution scene provided by the SGM. This is achieved by projecting, for each FLORIS pixel, the instrument PSF, F_{psf}, over the scene grid and perform the convolution with the input high resolution scene according to Eq. (4.3). This produces an intermediate high spectral resolution image, L'_{sen} at FLORIS spatial resolution and sampling grid.

$$L'_{sen}(l,c;\lambda_{scn}) = \iiint F_{psf}(l,c;\lambda_{scn}) \cdot L_{scn}(x,y;\lambda_{scn}) \cdot dxdy \tag{4.3}$$

2. The second step performs the spectral resampling of the intermediate high spectral resolution image, L$'_{sen}$, by its convolution with FLORIS ISRF, F_{isrf}, according to Eq. (4.4). This step generates a noise-free equivalent L1b radiance data, L^0_{sen}, used to analyze of the radiometric noises and calibrations errors.

$$L^0_{sen}(l,c;\lambda_{sen}) = \iiint F_{isrf}(\lambda_{sen};\lambda_{scn}) \cdot L'_{sen} \cdot d\lambda_{scn} \tag{4.4}$$

FLORIS PSF and ISRF are modeled through the effects of telescope diffraction, optical aberration, slit width in the along-track direction, smearing length, pixel size at detector level in the across-track direction (including binning), pixel spectral extent, along-track line spread function and uniformity of the detectors. In addition, the spatial and spectral stability effects such as keystone and spectral smile are included in order to model the acquisition for each line and column.

L^0_{sen} is then modified by the stray-light (L_s) contribution according to Eq. (4.5):

$$L_{sen} = L^0_{sen} + L_s(L^0_{sen};c,l,\lambda_{sen}) \tag{4.5}$$

L_s is obtained by applying a spatial-spectral kernel on L^0_{sen} at each acquisition line. This kernel includes effects of optical surfaces roughness/contamination, focal plane filter, grating dispersion and focal length of telescope. The resampled signal L_{sen} is then passed to the FLORIS acquisition chain, simulating all the sensor electronics and on-board processing. This produces at-sensor raw data in digital counts with the following features:

- Spectral/spatial radiometric random and systematic noises (i.e., vertical stripping pattern), dark current, temporal noise, photonic noise, read-out and smearing.
- Spatial and temporal co-registration between each FLORIS spectrometer and within each spectrometer.
- Detector and video-chain noises, including the Analog-to-Digital conversion with effects of relative gains, non-linearity in the detector and data quantization.

The FLORIS L1P module recovers the radiance level from the raw data by applying the dark signal and absolute/relative estimated calibration coefficients, thus including propagation of radiometric calibration errors. Spectral calibration errors are included through spectral shift and bandwidth stretch in the real central wavelengths λ_{sen}. The L1P module also corrects the non-uniformities in the detector caused by defective pixels or anomalies in the sensor [162]. The geolocation assigns the latitude/longitude coordinates to each pixel from the estimated platform orbit/attitude and the FLORIS mounting within the platform.

Regarding S3, an equivalent chain generating OLCI and SLSTR L1b data has been developed within the S3 Instrument and Level-1 Module (see Fig. 4.4). Given that S3 is an external mission, no performance tests on S3 instruments are carried out in FLEX-E. Therefore, the simulation of the instrument noises and their correction at L1 is simplified by considering a random noise realization based on the nominal SNR [55]. The custom-made S3 module includes all the relevant instrumental and platform characteristics [55] and allows to develop FLEX-E unconstrained by ESA's S3 E2ES yet with a representative simulation of the S3 instruments and their L1b processing.

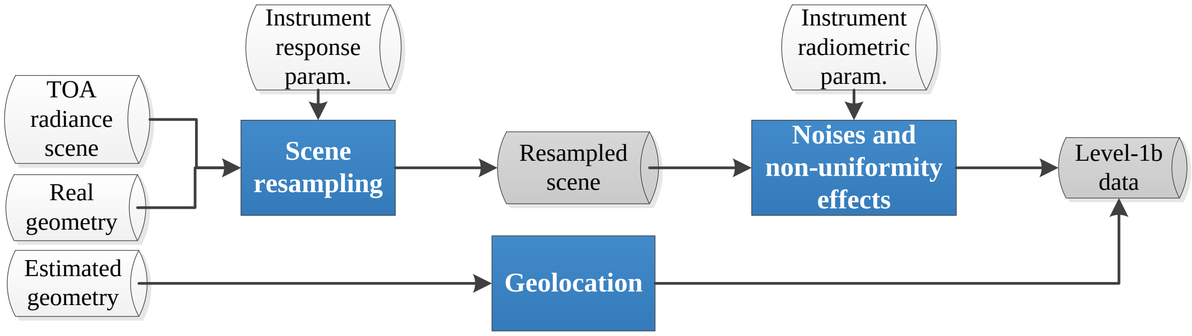

Figure 4.4: Architecture and building blocks of the S3 Instrument and Level-1 Module. The same architecture is applied separately in parallel for OLCI and SLSTR.

4.1.4 Level-2 Retrieval (L2R) module

The L2R module was designed in a way that it accounted for all atmospheric and surface effects included in the forward scene simulation and the realism of the instrument and L1 processing modeling. The implemented L2 R module aims to reproduce the ground processing with such a level of detail so that it can be re-used with real FLEX and S3 data and serves as basis for its future operational ground segment implementation. The synergy between FLORIS, OLCI and SLSTR L1b products is achieved by running the following sequence of image processing algorithms:

1. The FLEX and S3 L1b products are *geometrically co-registered* into a common spatial

grid in order to exploit their data in synergy. The co-registration uses the L1b geolocation coordinates without ground control points and makes a bidimensional cubic spline interpolation of OLCI, SLSTR and FLORIS-LR into the FLORIS-HR grid.

2. The *spectral re-calibration* of the FLORIS-HR L1b data reduces the residual errors from the on-board calibration. The implemented spectral re-calibration is a refined version of the O_2 absorption features matching algorithm in [174]. It approximates the instrument response by a double error function for which the central wavelength, bandwidth and shape parameters are tuned [210].

3. The *radiometric cross-calibration* of the co-registered FLORIS and OLCI L1b data enables having consistent radiance measurements and corrects for the residual radiometric calibration errors in FLORIS data. The cross-calibration simulates synthetic OLCI bands within the 500–800 nm range, excluding atmospheric absorptions features, by convolution of FLORIS spectrum with the OLCI spectral response function. The ratio between the synthetic and real OLCI bands is linearly interpolated to the full FLORIS spectral range.

4. The *atmospheric correction* scheme retrieves the aerosol properties (optical thickness, Angstrom exponent, Henyey-Greenstein parameter) and water vapor based on a MODTRAN5 LUT inversion method using the co-registered S3 L1b data (see [51, 211, 212] for more details). The atmospherically corrected data (i.e., surface apparent reflectance and at-surface solar irradiance) is obtained by inversion of the MODTRAN5 radiative transfer modeling based on the characterized atmospheric parameters. The atmospheric correction scheme includes a cloud-screening algorithm and obtains the surface temperature using the SLSTR thermal channels.

5. The FLORIS spectral range and resolution are suitable for the application of Spectral Fitting Methods (SFM) for *SIF retrieval*. SFM proved to be robust under noisy instrument data [45]. From FLORIS atmospherically corrected data, SFM decouple the surface reflectance and SIF within the O_2 absorption bands and reconstructs the full SIF emission spectrum (Fig. 4.5). An advanced SFM has been implemented and optimized for the FLORIS configuration [53]. Additionally, FLORIS and S3 data are used in synergy to retrieve additional key biophysical parameters (e.g., LAI, Chlorophyll content) [127].

4.1.5 Performance evaluation module (PEM)

The PEM module was implemented in FLEX-E as a plotting and reporting tool that evaluates the mission performance through the comparison of the L1b and L2 products against their reference data from the Geometry, SGM and instrument modules. This module is executed at the end of the simulation chain, and it is fully independent from the modules described in the previous Sections. The PEM aims to:

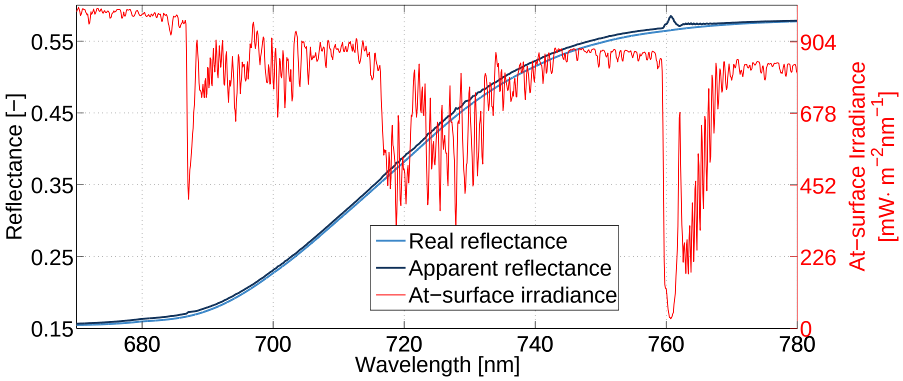

Figure 4.5: O_2 absorption bands allow decoupling the SIF emission from the real reflectance (**light blue**) based on the peaks in the apparent reflectance (dark blue).

- Verify that the SIF and key biophysical parameters are correctly retrieved, including retrieved atmospheric parameters and inverted surface reflectance.
- Analyze the performance of the geolocation algorithms and errors in the estimated observation geometry.
- Study the recovery of pixel uniformity and radiometric/spectral calibration in the L1b products and assess their impact on the L1b and L2 products.

For this purpose, the PEM includes these capabilities:

- Computation of band-per-band relative and absolute error maps and spectrum pixel wise error metrics (spectral angle mapper).
- Monte-Carlo statistical analysis for each dataset (R^2, RMSE, percentiles of the error distribution).
- Generation of spectral plots and images.

4.1.6 OpenSF: simulator framework

These FLEX-E high-level modules were integrated and streamlined within the openSF simulator framework. As described in [39], “OpenSF is a software framework to support a standardised end-to-end simulation capabilities. Scientific models and product exploitation tools can be plugged in the system platform with ease using a well-defined integration process”. Therefore, openSF framework allows users, through its graphical user interface, to integrate each high-level module of FLEX-E and interact with respect the definition of the simulation chain (see Fig. 4.6). The user can also access the contents of the simulator configuration files through openSF environment, allowing their edition and permitting the consistency checking of parameters (see Fig. 4.7).

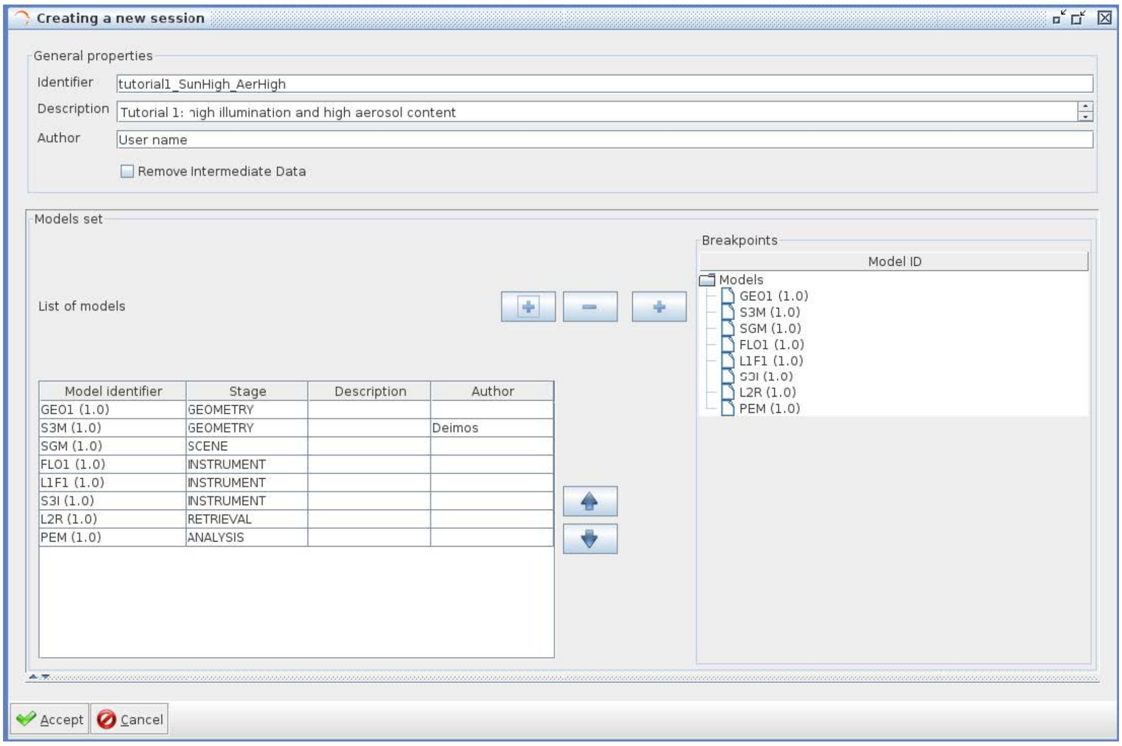

Identifier: tutorial1_SunHigh_AerHigh

Description: Tutorial 1: high illumination and high aerosol content

Author: User name

☐ Remove Intermediate Data

Model identifier	Stage	Description	Author
GEO1 (1.0)	GEOMETRY		
S3M (1.0)	GEOMETRY		Deimos
SGM (1.0)	SCENE		
FLO1 (1.0)	INSTRUMENT		
L1F1 (1.0)	INSTRUMENT		
S3I (1.0)	INSTRUMENT		
L2R (1.0)	RETRIEVAL		
PEM (1.0)	ANALYSIS		

Model ID
- Models
  - GEO1 (1.0)
  - S3M (1.0)
  - SGM (1.0)
  - FLO1 (1.0)
  - L1F1 (1.0)
  - S3I (1.0)
  - L2R (1.0)
  - PEM (1.0)

Figure 4.6: OpenSF graphical user interface for the creation of a new simulation chain. The user can select the high-level modules to be included in the simulation chain and their order of execution.

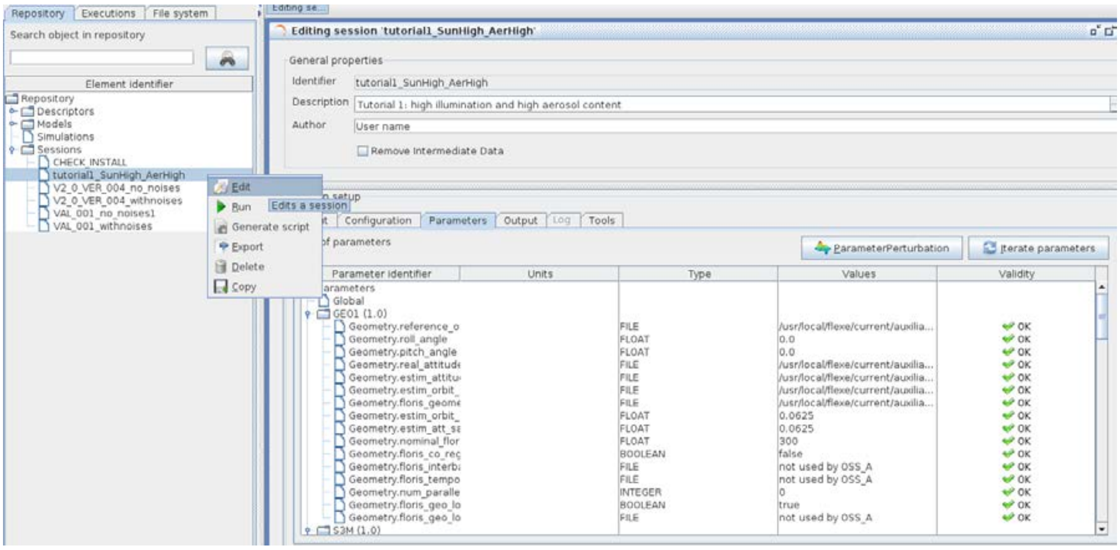

- Repository
  - Descriptors
  - Models
  - Simulations
  - Sessions
    - CHECK_INSTALL
    - tutorial1_SunHigh_AerHigh
    - V2_0_VER_004_no_noises
    - V2_0_VER_004_withnoises
    - VAL_001_no_noises1
    - VAL_001_withnoises

Editing session 'tutorial1_SunHigh_AerHigh'

General properties

Identifier: tutorial1_SunHigh_AerHigh

Description: Tutorial 1: high illumination and high aerosol content

Author: User name

☐ Remove Intermediate Data

Parameter identifier	Units	Type	Values	Validity
arameters				
Global				
GEO1 (1.0)				
Geometry.reference_o		FILE	/usr/local/flexe/current/auxilia...	✓ OK
Geometry.roll_angle		FLOAT	0.0	✓ OK
Geometry.pitch_angle		FLOAT	0.0	✓ OK
Geometry.real_attitude		FILE	/usr/local/flexe/current/auxilia...	✓ OK
Geometry.estim_attitu		FILE	/usr/local/flexe/current/auxilia...	✓ OK
Geometry.estim_orbit_		FILE	/usr/local/flexe/current/auxilia...	✓ OK
Geometry.floris_geome		FILE	/usr/local/flexe/current/auxilia...	✓ OK
Geometry.estim_orbit_		FLOAT	0.0625	✓ OK
Geometry.estim_att_sa		FLOAT	0.0625	✓ OK
Geometry.nominal_flor		FLOAT	300	✓ OK
Geometry.floris_co_reg		BOOLEAN	false	✓ OK
Geometry.floris_interba		FILE	not used by OSS_A	✓ OK
Geometry.floris_tempo		FILE	not used by OSS_A	✓ OK
Geometry.num_paralle		INTEGER	0	✓ OK
Geometry.floris_geo_lo		BOOLEAN	true	✓ OK
Geometry.floris_geo_lo		FILE	not used by OSS_A	✓ OK
S3M (1.0)				

Figure 4.7: OpenSF graphical user interface for the editing of configuration files for a selected simulation chain.

Therefore, starting from the definition of each single module within the OpenSF framework, it is possible to integrate the components by means of their input and output interfaces and then complete the simulation chain. Once all the models are perfectly defined within openSF, the infrastructure is responsible for the correct control of each simulation. Finally, openSF allows running several executions of different simulation chains at once.

4.2 Summary

The selection of FLEX as the future ESA's 8^{th} Earth Explorer mission has been based on a competitive process for which the overall mission performance assessment relied on the results provided by FLEX-End-to-End Mission Performance Simulator (FLEX-E). This E2ES software tool was required to integrate various aspects that affected the FLEX mission performance such as the instrument design, complexity of environmental effects or implementation of the full data processing algorithms. In addition, the design of the FLEX-E software was constrained by a set of guidelines in order to facilitate the comparison between the results produced by the E2ES of the different missions.

In this Chapter, the implementation of FLEX-E based on the generic E2ES architecture described in Chapter 3 was presented. The generic E2ES architecture concept was adapted to reproduce the FLEX/S3 tandem mission through the implementation of specific data processing algorithms, RTMs for the scene generation and instrument modeling. The example of FLEX-E shows that the proposed methodology can serve as baseline for next-generation passive optical satellite mission simulators. The implemented software allows the user to simulate a wide range of possible scenarios, from simple geometric patterns to complex scenes with realistic environmental conditions. The main premise in the design and implementation of FLEX-E was its capability to reproduce the complexity of the FLEX mission, which is mainly driven by the geometric aspects of the tandem flight, the high spectral resolution of the FLORIS instrument, and the global SIF monitoring. In addition, FLEX-E was conceived as a valuable tool to evaluate the performance of the final L2 mission products, which constrained the simulation of the reference scenarios. At the same time, FLEX-E was also designed with the purpose of being re-used for the implementation of the FLEX ground data processing and testing Cal/Val procedures.

The following Chapter 5 will demonstrate, using FLEX-E, the suitability of the proposed FLEX/S3 mission concept and implemented algorithms to retrieve SIF within the given mission requirements.

5

FLEX mission performance assessment

Contents

As introduced in Chapter 4, FLEX-E was designed and implemented as a tool for the evaluation of FLEX mission performance, specifically to determine the accuracy of the retrieved L2 SIF products. This was possible, on the one hand, due to the realism of the simulated environmental effects (e.g., natural variability of the key bio-geophysical parameters, use of state-of-the-art RTMs or consideration of bi-directional reflectance effects) that allowed us to realistically simulate a large variety of simple and complex scenes. On the other hand, FLEX-E implemented a detailed simulation of the instrument behavior and complete payload processing chain from the instrument raw data to the final L2 products. For these reasons, FLEX-E was used to assess the FLEX mission performance in terms of its main mission objective, i.e., "to provide robust estimates of the Sun-induced chlorophyll fluorescence emission at global scale".

This Chapter aims to demonstrate the feasibility of the proposed FLEX/S3 mission concept and implemented algorithms to retrieve SIF within the mission requirements by answering the following two **main research questions**:

- What is the accuracy of the FLEX L1b mission products in terms of spectral, geometric and radiometric performance?
- What is the impact of the current FLEX instrument design and implemented image processing algorithms to retrieve SIF?

These questions will be addressed through the assessment of FLEX-E simulated L1b and L2 data (see Section 5.1 and Section 5.2 respectively) over a set of simulated scenarios, allowing us to evaluate how the mission/instrument concept and the proposed image processing algorithms meet the mission and system requirements with traceability to the MRD [213] and the SRD.

This chapter is partly based on:

- **J. Vicent**, N. Sabater, C. Tenjo, J. R. Acarreta, M. Manzano, J.P. Rivera, P. Jurado, R. Franco, L. Alonso, J. Verrelst, J. Moreno, (2016). FLEX End-to-End Mission Performance Simulator. *IEEE Transactions on Geoscience and Remote Sensing*, Vol. 54, No. 7, pp. 4215-4223
- FLEX End-to-End Mission Performance Simulator, ESA-ESTEC Contract No. 4000108364/13/NL/BJ [2013-2015]
- ESA's 8th Earth Explorer User Consultation Meeting: www.esa.int/spaceinvideos/Sets/Earth_Explorer_8

5.1 Level-1b products performance

The quality assessment of the retrieved SIF needs prior validation of FLEX L1b products against the mission requirements. L1b performance was therefore assessed at three levels being 1) spectral performance; 2) geometric performance; and 3) radiometric performance.

5.1.1 Spectral performance

The realization of the required spectral resolution (SR) and sampling (SSI) for FLORIS-HR and -LR spectrometers was checked with a full-swath simulated L1b dataset. The FLEX-E simulation applied the expected FLORIS ISRF and performed the onboard binning for all spectral channels. The simulated L1b data included central wavelength position and FWHM for each spectral channel after onboard binning. The SSI was calculated through the wavelength difference between consecutive spectral channels. The SSI and SR for both FLORIS spectrometers are shown in Fig. 5.1 where it is seen that the instrument simulation in FLEX-E fulfils the design requirements. The subplots Fig. 5.1 (left) show that FLORIS-HR has an intrinsic SSI of 0.1 nm and SR of 0.3 nm before the spectral channels are binned. After onboard binning, the SSI for FLORIS-HR increases to 0.5 nm with a resolution of $\sim$0.5 nm. As for FLORIS-LR, the onboard binning reduces the sampling to 2 nm from an intrinsic sampling of 0.33 nm keeping the resolution at 2 nm. The spectral sampling and resolution requirements are therefore met by matching the optical performance (e.g., spot size and magnification), grating dispersion and detector pixel size.

The same full-swath simulation was then used to analyze the spectral co-registration, affected by the so called "smile" effect. The wavelength variation in the ACT direction was analyzed for both FLORIS spectrometers at four channels across the spectral range. The results

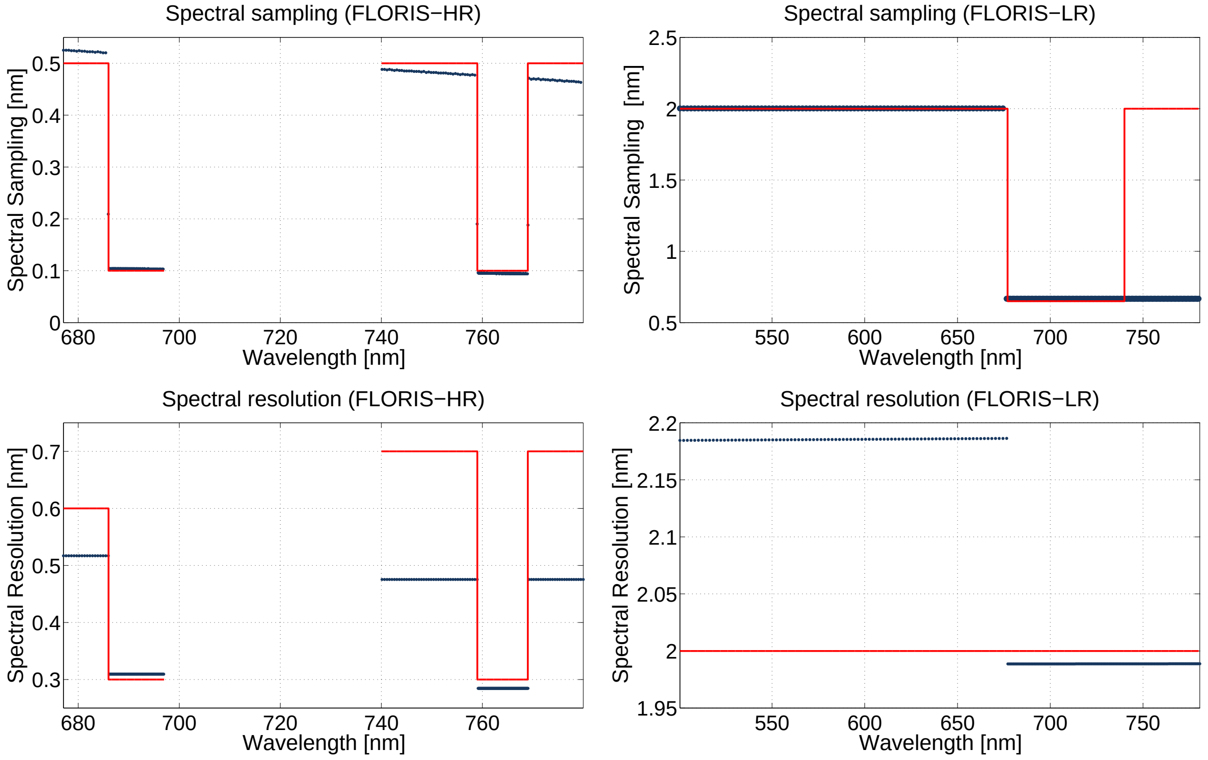

Figure 5.1: SSI (top) and SR (bottom) performance evaluated for FLORIS-HR and -LR spectrometers (left and right, respectively) compared against the requirement (red line).

in Fig. 5.2 show that the spectral co-registration has a smooth parabolic behaviour symmetric with respect the center of the CCD. The spectral co-registration performance (<0.015 nm for FLORIS-HR) is within the scientific requirements (<0.1 SSI) both for binned and non-binned spectral channels.

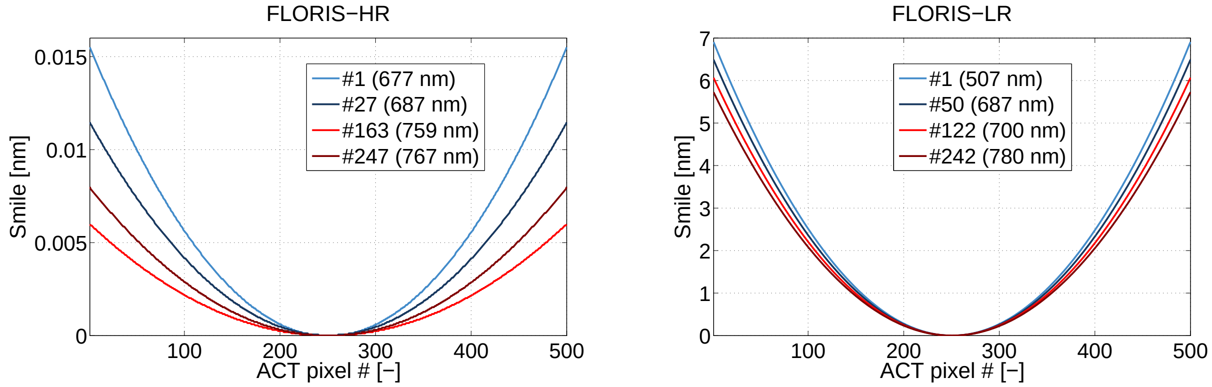

Figure 5.2: Spectral co-registration for FLORIS-HR (left) and -LR (right) spectrometers evaluated at four spectral channels.

The errors introduced by the spectral calibration of the L1b data were also analyzed. The results shown in Fig. 5.3 were obtained from a simulation that included spectral stability effects. The knowledge of the barycenter wavelength at each spectral channel was obtained from the absolute difference between error-free reference and estimated wavelength barycenter at each spectral channel. The absolute difference was calculated for all spectral channels and averaged for all ACT pixels. The results in Fig. 5.3 indicate that the spectral calibration errors are proportional to the spectral channel. The errors are below 0.08 nm and 0.35 nm for FLORIS-HR and -LR spectrometers respectively. Both are within the requirements (0.325 nm and 0.5 nm respectively). In addition, the results indicate that the spectral co-registration is correctly characterized at L1b with errors lower than 10^{-4} nm.

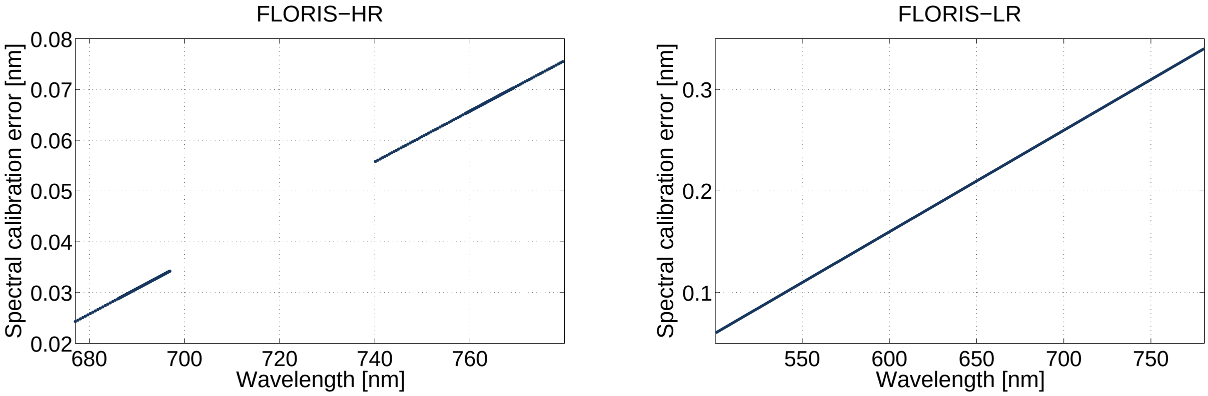

Figure 5.3: L1b spectral calibration errors for FLORIS-HR (left) and -LR (right) spectrometers.

5.1.2 Radiometric performance

FLORIS radiometric performance was studied through the impact of the implemented instruments noises and calibration errors in the FLORIS-HR and -LR L1b radiance data. For this, two main simulation outputs were used in the analysis:

- The reference L1b signal i.e., the high-resolution scene from the SGM spectrally and spatially resampled by FLORIS ISRF and PSF (including smile and keystone effects) without instrument systematic effects nor noises added (L^0_{sen} in Eq. (4.4) in Chapter 4).
- The L1b data, which includes the resampling by the ISRF/PSF, photonic noise and A/D conversion plus user-selected instrument noises and radiometric calibration errors.

A set of six configurations were initially run, each with a different activated instrument noise and calibration error:

- **A/D noise:** Only analog-to-digital conversion was included in the simulation.

- **Spectral radiometric noise:** Only spectral radiometric instrumental errors were included in the simulation. These errors are associated with a spectral relative knowledge error coming from a high frequency part (non-uniformity correction) and a low frequency part across the FLORIS spectral range.

- **Spatial radiometric noise:** Only spatial radiometric instrumental errors were included in the simulation. These errors[1] are associated with a spatial relative knowledge error, leading to an error on the high frequency non-uniformity correction across the swath.

- **Detector and Video-chain noises:** Only the detector and video chain instrumental noises were modelled. This scenario includes the temporal noise, smear noise, detector dark signal and non-uniformity, and detector non-linearity.

- **Radiometric calibration errors:** Only the global absolute radiometric error, affecting to all the FLORIS channel identically, was applied.

- **All instrument noises and calibration errors:** All the above instrument noises and calibrations errors were activated.

A common scene with the same viewing and solar zenith angles (1° and 47° respectively) was simulated to keep the same input radiance to the instrument in each configuration. The scene was configured with four homogeneous stripes of bare soil and vegetation (three different levels of reflectance and SIF), covering a wide range of input radiances to the instrument (see Fig. 5.4).

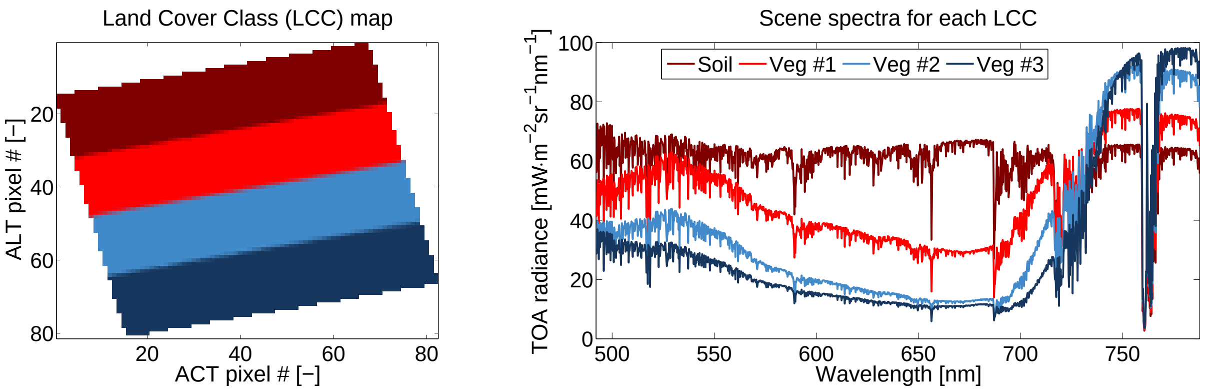

Figure 5.4: LCC map (right) and sample top-of-atmosphere high-resolution radiance (right).

The radiometric performance analysis did not include the *spatial co-registration errors* as they were separately studied (see Section 5.1.3). Also, the *stray-light* effect was separately studied due to the large computation time required to run a full-swath simulation, where the stray-light simulation is physically meaningful.

---

[1] Actually, these noises and their correction have not been modeled within FLORIS Instrument and L1P modules. Instead, the L1P module adds a residual error of their correction.

FLORIS-HR radiometric error budget analysis

The effect of these instrument noises and calibration errors in FLORIS-HR L1b data in spatial and spectral domains is shown in Fig. 5.5 and Fig. 5.6 through the differences between L1b and reference radiances. The contribution of A/D noise (present in all simulations) was subtracted from the other simulations (except from the "*all noises*" configuration) in order to analyze independently the effects of each individual instrumental noise and calibration error. A residual effect from this A/D noise compensation might still be present as the discrete radiometric quantization from the A/D conversion depends on the input radiances.

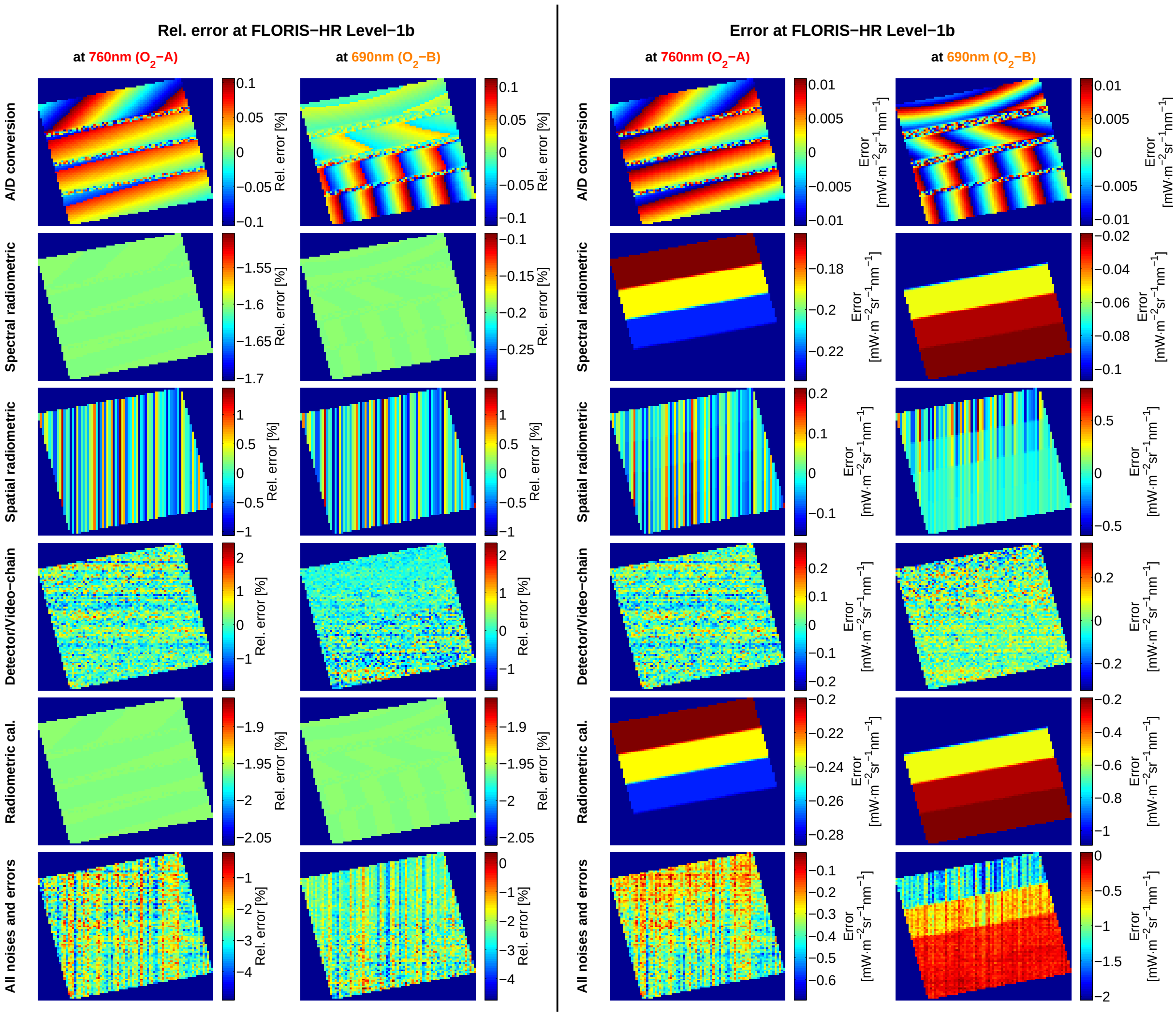

Figure 5.5: Spatial error distribution. Relative (two leftmost) and absolute (two rightmost) differences between the FLORIS-HR L1b data and reference radiance levels after convolution with ideal PSF and ISRF inside the O_2 bands for different instrument noises and calibration errors (top to bottom).

With respect to the spatial distribution of relative errors (see Fig. 5.5), it is observed that:

- Except for the detector/video-chain noises, all instrumental noises and calibration errors affect systematically to the total error at L1b.

- Given the 16 bits of the detector, the A/D conversion causes relative errors up to $\pm 0.1\%$ (0.05% average) and absolute variations in the range of ± 0.01 mW$\cdot$m^{-2}sr^{-1}nm^{-1}.

- The spectral radiometric noise is wavelength dependent (notice the different values in the color bars) but independent of the input radiance level (spatially homogeneous relative error). At the selected spectral channels, this error systematically reduces the measured radiance levels at the L1b data with respect the reference radiance.

- The spatial radiometric noise varies in the ACT pixels but, at first order, it is independent of the selected spectral channels and input radiance level. It produces systematic variations that range nearly from -1% to +1.2% (average absolute value of $\sim$0.5%).

- The contribution of all the detector and video-chain noises varies randomly for every ACT pixel and acquisition line. These errors range from nearly -1.2% to +2.1% with and average absolute value of 1.1% and have a small dependence on the input radiance as seen e.g., on the $\sim$0% error in the two brightest stripes at the O_2-B channel.

- The absolute radiometric calibration error is wavelength independent and does not depend on the input radiance. It systematically reduces the measured L1b radiance by nearly -1.95%.

- When including all noises and errors in the simulation, some systematic errors can compensate one another. The average absolute value of the relative error map is approx. 2.5% (for the O_2-A band) when all errors are included, being lower than the sum of the absolute values from each error/noise contributions. The spatial variability of the errors depends on the detector/video-chain noises and the systematic effect of spatial radiometric noises. The input radiance affects as a second order in the spatial distribution of the relative errors within each spectral band.

Fig. 5.6 offers complementary information by analyzing the effect of each error at each FLORIS-HR spectral channel. The evaluation was done for different ACT pixels (y-axis at first and third rows), in order to analyze the effect at different pixels of the detector, and for different ALT pixels (y-axis at second and fourth rows), in order to analyze the effect of different input radiances.

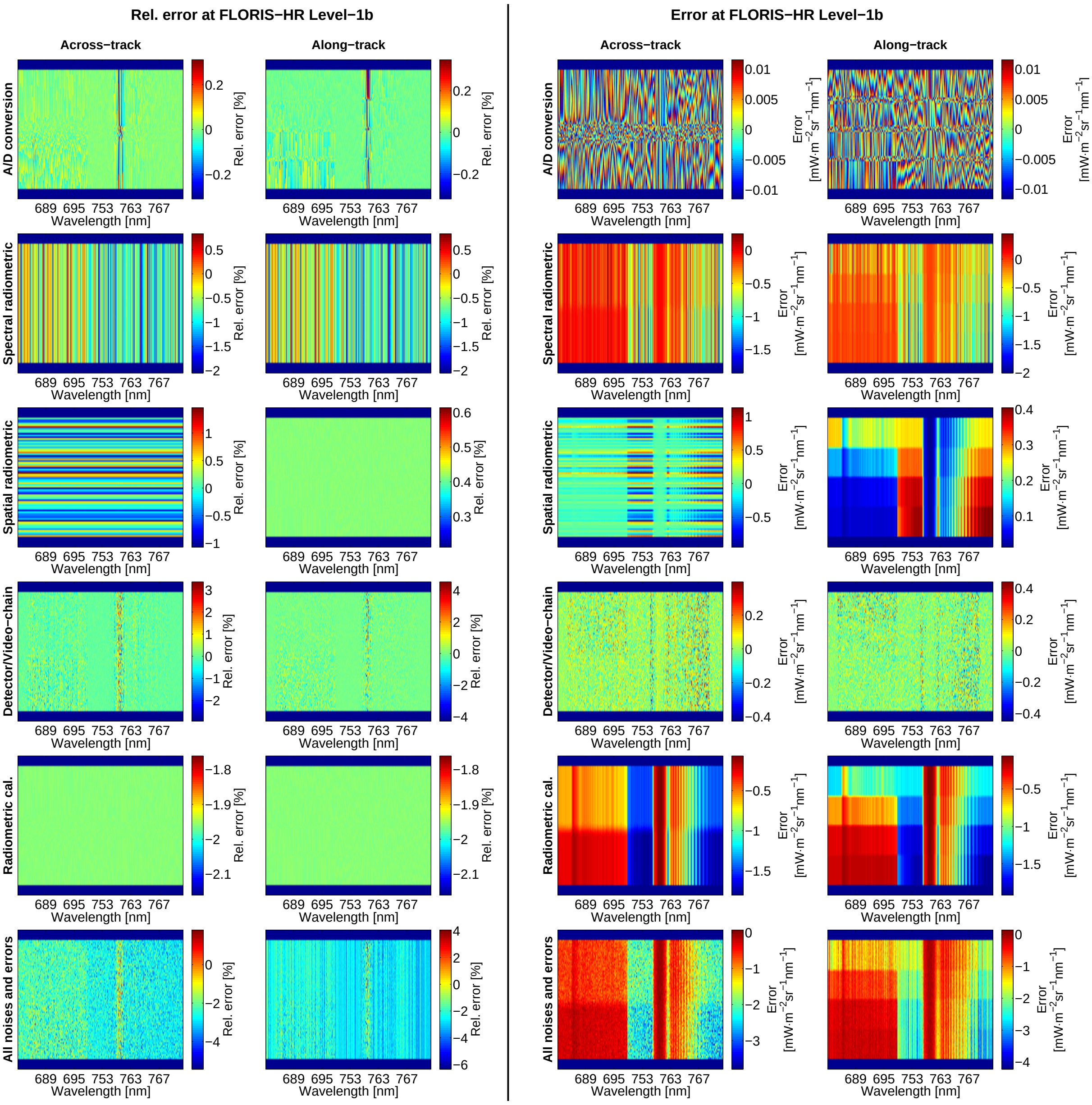

Figure 5.6: Spectral error distribution. Relative (two leftmost) and absolute (two rightmost) differences between the FLORIS-HR L1b data and reference radiance levels after convolution with ideal PSF and ISRF evaluated in the ACT and ALT dimensions for all the spectral channels at different instrument noises and calibration errors (top to bottom).

The following conclusions are derived from the analysis of the relative errors in Fig. 5.6:

- The A/D conversion error affects more the lowest radiance levels within the O_2 absorption bands and lower radiance stripes. The error varies up to ±0.1% in these channels while is nearly 0% for channels outside of absorption bands (e.g., at 780 nm).
- The spectral radiometric noise is wavelength dependent but independent of the ACT pixel

and the input radiance level. The errors range from -2% to nearly +0.6% (average absolute value of 1%) being positive at lower wavelengths (∼0% for wavelengths <720 nm) and negative at higher wavelengths (-1% for wavelengths >720 nm).

- The spatial radiometric noises are systematic with respect to the ACT pixel but independently of the input radiance (i.e., homogeneity on the ALT figure) and wavelength channel (constant value for all spectral channels at a given ACT pixel). The values range from -1% to +1.2% (average absolute value of 0.6%).

- The detector and video-chain noises are wavelength dependent following the SNR requirements i.e., higher error values within the O_2 absorptions. The errors in the O_2 absorptions range a maximum of ±4% (inside the O_2-A) and nearly 0% outside the O_2 bands (e.g., at 780 nm errors are within ±0.1%).

- As also seen in Fig. 5.5, the absolute radiometric calibration is pixel independent (i.e., ACT pixel and wavelength) and also independent of the input radiance with a value of -1.95%.

- The contribution of all errors in the spectral domain is dominated by the absolute calibration error and the spectral radiometric errors, which makes the average absolute relative error to vary between -2% at 680 nm and -3% at 780 nm. Within each spectral channel, the variability of the error in the ACT and ALT spatial domains comes mainly from the detector and video-chain random noises as well as the systematic spatial radiometric noises.

As a complementary information the absolute value of the relative error was derived for each image pixel, taking the mean and standard deviation of the absolute-value relative error map at each LCC for all wavelengths in FLORIS-HR L1b data (see Fig. 5.7). The mean relative error indicates the average magnitude of a given error/noise for different input radiances while the standard deviation is related with its spatial (ACT and ALT) variability. The following conclusions are obtained from Fig. 5.7:

- The A/D conversion, being a quantization effect of the input radiometric levels, results in higher relative errors for lower radiance levels, which is visible in the spectral behavior of this noise (higher in the O_2 bands) and with the dependency on the LCC (higher for the darkest vegetation). The spatial distribution is only dependent on the quantization of the radiometric levels and therefore causes variations on each stripe with a standard deviation <0.06% in the worst case (i.e., inside the O_2-A band).

- The spectral radiometric error is wavelength dependent but independent of the input radiance. This error affects differently at the two O_2 regions with a value of ∼0.5% in the O_2-B spectral region and ∼1% in the O_2-A spectral region. As for its spatial distribution, this error affects equally every ACT and ALT pixel, being the standard deviation affected by the residual of the compensation of the A/D conversion.

- The spatial radiometric errors are, at first order, spectrally independent (nearly constant) with a second order spectral dependency, particularly within the narrow O_2 absorption bands (i.e., a change of $\sim$0.06% between 755 nm and 760 nm). The error shows a small dependency (variations lower than 0.02%) on the input radiance (higher errors for higher radiance levels). The systematic ACT pixel distribution causes variations between pixels with a standard deviation of $\sim$0.33%

- The detector and video-chain noises are dependent on the input radiance level, being higher (in relative values) at lower radiances. This creates a spectral dependency which causes higher errors inside the O_2 bands. Together with the spatial radiometric errors, the detector and video-chain noises cause the largest error variability in the spatial domain, with standard deviations that can reach up to 1% in the O_2-A band.

- As for the radiometric calibration, it is independent of the input radiance. The absolute radiometric error is $\sim$1.95% across the spectral range with a a relative radiometric error contribution that affects mostly inside the O_2 bands, being higher in the O_2-A region with values that range from 1.7% to 2.15%. The error is spatially constant and the standard deviation reflects the residual of the compensation of the A/D conversion.

- Finally, some of the errors above can compensate each other so that the total error varies nearly linearly with wavelength, being lower at lower wavelengths. The total error is, at first order, independently of the input radiance (at the same wavelength). Nevertheless, the spatial distribution is sensitive to the input radiance, particularly in the O_2-B spectral region.

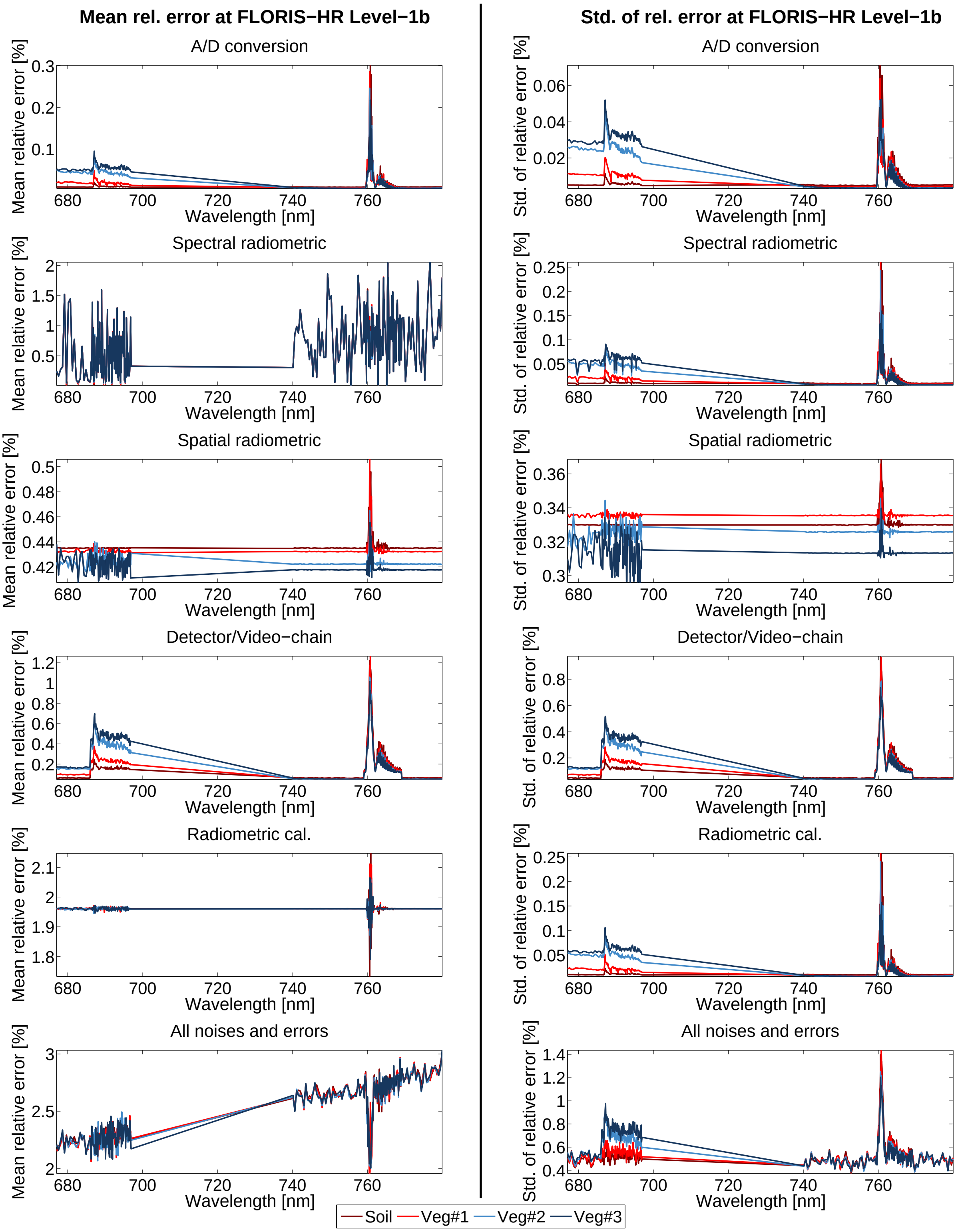

Figure 5.7: Mean relative error (left) and standard deviation (right) for the FLORIS-HR spectrometer at each LCC for different instrument noises and calibration errors (top to bottom).

FLORIS-LR radiometric error budget analysis

Similarly, Fig. 5.8 and Fig. 5.9 analyze the errors for FLORIS-LR L1b data both in the spatial and spectral domains.

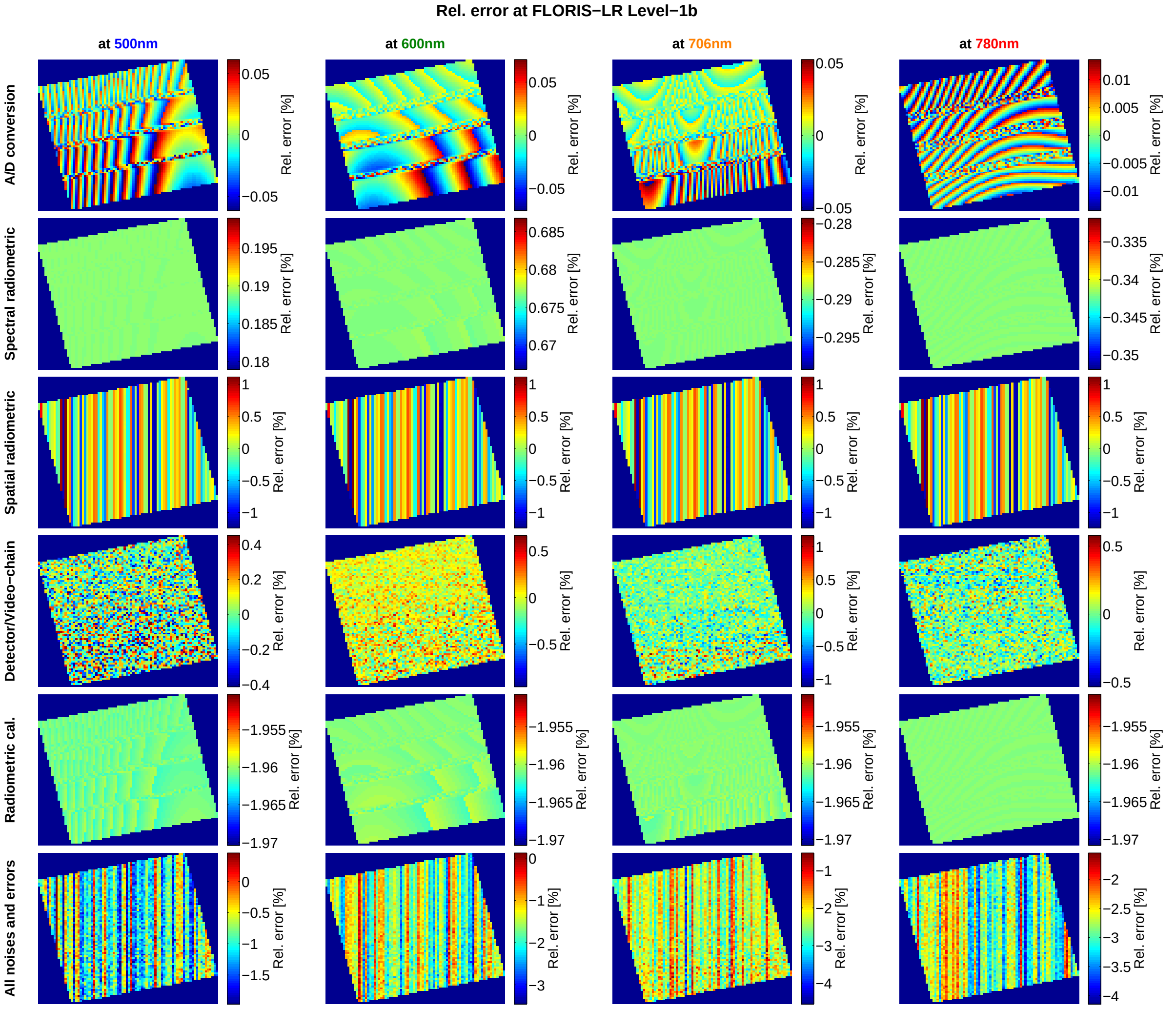

Figure 5.8: Spatial error distribution. Relative differences between the FLORIS-LR L1b data and reference radiance levels after convolution with ideal PSF and- ISRF at 500 nm, 600 nm, 706 nm and 780 nm (left to right) for different instrument noises and calibration errors (top to bottom).

With respect to the spatial distribution of the relative errors it is seen that all instrumental noises and calibration errors, except for the detector/video-chain noises, affect systematically to the total error at L1b. In particular, the quantization of the radiance levels causes by the A/D conversion depends on the input radiance, thus being lower for the higher radiances at 780 nm. As for FLORIS-HR, the spectral and spatial radiometric noises affect systematically in the spectral and spatial (i.e., ACT) dimensions of the focal plane, both being independent of the input radiance level. The variations causes by the spatial radiometric errors are, on average absolute value, of ~0.5%. The ramdonly varying effect of the detector and video-chain noises is shown to be dependent on the input radiance level and hence the wavelength dependency (e.g., 706 nm vs. 780 nm) and the spatial distribution (notice how e.g. the errors for the soil stripe are lower than in the veg#1 stripe at 706 nm). On the contrary, the absolute radiometric calibration error shows to be both wavelength input-radiance independent. In this study case, it contributes to a reduction of -1.95% of the measured L1b radiance. The small spatial variation appearing in the figures comes from the residual of the compensation of the A/D conversion. Finally, when including all noises and errors in the simulation, some different systematic errors can compensate one another. The average value of the relative error map (in absolute value) ranges from 1% at 500 nm to 3% at 780 nm. In addition, the spatial variability of the errors depends mainly on the detector/video-chain noises and the systematic effect of the spatial radiometric noises. The input radiance affects as a second order in the spatial distribution of the errors within each spectral band.

The error behavior of FLORIS-LR L1b data in the spectral domain was calculated for different ACT pixels (the effect at different pixels of the detector) and for different ALT pixels (effect of different input radiances). The following conclusions are obtained from the analysis of the relative errors in Fig. 5.9:

- The A/D conversion error is dependent of the input radiance, affecting more at the lowest radiance levels within the O_2 absorption bands and lower radiance stripes. The quantization error is between $\pm 0.02 \mathrm{mW \cdot m^{-2} sr^{-1} nm^{-1}}$ (±0.2%).
- As for the FLORIS-HR spectrometer, the spectral radiometric noise is wavelength dependent but independent of the ACT pixel and the input radiance level. On top of the variations between consecutive spectral channels, this error has spectral trend that goes from ~2% error at 500 nm to -2% at 780 nm.
- The spatial radiometric noises are systematic with respect to the ACT pixel but independent of the input radiance and wavelength channel. The values range from -1% to +1.2% (average absolute value of 0.6%).
- The wavelength-dependency of the detector and video-chain noises is consistent with the SNR requirements and therefore these noises are higher within the O_2 and lower radiances (e.g., inside of the water vapor absorption). The errors in the atmospheric absorptions regions range from -1.5% to +1% and nearly 0% outside of absorption channels (e.g., at 780 nm errors are within ±0.1%).
- The absolute radiometric calibration is pixel independent (i.e., ACT pixel and wavelength) and also independent of the input radiance with a value of -1.95%.
- The contribution of all errors in the spectral domain is dominated by the absolute calibration error and the spectral radiometric errors, varying the average absolute relative error between approx. -1% at 500 nm to approx. -3% at 780 nm. Within each spectral channel, the ACT and ALT spatial variability of the error comes mainly from the detector and

video-chain random noises as well as the systematic spatial radiometric noises. Variations due to different input radiances (within the same spectral channel) are of second order.

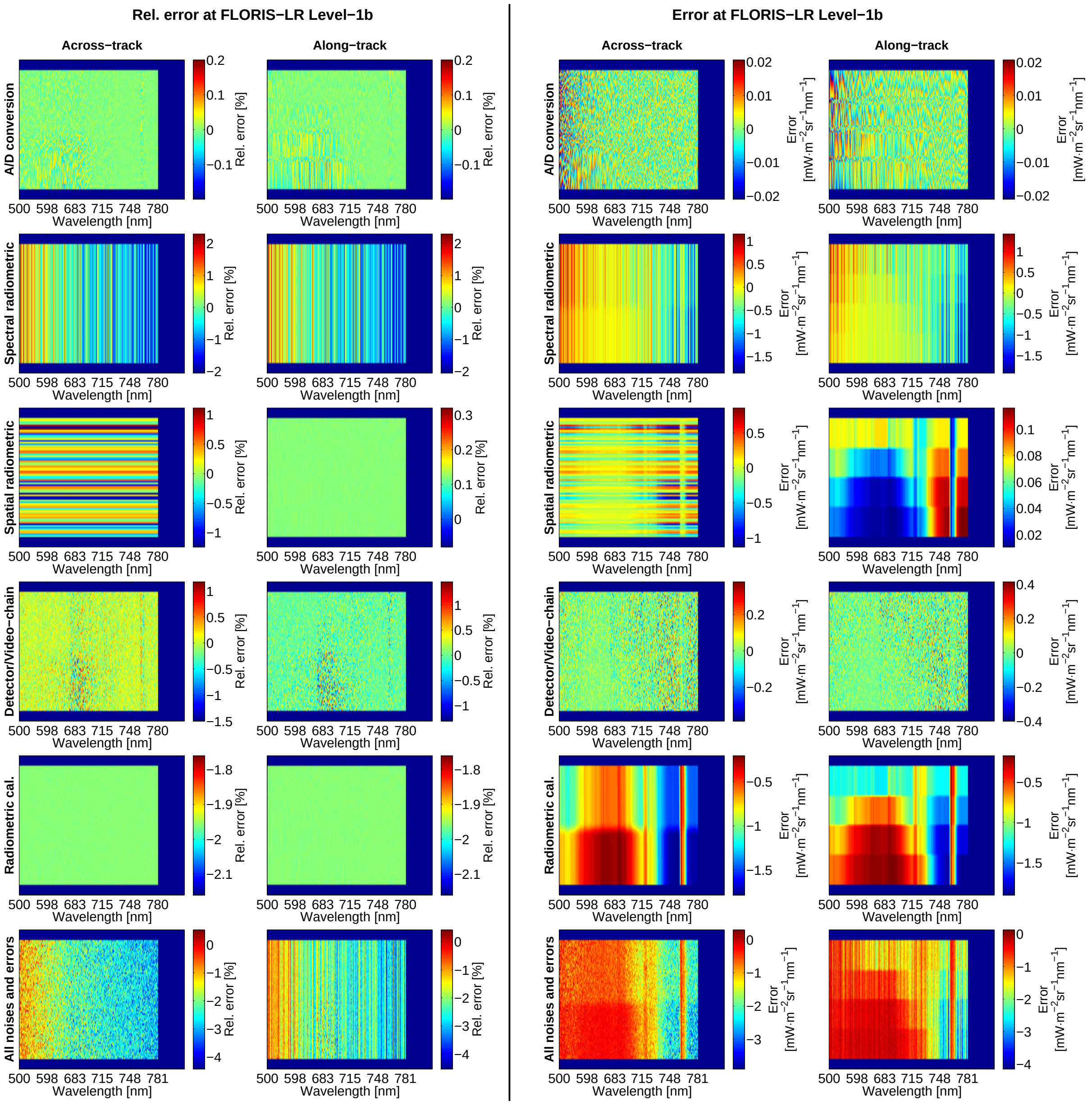

Figure 5.9: Spectral error distribution. Relative (two leftmost) and absolute (two rightmost) differences between the FLORIS-LR L1b data and reference radiance levels after convolution with ideal PSF and ISRF evaluated in the ACT and ALT dimensions for all the spectral channels at different instrument noises and calibration errors (top to bottom).

The mean relative error in absolute value and its standard deviation were calculated, for FLORIS-LR L1b data, in each LCC and wavelength. The results are shown in Fig. 5.10 as a complementary information to Fig. 5.8 and Fig. 5.9. The following conclusions are obtained from Fig. 5.10:

- The A/D conversion, being an effect of quantization of the input radiometric levels, results in higher relative errors for lower radiance levels, which is visible in the spectral behavior of this noise and with the dependency on the land cover class (higher for the darkest vegetation). The spatial distribution is only dependent on the quantization of the radiometric levels and therefore causes variations on each stripe with a standard deviation <0.025% in the worst case.

- The spectral radiometric errors are wavelength dependent but independent of the input radiance. These errors follow a quadratic behavior being $\sim$1% at 500 nm and 780 nm and decrease towards 0.25% at 650 nm with errors as higher as 2%. As for their spatial distribution, these errors affects equally for every ACT and ALT pixel, being the standard deviation affected by the residual of A/D conversion.

- The spatial radiometric errors are, at first order, spectrally constant with a second order spectral dependency causing random variations <0.02% between consecutive wavelengths. These errors shows a small dependency on the input radiance causing variations <0.04%. As for their systematic spatial distribution, they cause variations between pixels with a standard deviation of 0.29-0.33%.

- The detector and video-chain noises are dependent on the input radiance level, being higher for lower radiances. In addition, there is a sudden change between the binned channels (SSI=2 nm) below 676 nm and the non-binned channels (SSI=0.65 nm). The binning reduces the radiometric errors by a factor nearly 2 with respect the non-binned channels. Together with the spatial radiometric errors, the detector and video-chain noises causes the largest spatial variation, with standard deviations that reach up to 0.3%.

- As for the radiometric calibration, it is nearly independent of the input radiance and wavelength, with values that range from 1.94% to 1.99% (mean value of $\sim$1.96%). The error is spatially constant, the standard deviation showing the residual of the compensation of the A/D conversion.

- Finally, all the errors above compensate each other so that the total error varies nearly linearly with the wavelength, being lower at lower wavelengths. The total error is, at first order, independently of the input radiance (at the same wavelength). Nevertheless, the spatial distribution is sensitive to the input radiance, particularly in the O_2-B spectral region and red-edge.

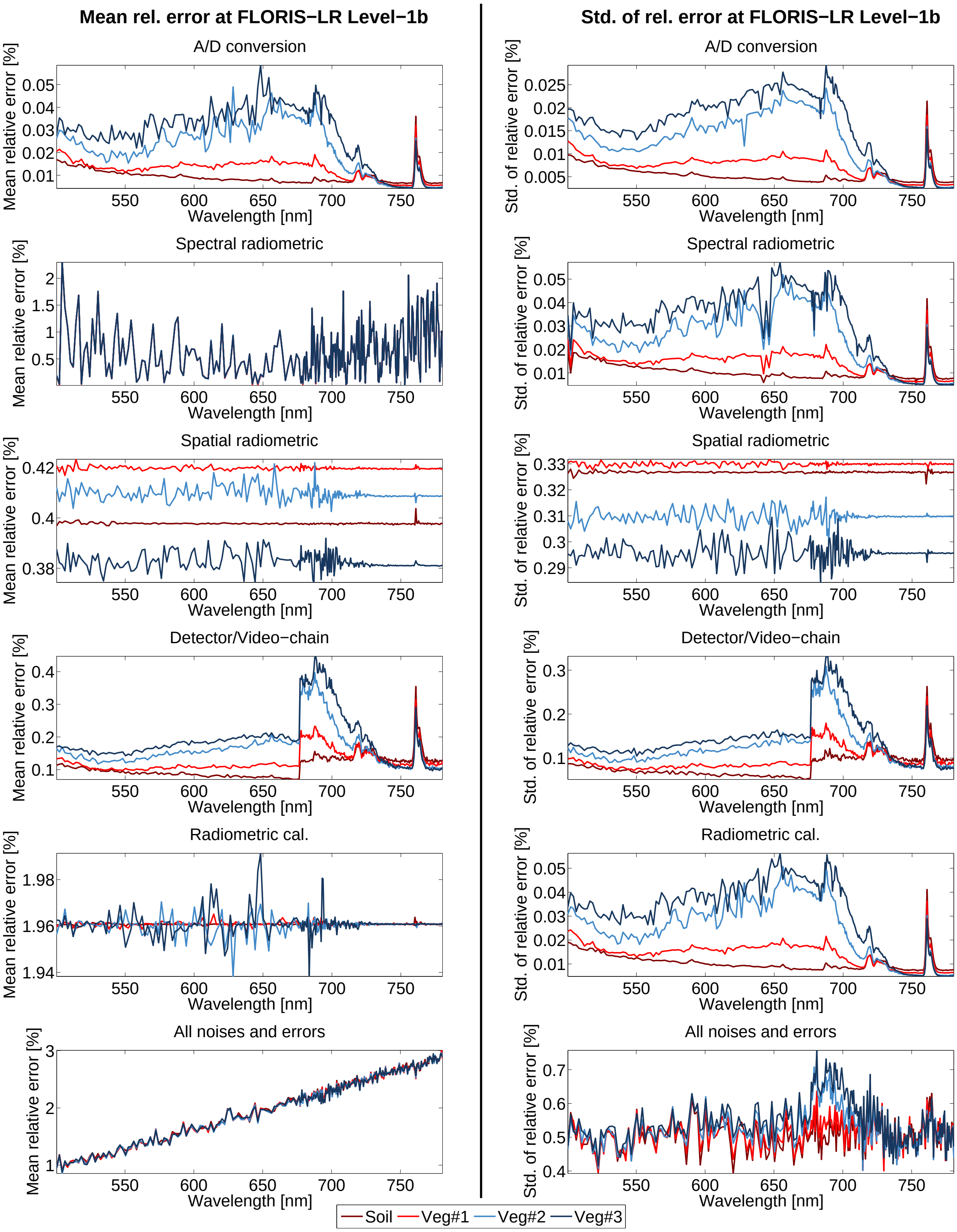

Figure 5.10: Mean relative error (left) and standard deviation (right) for the FLORIS-LR spectrometer at each LCC for different instrument noises and calibration errors (top to bottom).

Fig. 5.5 to Fig. 5.10 have shown the effects of FLORIS instrument noises and calibration errors as implemented in the simulator. These errors are composed by random contributions (modelled by Monte-Carlo methods) and scene-level systematic effects such as smile and non-uniformities on the detector. The implemented instrument noises and errors reproduce the expected error level and spatial pattern for real FLEX images. Indeed, the SNR derived from the L1b data with an input homogeneous scene at the reference radiance (see Fig. 5.11) shows a good matching with the mission requirement.

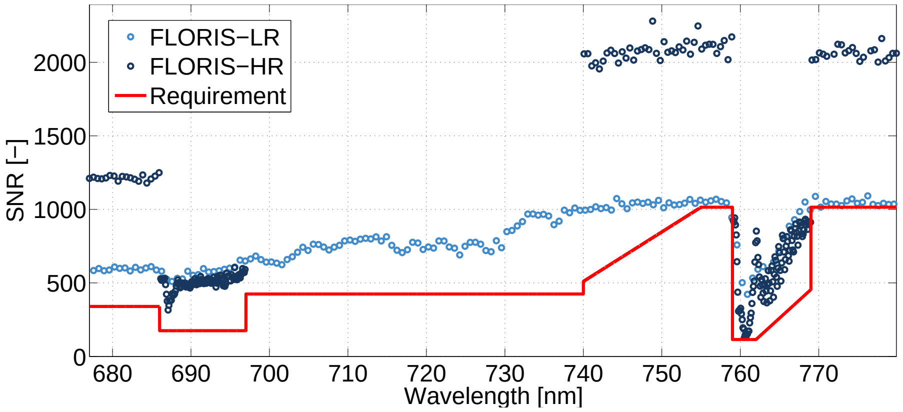

Figure 5.11: SNR for FLORIS-LR (**light blue**) and -HR (dark blue) spectrometers compared with the mission requirements (red line).

FLORIS absolute and relative radiometric calibration analysis

As seen in Fig. 5.5 to Fig. 5.10, the highest systematic effect in the final L1b error budget is caused by the radiometric calibration. In order to further evaluate the accuracy of the absolute radiometric calibration, a simulation test was run over a synthetic scene that ranges from low to high radiance levels as shown in the figure below:

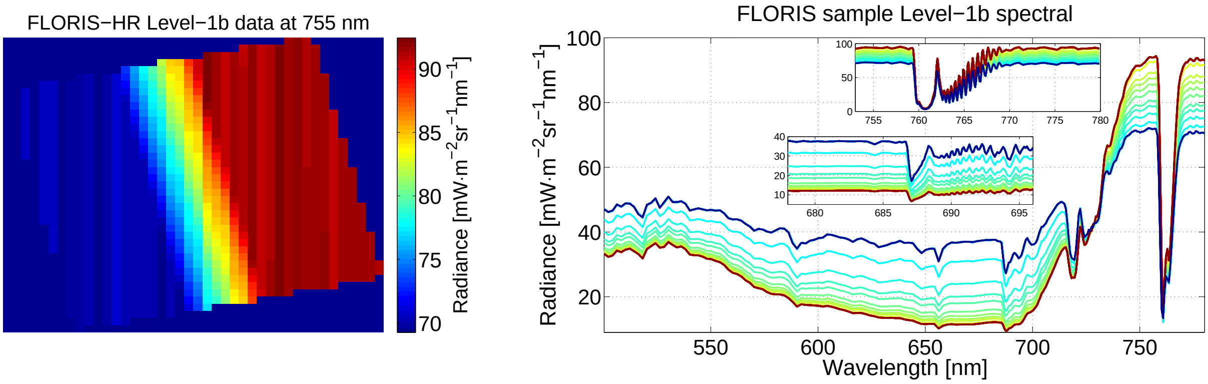

Figure 5.12: FLORIS-HR L1b image at 755 nm (left) and sample spectra (right) for FLORIS-LR spectrometer and FLORIS-HR spectrometer (zoomed plots) at different ACT pixels.

Fig. 5.13 and Fig. 5.14 show the spatial distribution of radiometric errors (evaluated through the absolute/relative difference between the reference signal and the L1b image) for a few selected bands in the FLORIS-HR and -LR spectrometers. The relative error maps shown in these two figures indicate that the effect of the fixed pattern noise (i.e., vertical stripping) is higher than the variations in the absolute radiometric accuracy caused by different radiance levels.

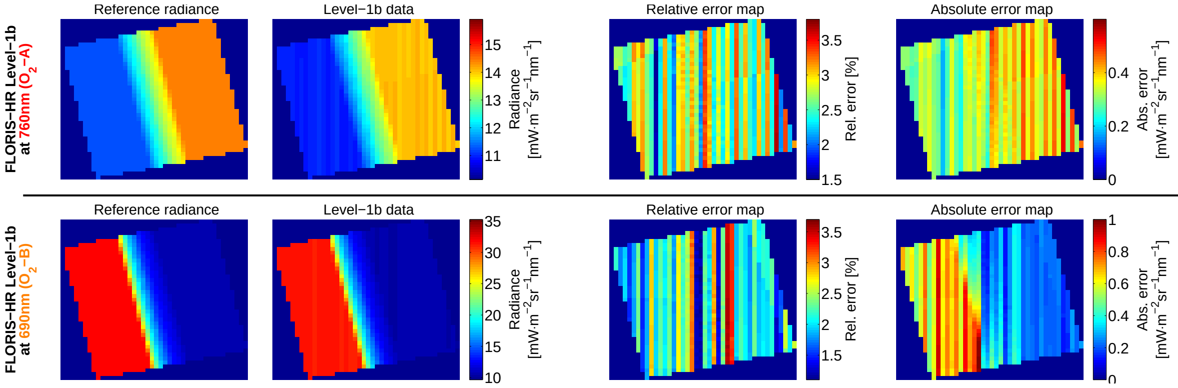

Figure 5.13: FLORIS-HR L1b performance evaluated at 690 nm (top) and 760 nm (bottom). From left to right: reference radiance level after convolution with ideal PSF and ISRF; L1b data affected by instrument noises; relative and absolute error maps between reference and L1b.

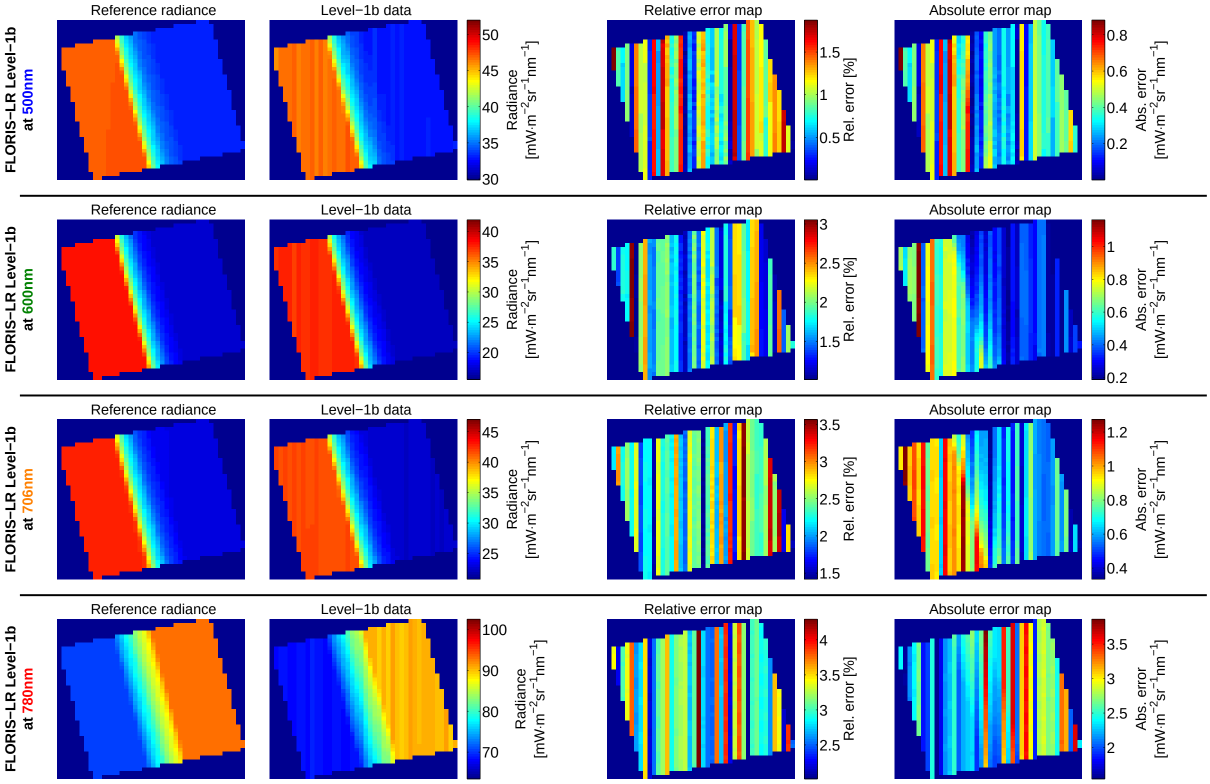

Figure 5.14: FLORIS-LR L1b performance evaluated from top to bottom at 500 nm, 600 nm, 706 nm and 780 nm. From left to right: reference radiance level after convolution with ideal PSF and ISRF; L1b data affected by instrument noises; relative and absolute error maps between reference and L1b.

In order to study the radiance dependency of the absolute radiometric accuracy without the effect of the fixed pattern noise, the average relative error for each ACT was subtracted. The scatterplots between reference radiance and relative error in FLORIS-HR and -LR L1b data are shown in Fig. 5.15 for a few selected channels:

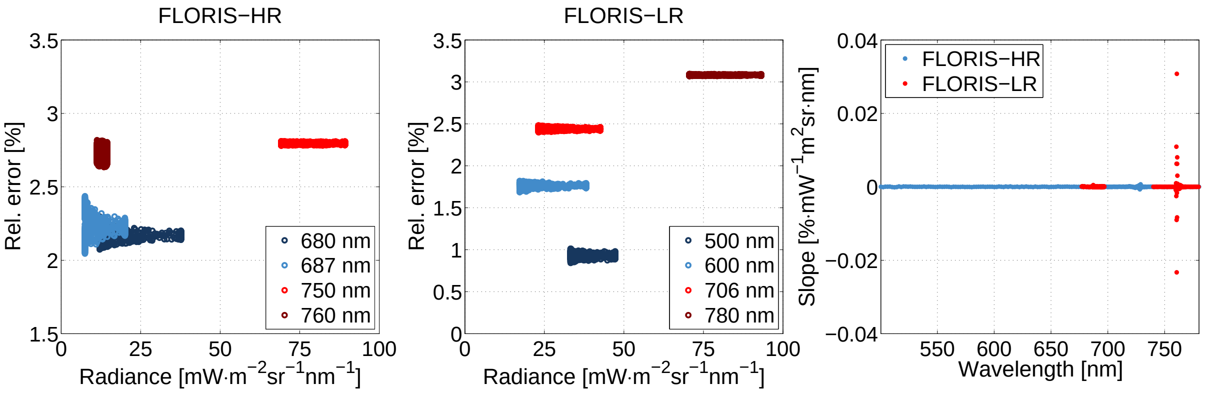

Figure 5.15: Scatterplot for FLORIS-HR (left) and -LR (mid) L1b errors against the input radiance for four selected spectral channels. Right: Slope of the scatterplot relative error against radiance evaluated at every spectral channel in the FLORIS-HR and -LR spectrometers.

The scatterplots (left and mid plots) show how, for lower radiance levels at each spectral channel, the random instrument noise increase the L1b radiance errors. This is particularly important within the O_2 bands (687 nm and 760 nm). Nonetheless, the absolute radiometric calibration does not depend on the input radiance level at the different spectral channels. This is seen by the horizontal scattering of the points (left and mid plots), and by the nearly zero spectrally constant slope (rightmost plot). The exception is found at the bottom of the O_2 absorption bands for the FLORIS-HR spectrometer for which the slope increases up to 0.03 $\%\cdot\text{mW}^{-1}\text{m}^2\text{sr}\cdot\text{nm}$. This effect was also observed in Fig. 5.10.

The variation of the radiometric calibration due to variability of radiance levels in the image is shown in Fig. 5.16. Here, the histogram of image pixels with respect to the L1b radiance relative error was calculated at each spectral channel. The figure shows that the spectral behavior of the calibration error varies almost linearly with an average value from 1% at 500 nm to 3% at 780 nm. These results also indicate that the standard deviation of the radiometric accuracy is nearly constant across the spectral range with a value of 0.57±0.06%.

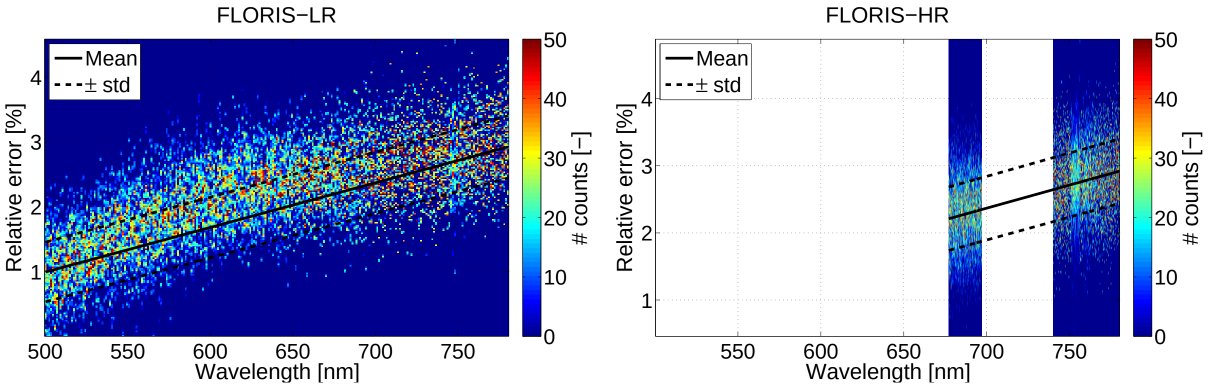

Figure 5.16: Image plot of the histogram of the L1b relative error of FLORIS-LR (left) and -HR (right) at every spectral channel. The solid/dashed black lines represent the mean/standard deviation.

FLORIS stray-light analysis

The effect of instrument stray-light on the output L1b data and the retrieved SIF was studied over a full-swath simulation based on a homogeneous vegetation scene with a bright cloud stripe placed nearly in the middle of the swath (see Fig. 5.17). The scene homogeneity was given in terms of constant input key biophysical and atmospheric parameters (rural aerosols with 0.05 optical thickness (AOT)) defining the scene, but the generated output radiances explicitly take into account variations in illumination and observation conditions for each ACT pixel and acquisition line.

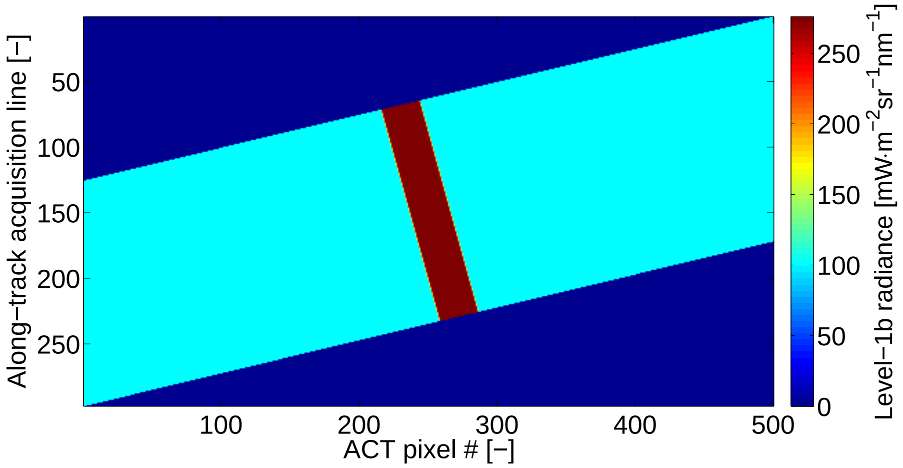

Figure 5.17: Reference FLORIS-HR L1b data at 755 nm spectral channel.

The stray-light map is given by the absolute (and relative) difference between reference and L1b radiance data. Fig. 5.18 shows the stray-light map on FLORIS-HR focal plane for the acquisition line #150. The following conclusions are derived from this figure:

- The effect of the focal plane filter separates, within the HR spectrometer, the regions around the O_2-B (channels #1 to #120) and O_2-A (channels #121 to #290). This focal plane filter is implemented to avoid stray-light contamination between the O_2-A and O_2-B parts of the FLORIS-HR CCD.

- The relative and absolute difference maps show that stray-light is more important in the O_2-A spectral region. In terms of absolute value, it contributes more in those spectral channels outside of the absorption band (e.g., around channels #150 and #260) given the higher radiance at these spectral channels.
- However, the relative difference map clearly indicates that the bottom of the O_2-A band (around 760 nm) is the most affected region by stray-light. In this region, the stray-light contributes $\sim$2% close to the cloud and decreases down to $\sim$1% after nearly 30 pixels.

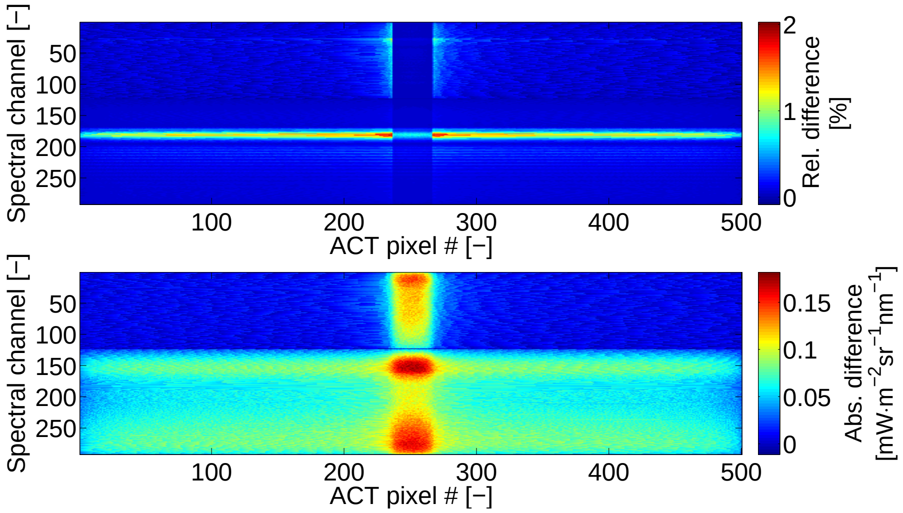

Figure 5.18: Stray-light map (relative-top and absolute-bottom) on the FLORIS-HR focal plane.

The stray-light ACT profile was evaluated at two spectral channels in the O_2 regions (see Fig. 5.19).

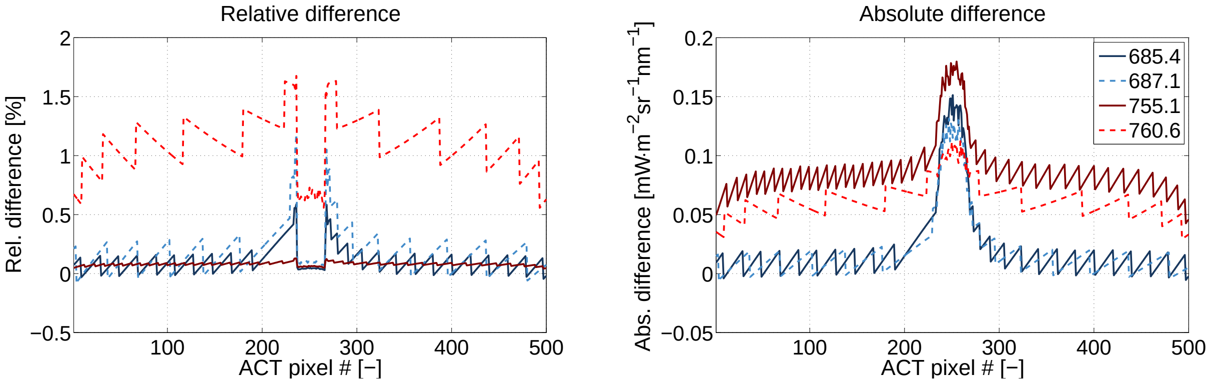

Figure 5.19: ACT variation of stray-light at 685.4 nm and **687.1 nm** (O_2-B) and 755 nm and 760.62 nm (O_2-A) given by the absolute/relative difference between the reference and L1b radiance (right/left).

The stray-light effect is overlapped with the quantization from the A/D conversion (bins of 0.02 mW·m^{-2}sr^{-1}nm^{-1}). Nevertheless, the stray-light contribution in the O_2-B band decreases from 0.075 mW·m^{-2}sr^{-1}nm^{-1} to 0.016 mW·m^{-2}sr^{-1}nm^{-1} for a distance of 30 ACT pixels from the cloud. Given the signal level inside and outside of the O_2-B absorption band, the relative errors are similar in both selected spectral channels (see blue lines in the left plot). As for the O_2-A absorption, the stray-light contribution is higher outside of the absorption band (at 755 nm). Notwithstanding, the difference in radiance levels within and outside the O_2 absorption causes larger relative errors for the spectral channels inside the absorption band (see red lines in the left plot) with variations at 760.62 nm between 0.5% at nearly 220 ACT pixels far from the cloud, in the extreme of the swath, up to 1.3% at 30 ACT pixels from the cloud or even up to 1.6% right next to the clouds.

The impact of stray-light in the SIF retrieval was evaluated by comparing the results in Fig. 5.19 against the radiance contribution at L1b (see Fig. 5.20) for an increase of 10% SIF (i.e., error in SIF). When comparing these two figures, it is seen that the stray-light effect within the O_2-B (687.1 nm) is a factor 1.3 (next to the cloud) to 3-10 (>30 ACT pixels from the cloud) lower than the 10% SIF error contribution (0.11mW·m^{-2}sr^{-1}nm^{-1}). However, the stray-light effect at the bottom of the O_2-A band (760.62 nm) is a factor nearly 2-4 times higher than the 10% SIF error contribution (>30 ACT pixels from the cloud) or even a factor 5 higher next to the clouds. Based on this analysis, it is expected that the errors in SIF caused by the stray-light would be between <10% at the bottom of the O_2-B and 20-40% at the bottom of the O_2-A.

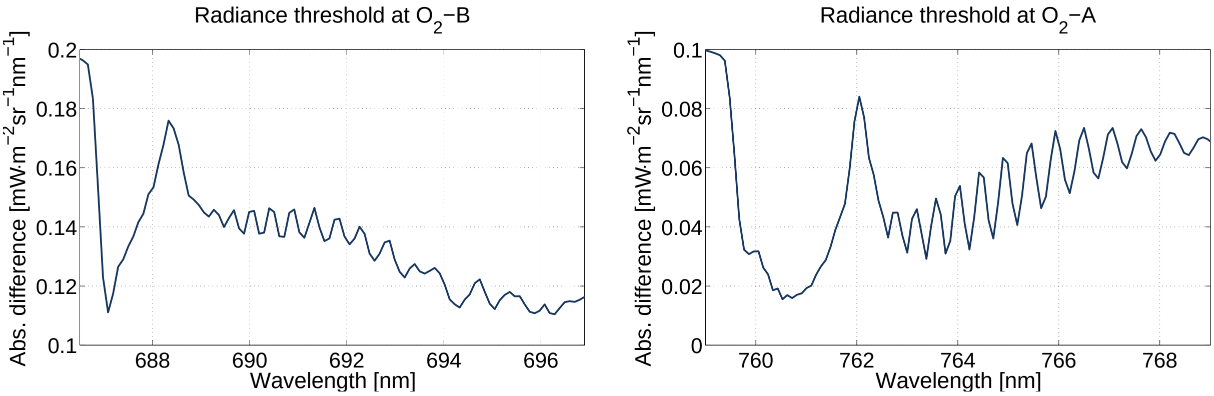

Figure 5.20: Absolute difference at FLORIS-HR L1b radiance caused by an increase of 10% SIF within the O_2-B (left) and O_2-A (right).

The effect of stray-light on the retrieved SIF is seen in Fig. 5.21). In order to decouple the uncertainties introduced by the L2 processing, the retrieved SIF from the L1b data (red) was compared against that from the noise-free L1b data (blue).

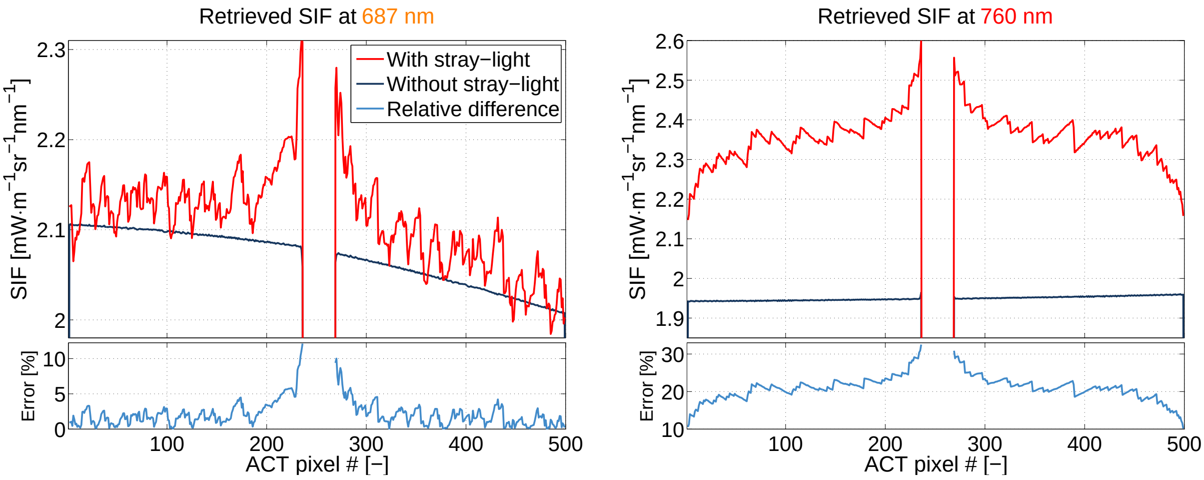

Figure 5.21: Stray-light impact on the retrieved SIF in the O_2-B (left) and O_2-A (right) for different ACT pixels with and without the effect of stray-light (top) and their relative difference (bottom).

Fig. 5.21 is in agreement with the conclusions derived from Fig. 5.20 showing that, within the O_2-B region (left plots), SIF is retrieved with errors of 0-5% (mostly due to the A/D conversion effect) up to 12% right next to the cloud. Notwithstanding, the retrieved SIF error in the O_2-A region (right plots) varies from ∼32% next to the clouds down to 10% in the best case for pixels in the extremes of the swath, far from bright clouds and with no contribution from out-of-field objects (“pixels” <1 and >500), that is errors higher than the goal accuracy of 0.2 $\mathrm{mW \cdot m^{-2} sr^{-1} nm^{-1}}$).

FLORIS-LR is also affected by stray-light as shown in Fig. 5.22 and Fig. 5.23. Both in terms of absolute and relative differences, the stray-light affects more in the first 150 spectral channels (500-680 nm) with contributions up to 0.8% right next to the cloud.

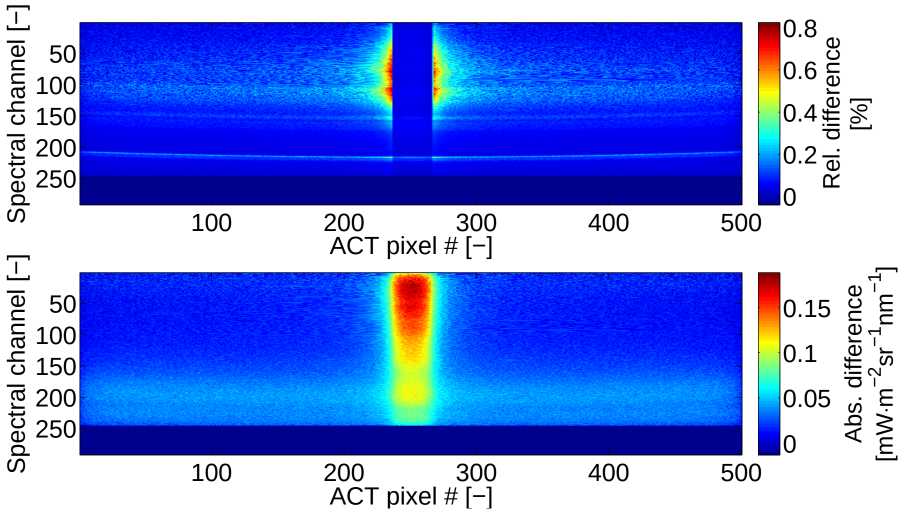

Figure 5.22: Stray-light map (relative-top and absolute-bottom) on the FLORIS-LR focal plane.

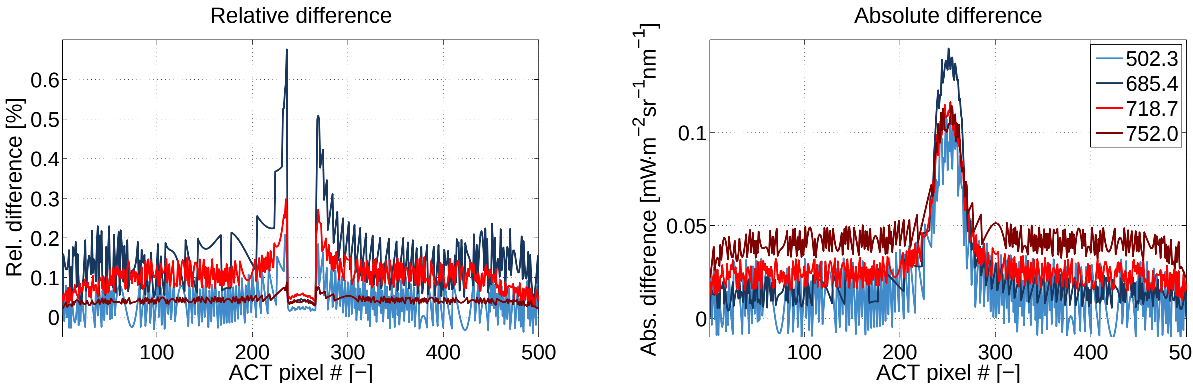

Figure 5.23: ACT variation of the stray-light contribution at different wavelengths represented as the absolute/relative difference between the reference and L1b radiance (right/left).

5.1.3 Geometric performance

The FLORIS geometric performance was analyzed from the results of a full FLORIS swath (150 km) and ∼450 acquisition lines simulation test . The synthetic L1b geolocated data was compared against the reference geolocation in order to evaluate the geometric performance in terms of geolocation accuracy, spatial sampling distance and spatial co-registration. The simulation included all geometric effects and geolocation errors such as characterization errors of FLORIS mounting on FLEX platform; and orbit and attitude estimation errors. The simulation also included the effects of relative geometry between the two FLORIS spectrometers due to angular shifts and slit rotation in yaw as well as rotations of the detectors generating ACT shifts as function of wavelength (keystone).

By converting the geolocation data from latitude/longitude coordinates into UTM coordinates, the distance between two consecutive FLORIS ACT and ALT pixels was calculated. The mean and standard deviation of these distances provide an estimate of the Spatial Sampling Distance (SSD) in the simulated data of 297.3±0.9 m (ACT) and 304±1 m (ALT), both compatible with the 300 m mission requirement.

The geolocation accuracy at L1b was also determined from the absolute error between reference and estimated (after L1b geolocation) pixel coordinates. This was possible given that FLEX-E included the estimated attitude and orbit temporal profiles. With the simulated scenario, an average geolocation accuracy of 12±4 m was achieved, fulfilling the specification of 0.4 SSD (120 m). This results does not include the error in the knowledge of FLORIS mounting Euler angles. Increasing this error to100 μm in reduces the geolocation accuracy to ∼90 m. The errors in the L1b geolocation are however still within the requirements, even without the use of ground control points.

FLORIS is a multi-camera instrument composed of two spectrometers (FLORIS-HR and -LR). In addition, FLORIS-HR has focal plane separation between the O_2-B and O_2-A regions. Therefore, spatial co-registration errors are expected between FLORIS-HR_A, FLORIS-HR_B and FLORIS-LR (interband) and between spectral channels within each spectrometer (intra-band). This spatial co-registration error might derive errors in the retrieved SIF. Thus, the interband co-registration between FLORIS-HR and FLORIS-LR was estimated through image correlation, determining the displacement between the images acquired by these two spectrometers. The correlation was calculated in small windows of the L1b images in order to determine local displacement. A window size of 10×10 pixels was selected as compromise between calculation time and local analysis of co-registration errors ACT and ALT. The 10×10 pixels window also reduced the uncertainties in the calculation due to homogeneities in the image. The process consisted in seven steps:

1. A *fixed* window at (x_0, y_0) pixel coordinates was located in first image.
2. A *movable* window of the same size was displaced in the second image ±5 pixels around (x_0, y_0) in steps of 1 pixel (coarse displacement).
3. For every displacement of the movable window, the correlation between the *fixed* and the *movable* window images was computed. The maximum correlation indicated the coarse displacement between the two spectrometers (dx, dy).
4. For a sub-pixel determination of the displacement, both images were resized a factor 10 by nearest neighbor.
5. Step 2 was repeated, displacing the *movable* window in the second image ±1 pixel around (x_0+dx, y_0+dy) in steps of 0.1 pixels (fine displacement).
6. As in step 3, the correlation was calculated at each fine displacement. The maximum correlation determined the fine displacement between the two spectrometers, (ddx,ddy).
7. The co-registration between the two spectrometers at (x_0, y_0) was given by the total displacement: (dx+ddx, dy+ddy).

The steps above were repeated for different positions (x_0, y_0) of the *fixed* window in the first image. These positions were selected to number of spatial features in the image window in order to better calculate the ACT and ALT displacements avoiding undetermined solutions. For this reason, the scene was simulated as a synthetic LCC map composed of rectangles of various sizes. Each rectangle was associated with a dark surface reflectance spectrum while the background LCC was associated with a bright surface reflectance spectrum in order to maximize the contrast between both classes. The corners of the rectangles were selected as the center position of each 10×10 pixel-size window (see Fig. 5.24).

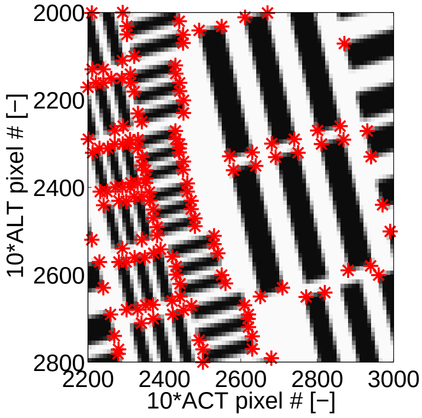

Figure 5.24: FLORIS-HR image (zoom) in gray scale overlapped with automatically detected rectangle pixel coordinates (∗).

In order to better determine the correlation between these two images, it is important to have similar contrast between them. To do so, the spectral channels in both spectrometers were selected to avoid atmospheric absorption bands and minimize the spectral smile effect. Fig. 5.25 shows three main issues: **(1)** There is a wavelength offset between FLORIS-HR and -LR spectra, particularly visible within the O_2 absorption region, caused by the combination of smile effect and different spectral resolution; **(2)** The radiances acquired by FLORIS-LR channel #200 (∼752 nm) are nearly constant within the ACT wavelength variation caused by the smile effect at channel #200 (750-756 nm); **(3)** FLORIS-LR channel #200 is not affected by any deep absorption band, which leads to a similar radiance acquired by FLORIS-HR channel #148 (751.7 nm).

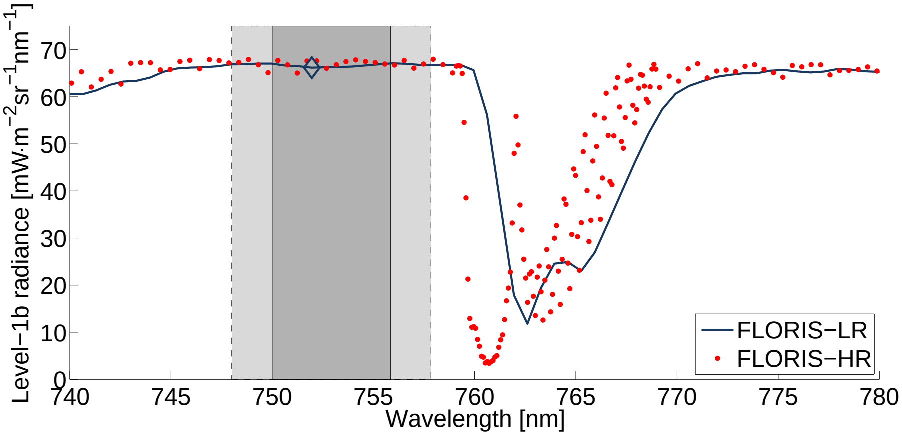

Figure 5.25: FLORIS-HR (red) and -LR (dark blue) L1b radiance sample spectra. The gray shadowed areas range between the minimum and maximum wavelengths ±1 FWHM (2 nm) for the LR band #200 whose average wavelength is 752 nm (◊).

In order to further minimize the effects of smile in FLORIS-LR and different resolution between the two spectrometers (i.e., 0.5 nm for FLORIS-HR channel #148 and 2 nm for FLORIS-LR channel #200), the higher spectral resolution and sampling of the HR spectrometer was resampled by FLORIS-LR ISRF to create a compatible image. Fig. 5.26 shows the difference between FLORIS-LR radiance map at channel #200 and the resampled FLORIS-HR radiance map (left) or FLORIS-HR at channel #148 (right).

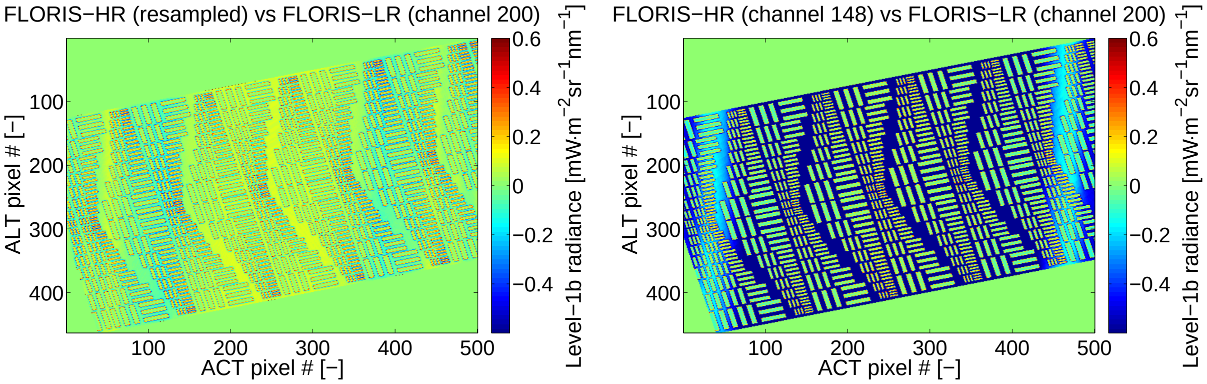

Figure 5.26: Difference between FLORIS-LR L1b radiance map at channel #200 with resampled HR data (left) and with FLORIS-HR L1b radiance map at channel #148 (right).

The figure above shows how the discrepancies between radiance levels due to smile and FWHM decrease, after applying the convolution by the ISRF, from an average value of 0.4 mW·m^{-2}sr^{-1}nm^{-1} down to 0.1 mW·m^{-2}sr^{-1}nm^{-1}. Some differences persists, particularly on the boundaries between the two land cover classes due to the effect of the PSF.

Using these two images, the spatial co-registration error was calculated. Fig. 5.27 shows the displacement vector on each selected image pixel. An observed displacement of 0 pixels for most ACT and ALT pixels indicates that the co-registration error between FLORIS-HR and -LR is negligible. However, some pixels at the extremes of the swath show a displacement that can reach up to 6 pixels in ACT and/or ALT direction (see zoom windows in Fig. 5.27).

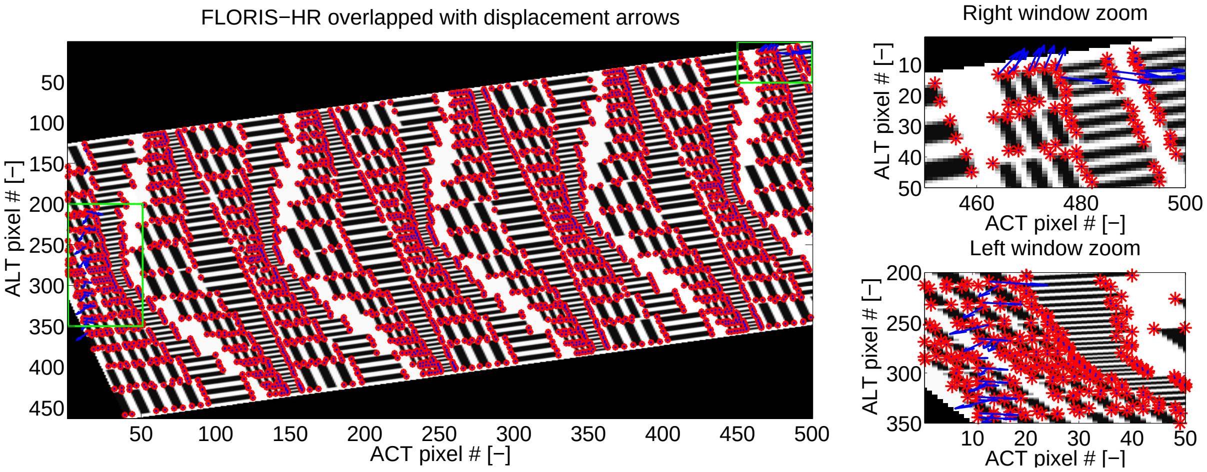

Figure 5.27: Displacement arrows (blue) multiplied by a factor 5 on each selected pixel coordinates.

The histogram of the ACT and ALT displacements (see Fig. 5.28 left) indicates again that most pixels have a nearly zero displacement (±0.5 pixels). The pixels with non-zero displacement are located in particular areas of the image (see Fig. 5.27) where the correlation obtained by the implemented algorithm was well below 0.8 (see Fig. 5.28 right). In fact, all the pixels with zero-displacement (no co-registration error) have a correlation 0.99±0.05. Most probably these large co-registration errors are caused errors in the algorithm near the image borders.

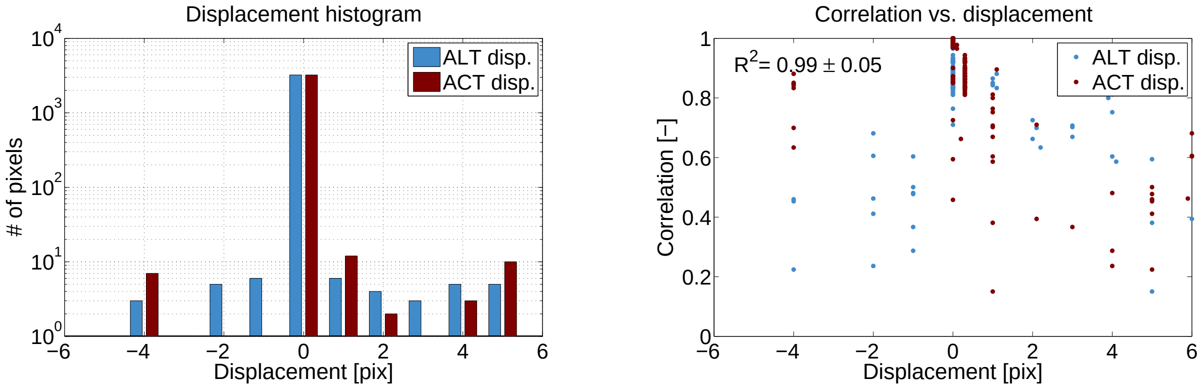

Figure 5.28: Displacement histogram (left) and scatter plot between maximum correlation for each displaced pixel (right).

The simulation done with FLEX-E indicated that spatial interband co-registration error was therefore about zero pixels. In fact, the retrieved 0 pixels misregistration is in line with the fact that, in the current Phase A/B1, the configuration of FLORIS spectrometer and its implementation in the simulator did not consider for thermo-elastic deformations of the mechanical structure of the instrument. Notwithstanding, the implemented FLEX-E software was conceived to eventually test the geometric distortions of the instrument and the misregistration between FLORIS spectrometers.

5.2 Level-2 products performance

Preliminary SIF retrieval performance

In order to evaluate the FLEX mission performance to retrieve SIF below the goal of 0.2 $mW \cdot m^{-2} sr^{-1} nm^{-1}$ error, FLEX-E was run on a 20×20 km^2 test scene (see Fig. 5.29). This scene was made of four homogeneous LCC: a non-fluorescent target (bare soil) and three vegetation classes ranging from low to high SIF based on the input Chlorophyll content (20, 40 and 80 mg/cm^2) and LAI values (1, 3 and 6). The digital elevation model consisted of two vertical stripes of 10×20 km^2 at an altitude of 0 km and 2 km respectively. The two extreme altitudes allowed us to check the impact of surface pressure due to topography in the atmospheric correction within the O_2 bands and the retrieved SIF. A cumulus cloud cover was included in order to add the effect of instrument stray-light in the mission products. Shadows caused by the terrain topography and cloud cover were also included according to the illumination geometry. The atmosphere was defined as the standard mid-latitude summer type with a continental aerosols load of 0.15 optical thickness. The scene is observed with mean zenith angle of 1° and a mean solar zenith angle (SZA) of 43°.

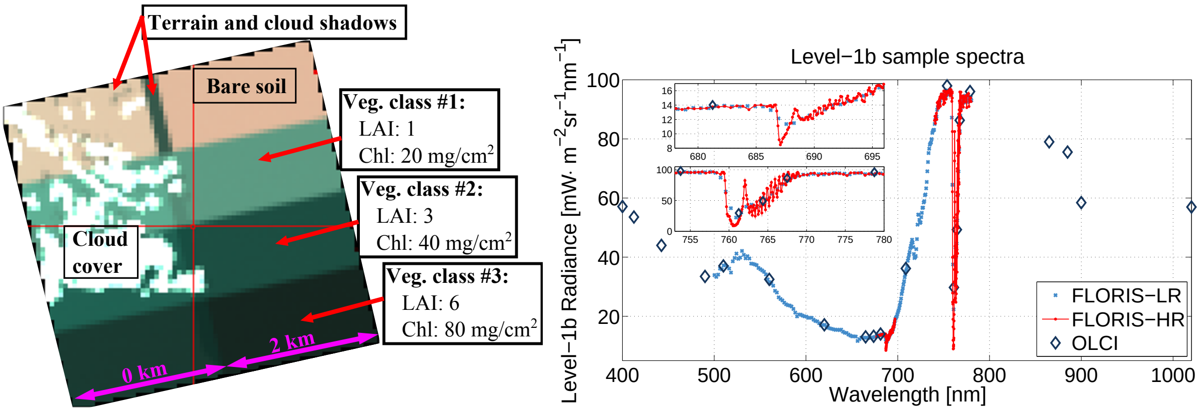

Figure 5.29: Left: RGB composite of the test scenario L1b image (left). Right: Sample L1b radiance spectra for FLORIS-LR (**light blue**), FLORIS-HR (red) and OLCI (dark blue).

The simulation included all instrumental noises, non-uniformity effects and L1b calibration errors such as stray-light, spectral stability, spectral/spatial radiometric noises, detector and video chain noises, spatial/spectral/temporal co-registration errors, geolocation errors and spectral/radiometric calibration errors, as described in Section 4.1 and analyzed in Section 5.1. Fig. 5.29 (right) shows a sample FLORIS and OLCI L1b TOA radiance from vegetation class #2.

Despite FLEX-E capabilities to generate complex and realistic scenes, the simulation of a scene made of simple geometric patterns facilitated the evaluation of the mission performance and the determination of the expected SIF retrieval accuracy. This was possible on the one hand, due to the realism of the simulated environmental effects (e.g., natural variability of key bio-geophysical parameters, use of state-of-the-art RTMs or consideration of bi-directional reflectance effects). On the other hand, the implemented instrumental and L1b calibration effects reproduced with great detail the actual instrument configuration. Thereby, the L2 processing within FLEX-E was considered to be representative of the expected ground segment processing, dealing with effects such as characterization of the instrument response function, radiometric cross-calibration between OLCI and FLORIS L1b data and synergistic L2 retrieval algorithm.

The achieved mission performance at L2 was evaluated through the absolute error between reference and retrieved SIF (see Fig. 5.30). The highest errors were found at O$_2$-B for veg. class #1 and at O$_2$-A for veg. class #3, both corresponding to the highest proportion of reflected radiance with respect to SIF of all vegetation classes. In particular, in the case of O$_2$-B and low vegetation (LAI=1) there is a larger contribution of the background soil that increases the reflected red signal together with a smaller chlorophyll absorption, resulting in a small SIF emission. In the case of O_2-A, the very dense vegetation (LAI=6) produces a strong multiple scattering inside the canopy resulting in an increased reflected radiance, whereas the rapid decrease in photosynthetic active radiation intensity in the inner part of the canopy causes that the added chlorophyll content only provides a slight increase in SIF emission. Aside from these physiological effects, it is necessary to consider the added effect of noise, which increases with intensity, and the atmospheric perturbation that cannot be perfectly compensated. These results are in agreement with [53].

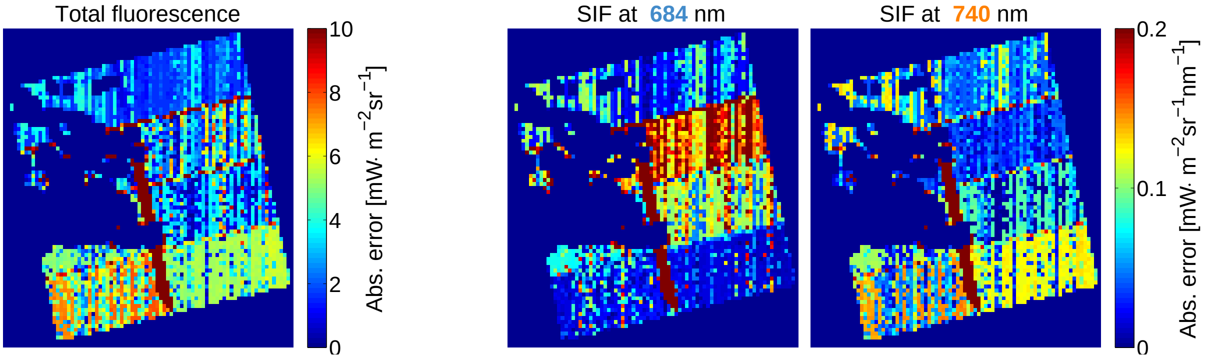

Figure 5.30: Absolute errors maps for the L2 retrieved total SIF (left) and peak values at 684 nm and 740 nm (two rightmost figures). Clouds are masked in the retrieval process.

The histograms of these error maps (see Fig. 5.31) show a multivalued error distribution due to the performance of the SIF retrieval in each vegetation class. In addition, those pixels with an error above the mission requirements are mostly located in: **(1)** the vicinity of clouds, due to scattering and stray-light contamination; and **(2)** the shaded regions, which can affect the atmospheric correction of those pixels.

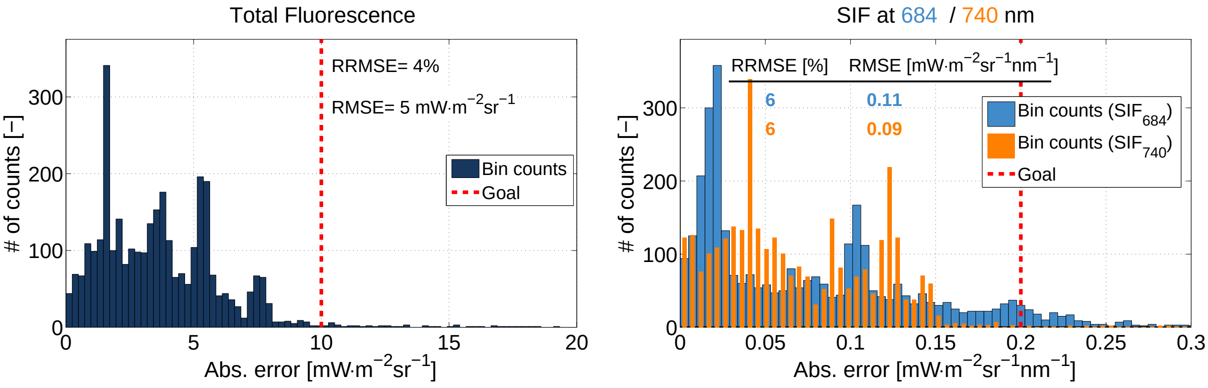

Figure 5.31: Absolute errors histogram for the L2 retrieved total SIF (left) and peak values at 684 nm and 740 nm (right).

Overall, these histograms indicate that the retrieval was performed with an error below the mission requirements (red dashed line) for all three SIF products.

SIF retrieval performance. Sensitivity analysis

The previous preliminary test was limited with respect to the variability of SIF spectra (i.e., only three vegetation classes). In order to increase this variability, these results were complemented with the performance analysis over a simulated image dataset. This dataset consisted of six images with a varying configuration of aerosol types and illumination conditions (see Tab. 5.1). As in the previous test, all instrument noises and L1b calibration errors were included in each simulated image.

Table 5.1: Definition of the sensitivity analysis test cases. Cases #1 to #3 had varying illumination conditions while cases #4 to #6 had varying aerosol types.

Case #	#1	#2	#3	#4	#5	#6
Aerosol type (AOT)	Rural (0.05)	Rural (0.05)	Rural (0.05)	Rural (0.25)	Maritime (0.25)	Urban (0.25)
Illumination (SZA [deg])	Low (60)	Mid (45)	High (25)	Mid (45)	Mid (45)	Mid (45)

Each image consisted of a cloud free scene at 0 km constant surface elevation and a LCC map made of six horizontal stripes with key biophysical parameters defined as per Tab. 5.2. Among the different LCC, Veg.#1 to #5 were vegetation targets with a SIF emission ranging from low to high. Veg.#1 and #2 were defined as two extreme combinations of high-low LAI and Chlorophyll, whereas Veg.#3 to #5 are equivalent to the low-to-high stripes analyzed in Fig. 5.29. Also, a Bare Soil stripe was included in the analysis as a reference non-fluorescent target.

Table 5.2: LCC map configuration for the sensitivity analysis test case.

Class ID	Veg.#1	Veg.#2	Veg.#3	Veg.#4	Veg.#5	Bare soil
LAI [-] / Chl-a [mg·cm^{-2}]	5 / 20	1 /80	5 / 80	3 / 40	1 / 20	N.A.
SIF (Yes/No)	Yes	Yes	Yes	Yes	Yes	No

The various atmospheric and illumination conditions within the image dataset, combined with the variability of key biophysical parameters, increased the number of SIF spectra to 36 different cases. This allowed us to analyze the robustness of the SIF retrieval algorithm in a larger set of SIF values, illumination and atmospheric conditions for a realistic configuration of the actual FLEX platform and FLORIS instrument. Fig. 5.32 shows the results from the image dataset by comparing the retrieved SIF against its reference value averaged at each LCC. The total SIF (top row) and peak values at 684 nm and 740 nm (middle and bottom rows respectively) were analyzed, from left to right, according to:

- **Bar plot analysis:** Retrieved (black points) vs reference values (bars) with the precision of the retrieval indicated with black error bars.
- **Retrieval accuracy:** Difference between retrieved and reference values. The red dashed lines indicate the required goal accuracies.
- **Scatterplot** of retrieved vs reference values with the dashed lines indicating the ideal retrieval (black) and the required goal accuracies (red).

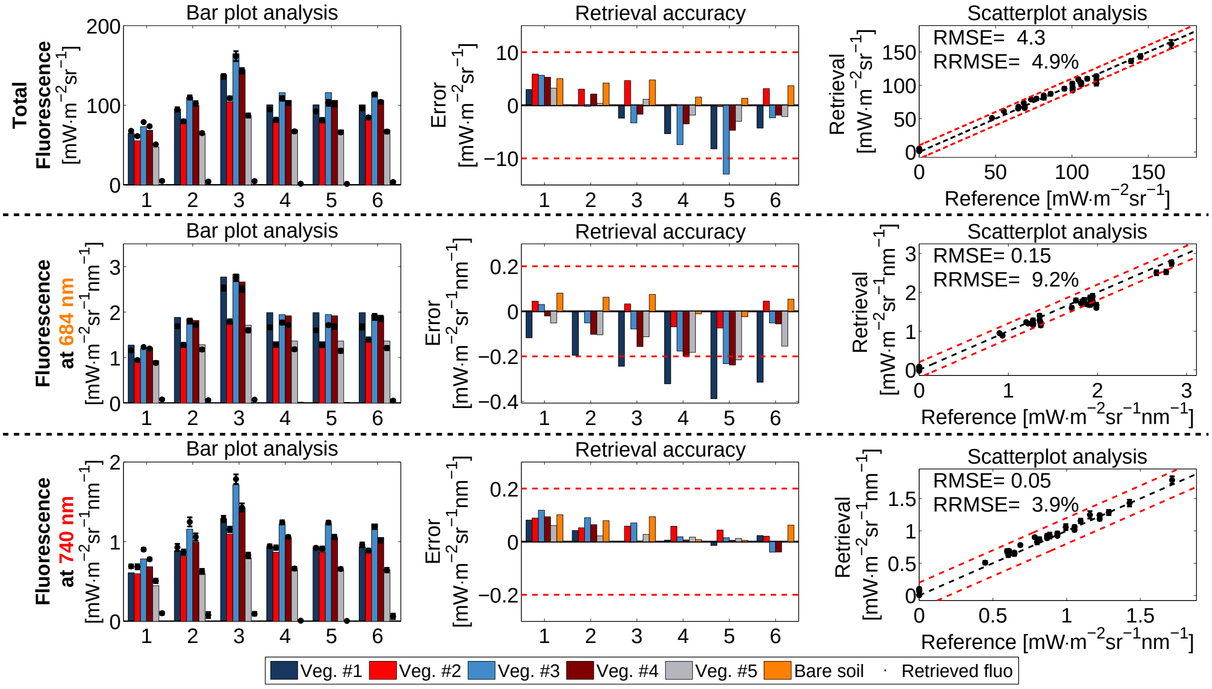

Figure 5.32: Sensitivity analysis for the total SIF (top row) and peak values at 684 nm and 740 nm (middle and bottom rows respectively).

Overall, the results in Fig. 5.32 indicate that the retrieval is within the goal accuracy of 10 mW·m^{-2}sr^{-1} (for the total SIF) and 0.2 mW·m^{-2}sr^{-1}nm^{-1} (for the SIF peak values) with a RMSE of 4.3 mW·m^{-2}sr^{-1}, 0.15 mW·m^{-2}sr^{-1}nm^{-1} and 0.05 mW·m^{-2}sr^{-1}nm^{-1} respectively for the total SIF and the peak values at 684 nm and 740 nm. The results obtained in each case are similar to those observed in Fig. 5.31. In particular, the SIF at 684 nm was retrieved with lower accuracy for the sparser (Veg. #5) than the denser vegetation (Veg. #3) due to the lower SIF value and higher amount of reflected light. In the case of SIF at 740 nm, the accuracy was lower for the denser than the sparser vegetation given the higher reflected signal (i.e., higher noises) with respect to the increase of emitted SIF. Also, the retrieval of SIF at 684 nm on target Veg.#1 was systematically underperforming, most probably due to a poor fitting of the polynomial modeling the reflectance in the reddish wavelength range for a combination of high canopy density (LAI=5) and low Chlorophyll content (20 mg·m^{-2}). The retrieved SIF over the bare soil was also achieved within the requirements with an error below 0.1 mW·m^{-2}sr^{-1}nm^{-1} for both peaks in the various illumination and atmospheric conditions.

The intercomparison of the first three cases indicates that the retrieval performed differently for the two peaks under variations of illumination. In the case of SIF at 684 nm, the retrieval had lower accuracy as the SZA increases despite of the increase of the SIF signal. Higher SZA implies higher radiances and thus higher noises that were not compensated by the increase of SIF. These larger noises reduced the accuracy in the retrieved SIF at 684 nm. In the case of SIF at 740 nm, the noises were also increased for higher SZA but the increase of emitted SIF compensated the noises leading to lower SIF retrieval error for higher illumination conditions.

The quality of the atmospheric correction was evaluated through the evaluation of cases #2 and #4 to #6 (variability of aerosol types). The results indicate that the atmospheric correction was successful under different aerosol conditions. However, the accuracy of the retrieved SIF at 684 nm was lower when compared against case #2 (same illumination but lower aerosol content). This was due to the propagation of aerosol characterization errors through the atmospheric correction, which had a larger impact in the visible wavelength range. These results indicate that the atmospheric correction was one of the key steps in the L2 processing chain and directly affected the accuracy of the retrieved SIF. In order to further analyze the performance of the atmospheric correction, the retrieved atmospheric parameters were compared against their reference values for these test cases. Tab. 5.3 shows that the AOT was well characterized for all aerosol types and loads. However the aerosol type, described by its spectral dependency (through the Angstrom coefficient) and phase function (through the Henyey-Greenstein parameter), was not perfectly characterized. In the case of SIF at 684 nm, the errors in the characterization of the phase function were largely propagated to errors in the retrieved SIF (i.e., higher errors for maritime aerosols than urban aerosols). As for SIF at 740 nm, higher errors in the characterization of the Angstrom coefficient leaded to higher errors in the retrieved SIF.

Table 5.3: Accuracy of the retrieved atmospheric parameters.

Atmospheric parameter	**Rural**	**Rural**	**Maritime**	**Urban**
	ε_{rel} **[%] (ref.)**	ε_{rel} **[%] (ref.)**	ε_{rel} **[%] (ref.)**	ε_{rel} **[%] (ref.)**
AOT [-]	0 (0.05)	0 (0.25)	0 (0.25)	0 (0.25)
Angstrom coefficient [-]	0.06 (1.54)	0.06 (1.54)	0.06 (1.54)	13 (1.54)
Henyey-Greenstein parameter [-]	50 (0.81)	14 (0.81)	26 (0.81)	7 (0.54)
Columnar water vapor (CWV) [g·cm^{-3}]	0.3 (2.92)	1.5 (2.92)	3 (2.92)	1.4 (2.92)

Level-2 products performance over a realistic scene

While the results in Fig. 5.31 and Fig. 5.32 indicate that the FLEX mission is able to retrieve SIF with an error below the goal accuracy, these test cases were based on simple scenarios not fully representative of a realistic FLEX image. Thus, FLEX-E was used to evaluate the accuracy of the retrieved SIF for a realistic scenario located on the Majorca Island (Spain). This realistic configuration was achieved by firstly including the variability of surface topography (through the real DEM) and LCC (through the Corine LCC map). Vegetation classes were configured with a wide range of key biophysical parameters and the LCC map also included non-fluorescent surface reflectance such as bare soils, urban areas and water bodies. Secondly, the atmospheric conditions were defined with a mid-latitude summer atmosphere and default aerosol (0.15 AOT) and water content based on the ECMWF data for the selected location and acquisition epoch (SZA=40°). Finally, the simulation test included all instrument noises and L1b calibration errors for a realistic representation of the instrument behavior. The retrieved SIF products are shown in Fig. 5.33 through the relative and absolute errors between the reference and retrieved SIF maps.

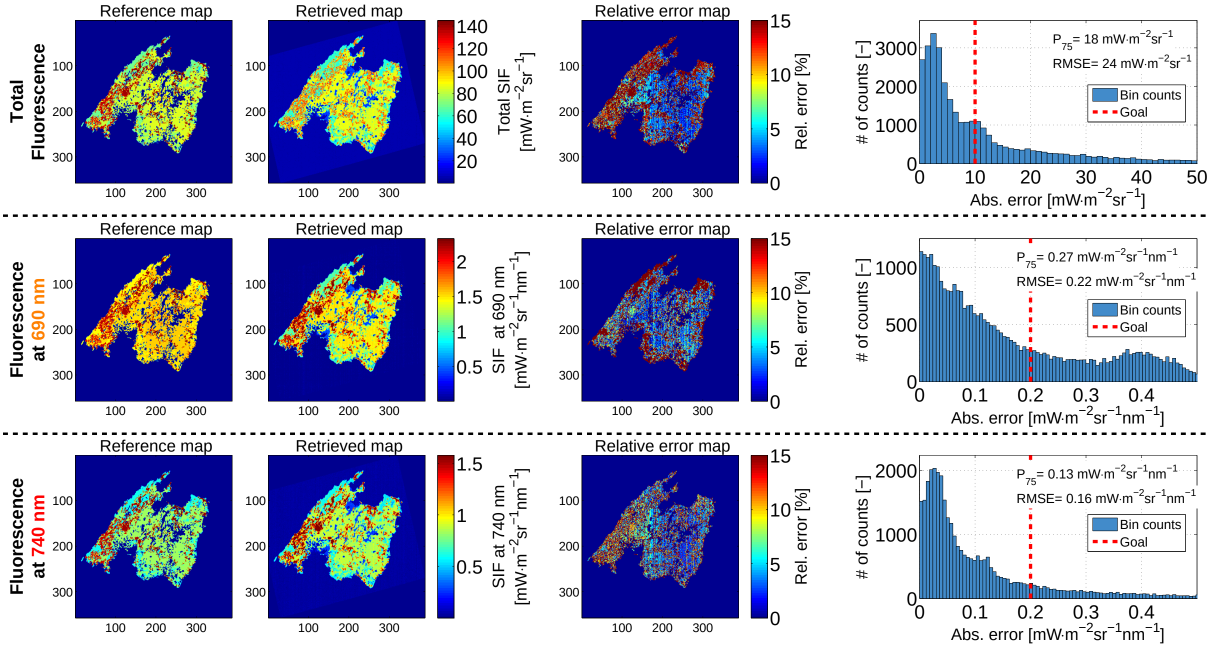

Figure 5.33: L2 performance on the total SIF and peak values at 684 nm and 740 nm (top to bottom rows). From left to right: reference and retrieved SIF maps; relative error map between reference and retrieved SIF; and histogram of the absolute errors. Percentile 75% (P_{75}) and RMSE are given within each histogram.

Qualitatively, the comparison between reference and retrieved SIF maps (first and second column) indicates that the FLEX mission is sensitive to the variety of SIF spectra from the different classes, retrieving similar values and spatial distribution. The relative error maps indicate that systematic effects in the ALT dimension (i.e., vertical stripping) and pixel-wise random noise have an impact on the retrieved SIF with an error below 15% for most of the pixels in the image. Quantitatively, the histograms (fourth column) show that for most of the image pixels, the retrieved SIF errors are below the requirements (red dashed lines). In particular, Tab. 5.4 evaluates the accuracy of the retrieved SIF through the RMSE and the percentile 75% (i.e., the value below which a 75% of the errors fall). The results show that the SIF peak values are obtained with an error below or close to the requirements (RMSE of 0.22 mW·m^{-2}sr^{-1}nm^{-1} and 0.16 mW·m^{-2}sr^{-1}nm^{-1} respectively for the first and second peaks). Nonetheless, the retrieved total SIF shows that 75% of the pixels are retrieved with an error below 18 mW·m^{-2}sr^{-1}, which is above the requirement of 10 mW·m^{-2}sr^{-1}. This is due to the influence of the outliers in the histogram evaluation. In fact, the mean and median statistics are closer to the requirement (12 mW·m^{-2}sr^{-1} and 5 mW·m^{-2}sr^{-1} respectively).

Table 5.4: Absolute error statistics for the realistic test case.

SIF product	Percentile 75 %	RMSE	Mean	Median
Total SIF [mW·m^{-2}sr^{-1}]	18	24	12	5
SIF at 684 nm [mW·m^{-2}sr^{-1}nm^{-1}]	0.27	0.22	0.14	0.10
SIF at 740 nm [mW·m^{-2}sr^{-1}nm^{-1}]	0.13	0.16	0.10	0.05

The relative error maps indicate that errors are systematically obtained in LCC placed along coastal areas, close to urban areas and in terrains with high topographic variation (north-west of the island). These LCC have large proportion of heterogeneous pixels, which seem to reduce the performance of the retrieval algorithm.

Impact of pixel heterogeneity at Level-2 products performance

It was necessary to study the sensibility of the instrument response function to surface heterogeneity and its effect on the retrieved SIF. For this reason, a simulation test was carried out based on the synthetic scene shown in Fig. 5.34. This scenario consisted into two classes (vegetation and bare soil) randomly distributed over the scene in areas where they are combined in proportions ranging from 0% vegetation (100% bare soil) to 100% vegetation (0% bare soil) in steps of 10%. The scene grid resolution was set to 30 m, thus one FLORIS pixel contained, through its PSF, approx. 100 scene grid points. This high resolution allows to study the effect of sub-pixel heterogeneity.

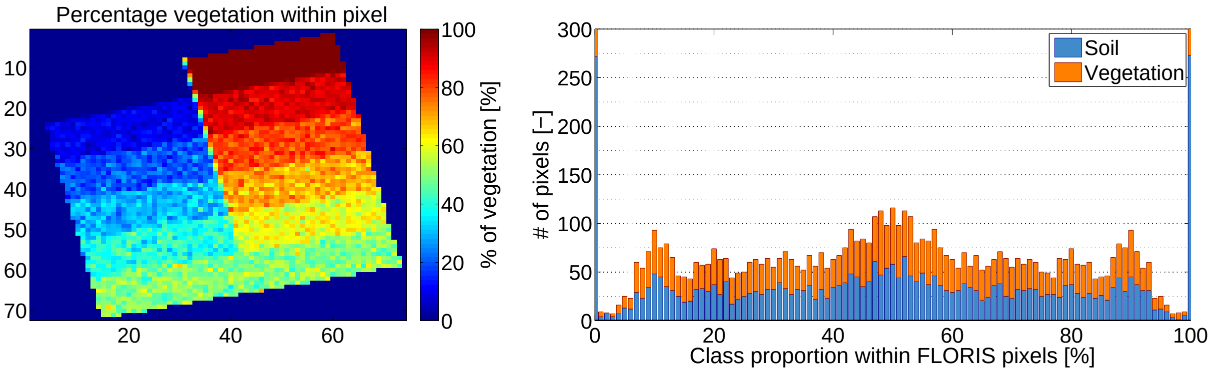

Figure 5.34: Percentage of vegetation cover within FLORIS pixel (left) and class proportion distribution (right).

The retrieved SIF maps in Fig. 5.35 show the sensitiveness of the retrieval algorithm to different SIF levels, and thus to the proportion of bare soil within the FLORIS pixels. The error statistics (fourth column) indicate that the three SIF products were obtained within the requirements. However, the spatial distribution of the errors (third column) shows that the accuracy of the retrieved SIF was influenced by the percentage of vegetation cover (see the difference between top and bottom rows of the absolute error maps), being lower the accuracy for a mix of 50-50% vegetation-soil.

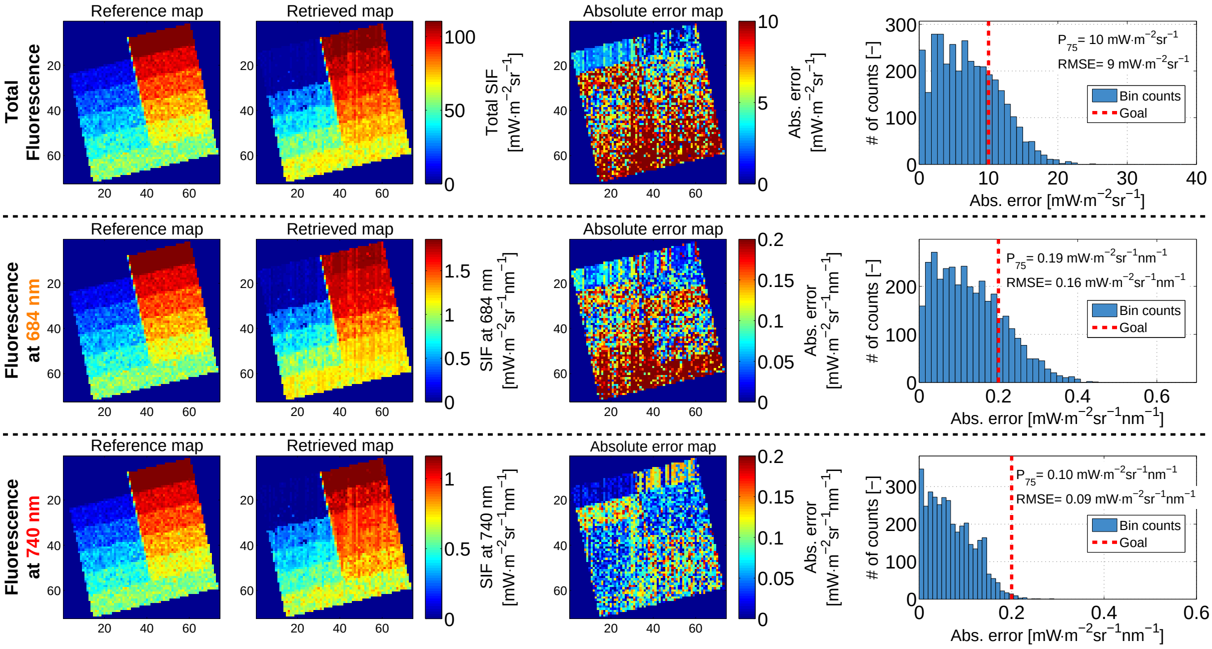

Figure 5.35: L2 performance on the total SIF and peak values at 684 nm and 740 nm (top to bottom rows). From left to right: reference and retrieved SIF maps; relative error map between reference and retrieved SIF; and histogram of the absolute errors. Percentile 75% (P_{75}) and RMSE are given within each histogram.

In order to quantify the performance of the retrieval under different proportions of vegetation/soil within the pixel, the RMSE was calculated in each area with constant soil proportion. The results in Fig. 5.36 shows on the one hand that, both for the total SIF and the SIF at 684 nm, lower errors were generally obtained when the vegetation (or soil) cover was closer to 100%. The errors were increasing as the sub-pixel heterogeneity was also increasing, reaching the highest errors for a 40-50% LCC mixture. Particularly, the SIF at 684 nm was reaching the highest errors (0.25 mW·m^{-2}sr^{-1}nm^{-1}) in line with the results obtained in the test case in Fig. 5.33. On the other hand, the retrieved SIF at 740 nm shows variations on the accuracy depending on the percentage of vegetation cover with two maximums at 10% and 65%. This is most probably caused by the separation between real reflectance and SIF from the atmospherically corrected apparent reflectance. Notwithstanding, the errors in this case were well below the requirement (0.05-0.12 mW·m^{-2}sr^{-1}nm^{-1}).

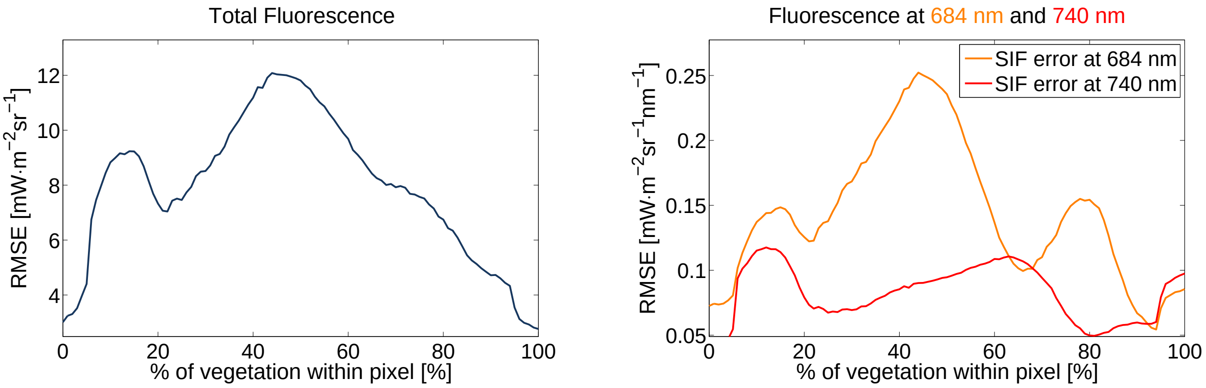

Figure 5.36: RMSE for the total SIF (left) and peak values at 684 nm and 740 nm (right).

This analysis indicates that errors in the retrieved SIF are higher for mixed pixels, in particular for total SIF and first peak value.

However, this test scenario was based on two LCC and does not include the complexity of sub-pixel heterogeneity. For this reason, an additional simulation test case was run based on the scenario shown in Fig. 5.37. Here, the scene was defined with 6 LCC: a bare soil and 5 vegetation LCC with different combinations of key biophysical parameters. The scene grid resolution was also set to 30 m so that the image pixels had various degrees of sub-pixel heterogeneity, from fully homogeneous pixels to very heterogeneous pixels, with combinations of 6 pure spectra in different proportions. In addition, the simulation was configured with all instrument noises, including stray-light, and L1b calibration errors.

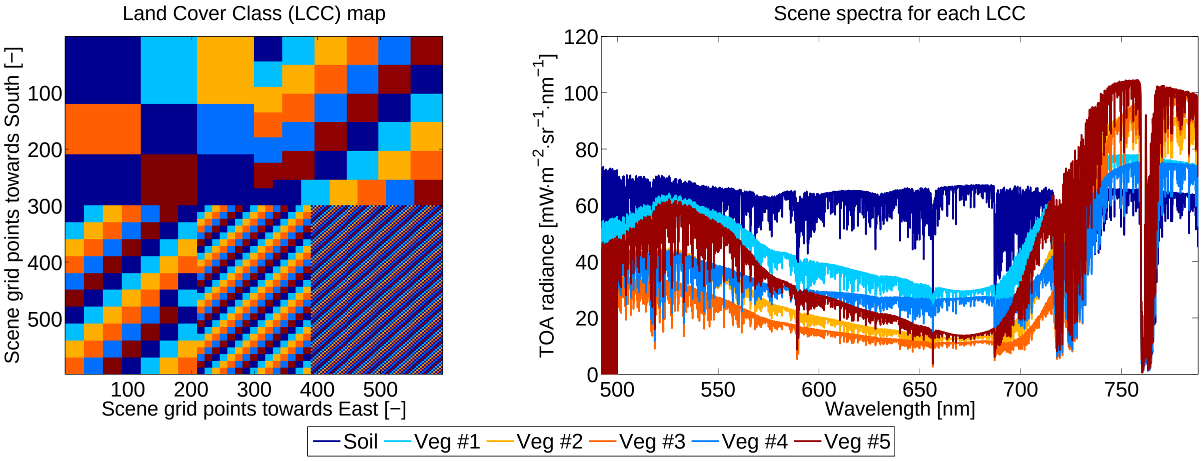

Figure 5.37: Land Cover Class map (left) and sample TOA radiance scene spectra (right).

The resampling of the high-resolution scene to the FLORIS image grid and resolution generated regions with different levels of heterogeneity at sub-pixel leve. Fig. 5.38 indicates the predominant LCC type and its percentage within each pixel (mid and left images). E.g. the pixel (60,60) is dominated by the Soil class with a cover percentage of ∼50% while the pixel

(20,20) is dominated by the Veg#1 class with a coverage of 100%. The histogram in Fig. 5.38 indicates that most of the image pixels are fully homogeneous or with a heterogeneity below 50%. The histogram also shows that most of image pixels are dominated by the soil LCC, thus the analysis will be more robust for this class.

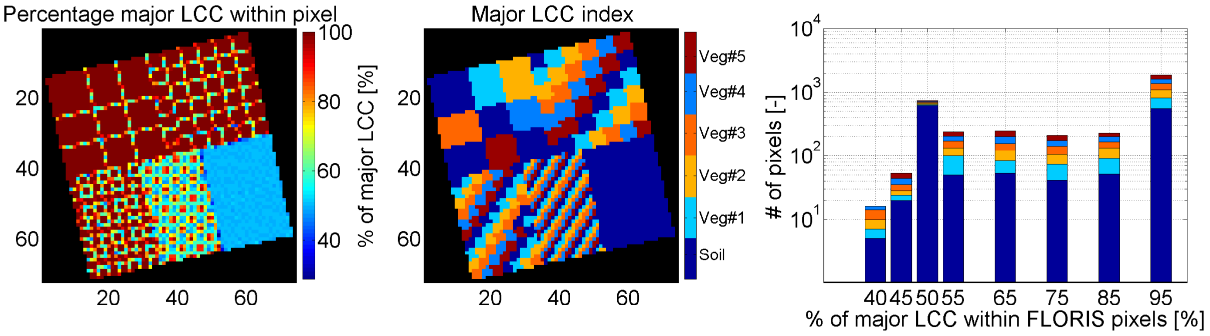

Figure 5.38: Distribution of LCC within each FLORIS pixel with the percentage of the major LCC type (left) and its LCC type index (mid). On the right, number of pixels for which each class is major within FLORIS pixels at different percentages.

Fig. 5.39 shows the performance of FLEX L2 retrieval algorithms by evaluating the errors obtained in the retrieved SIF.

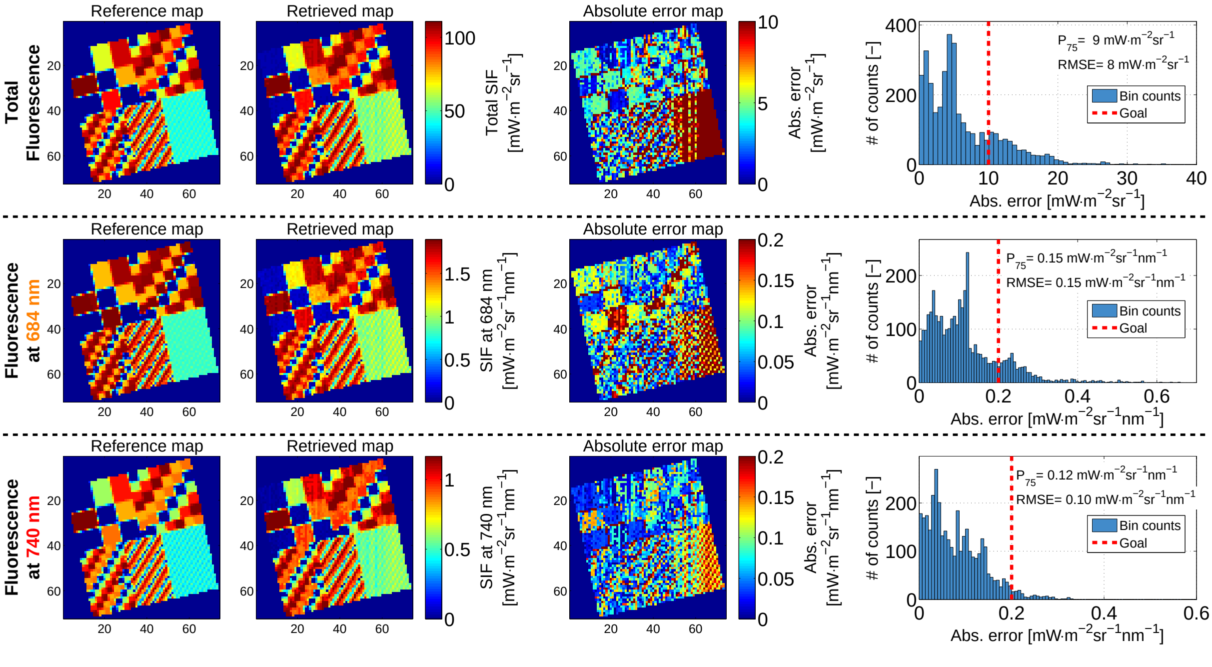

Figure 5.39: L2 performance on the total SIF and peak values at 684 nm and 740 nm (top to bottom rows). From left to right: reference and retrieved SIF maps; relative error map between reference and retrieved SIF; and histogram of the absolute errors. Percentile 75% (P_{75}) and RMSE are given within each histogram.

The spatial distribution of the absolute errors (third column) indicates that the highest errors for the three SIF products were in the area of highest pixel heterogeneity i.e., where the pixel contains ∼50% of the predominant class. These higher errors can also be noticed in the boundary regions between two classes. However, the histograms of the absolute errors shows that the retrieval was within the requirements (see RMSE and percentile 75% values).

In order to further evaluate the impact of pixel heterogeneity, the retrieved SIF accuracy was evaluated as a function of the percentage of the major LCC within each FLORIS pixels. The result in Fig. 5.40 shows that, for each LCC, the RMSE is generally reduced when the pixel homogeneity is larger than 55% in agreement with the results in Fig. 5.36. After this percentage the RMSE keeps nearly constant with the same value as the obtained over fully homogeneous pixels (100% LCC percentage). SIF was generally retrieved with an error below the requirement except for the pixels with soil coverage below 45%. The Veg#5 LCC type also had a bias in the retrieved SIF at 684 nm with an error above the requirement due to the reconstruction of the reflectance spectral shape.

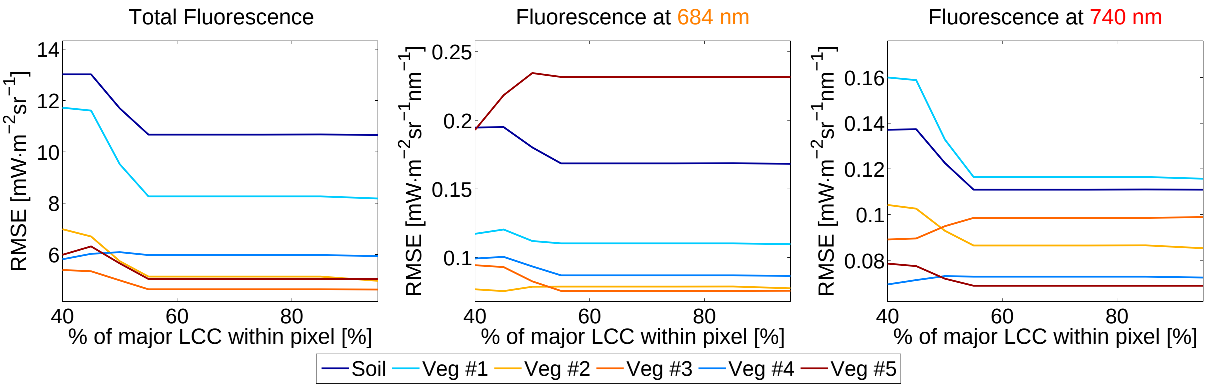

Figure 5.40: RMSE for the total SIF (left) and peak values at 684 nm (mid) and 740 nm (right).

The results shown in Fig. 5.36 and Fig. 5.40 indicate that SIF is retrieved with higher errors in those areas with a higher sub-pixel heterogeneity. The heterogeneity affects more the retrieved SIF at 684 nm and it is propagated to the total SIF. This is most probably due to the higher complexity of Spectral Fitting Method to reconstruct the reflectance spectrum in the red wavelength range and decouple the SIF spectral emission.

5.3 Summary

The generic E2ES architecture concept described in Chapter 3 and implemented in Chapter 4 for the FLEX mission was evaluated in this Chapter through the validation of the L1b and L2 results, demonstrating the suitability of the FLEX-E tool to do performance analysis of the mission concept and its algorithms. The flexibility of FLEX-E allowed to generate simulated data for three different sensors through a realistic radiative transfer and instrument modeling.

Based on the results shown in this Chapter, it was possible to demonstrate that FLEX fulfills its mission requirements by retrieving SIF with an error below the 0.2 $mW{\cdot}m^{-2}sr^{-1}nm^{-1}$ goal accuracy at peak values. In particular, the following conclusions are obtained with respect the accuracy of the L1b and L2 products:

- Both FLORIS-HR and -LR achieve the spectral requirements with an SSI of 0.1 nm (0. 65 nm) for FLORIS-HR (FLORIS-LR) at non-binned channels, and spectral resolution of 0.3 nm (2 nm) for FLORIS-HR (FLORIS-LR). The spectral co-registration was also achieved for FLORIS-HR with values below 0.015 nm. Finally, the accuracy of the spectral calibration is better than 0.08 nm and 0.35 nm for FLORIS-HR and -LR respectively.

- With respect to FLORIS-HR and -LR radiometric performance, the combination of the various instrument noises, systematic effects and calibration errors results in an average total mean error in the L1b TOA radiance that varies linearly between 1% at 500 nm and 3% at 780 nm, mainly due to the systematic ∼2% radiometric calibration error and the spectral radiometric error. The error has a small dependency on the input radiance, mostly caused by the detector and video-chain noises. The error spatial distribution was dominated by the systematic spatial radiometric noises (i.e., non-perfect correction of the vertical stripping) and the pixel-to-pixel error from the detector and video-chain noises. Whereas the former, being a systematic effect, can still be reduced through improved image processing algorithms at L1b or L2, the video-chain noises are a random effect that can only be reduced through a sensor that reduces the SNR. Thus, its effect can only be reduced at L2 by weighting less those spectral channels with lower SNR.

- The combination of all instrument noises and calibration errors results in a SNR that is more critical in the O_2-A spectral region. The most driving error contributor are the detector and video-chain noises, particularly photon noise. Notwithstanding, the obtained SNR matches the mission requirements.

- The radiometric calibration was achieved within the requirements with an absolute accuracy of 1.95% that was independent on the input radiance level. The relative accuracy is below 1% with maximum variations of ±0.4% in FLORIS-HR at the bottom of the O_2-A band.

- The instrument is affected by stray-light, causing an infilling of the O_2 bands. The stray-light effect is shown to be not-negligible even to distances higher than 30 ACT from bright objects, indicating that the spectral stray-light is dominating with respect to spatial stray-light. Whereas stray-light is not influencing strongly in the O_2-B region (SIF errors below 5%), the effect within the O_2-A region affects with errors in the retrieved SIF between 10% and 30%. This indicates that the stray-light effect should be reduced through two possibilities: **(1)** improved hardware and optics to reduce the stray-light effect below 0.02 $mW{\cdot}m^{-2}sr^{-1}nm^{-1}$ or; **(2)** implementation of a robust stray-light correction algorithm as part of the L1 data processing.

5.3 SUMMARY

- With respect to the geometric performance, FLORIS achieves a SSD of nearly 300 m and a geolocation error below 90 m, both within the mission requirements.

- When evaluating the accuracy of the retrieved SIF products, it was demonstrated that SIF was retrieved within the accuracy of 10% (for the total SIF) and 0.2 $\mathrm{mW{\cdot}m^{-2}sr^{-1}nm^{-1}}$ (for the SIF peaks). The atmospheric correction was a critical step in the processing particularly for the SIF retrieval at the first peak (684 nm), where it was shown that a wrong characterization of the phase function (relative error of $\sim$25% in the Henyey-Greenstein parameter) was deriving SIF errors of $\sim$0.25 $\mathrm{mW{\cdot}m^{-2}sr^{-1}nm^{-1}}$ at the first peak, slightly above the accuracy requirement of 0.2 $\mathrm{mW{\cdot}m^{-2}sr^{-1}nm^{-1}}$.

- The analysis on a realistic FLEX image indicated that the SIF retrieval might be performing with a lower accuracy on highly heterogeneous areas than in homogeneous pixels. The analysis done with FLEX-E with respect to the pixel heterogeneity showed indeed that the performance was underperforming in pixels with a 50% mix of vegetation and soil. This effect was particularly important for the first peak (684 nm) with a RMSE of 0.25 $\mathrm{mW{\cdot}m^{-2}sr^{-1}nm^{-1}}$, higher than the goal accuracy 0.2 $\mathrm{mW{\cdot}m^{-2}sr^{-1}nm^{-1}}$.

6

Summary and conclusions

Contents

6.1 Summary. Main results

As part of the development and performance assessment of EO satellite missions, E2ESs have been studied, developed and applied in the last decades. In the last years, ESA and other space agencies have relied on E2ES for the selection of future remote sensing missions and in preparation of ground data processing implementation. Within Chapter 3, this Thesis aimed to design a generic E2ES architecture that could easily be adapted to reproduce most present and near future passive optical spaceborne missions. Setting this generic architecture concept is important in the frame of EO science strategy for ESA and other national and international space agencies and organizations, facilitating the planning, development and analysis of new satellite missions. Then, the conceptual architecture was further elaborated in Chapter 4 for the specific implementation of ESA's FLEX/S3 tandem mission E2ES (FLEX-E), validating the conceptual generic E2ES architecture given that:

- ESA's request to develop an E2ES for the FLEX/S3 mission evaluation implied that the generic E2ES architecture concept would be demonstrated in a real case scenario for the ESA's 8th Earth Explorer mission selection process.

- FLEX/S3 is a multiplatform and multi-instrument mission in tandem flying formation and with product synergy at L2, which allowed testing the generic E2ES architecture concept in this complex scenario.
- FLEX mission instruments span several categories (i.e., multi-angularity, pushbroom and whiskbroom, VIS-TIR, spectral resolution, multi-camera), which allowed testing how the generic E2ES architecture coped with differences between them.

FLEX-E provides the capabilities to evaluate the mission performance and specifically determining the accuracy of the retrieved L2 SIF products. Within Chapter 5, the implemented software was used to assess the FLEX mission performance in terms of its main mission objective, i.e., "to provide robust estimates of the Sun-induced chlorophyll fluorescence emission at global scale". In particular, FLEX-E allowed checking the fulfillment of mission and system requirements with traceability to the MRD [213] and the SRD through the FLEX mission performance evaluation with respect to the accuracy of its L1b (i.e., geometric, spectral and radiometric characteristics) and L2 products (i.e., SIF retrieval).

6.1.1 Design of a generic E2ES for passive optical missions

1. *What are the main mission and instrument characteristics that should be modeled in an E2ES for EO passive optical missions?* In Chapter 3, a review of past, present and planned EO missions was carried out with the goal of extracting commonalities among them. These surveyed missions were classified in terms of the mission design and the technical aspects of the instruments onboard these missions. This classification was proposed considering those characteristics that have impact in the mission performance and thus, that should be included within a generic E2ES architecture.

With respect to the mission design classification, it was considered that EO missions could be categorized based on the number of satellites and possibility of formation flying. This would have implications on the modelization of multiple satellite orbit types and instrument observation geometries, which should model the data acquisition over a common target scene. In addition, the number of instruments within the mission and the possibility of performing synergy between their products had an implication with respect to the modelization of these multiple instrument data processing chains and the synergy between them. EO missions were also classified regarding their mission goal and application, which had a direct impact on the modelization of the signal acquired by the instrument(s). This last point indicated that a generic E2ES should allow including specific radiative transfer models (e.g., vegetation, water, urban) and datasets (e.g., global DEM, land cover maps, meteorological variables, reflectance databases).

With respect to passive optical instruments, they were analyzed following classification criteria such as geometric aspects, spectral and spatial characteristics and other instrument technical issues. All these aspects should be considered at different levels in the E2ES simulation chain, from those that involve simulating temporal and geometric aspects of data acquisition to those aspects that imply the use of a specific radiative transfer.

2. *What are the common elements that are required to develop a generic E2ES architecture for EO passive optical instruments?* Based on the analysis of instrument categories and the number of instruments, the combination of six high-level modules in three possible E2ES architecture variations are sufficient to develop most single-platform EO missions, both single-instrument or multi-instrument with or without products synergy at L2. From an architectural point of view, the most simple case is a single-platform with one instrument as it contains one of each high-level modules with a sequential dataflow from Geometry to L2 retrieval. For multi-instrument missions, a single geometry module generates the observation geometry for each instrument within the platform. In case of synergy at L2, a multi-instrument mission will have a common scene generator module that generates the input scenes to the various instrument processing chains. Also, a common L2 retrieval module will ingest the L1 data from the various instruments to retrieve the final L2 products. This architecture is different for multi-instrument missions with no synergy between their products. In this case, as the various instruments observe different targets, there will be as many scene generator modules as instruments in the platform, generating the scenes that are acquired and processed to L1 and L2 in several parallel chains.

Multi-platform missions (e.g., constellations, tandem missions) can also be reproduced with these architectures considering two possibilities: **(1)** a geometry module generates the geometry of both platforms and instruments; **(2)** the architectures above are applied for the various platforms using common scene generator and Level-2 modules in case of data synergy.

After proposing the high-level E2ES architecture, each high-level module was further described in terms of their internal architecture based on common building blocks as a suitable solution to reproduce most passive optical instrument mission. Each building block can then be adapted to different instrument categories by implementing specific algorithms that account for specific characteristics of each instrument and mission.

6.1.2 Implementation of FLEX/S3 E2ES based on a generic architecture

3. *How should be implemented a specific E2ES for ESA's FLEX/S3 tandem mission based on a generic E2ES architecture concept?* The selection of FLEX as the future ESA's 8th Earth Explorer mission has been based on a competitive process for which the overall mission performance assessment mostly relied on the results provided by FLEX-E. This E2ES software tool integrates various aspects that affected FLEX mission performance such as instrument design, complexity of environmental effects or implementation of full data processing algorithms. In addition, the design of the FLEX-E software was constrained by a set of guidelines in order to facilitate the comparison between results produced by the E2ES of different missions in the competitive selection process.

The implementation of FLEX-E based on the generic E2ES architecture developed in Chapter 3 was presented in Chapter 4. The generic E2ES architecture concept was adapted to reproduce the FLEX/S3 tandem mission through the implementation of specific solutions:

- The tandem flight between FLEX and Sentinel-3 was simulated by incorporating externally computed FLEX and S3 orbits. The common scene grid definition ensures that each instrument acquires data over the same target at their corresponding acquisition times and specific observation geometries.
- The SCOPE (canopy) and MODTRAN5 (atmosphere) models were implemented in order to simulate high-spectral resolution scenes in the VIS to TIR spectral range that includes fluorescence emission from vegetation. The 3D modeling of the scene generated intrinsically different scenes for each instrument by considering their specific observation geometry, particularly important for the dual view of SLSTR.
- Given that S3 is an external "secondary" mission supporting FLEX, the simulation of S3 passive optical instruments and their L1b data processing was performed on a single custom-made module that models the most relevant characteristics of OLCI and SLSTR in terms of the final performance.

The example of FLEX-E showed that the proposed generic E2ES architecture concept and methodology could be applied to a complex EO mission and thus, it could serve as baseline for next-generation passive optical satellite mission simulators. The implemented software allows users to simulate a wide range of possible scenarios with physically consistent environmental conditions and complex sensor description. The main premise in the design and implementation of FLEX-E was its capability to reproduce the complexity of the FLEX mission so that FLEX-E serves to evaluate the performance of the FLEX L2 products. At the same time, FLEX-E was also designed with the purpose of being re-used for the implementation of FLEX ground data processing and testing of Cal/Val procedures.

6.1.3 Level-1 performance of ESA's FLEX/Sentinel-3 mission

4. *What is the accuracy of the FLEX L1b mission products in terms of spectral, geometric and radiometric performance?* The following results are obtained with respect to the accuracy of FLEX L1b products:

- FLORIS-HR (-LR) achieve the spectral requirements with a SSI of 0.1 nm (0.65 nm) at non-binned channels, a spectral resolution of 0.3 nm (2 nm) and an accuracy of the spectral calibration higher than 0.08 nm (0.35 nm). Also, the FLORIS-HR spectral co-registration was achieved with values below 0.015 nm.
- With respect to FLORIS-HR and -LR radiometric performance, the combination of the various instrument noises, systematic effects and calibration errors results in an average error in the L1b TOA radiance that varies linearly between 1% at 500 nm and 3% at 780 nm, mainly due to the systematic $\sim$2% radiometric calibration error and the spectral radiometric error. The error has a small dependency on the input radiance, mostly caused by the detector and video-chain noises. The error spatial distribution was dominated by

the systematic spatial radiometric noises and the pixel-to-pixel error from the detector and video-chain noises. Whereas the former, being a systematic effect, can still be reduced through improved image processing algorithms at L1b or L2, the video-chain noises are a random effect that cannot be reduced unless the instrument implements improved electronics or detector. Thus, its effect can only be reduced at L2 by giving lower weight to those spectral channels with lower SNR.

- The combination of all instrument noises and calibration errors results in a SNR that is more critical in the O_2-A spectral region. The most driving error contributor are the detector and video-chain noises, particularly photon noise. Notwithstanding, the obtained SNR matches the mission requirements.

- The radiometric calibration was achieved within the requirements with an absolute accuracy of 1.95% independently on the input radiance level. The relative accuracy is below 1% with maximum variations of ±0.4% in FLORIS-HR at the bottom of the O_2-A band.

- The stray-light effect causes an infilling of the O_2 bands whose impact is shown not to be negligible even to distances higher than 30 ACT from bright objects. This indicates that the spectral stray-light dominates over the spatial stray-light. Whereas stray-light is not strongly influencing in the O_2-B region (SIF errors below 5%), the effect within the O_2-A region causes errors in the retrieved SIF between 10% and 30%. Therefore, a stray-light correction algorithm should be implemented at L1b or L2.

- With respect to the geometric performance, FLORIS achieves a SSD of nearly 300 m and a geolocation accuracy below 90 m, both within the mission requirements.

6.1.4 Level-2 performance of ESA's FLEX/Sentinel-3 mission

5. *What is the impact of the current FLEX instrument design and implemented data processing algorithms to retrieve Sun-induced fluorescence?* Overall, the results shown in Chapter 5 demonstrate that the FLEX mission design and its instrument fulfills the mission requirements by retrieving SIF with an error below the goal accuracy. In particular,

- When evaluating the accuracy of the retrieved SIF products, it was demonstrated that SIF was retrieved with an error below 10% (for the total SIF) and 0.2 $\text{mW}\cdot\text{m}^{-2}\text{sr}^{-1}\text{nm}^{-1}$ (for the SIF peaks).

- The atmospheric correction was a critical step in the processing particularly for the SIF retrieval at the O_2-B band, where it was shown that a wrong characterization of the phase function (relative error of ∼25% in the Henyey-Greenstein parameter) was deriving SIF errors of ∼0.25 $\text{mW}\cdot\text{m}^{-2}\text{sr}^{-1}\text{nm}^{-1}$ at the first peak.

- The analysis on a realistic FLEX image indicated that the SIF retrieval might be performing with a lower accuracy on highly heterogeneous areas than in homogeneous pixels. The analysis done with FLEX-E with respect to the pixel heterogeneity showed indeed that the performance was lower in pixels with a 50% mix of vegetation and soil. This effect was particularly important for the first peak (684 nm) with a RMSE of 0.25 $\text{mW}\cdot\text{m}^{-2}\text{sr}^{-1}\text{nm}^{-1}$, higher than the goal accuracy 0.2 $\text{mW}\cdot\text{m}^{-2}\text{sr}^{-1}\text{nm}^{-1}$.

6.2 General conclusions

This Thesis proposed, after a review and classification of EO passive optical missions, a generic design for the architecture of an E2ES that can be applicable for most of these missions. In view of an E2ES architecture and impact in mission performance, missions were firstly classified in terms of the number of satellites (with possibility of flying formation), number of instruments (and synergy between them), orbit types and mission goal and application. This classification allowed setting a few variations of a generic E2ES architecture in order to cover these characteristics. Secondly, passive optical instruments were analyzed regarding their geometric, spectral and spatial characteristics as well as sensor/instrument technology. Despite the large variety of instruments, they can all be simulated with a common generic E2ES architecture broken down in high-level modules and lower-level building blocks. The instrument specificities affect to the implemented algorithms and models within each module as well as minor variations of the generic interfaces between modules. It was therefore concluded that the proposed generic architecture is suitable to reproduce most EO passive optical missions.

The conceptual generic E2ES architecture was then validated through its implementation, with a few variations, on ESA's FLEX/S3 tandem mission, showing its suitability for the modelization of the FLEX mission. The FLEX-E tool was used to evaluate the accuracy of the mission L1b products with traceability to the mission requirements, showing that FLEX accomplish the main spectral, geometric and radiometric mission requirements. In addition, FLEX-E was used to analyze the performance of FLEX mission to retrieve SIF, showing that SIF is retrieved with an accuracy below 0.2 $\text{mW}\cdot\text{m}^{-2}\text{sr}^{-1}\text{nm}^{-1}$ at peaks. The accuracy is degraded for highly heterogeneous pixels, particularly for SIF at 685 nm. The atmospheric correction was shown to be well performing though the results analysis indicated that the first SIF peak was sensitive to errors in the characterization of aerosol phase function given the higher scattering in red wavelengths than in infrared spectral wavelengths. It was therefore demonstrated that the generic E2ES architecture and its implementation into the FLEX-E software was useful for assessing the mission performance at Phase A/B1 both for L1b products (geometry, radiometry and spectral) and L2 products (atmospheric correction and SIF retrieval). In addition, it is considered that FLEX-E design is flexible enough for its evolution into the future FLEX Phase C/D simulator, GPP and Ground Segment.

While FLEX-E was developed specifically for the FLEX mission, it was designed based on the generic E2ES architecture concept developed in this Thesis and thus, eventually re-adaptable to other EO passive optical missions. The methodology implemented in this Thesis can be used to develop next-generation satellite mission simulators. Particularly, the following conclusions are derieved for the implementation of a generic E2ES for passive optical missions based on the lessons learned from the implementation of FLEX-E:

- The implementation of a generic geometry module should be based on the concepts introduced in Chapter 3 using standard satellite geometry libraries such as ESA's EOCFI. The geometry module should simulate the LOS for whiskbroom, pushbroom and frame instruments, and their output file format should consider the acquisition time for each pixel, line and frame respectively. The sequential acquisition of different spectral channels (e.g. using various cameras or in field separation (focal plane)) should be also included in a generic Geometry module.
- The interfaces between modules should be fully generic, particularly for the interfaces between Geometry and Scene Generator modules and between this and the instrument modules. By considering the specific instrument types (e.g., hyperspectral/multispectral) and the variability of instrument geometric conditions, the SGM can be adapted to accommodate these characteristics, making it more generic.
- The implemented SGM simulates scenes based on thematic LCC maps where two main surface types are defined (see Annex B.2 for further description) *surface reflectance database classes* and *RTM classes*. The SGM can therefore extend its capabilities to incorporate any user-input RTM associated to specific classes. The key bio-geophysical parameter databases should then also be extended to incorporate additional key parameters as input variables to the user-input RTM and (reflectance/emissivity) spectral databases. It is considered that a fully generic SGM should have access to additional global and multitemporal maps of meteorological variables, DEM, land cover and bio-geophysical variables. The link between the SGM and databases (e.g., ESA's CCI, ECMWF, Aeronet, Google Earth Engine) could be implemented via an online *file transfer protocol* reducing the amount of stored data in a local computer.
- The detailed simulation of instrument characteristics strongly depends on the implemented industrial instrument concept. For Phase A/B studies, a parametric instrument model with simplified but still realistic equations can describe the main characteristics and behavior of a large variability of passive optical instruments and sensors of different types. A detailed bibliography research should be carried out in view of implementing these parametric equations into a generic instrument module.

6.3 Outlook

With the selection of FLEX as the future ESA's 8th Earth Explorer mission, the mission will evolve from the preliminary design and baseline technical solution stages (Phase A/B1) into Phase C/D, which involves actual manufacturing of instrument, platform and ground segment. In this context, the current version of FLEX-E will evolve into the Phase C/D FLEX simulator and GPP and, eventually, the Ground Segment. Therefore, several additional capabilities should be included in the current FLEX-E version for its evolution into Phase C/D to support the implementation of the enhanced FLORIS instrument simulator, L1 and L2 prototype processors.

With respect to the SGM, the current FLEX-E version is limited to the use of the SCOPE leaf-canopy RTM for the simulation of bi-directional reflectance and SIF emission. After the selection of the FLEX mission as the future 8th Earth Explorer, the scientific community proposed that FLEX might eventually be also useful to determine the SIF emission from the phytoplankton. In order to analyse FLEX feasibility to retrieve SIF over coastal and inland waters, the future version of the SGM will incorporate the HydroLight RTM for the simulation of water-leaving radiances. The incorporation of this water RTM will also help engineers to understand the impacts in the instrument configuration (e.g., spectral/spatial binning, different FLORIS operation modes in land and water).

Also, the SGM has not incorporated the radiative transfer equations for the light propagation through the atmosphere in the TIR spectral range. This is due to the fact that the thermal information is retrieved by the implemented operational algorithms from SLSTR/Sentinel-3 data, particularly SLSTR thermal spectral channels. Through the capabilities offered by MODTRAN, the future version of the SGM will incorporate the equations in Annex B.3 for the simulation of thermal radiances. This will imply that current atmospheric LUTs should be extended to cover the TIR spectral range. In addition, the SGM will associate to each scene grid element a surface emissivity spectra from an external database similar to what is currently done with the *surface reflectance database classes*.

Foreseeing the possibility to perform data assimilation and analysis of temporal series of retrieved FLEX L2 data, the enhanced SGM could incorporate temporal dynamics of key biophysical parameters used in the RTM. This would imply to adapt the *surface definition database* in Tab. B.3 (Annex B.2) to consider a specific temporal evolution of the statistical distribution parameters (e.g., mean and standard deviation values) at each LCC. These temporal dynamics could be obtained from time series of external satellite data (e.g., [214]) or from the implementation of phenology models (e.g. [215]). Temporal dynamics do not affect just the synthetic scene but also the FLEX platform and instrument properties. While typical AOCS error (temporal) profiles are already included in the simulator, the FLORIS instrument simulator should include the effect of temporal stability of the detectors as it affects to the spectral calibration whose errors might be propagated to the retrieved SIF. This also implies that the SGM should be capable of simulating a scene consisting of a full FLEX orbit or several succesive orbits.

The analysis of the impact of stray-light in the retrieved SIF showed that this systematic instrument noise was largely propagated into the final L2 products. A robust stray-light correction algorithm will be incorporated as part of the L1 data processing and eventually at L2.

The Copernicus' S3 satellite was launched in February 2016 and it is currently in the commissioning Phase E1 that will last approximately 5 months after which the exploitation Phase E2 will start releasing data to user communities. The S3 modules were developed with a data file format specific for its use within the FLEX-E tool. In order to evolve towards a FLEX

GPP and its future Ground Segment, the interfaces between the S3 Geometry, SGM, S3 Instrument and L2R modules will be adapted in FLEX-E to use the format as used in the S3 payload data Ground Segment. This will allow us to generate synthetic scenes for S3 while at the same time adapt the Level-2 algorithms (e.g., atmospheric correction, FLORIS/OLCI/SLSTR co-registration, FLORIS/OLCI cross-calibration) to use real OLCI and SLSTR data.

Finally, the use of high-level languages like MATLAB to develop the FLEX-E modules have unavoidable performance limitations. Recoding them in languages like C shall be done in future project phases. This is of paramount importance in view of its impact on the operational ground segment, particularly for L1 and L2 processing prototypes.

7

Relevance

The results generated during this Thesis contributed to the successful selection of ESA's FLEX mission as the future 8th Earth Explorer, in particular, as part of the following list of documents and presentations:

- Chapter 7: Performance Estimation, (2015). In: ESA. *Report for Mission Selection: FLEX*, pp.129-135 & pp.150-158. ESA SP-1330/2 (2 volume series), European Space Agency, Noordwijk, The Netherlands
- ESA's 8th Earth Explorer – User Consultation Meeting (Scientific presentation II – scientific performance).

The lessons learned from the design and implementation of the FLEX-E tool are serving as baseline for the implementation of the future FLEX GPP and Ground Segment through the future ESA's project FLEX L2 End-to-End Mission Performance Assessment.

In addition, these results have also been presented at several conferences and published as research papers on different international journals. The following list summarizes the published journal and conference papers directly related to this Thesis:

International journal papers:

1. **J. Vicent**, N. Sabater, C. Tenjo, J. R. Acarreta, M. Manzano, J.P. Rivera, P. Jurado, R. Franco, L. Alonso, J. Verrelst, J. Moreno, (2016). FLEX End-to-End Mission Performance Simulator. *IEEE Transactions on Geoscience and Remote Sensing*, Vol. 54, No. 7, pp. 4215-4223

2. N. Sabater, **J. Vicent**, L. Alonso, J. Verrelst, J. Moreno, (2016). An atmospheric correction algorithm for FLEX/S3 tandem mission. (Submitted)

3. S. Cogliati, W. Verhoef, S. Kraft, N. Sabater, L. Alonso, **J. Vicent**, J. Moreno, M. Drusch, R. Colombo, (2015). Retrieval of sun-induced fluorescence using advanced spectral fitting methods. *Remote Sensing of Environment*, 169, pp. 344-357.

4. C. Tenjo, J.P. Rivera, N. Sabater, **J. Vicent**, L. Alonso, J. Verrelst, J. Moreno, (2016). Design of a Generic 3D Scene Generator for Passive Optical Missions and its Implementation for ESA's FLEX/Sentinel-3 Tandem Mission. *IEEE Transactions on Geoscience and Remote Sensing*, (In preparation).

Conference contributions:

1. **J. Vicent**, L. Alonso, N. Sabater, C. Miesch, S. Kraft, J. Moreno, (2015). Propagation of spectral characterization errors of imaging spectrometers at Level-1 and its correction within a Level-2 recalibration sceheme. In: SPIE Optics+Photonics 2016, August, San Diego (CA), USA.

2. **J. Vicent**, N. Sabater, C. Tenjo, J.R. Acarreta, M. Manzano, J.P. Rivera, P. Jurado, R. Franco, L. Alonso, J. Moreno, (2015). Design of a satellite end-to-end mission performance simulator for imaging spectrometers and its application to the ESA's FLEX/Sentinel-3 tandem mission. In: SPIE Optics+Photonics 2016, August, San Diego (CA), USA.

3. **J. Vicent**, N. Sabater, C. Tenjo, A. Ruiz-Verdú, J. Delegido, R. Peña-Martínez, J. Moreno, (2015). HICO L1 and L2 data processing: radiometric recalibration, atmospheric correction and retrieval of water quality parameters. In: International Geoscience and Remote Sensing Symposium (IGARSS) 2015, 26-31 July, Milan, Italy.

4. C. Tenjo, **J. Vicent**, N. Sabater, J.P. Rivera, L Alonso., J. Verrelst, J. Moreno, (2015). Hyperspectral synthetic scene simulator for for the assessment of fluorescence retrieval with ESA's FLEX/Sentinel-3 tandem mission. In: 9th EARSeL SIG Imaging Spectroscopy Workshop 2015, 14-16 April, Luxembourg, Luxembourg.

5. J.P. Rivera, N. Sabater, C. Tenjo, **J. Vicent**, L. Alonso, J. Moreno, (2014). Synthetic scene simulator for hyperspectral spaceborne passive optical sensors. Application to ESA's FLEX/Sentinel-3 tandem mission. In: 6th workshop on hyperspectral image and signal processing 2014, 24-27 June, Lausanne, Switzerland.

6. **J. Vicent**, J.R. Acarreta, R. Franco, M. Manzano, J.P. Rivera, N. Sabater, C. Tenjo, J. Verrelst, J. Moreno, (2014). FLEX-E: ESA's FLEX End-to-End Mission Performance Simulator. Architecture design, current status and preliminary results. In: 5th Int. Workshop on Remote Sensing of Vegetation Fluorescence 2014, 22-24 April, Paris, France.

7. N. Sabater, J.P. Rivera, C. Tenjo, **J. Vicent**, L. Alonso, J. Verrelst, J. Moreno, (2014). The scientific modules of FLEX End-to-End simulator: the Scene Generator Module and

the Level-2 Retrieval Module. In: 5th Int. Workshop on Remote Sensing of Vegetation Fluorescence 2014, 22-24 April, Paris, France.

8. J. Moreno, L. Alonso, J. Delegido, J.P. Rivera, N. Sabater, C. Tenjo, J. Verrelst, **J. Vicent**, (2013). Misión FLEX (Fluorescence Explorer): observación de la fluorescencia por teledetección como nueva técnica de estudio del estado de la vegetación terrestre a escala global. In: XV Congreso de la Asociación Española de Teledetección (AET) 2013, 22-24 October, Madrid, Spain.

9. **J. Vicent**, U. del Bello, M. Drusch, R. Franco, S. Kraft, J.R. Acarreta, L. Alonso, C. de Negueruela, J.P. Rivera, N. Sabater, C. Tenjo, J. Moreno (2013). End-to-End Mission Performance Simulators for Earth Observation convoy missions: Application to FLEX/Sentinel-3 mission. In: 1st Int. Earth Observation Convoy and Constellation Concepts Workshop 2013, 09-11 October, Noordwijk, The Netherlands.

10. **J. Vicent**, N. Sabater, L. Alonso, J. Verrelst, J.P. Rivera, C. Tenjo, J. Moreno (2013). FLEX End-to-End Mission Performance Simulator Architecture Design using a Generic Reference Architecture for EO Missions. In: ESA Living Planet Symposium 2013, 09-13 September, Edinburgh, UK.

11. J. Delegido, S. Van Wittenberghe, J. Verrelst, L. Alonso, J.P. Rivera, J. Sabater, **J. Vicent**, V. Ortiz, J. Moreno (2012). Chlorophyll fluorescence: the signal hidden behind leaf reflectance. A new technique for the study of plant status by remote sensing. In: XV symposium of SELPER. 2012, 19-23 November, Cayenne, French Guyana.

12. C. de Negueruela, M. Scagliola, D. Guidici, J. Moreno, **J. Vicent**, A. Camps, H. Park, P. Flamant, R. Franco, (2012). ARCHEO-E2E: A Reference Architecture for Earth Observaion End-to-End Mission Performance Simulators. In: SESP, Simulation and EGSE facilities 2012, 25-27 September, Noordwijk, The Netherlands.

The outcome of this work was relevant for the research carried out by the author in the context of various research projects in which he was involved. A list of these related projects is provided:

- FLEX End-to-End Mission Performance Simulator, ESA-ESTEC Contract No. 4000108364/13/NL/BJ [2013-2015].
- FLEX - Performance Analysis and Requirements Consolidation Study (PARCS), ESA-ESTEC Contract No. 4000105078/11/NL/AF [2012-2014].
- Reference Architecture for Earth Observation End-to-End Mission Performance Simulators (ARCHEO-E2E), ESA-ESTEC Contract No. 4000104547/11/NL/AF [2012]

8

Resumen en Español

8.1 Introducción

La Observación de la Tierra por teledetección mediante satélite es un campo interdisciplinario de la Ciencia y Tecnología que tiene como objetivo monitorizar los procesos bio-geofísicos que ocurren en la superficie y atmósfera terrestres usando una amplia gama de sensores remotos tanto activos como pasivos, cubriendo todo el rango del espectro electromagnético. Mediante la utilización de instrumentación en satélites, una gran variedad de procesos terrestres pueden ser estudiados con una cobertura global y continuidad temporal, lo cual permite a científicos y responsables políticos tener un amplio conocimiento de los cambios en el medioambiente, produciendo grandes avances científicos y beneficios para la sociedad. Algunos ejemplos de productos ofrecidos por la teledetección satelital y sus aplicaciones son, entre muchos otros, la caracterización de la composición atmosférica, cambios en la cubierta terrestre, estimación de parámetros biofísicos para la evaluación en la calidad de aguas y vegetación. Por tanto, la Observación de la Tierra por satélite ha evidenciado el significante impacto de la actividad humana en cambio climático y medioambiental.

En este contexto, y teniendo en cuenta la madurez de la tecnología espacial y los recientes avances en el procesado de datos, varias agencias espaciales nacionales e internacionales así como institutos de investigación están desarrollando su propia estrategia científica para la Observación de la Tierra con el fin de diseñar detalladamente nuevas y complementarias misiones satelitales que aseguren una continuidad en las observaciones de los procesos bio-geofísicos y con la capacidad de llenar los vacíos en nuestro actual conocimiento del sistema Tierra. La Agencia Espacial Europea (ESA) está desarrollando las misiones Sentinel, Earth Watch y los Earth Explorers dentro del marco ‘Copernicus’ y el programa ‘Living Planet’, con el objetivo de proporcionar un monitoreo continuo de la Tierra, previsión meteorológica y promover el avance científico en la Observación de la Tierra por teledetección. Estas misiones están siendo desarrolladas mediante el trabajo conjunto de científicos e ingenieros en “fases” sucesivas que van desde el diseño conceptual hasta las operaciones con satélites. Las primeras fases consisten en el análisis del rendimiento de la misión; consolidación de sus requisitos técnicos; y testeo y optimización de los algoritmos de procesado de datos. Por tanto, son necesarias nuevas herramientas de ingeniería con el fin de entender el impacto de la configuración del instrumento en los productos finales y así acelerar el desarrollo de la misión entre las fases de concepto y lanzamiento. Al mismo tiempo, estas herramientas económicas y flexibles deberían servir para definir una metodología para la consolidación de requisitos y la evaluación del rendimiento de estas nuevas misiones satelitales, proporcionando un criterio de selección de misiones por las juntas de evaluación de las diferentes agencias espaciales.

Durante las últimas décadas, los simuladores de misión (E2ES) han sido estudiados y desarrollados tanto en misiones satelitales específicas como en conceptos genéricos. Estas herramientas, basadas en recientes avances en ciencias computacionales y modelos de transferencia radiativa, simulan de forma realista el concepto de misión propuesto, las condiciones ambientales y los algoritmos de procesado de datos. Por tanto, ofrecen un marco único con el que determinar aquellas características de la misión que tienen mayor impacto en la calidad de los datos y la consecución de los objetivos científicos, permitiendo consolidar los requisitos de la misión y comprobar la consistencia entre las especificaciones técnicas de la plataforma e instrumento. Los E2ES sirven para realizar estudios de trade-off y son útiles en la preparación de pruebas para los sistemas de calibración. Desde la perspectiva del procesado de imágenes, los E2ES permiten probar y optimizar los esquemas de procesado antes de la operación de la misión [8, 9]. A pesar de que el concepto de un E2ES es sencillo, su implementación en cada nueva misión satelital conlleva un esfuerzo importante que requiere complejas y costosas actividades de re-ingeniería. Por un lado, los esfuerzos hechos en el desarrollo de conceptos genéricos para los E2ES han tenido una aplicabilidad limitada en los E2ES para misiones específicas debido a **(1)** las aproximaciones realizadas en los algoritmos, simulaciones de los procesos de transferencia radiativa e instrumento y **(2)** el alcance limitado en la simulación de escenarios y tipos de instrumentos. Por otro lado, algunas misiones satelitales han implementado sus propios E2ES que son dificilmente adaptables a nuevas misiones espaciales. Por estas razones, es necesario desarrollar un concepto de un E2ES genérico que sea a la vez riguroso y avanzado de forma que pueda ser aplicado a la mayoría de misiones satelitales para la teledetección. El uso de una arquitectura común para un E2E permitiría comparar misiones en un proceso de selección competitivo (p.ej., los Earth Explorer de la ESA), acelerando el análisis de los requisitos técnicos de la misión y, por lo general, las primeras fases de diseño y desarrollo.

8.2 Objetivo y metodología

Esta Tesis investigará un problema recurrente en el diseño de misiones satelitales para teledetección, donde cada nueva misión de Observación de la Tierra tiene que desarrollar su propio

E2ES, lo cual implica un costoso y complejo problema de ingeniería. Por un lado, este problema se abordará mediante una revisión de los simuladores E2ES desarrollados en las pasadas décadas con el objetivo de estudiar los elementos comunes implementados y analizar si las soluciones adoptadas pueden ser extendidas a cualquier misión óptica pasiva en sus primeras fases de desarrollo. Por otro lado, las misiones para la Observación de la Tierra, pasadas, presentes y futuras, serán categorizadas con el fin de extraer los elementos comunes que afectan al rendimiento de una misión satelital. La metodología adoptada en esta Tesis considera ambos enfoques con el fin de diseñar una arquitectura genérica para los E2ES de misiones ópticas pasivas que pueda ser adaptado a misiones satelitales con diferentes aplicaciones, tipos de instrumento y diseño. En segundo lugar, y con el fin de validar la propuesta de un E2ES genérico, la herramienta será desarrollada para una misión satelital real, la misión FLEX/Sentinel-3 de la ESA, y será sometida a prueba a través del análisis del rendimiento de los productos de la misión FLEX. Este enfoque proporcionará dos resultados principales: **(1)** se definirá una arquitectura genérica para los E2ES de misiones ópticas pasivas con la posibilidad de ser implementado en una amplia variedad de nuevas misiones de teledetección; y **(2)** mediante la implementación de esta arquitectura genérica para el caso de la misión FLEX/Sentinel-3, el rendimiento de esta misión será analizado, proporcionando conclusiones respecto a la precisión de los productos de la misión FLEX.

Por tanto, esta tesis tiene como objetivo apoyar el desarrollo científico y tecnológico en el campo de los simuladores E2ES para misiones de Observación de la Tierra, particularmente con instrumentos ópticos pasivos. Dos puntos principales motivan el diseño y desarrollo de una arquitectura genérica para los E2ES. Por un lado, el diseño de esta arquitectura genérica permitiría acelerar el desarrollo conceptual de nuevas misiones satelitales a través de la consolidación de sus requisitos técnicos, evaluación de trade-offs y desarollo de algoritmos para el procesado de datos. Por otro lado, el uso de una arquitectura genérica para varias misiones satelitales permitiría comparar sus rendimientos y determinar si se cumplen los requisitos respecto a la precisión de sus productos a la vez que maximice las medidas en sinergia entre estas misiones satelitales.

La Tesis en resumen

- **¿Cuales son losl principale objetivos? (1)** Diseñar una arquitectura genérica para los simuladores E2ES que pueda ser fácilmente adaptada para reproducir la mayoría de misiones satelitales, presentes y futuras, con instrumentos ópticos pasivos, y **(2)** apoyar la misión FLEX para la obtención de la fluorescencia inducida por el la luz solar usando un E2ES desarrollado específicamente de acuerdo al concepto de arquitectura genérica.

- **¿Por qué el tema es importante?** Diseñar una arquitectura genérica para los simuladores E2ES en misiones de teledetección con instrumentos ópticos pasivos es importante en el marco de la estrategia científica de la ESA para la Observación de la Tierra y otras agencias espaciales y organizaciones nacionales e internacionales. Proporcionar esta herramienta podría tener un impacto positivo en la planificación, desarrollo y análisis de nuevas misiones satelitales. Esto ofrecerá un marco donde se puedan implementar nuevos algoritmos de procesado de datos. El objetivo de esta Tesis también es importante en el campo de la ciencia y tecnología para la Observación de la Tierra puesto que requiere extraer los elementos comunes de una amplia gama de misiones con sensores remotos ópticos pasivos y aplicaciones, a la vez que el E2ES diseñado sea aplicable a misiones satelitales específicas tales como la aquí considerada (FLEX/Sentinel-3).
- **¿Como se enfoca el tratamiento del tema investigado?** En primer lugar se realizará una revisión y categorización de misiones espaciales (pasadas, presentes y futuras) con instrumentos ópticos pasivos para determinar las principales características que tienen un impacto directo en el rendimiento de una misión así como identificar los elementos requeridos para desarrollar una arquitectura genérica para un simulador E2ES. El diseño conceptual de la arquitectura para el E2ES genérico será posteriormente implementado para el caso específico de la misión FLEX/Sentinel-3 de la ESA, el cual será utilizado para analizar el rendimiento de la misión FLEX en términos de la precisión de sus productos, mostrando la idoneidad de este concepto genérico para los simuladores E2ES en un escenario realista.

Esta Tesis contribuye al avance en el campo de los simuladores E2ES en relación al diseño y desarrollo de una herramienta robusta que pueda ser implementada en una amplia variedad de misiones ópticas pasivas. La implementación de estos avances en un software operacional permitiría evaluar el rendimiento de cualquier misión óptica pasiva como es el caso de la misión FLEX/Sentinel-3. Los principale objetivos son, por tanto: **(1)** *’Diseñar un E2ES genérico que pueda ser fácilmente adaptado para reproducir la mayoría de misiones satelitales ópticas pasivas presentes y futuras’* y **(2)** *‘apoyar la misión FLEX para la obtención de la fluorescencia inducida por el la luz solar usando un E2ES desarrollado específicamente de acuerdo al concepto de arquitectura genérica’*. Estos objetivos serán guiado mediante las siguientes preguntas científicas:

1. *¿Cuáles son las principales características de los instrumentos y misiones espaciales que deberían ser tenidos en cuenta para su modelización dentro de un simulador E2ES para misiones ópticas pasivas?* Una gran variedad de misiones de Observación de la Tierra con instrumentos ópticos pasivos se han lanzado en las últimas décadas. Estas misiones tienen aplicaciones científicas tales como el estudio de océanos, atmósfera, superficie terrestre o cobertura de hielo/nieve, a través del uso combinado de datos adquiridos por uno o más instrumentos. Estos instrumentos adquieren la señal electromagnética en partes

específicas del espectro óptico (desde el ultravioleta hasta el infrarrojo térmico) con una gran variedad de tipos de instrumentos que usan diferentes tecnologías, mecanismos de apuntamiento y ópticas. El problema es por tanto identificar entre esta gran variedad de instrumentos y misiones satelitales, cuáles son las principales características que tienen un impacto en el rendimiento de misiones satelitales en teledetección.

2. *¿Cuáles son los elementos comunes que se necesitan desarrollar en una arquitectura genérica para un simulador E2ES en misiones ópticas pasivas para la Observación de la Tierra?* Como se verá, proponer una arquitectura genérica para un simulador E2ES en misiones ópticas pasivas para la Observación de la Tierra requiere identificar los elementos básicos que conforman esta arquitectura. Varias arquitecturas serán propuestas para un amplio rango de misiones satelitales. Además, cada elemento básico común será definido de forma que pueda llevar a cabo la simulación de diferentes tipos de instrumentos y aplicaciones científicas y a la vez sea aplicable con la misma arquitectura genérica.

3. *¿Cómo debería implementarse un E2ES específico para la misión FLEX/Sentinel-3 de la ESA basado en el concepto de una arquitectura genérica para un simulador E2ES?* Como parte del proceso de selección de la octava misión Earth Explorer de la ESA, un simulador E2ES para la misión FLEX/Sentinel-3 debía ser implementado para evaluar el rendimiento de la misión y ayudar a la consolidación de los requisitos técnicos. Esta pregunta se centra en analizar si la propuesta del simulador E2ES genérico puede tomarse como base para la implementación del E2ES de FLEX. Responder a esta pregunta implica validar la arquitectura del simulador E2ES genérico como un concepto que puede ser aplicado a otras misiones ópticas pasivas en teledetección.

4. *¿Cuál es la precisión de los productos de Nivel-1b en la misión FLEX en términos de su rendimiento espectral, geométrico y radiométrico?* La evaluación del rendimiento de cualquier misión satelital debe hacerse en función de la precisión de sus principales productos de misión. Los productos de Nivel-1b (es decir, los datos instrumentales geolocalizados y radiométricamente calibrados) están directamente relacionados con la precisión en la determinación de la órbita y actitud del satélite, el rendimiento de la óptica y sensor en el instrumento, la calibración del instrumento y el procesado de los datos para la corrección de errores sistemáticos en el instrumento. Esta pregunta se centra en evaluar la precisión de estos productos de Nivel-1b para los instrumentos de la misión FLEX.

5. *¿Cuál es el impacto del diseño actual del instrumento de FLEX y los algoritmos de procesado de datos para la obtención de los productos de Nivel-2 de la misión FLEX?* Desde el punto de vista de un usuario final, el rendimiento de una misión satelital es, en esencia, evaluado por la calidad de sus productos de Nivel-2 es decir, los parámetros biogeofísicos objetivo de la misión. Esta pregunta evaluará la precisión de la fluorescencia emitida por la vegetación obtenida a partir del procesado de los datos obtenidos por la misión FLEX/Sentinel-3.

8.3 Estructura

Esta Tesis se organiza en seis capítulos cubriendo una introducción al desarrollo de misiones satelitales, una visión general de la misión FLEX/Sentinel-3 de la ESA, la descripción de un diseño conceptual de un simulador genérico para misiones de Observación de la Tierra con instrumentos ópticos pasivos, una descripción del simulador implementado para la misión FLEX y un análisis de su rendimiento, y una discusión y conclusión general del trabajo realizado. La estructura de esta Tesis se organiza como sigue:

- El CAPÍTULO 2 presenta una visión general respecto a las misiones de Observación de la Tierra en desarrollo y, en particular, introduce el concepto de los simuladores de misión (E2ES). Este capítulo también describe la misión FLEX/Sentinel-3 de la ESA como un caso específico para la implementación de un E2ES.
- El CAPÍTULO 3 describe, basado en una revisión y clasificación de misiones satelitales para la Observación de la Tierra, la propuesta para el diseño de una arquitectura e interfaces genéricas para los E2ES en misiones con instrumentos ópticos pasivos.
- El CAPÍTULO 4 describe como la arquitectura genérica propuesta para los E2ES fue implementada para el caso específico de la misión FLEX/Sentinel-3 de la ESA.
- El CAPÍTULO 5 analiza los resultados de las simulaciones llevadas a cabo para evaluar el rendimiento de la misión FLEX en términos de sus productos de Nivel-1b (radiometría, geolocalización y configuración espectral) y Nivel-2 (obtención de la fluorescencia emitida por la vegetación).
- El CAPÍTULO 6 resume los objetivos cumplidos y los principales logros científicos, así como discute las conclusiones principales y propone futuras líneas de investigación.

Específicamente, los tres capítulos temáticos (Capítulos 3-5) representan una respuesta a las preguntas de la investigación detalladas en la sección anterior.

8.4 Resultados

Como parte del desarrollo y análisis del rendimiento de misiones satelitales para la Observación de la Tierra, los simuladores E2ES han sido estudiados, implementados y utilizados en las últimas décadas. En los últimos años, la ESA y otras agencias espaciales han utilizado los E2ES para la selección de futuras misiones para teledetección y para la preparación de la implementación del Segmento Tierra. El Capítulo 3 de esta Tesis se centraba en el diseño de una arquitectura genérica para simuladores E2ES que pudiese ser fácilmente adaptable y simular la mayoría de misiones ópticas pasivas presentes y futuras. El concepto de arquitectura genérica es importante en el marco de la estrategia científica de Observación de la Tierra de la ESA y otras agencias espaciales, con el fin de facilitar la planificación, desarrollo y análisis de nuevas misiones satelitales. Este concepto genérico fue posteriormente elaborado en el Capítulo 4 mediante su implementación para la misión FLEX/Sentinel-3 de la ESA, validando la arquitectura genérica para simuladores E2ES dadas las siguientes características:

- La ESA pidió desarrollar un E2ES para la evaluación de la misión FLEX/Sentinel-3. En este contexto, la arquitectura genérica podía ser demostrada en un escenario real como es el proceso de selección del octavo Earth Explorer de la ESA.
- La misión FLEX/S3 es multiplataforma y multi-instrumento con una configuración de vuelo en tándem y con sinergia de productos a Nivel-2, lo cual permitía comprobar la arquitectura genérica en este complejo escenario.
- Los instrumentos involucrados en la misión FLEX abarcan varias categorías tales como multi-angularidad, barrido tipo pushbroom/whiskbroom, rango espectral del visible and infrarrojo térmico, diferentes rangos de resolución espectral o multi-camaras, entre otras categorías. Esto permitía comprobar que el concepto de arquitectura genérica podía encajar con todas estas diferentes categorías.

Tal como se introdujo en el Capítulo 4, el simulador E2ES para la misión FLEX es una herramienta con la que se puede evaluar el rendimiento de la misión y, específicamente, determinar la precisión de los productos de fluorescencia a Nivel-2. El software implementado fue posteriormente usado, como parte del Capítulo 5, para evaluar el rendimiento de la misión FLEX en términos de su principal objetivo científico, es decir “proveer unas estimaciones robustas de la actividad fotosintética a escala global”. En particular, el simulador E2ES de la misión FLEX permitió comprobar el cumplimiento de los requisitos de la misión con trazabilidad a la MRD [213] y SRD a partir de la evaluación del rendimiento de la misión FLEX con respecto a la precisión de sus productos de Nivel-1 y Nivel-2.

En los siguientes párrafos se resumen los resultados principales de acuerdo a las preguntas científicas principales tal como están planteadas en la metodología de esta Tesis:

1. *¿Cuáles son las principales características de los instrumentos y misiones espaciales que deberían ser tenidos en cuenta para su modelización dentro de un simulador E2ES para misiones ópticas pasivas?* En el Capítulo 3, la revisión de misiones satelitales pasadas, presentes y futuras permitió extraer elementos comunes entre todas ellas. Estas misiones fueron clasificadas en términos del diseño de la misión y los aspectos técnicos de los instrumentos ópticos abordo. La clasificación fue propuesta considerando aquellos elementos que tuviesen un impacto en el rendimiento de la misión y, por tanto, que tuviesen que considerarse dentro de la arquitectura genérica de un simulador E2ES.

Con respecto a la clasificación del diseño de misiones satelitales, se consideró que estas misiones podían ser categorizadas según el número de satélites involucrados y la posibilidad de tener vuelo en formación. Esto tendría implicaciones en la modelización de las órbitas de los diferentes satélites y la geometría de observación de sus instrumentos, las cuales tendrían que modelizar la adquisición de datos sobre una misma escena. Además, el número de instrumentos involucrados en una misión y la posibilidad de tener sinergias entre sus productos tenía implicaciones respecto a la modelización de la cadena de procesado de los múltiples instrumentos. Las misiones de Observación de la Tierra también fueron clasificadas con respecto al objetivo científico, el cual tiene un impacto directo en la modelización de la señal adquirida por los instrumentos. Este último punto indicó que un E2ES genérico debería ser capaz de incluir una variedad de modelos de transferencia radiativa específicos (p.ej. vegetación, aguas, urbano) y bases de datos globales (p.ej. mapas de elevación, mapas temáticos de cubierta terrestre, bases de datos de reflectancias y emisividades).

Con respecto a los instrumentos ópticos pasivos, estos fueron analizados con según unos criterios de clasificación que incluían aspectos geométricos, características espectrales y espaciales del sensor y otros aspectos técnicos del instrumento. Todos estos aspectos deberían ser considerados a diferentes niveles dentro de la cadena de simulación de un E2ES, desde aquellos aspectos que involucran la simulación temporal y geométrica de la adquisición de los datos hasta aquellos aspectos que involucran el uso de modelos de transferencia radiativa específicos.

2. *¿Cuáles son los elementos comunes que se necesitan desarrollar en una arquitectura genérica para un simulador E2ES en misiones ópticas pasivas para la Observación de la Tierra?* Basado en el análisis de las clases y categorías de instrumentos y misiones satelitales, se consideró suficiente la combinación de seis módulos principales en tres variaciones de la arquitectura genérica de un simulador E2ES de modo que pudiesen reproducirse la mayoría de misiones de un único satélite para la Observación de la Tierra. En cuestión de arquitectura, el caso más sencillo es el de una única plataforma con un solo instrumento a bordo puesto que contiene cada uno de los seis módulos principales con un flujo de datos secuencial desde Geometría hasta Procesado de Nivel-2. En caso de sinergía a Nivel-2, una misión con varios instrumentos tendrá un Generador de Escena común que produzca las escenas de entrada para cada una de las cadenas de procesado de los diferentes instrumentos. En este caso, un único módulo de procesado a Nivel-2 procesa en singergia los datos de Nivel-1 de cada instrumento para producir los productos de Nivel-2 finales de la misión. Esta arquitectura es diferente para misiones con varios instrumentos pero sin sinergia entre sus productos. En este caso, como los diferentes instrumentos observan diferentes objetivos radiométricos, habrán tantos Generadores de Escena como instrumentos en la plataforma, generando escenas que serán adquiridas y procesadas a Nivel-1 y Nivel-2 en varias cadenas en paralelo.

Las misiones multi-plataforma (p.ej. constelaciones y misiones en tándem) pueden ser reproducidas con la arquitectura genérica propuesta a considerando dos posibilidades: **(1)** el módulo de Geometría genera la geometría de ambas plataformas e instrumentos; **(2)** las arquitecturas definidas en los puntos anteriores se aplican para cada una de las plataformas usando un Generador de Escena común y un mismo Procesador de Nivel-2 en caso de que haya sinergia de los datos a Nivel-1.

La arquitectura interna de cada uno de los seis módulos principales se detalló en forma de bloques que podían ser re-utilizados para reproducir la variedad de instrumentos ópticos pasivos analizados en el proceso de clasificación y categorización mediante la implementación de algoritmos específicos que tengan en cuenta las características específicas de cada instrumento y misión.

3. *¿Cómo debería implementarse un E2ES específico para la misión FLEX/Sentinel-3 de la ESA basado en el concepto de una arquitectura genérica para un simulador E2ES?* La selección de FLEX como futura misión Earth Explorer de la ESA ha estado ligada a un proceso competitivo en el cual el análisis del rendimiento de la misión se basó en gran parte gracias a los resultados producidos por el simulador E2ES de la misión FLEX. El desarrollo de este E2ES requirió integrar varios aspectos que afectaban al rendimiento de la misión tales como el diseño del instrumento, la complejidad de los efectos ambientales o la implementación de una cadena de procesado completa de Nivel-1 y Nivel-2. Además, el diseño de esta herramienta estaba constreñido por una serie de directrices con el fin de facilitar la comparación de los resultados producidor por los E2ES de las misiones en el proceso de selección.

La implementación del simulador E2ES para la misión FLEX se basó en la arquitectura genérica desarrollada en el Capítulo 3, la cual fue adaptada para reproducir las particularidades de la misión FLEX/Sentinel-3:

- La configuración de vuelo en tándem entre FLEX y Sentinel-3 se simuló mediante la incorporación de los ciclos orbitales de FLEX y Sentinel-3 calculados externamente. La definición de una misma cuadrícula sobre la que generar la escena para cada uno de los instrumentos de la misión permitía generar los datos radiométricos teniendo en cuenta los tiempos de adquisición y geometría de observación específica de cada instrumento.
- Los modelos SCOPE (para la cubierta vegetal) y MODTRAN5 (para la atmósfera) fueron implementados para simular escenas de alta resolución espectral en el rango espectral del visible al infrarojo térmico incluyendo la emisión de fluorescencia por parte de la vegetación. El modelado 3D de la escena generó escenas intrínsecamente diferentes para cada instrumento teniendo en cuenta la geometría de observación específica de cada instrumento, particularmente importante para la visión multi-angular del instrumento SLSTR.
- Dado que Sentinel-3 es una misión externa de apoyo a FLEX, la simulación de los instrumentos ópticos pasivos de Sentinel-3 y su procesado de datos a Nivel-1b fue implementado en un único módulo hecho a medida que modeliza las características más relevantes de OLCI y SLSTR en términos de su rendimiento final.

El ejemplo del simulador para la misión FLEX mostró que el concepto propuesto para una arquitectura genérica para simuladores E2ES puede ser aplicado a misiones de Observación de la Tierra y que, por tanto, sirve de base para la generación de simuladores de misiones satelitales de nueva generación. El software implementado permite al usuario simular una amplia variedad de posibles escenarios con consistencia de las condiciones físicas medioambientales y una descripción compleja del sensor. La principal premisa en el diseño e implementación del simulador E2ES de la misión FLEX fue que este fuese capaz de reproducir toda la complejidad de la misión FLEX de modo que este sirviese para evaluar el rendimiento de la misión. Al mismo tiempo, el simulador de FLEX también fue diseñado con el propósito de ser re-utilizado para la implementación del futuro Segmento Tierra de FLEX y el ensayo de los procedimientos de Calibración/Validación.

4. *¿Cuál es la precisión de los productos de Nivel-1b en la misión FLEX en términos de su rendimiento espectral, geométrico y radiométrico?* Se obtuvieron los siguientes resultados respecto a la precisión de los productos de Nivel-1b de la misión FLEX:

- FLORIS-HR (-LR) satisface los requisitos espectrales con un espaciado espectral de 0.1 nm (0. 65 nm) en los canales espectrales no agrupados, una resolución espectral de 0.3 nm (2 nm) y una precisión de la calibración espectral es mayor que 0.08 nm (0.35 nm) . El co-registrado espectral también se consiguió para FLORIS-HR con valores por debajo de 0.015 nm.

- Con respecto al rendimiento radiométrico de FLORIS-HR y FLORIS-LR, los resultados mostraron que la combinación de varios ruidos instrumentales, efectos sistemáticos en el detector y errores de calibración producen en promedio un error total en los productos de radiancia de Nivel-1b que varía linealmente entre 1% en 500 nm y 3% en 780 nm, principalmente debido a un error sistemático en la calibración radiométrica de $\sim$2% y los ruidos espectrales radiométricos. El error tiene una pequeña dependencia en la radiancia de entrada, principalmente causada por los ruidos del detector. La distribución espacial de los errores radiométricos está dominada por el efecto sistemático espacial y la variabilidad pixel-a-pixel de los ruidos en el detector. Mientras que el primero, siendo un error sistemático, puede aún ser reducido mediante la mejora de los algoritmos de tratamiento de imagen a Nivel-1 o Nivel-2, el efecto aleatorio de los ruidos en el detector sólo puede ser reducido con cambios en el sensor que reduzcan la relación señal-ruido. Por tanto, este efecto sólo puede ser reducido en el Nivel-2 dando menos peso a aquellos canales espectrales con menor relación señal-ruido.

- La combinación de todos los ruidos instrumentales y errores de calibración obtiene una relación señal-ruido que es más crítica en la región espectral del O_2-A. La mayr contribución viene de los ruidos del detector, particularmente el ruido fotónico. Sin embargo, la relación señal-ruido está dentro de los márgenes requeridos para la misión.

- La calibración radiométrica se alcanzó con unos errores por debajo de los límites establecidos, con una precisión absoluta de 1.95% independientemente de la radiancia de entrada en el instrumento. La calibración radiométrica relativa está por debajo del 1% y con variaciones máximas de ±0.4% en FLORIS-HR al fondo de la banda del O_2-A.

- El afecto por luz parásita causa un incremento de radiancia en las bandas de absorción del O_2 cuyo impacto es no despreciable incluso a distancias mayores de 30 pixeles de objetos brillantes. Esto indica que la contribución de la luz parásita a nivel espectral en la CCD domina respecto a la contribución espacial. A pesar de que este efecto no afecta de forma importante en la región del O_2-B (errores en la estimación de fluorescencia por debajo del 5%), el efecto en el O_2-A afecta con errores en la obtención de la fluorescencia entre 10% y 30%. Esto indica que se debería implementar un algoritmo de corrección de luz parásita en la cadena de procesado a Nivel-1 o Nivel-2.

- Con respecto al rendimiento geométrico, FLORIS consigue un espaciado entre pixeles de 300 m y una precisión en la geolocalización por debajo de 90 m, ambos estando dentro de los requisitos para la misión.

5. *¿Cuál es el impacto del diseño actual del instrumento de FLEX y los algoritmos de procesado de datos para la obtención de los productos de Nivel-2 de la misión FLE?* En general, los resultados del Capítulo 5 muestran que el diseño de misión FLEX y sus instrumentos cumple los requisitos con respecto a los errores en la estimación de la fluorescencia. En particular,

- Cuando se evaluó la precisión de los productos de fluorescencia, se demostró que la precisión en la estimación de la fluorescencia SIF está por debajo del 10% para la fluorescencia integrada y por debajo de 0.2 $\mathrm{mW{\cdot}m^{-2}sr^{-1}nm^{-1}}$ para los picos de fluorescencia.

- La corrección atmosférica es un paso crítico en el procesado de los datos en particular para la obtención de fluorescencia en la banda del O_2-B, donde se mostró que una caracterización incorrecta de la función de fase de los aerosoles (i.e., con un error relative de $\sim$25% in el parámetro de Henyey-Greenstein) reduce de forma importante el rendimiento del algoritmo, obteniendo errores en el primer pico de SIF de $\sim$0.25 $\mathrm{mW{\cdot}m^{-2}sr^{-1}nm^{-1}}$.

- El análisis de los resultados en una imagen realista indicó que la estimación de fluorescencia podría tener una precisión menor en áreas altamente heterogéneas. El análisis hecho con el simulador de FLEX con respecto a la heterogeneidad sub-pixel mostró de hecho que la precisión era más baja en pixeles con una mezcla de 50% vegetación y suelo. Este ejecto es particularmente importante para el primer pico (684 nm) con unos errores RMSE de 0.25 $\mathrm{mW{\cdot}m^{-2}sr^{-1}nm^{-1}}$, más altos que el requisito de 0.2 $\mathrm{mW{\cdot}m^{-2}sr^{-1}nm^{-1}}$.

8.5 Conclusiones

Esta Tesis propuso, tras una revisión y clasificación de misiones ópticas pasivas para la Observación de la Tierra, un diseño genérico para la arquitectura de un simulador E2ES que pudiese ser aplicable a la mayoría de estas misiones. En vista al impacto en la arquitecutra de simuladores E2ESy el rendimiento de una misión satelital, estas misiones fueron en primer lugar clasificadas en términos del número de satélites con posibilidad de vuelo en formación, número de instrumentos y sinergia entre ellos, tipos de órbita y objetivo radiométrico (es decir, el objetivo y aplicación de una misión). Esta clasificación permitió establecer unas pocas variaciones de una arquitectura genérica para un simulador E2ES de forma que este cubra la mayoría de misiones ópticas pasivas para la Observación de la Tierra. En segundo lugar, los instrumentos ópticos pasivos fueron analizados teniendo en cuenta sus características geométricas, espectrales y espaciales así como la tecnología del sensor e instrumento. A pesar de la gran variedad de instrumentos ópticos pasivos, estos pueden ser simulados con una arquitectura común genérica para un simulador E2ES con una estructura interna para cada uno de los módulos de más alto nivel confeccionada a partir de bloques de bajo nivel. Las particularidades de cada instrumento afecta a la implementación de los algoritmos y modelos que simulan cada uno de estos instrumentos así como pequeñas variaciones en las interfaces genéricas entre módulos. Por tanto, se concluyó que la arquitectura genérica propuesta es apta para reproducir la mayoría de misiones ópticas pasivas para la Observación de la Tierra.

La arquitectura conceptual fue entonces validada a través de su implementación, con ligeras variaciones, en la misión tandem FLEX/Sentinel-3 de la ESA, mostrando su idoneidad para la modelización de la misión FLEX. La herramienta FLEX-E fue empleada para evaluar la precisión de los productos de Nivel-1b con trazabilidad a los requisitos de la misión, demostrando que FLEX cumple con los principales requisitos espectrales, geométricos y radiométricos. Además, FLEX-E fue utilizado para analizar el rendimiento de la misión FLEX con respecto a la obtención de flurescencia, obteniendo resultados con un error por debajo de los 0.2 $\mathrm{mW{\cdot}m^{-2}sr^{-1}nm^{-1}}$. La precisión en la obtención de fluorescencia es menor para pixeles muy heterogéneos, particularmente en el primer pico a 685 nm. También se observó que la corrección atmosférica funciona adecuadamente a traves de los resultados obtenidos, indicando que el primer pico en la fluorescencia es más sensible a errores en la caracterización de la función de fase de los aerosoles dada la mayor dispersión en longitudes de onda del rojo respecto al infrarojo. Se demostró por tanto que la arquitectura genérica para un simulador e2ES y su implementación en la herramienta FLEX-E fue útil para evaluar el rendimiento de la misión en Fase A/B1 tanto para los productos de Nivel-1b (geométricos, radiométricos y espectrales) y de Nivel-2 (corrección atmosférica y obtención de fluorescencia). Además, se considera que el diseño de FLEX-E es suficientemente flexible para su evolución en la futura Fase C/D y su implementación dentro del Prototipado de Procesado en Tierra (GPP) y el Segmento Tierra.

A pesar de que FLEX-E se desarrolló especificamente para la misión FLEX, su diseño se basó en el concepto de arquitectura genérica desarrollado en esta Tesis y por tanto, es susceptible de ser readaptado a otras misiones ópticas pasivas. La metodología implementada en esta Tesis puede ser usada para desarrollar los simuladores de misión para satélites de nueva generación. Particularmente, las siguientes conclusiones se derivan para la implementación de un simulador E2ES genéico para misiones ópticas pasivas basado en las lecciones aprendidas en la implementación de FLEX-E:

- La implementación de un módulo geométrico debería estar basado en los conceptos introducidos en el Capítulo 3 mediante el uso de librerías estandar sobe los aspectos geométricos en satélites tales como la librería EOCFI de la ESA. El módulo de geometría debería simular la linea de visión para cada pixel en instrumentos de tipo ‘’whiskbroom”, “pushbroom” y “frame”. La salida de este módulo debería por tanto considerar el tiempo de adquisición para cada pixel, linea e imágen respectivamente. La adquisición secuencial para diferentes canales espectrales (p.ej., usando varias cámares o rueda de filtros) debería también ser incluida en un módulo genérico de geometría.

- Las interfaces entre módulos deberían ser completamente genéricas, en particular para las interfaces entre los módulos de Geometría y Generador de Escena y entre este y el de Instrumento. Considerando los diferentes tipos de instrumento (p.ej., hiperespectral/multiespectral) y la variabilidad de condiciones geométricas del instrumento, el Generador de Escena podría ser adaptado para acomodar estas características, haciéndolo más genérico.

- El Generador de Escena implementado en FLEX-E se basa en el uso de mapas temáticos de cobertura de clases donde se definen dos tipos de superficie (ver Anexo B.2 para uan descripción detallada): *clases basadas en bases de datos de reflectancia en superficie* y *clases de modelos de transferencia radiativa*. El Generador de Escena puede por tanto extender sus capacidades al incorporar cualquier modelo de transferencia radiativa incluido por el usiario y asociado a clases específicas. Las bases de datos de parámetros bio-geofísicos clave también debería ser extendido para incorporar parámetros adicionales como variables de entrada a los modelos de transferencia radiativa y las bases de datos espectrales (de reflectancia y emisividad). Se considera que un Generador de Escena totalmente genérico debería ser capaz de incluir mapas globales y multitemporales adicionales tales como variables meteorológicas, modelos digitales de elevación, mapas de cobertura de clases y mapas de parámetros bio-geofísicos. El link entre el Generador de Escena y bases de datos tales como en proyecto CCI de la ESA, ECMWF, Aeronet o Google Earth Engine podría ser implementado de forma online via acceso por *ftp*, reduciendo la cantidad de datos almacenados en un ordenador local.

- La simulación detallada de las características e un instrumento dependen en gran manera del concepto industrial implementado para el instrumento. Para estudios en Fase A/B, un modelo paramétrico para el instrumento con ecuaciones simplificadas pero realistas puede describir las principales características y el comportamiento de una gran varibilidad de instrumentos ópticos pasivos y sensores de diferentes tipos. Una búsqueda bibliográfica detallada debería ser llevada a cabo con el objetivo de implementar estas ecuaciones paramétricas en un módulo de instrumento genérico.

A

List of EO passive optical missions

Contents

A.1 List of EO passive optical missions

Past, present and planned EO passive optical missions were analyzed in this Thesis with the aim of extracting commonalities and study particularities that affected their performance and with objective to classify and categorize them in terms of their impact with respect the architecture of an E2ES. According to ESA's initiatives in EO Handbook [56] and EOportal [57], more than 450 EO missions have been flown or are currently in operations. A subset of nearly 100 missions (instruments) (see Tab. A.1) were studied in this Thesis, focusing on those that are more relevant in terms of its instrument characteristics and scientific and/or societal impact.

Table A.1: Past, current and planned ESA passive optical instruments.

Instrument	Mission(s)	Instrument	Mission(s)
AATSR	Envisat	FLORIS	FLEX
ATSR, ATSR/M	ERS-1, ERS-2	GERB	MSG
BBR	EarthCARE	GOME	ERS-2
CHRIS	Proba-1	GOME-2	Metop-(A to C)
FCI	MTG-I (1 to 4)	GOMOS	Envisat

Table A.2: Past, current and planned ESA passive optical instruments (cont.).

Instrument	Mission(s)	Instrument	Mission(s)
ISR	MTG-S, Sentinel-4/-5	SCIAMACHY	Envisat
LI	MTG-I (1 to 4)	SEVIRI	MSG
MERIS	Envisat	SLSTR	Sentinel-3
MIPAS	Envisat	UVAS	Ingenio
MSI (EarthCARE)	EarthCARE	UVN	Sentinel-4
MSI (Sentinel-2)	Sentinel-2	UVNS (post-EPS)	Sentinel-5
MVIRI	MFG	UVNS	Sentinel-5P
OLCI	Sentinel-3	VGT-P	Proba-V
PAN+MS	Ingenio		

Table A.3: Past, current and planned non-ESA passive optical instruments.

Instrument	Mission(s)	Instrument	Mission(s)	Instrument	Mission(s)
ABI	GOES-R	HyspIRI	HyspIRI	PSA	Monitor-E
ACE	SciSat-1	IIR	Calipso	RSI	FormoSat-2
AEISS	Kompsat-3	IRAS	FY-3	SBUS	FY-3
ALI	EO-1	IRMS	HJ-1	SeaWIFI	ObrView-2
AIRS	Aqua	ISUAL	FormoSat-2	ShMSA	Resurs-P
ASTER	Terra	IRS	CBERS-3/-4	Sounder	INSAT-3D
AVHRR	POES	LISS-III/IV	IRS-P6	TANSO	GOSAT
AWFI	Amazonia-1	MERSI	FY-3	TES	Aura
CERES	Aqua, Terra	MISR	Terra	TIRS	Landsat-8
CIRC	ALOS-2	MODIS	Aqua, Terra	TM	Landsat-4/-5
ETM+	Landsat-7	MOPITT	Terra	TOU	FY-3
Geoton-L1	Resurs-P	MUXCam	CBERS-3/-4	VHRR/2	INSAT-3D
GSA	Resurs-P	NAOMI	SPOT-6/-7	VIRR	FY-3
HiRAIS	Deimos-2	NIRST	Aquarius/SAC-D	WFC	Calipso
HIRDLS	Aura	OCM	OceanSat-2	WFI	CBERS-3/-4
HIRS	POES	OCO-2	OCO-2	ISS missions	
HIS	HJ-1	OLI	Landsat-8	ASIM	
HRG	SPOT-4/-5	OMI	Aura	HICO	
HRVIR	SPOT-4/-5	OSA	Ikonos-2	ISSAC	
HSC	Aquarius/SAC-D	OSIRIS	Odin	Rusalka	
Hyperion	EO-1	PanCam	CBERS-3/-4	SAGE-III	

A.2 Classificastion criteria for EO passive optical missions

The instruments presented in the previous Section were classified according to the criteria given in Tab. A.4 and Tab. A.5 taking into account those elements that affect to an EO mission performance and their impact with respect the architecture of an E2ES.

Table A.4: Characterization of passive optical instruments.

Feature	Type		Sample mission	Description
Acquisition mode	Continuous (global)		MSI (Sentinel-2)	Acquires data continuously from pole to pole
	Localized (target)		CHRIS (Proba)	Acquires data from selected target areas around the world
Pointing (platform / instrument)	Fixed		MSI (Sentinel-2)	Platform attitude is modified only to keep pointing fixed
	Angular	Along-track	SLSTR (Sentinel-3)	Platform attitude is modified to change pointing ALT
		Across-track	HRVIR (SPOT)	Platform attitude is modified to change pointing ACT
		Bi-directional	CHRIS (Proba)	Platform attitude is modified to change pointing ALT and ACT
	Limb-pointing / tracking		SCHIAMACHI (Envisat)	Pointing to scan the atmospheric limb or to track a light source from the occultation method
	Slow down		CHRIS (Proba)	Pointing to to increase the integration time over a given target
Multiangularity (image)	By steering		CHRIS (Proba)	Platform maneuvers to acquire at different angles
	By image overlap		POLDER-P (PARASOL)	Successive images partially overlap with different view angles
	Conical scanning / flipping mirrors		SLSTR (Sentinel-3)	Sensor acquires alternating two view angles (typically nadir and forward)
	Multi-camera		MISR (Terra)	Several cameras onboard point in different directions
Spatial resolution	Low (>500m)		SEVIRI (MSG)	
	Mid (<500m)		FLORIS (FLEX)	
	High (<50)		MSI (Sentinel-2)	
	Very high (<10 m)		PAN+MS (Ingenio)	
Polarization	Measuring		TANSO (GOSAT)	Instrument is designed to measure light polarization
	Insensitive		FLORIS (FLEX)	Instrument is designed to be insensitive to light polarization
Spectral mode	Single band		HRC (Proba)	Measures at a single band
	Multispectral/PAN		PAN+MS (Ingenio)	Three of four broad bands with high spatial resolution and an additional panchromatic band at higher resolution
	Superspectral		OLCI (Sentinel-3)	Fine spectral resolution and a few tens of bands
	Hyperspectral		HICO (ISS)	Fine spectral resolution and several tens of contiguous bands
	Ultraspectral		FLORIS (FLEX)	Very fine spectral resolution and hundreds of contiguous bands

Table A.5: Characterization of passive optical instruments (cont. 1).

Feature	Type		Sample mission	Description
Spectral range	UV		UVNS (Sentinel-5)	<400 nm
	VIS		MSI (Sentinel-2)	400–750 nm
	NIR		OLCI (Sentinel-3)	750–1020 nm
	SWIR		MSI (Sentinel-2)	1.4–3 μm
	MIR		SLSTR (Sentinel-3)	3–8 μm
	TIR		SLSTR (Sentinel-3)	>8 μm
Scanning geometry	Linear		OLCI (Sentinel-3)	Scanning along a line perpendicular to the motion of the platform
	Conical/circular		SLSTR (Sentinel-3)	Scanning in conical shape that intersects the Earth surface in two sections of ellipse. Used for dual view systems
Swath	Full Earth disk		SEVIRI (MSG)	The instrument takes a whole picture of the Earth disk
	Carpet mode		OLCI (Sentinel-3)	The Earth is scanned by a continuous stripe defined by its swath
	Scene mode		HRVIR (SPOT)	The instrument covers the Earth imaging different areas
Number of cameras	Solidary		OLCI (Sentinel-3)	
	Independent		HRVIR (SPOT)	
Instrument type	Whiskbroom		TM (Landsat)	Every image pixel is taken in sequence
	Pushbroom		FLORIS (FLEX)	Every image line is taken at once
	Frame		HRC (Proba)	A full image frame is taken at once
Spectro-radiometer type	Radiometer	Multi-camera	PAN+MS (Seosat)	Bands acquired by independent cameras after proper filters
		Filter wheel	POLDER-P (PARASOL)	A single camera acquired bands in sequence by changing filters
	Spectro-radiometer	Grating	CHRIS (Proba)	Spectra separation is achieved by grating diffraction
		Fabry-Perot		Spectra separation is achieved by Fabry-Perot interferometry
		Variable filter	MISR (Terra)	Spectra separation is achieved by a linear variable filter
		Fourier transform	MIPAS (Envisat)	Spectra separation based on measuring the temporal coherence of the light
		Prism	HSI (EnMap)	Spectra separation is achieved by prism diffraction

B

Scene radiative transfer for passive optical instruments

Contents

B.1 List of radiative transfer models

RTMs are mathematical abstractions of the physical laws governing light absorption and scattering processes within a media (e.g., vegetation canopy, atmosphere, water). These RTMs implement approximations in the modelization and properties of the media in which radiation is propagated. These approximations depend on the application of an RTM or spectral range of the reflected/emitted light. This Section provides a non-exhaustive list of some RTMs used in vegetation, water bodies, urban and atmosphere with the aim of showing the variety of RTMs available in the literature. This list is based on initiatives such as the Radiation transfer Model Intercomparison project [143–146] for evaluation of vegetation RTMs or the work by Kotchenova et al. (2008) [147] and ESA's project *ESAS-Light* [148] on the comparison of atmospheric RTMs.

B.1.1 Surface radiative transfer models

Table B.1: Surface RTM characteristics.

Model name	Spectral range	1D/ 3D	Surface type	Other characteristics
4SAIL2 [216]	VIS-SWIR	3D	Vegetation	Non-lambertian soil BRDF and the consideration of vegetation with ground of crown coverage
5-scale [217]	VIS-SWIR	3D	Vegetation	Non-random spatial dispersion with internal structures and biochemical properties
ACRM [218]	VIS-SWIR	1D	Vegetation	Non-lambertian soil BRDF, specular reflection of direct Sun radiation, hot spot effect, 2-parameter leaf angle distribution
DART [219, 220]	UV-TIR	3D	Any	
DLM [221]	VIS-SWIR		Vegetation	Leaf RTM
FLIGHT [222]	VIS-SWIR	3D	Vegetation	
FluorMOD [223]	VIS-NIR	1D	Vegetation	Includes fluorescence emission
HydroLight [224]	UV-NIR	1D	Ocean color	Includes fluorescence emission
HYEMALIS [225]	VIS-SWIR	3D	Landscape	
MBRF [226]		1D	Vegetation	Multicomponent canopies with non-uniformity vertical distribution of foliage area density and non-random spatial dispersion
Mie-based [227]	TIR	1D	Snow/Ice	
MOX [228]		1D	Ocean color	
MuSES [229]	NIR-TIR	3D	Vehicles	For active heat sources
OSIrIS [230]	MIR-TIR	3D	Urban area	
PROSAIL [231, 232]	VIS-SWIR	1D	Vegetation	Dense homogeneous vegetation with random leaf distribution
PROSPECT(-3/-4/-5) [233]	VIS-SWIR		Vegetation	Leaf RTM. Integrated in PROSAIL
Raytran [234]		3D	Vegetation	Ray tracing
RGM [235]		3D	Vegetation	
SAIL [236]	VIS-SWIR	1D	Vegetation	Dense homogeneous vegetation with random azimuth distribution
SCOPE [237]	VIS-SWIR	1D	Vegetation	Includes fluorescence emission
SLC (4SAIL2) [238]	VIS-SWIR	1D	Vegetation	Coupled soil-leaf-canopy
SOLENE [239]		3D	Urban area	
SPIRou [240]	MIR-TIR	1D	Landscape	
WASI [241]	VIS-TIR	1D	Ocean color	

B.1.2 Atmosphere radiative transfer models

Table B.2: Atmosphere RTM characteristics.

Model name	Spectral range (resolution)	Other characteristics
5S, 6S, 6SV [242, 243]	VIS-MIR (2.5 nm)	Plane-parallel. 6SV includes polarization
LibRadTran [244, 245]	UV-TIR (0.1 cm^{-1})	Pseudo plane-parallel or pseudo-spherical. Includes polarization
MODTRAN [16]	UV-TIR (0.1 cm^{-1})	Pseudo-spherical
MOMO [246]	UV-TIR (0.05-100 nm)	Plane-parallel
MOSART [247]	UV-TIR (1 $\mathrm{cm}^{-}1$)	MODTRAN-based band model. Includes turbidity
SCIATRAN [248]	UV-TIR (0.05-100 nm)	Plane-parallel, pseudo-spherical or spherical. Includes polarization
SMART [249]	VNIR	Plane-parallel. Fast execution

B.2 Spectral and bio-geophysical parameters databases

Within the Scene Generator Module (SGM), the *Surface definition* building block is in charge of distributing key input bio-geophysical parameters and surface reflectance spectra that is later used for the radiative transfer modeling of the TOA radiance scenes. This distribution is based on an automatically-generated, external input or global (e.g., Corine) LCC map that associates a specific thematic class to each scene grid point. These classes are described by a set of configuration parameters given in Tab. B.3.

Table B.3: Surface definition database.

Parameter: Values	**Description**
Class ID: 1, 2,... N_{class}	Identifies each LCC.
Class Name: Forest, Crop, Urban, Lake...	Describes each LCC.
RTM: Yes/No	Determines whether the given class is associated with a RTM (Yes) or with a reflectance spectral database (No).
Radiative Transfer Model classes	
RTM ID: 1, 2,... N_{rtm}	Identifies the RTM used for the class ID.
Parameter ID: 1, 2,... N_{param}	Identifies each key input bio-geophysical parameter used in the selected RTM.
Param. Name: LAI, Chlorophyll...	Describes each input parameter for the selected RTM.
Spatial distribution: Concentric, Linear, Radial, Random	Spatial distribution of the parameters among all the scene grid points of a given class ID. It might be different for each parameter ID.
Statistical distribution: Gaussian, Poison, Uniform	Statistical distribution of the parameters among all the scene grid points of a given class ID. It might be different for each parameter ID.
Statistical distribution parameters	Parameters describing the statistical distribution of the bio-geophysical parameter (e.g., mean, standard deviation, minimum/maximum range).
Surface reflectance database classes	
Reflectance IDs: 1, 2,... N_{db}	Set of number(s) identifying the reflectance spectra used for the class ID.
Parameter ID: 1, 2,... N_{param}	Identifies a set of bio-geophysical parameters associated with the class ID (optional).
Param. Name: LAI, Chlorophyll...	Describes each bio-geophysical parameters associated with the class ID (optional).
Parameter values:	Values of bio-geophysical parameters associated with each surface spectra on the class ID (optional).

The RMT classes are associated with an RTM to be run (e.g., SCOPE) and a set of key input bio-geophysical parameters. This set of input parameters together with the spatial and statistical distribution define univocally each RTM class.

With respect to surface reflectance database classes, these are associated with one or more (to simulate sub-pixel heterogeneity) spectral reflectance from a user-input database (e.g., ASTER [250], USGS [251], field campaigns). In addition, each of these surface reflectance spectra might be described by a set of bio-geophysical parameters to compare against the retrieved L2 values. The default surface reflectance spectra used in the FLEX-E SGM module for the Corine Land Cover classes are shown in Fig. B.1 where each LCC is associated with only one surface reflectance spectrum.

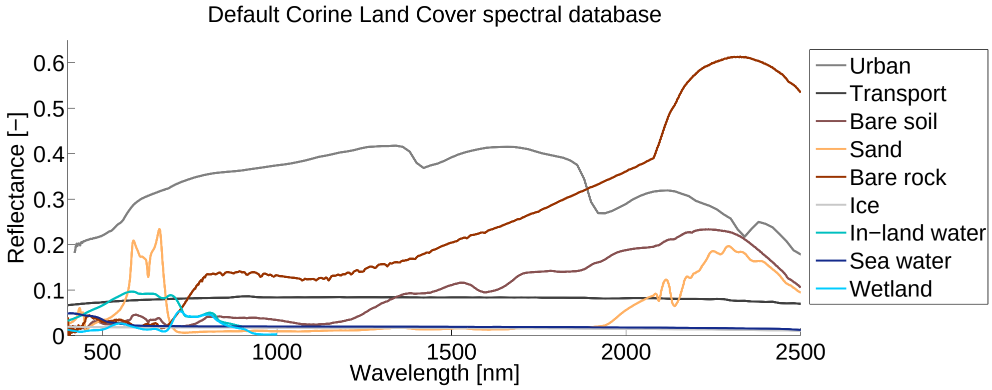

Figure B.1: Default surface reflectance dataset used for the Corine Land Cover classes according as used in Fig. 4.3 in Chapter 4.

B.3 Surface-Atmosphere radiative transfer

The surface-atmosphere coupling presented in this annex is based on the 4-streams model developed by Verhoef et al. [208, 216, 252] and represented in Fig. B.2.

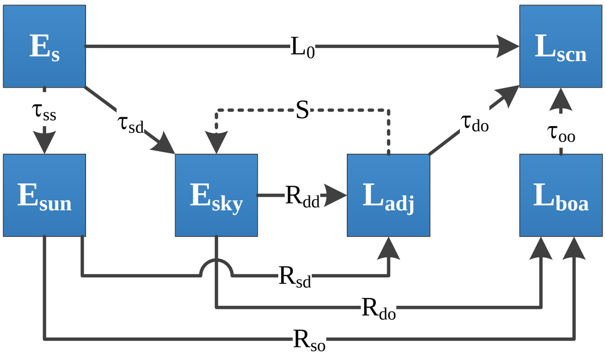

Figure B.2: Flux-interaction diagram of the atmosphere over a non-Lambertian reflecting Earth's surface. Adapted from [216].

The radiance signal observed by an airborne or spaceborne sensor due to the light emitted and reflected from a surface target is given by the three terms in Eq. (B.1): **(1)** the atmospheric reflected radiance, or path radiance (L_0); **(2)** the target-to-observer directly transmitted radiance ($L_{boa}\tau_{oo}$); and **(3)** the contribution from adjacency effects, diffusely transmitted to the observer ($L_{adj}\tau_{do}$).

$$L_{scn} = L_0 + L_{boa}\tau_{oo} + L_{adj}\tau_{do} \tag{B.1}$$

In case of Sun-reflected radiance in the VIS-SWIR spectral range, the terms L$_{boa}$ and L$_{adj}$ (in [mW·m^{-2}sr^{-1}nm^{-1}]) are defined by the following equations[1]:

$$L^0_{boa} = \frac{R_{so}E_{sun} + R_{do}E_{sky}}{\pi} \tag{B.2}$$

$$L^0_{adj} = \frac{E_s\mu_{il}(\tau_{sd}R_{dd} + \tau_{ss}R_{sd})}{\pi(1 - SR_{dd})} \tag{B.3}$$

where

$$E_{sun} = E_s\mu_{il}\tau_{ss} \tag{B.4}$$

$$E_{sky} = \frac{E_s\mu_{il}(\tau_{sd}R_{dd} + \tau_{ss}SR_{sd})}{(1 - SR_{dd})} \tag{B.5}$$

In the equations above, E_s is the extraterrestrial solar irradiance, in [mW·m^{-2}nm^{-1}]; μ_{il} is the cosine of the solar zenith angle; and E$_{sun}$ and E$_{sky}$ are respectively the direct and diffuse solar at-surface irradiance, in [mW·m^{-2}nm^{-1}]. In addition,

- τ_{ss}, τ_{sd}, τ_{oo} and τ_{dd} are the dimensionless atmospheric transmittance for the direct-downward, diffuse-downward, direct-upward and diffuse-upward fluxes respectively.
- and R$_{so}$, R$_{do}$, R$_{sd}$ and R$_{dd}$ are the dimensionless surface bi-directional reflectance factors according to the direct/direct, diffuse/direct, direct/diffuse and diffuse/diffuse downward/upward transmittance respectively.

Eq. (F.1) can be further extended to the thermal domain. First, the atmospheric thermal emitted radiance, L$_a$, is added on top to the reflected radiance L$_0$. Secondly, the L$_{boa}$ term includes the thermal emitted blackbody radiance from the surface, L$_s$, and both L$_a$ and L$_s$ as sources of the diffuse at-surface irradiance i.e.,

$$L^0_{boa} = \frac{R_{so}E_{sun} + R_{do}E_{sky}}{\pi} + (1 - R_{do})L_s \tag{B.6}$$

where

$$E_{sky} = \frac{E_s\mu_{il}(\tau_{sd}R_{dd} + \tau_{ss}SR_{sd}) + \pi R_{dd}L_a + \pi(1 - R_{dd}L_s)}{(1 - SR_{dd})} + \pi L_a \tag{B.7}$$

---

[1] The ^{0} superspercript refers to Sun-reflected radiance.

Finally, the adjacency effects from the thermal surface and atmosphere radiances are added to Eq. (F.3) as follows:

$$L_{adj}^{0} = \frac{E_s \mu_{il} (\tau_{sd} R_{dd} + \tau_{ss} R_{sd}) + R_{dd} L_a + (1 - R_{dd}) L_s}{\pi (1 - S R_{dd})} \tag{B.8}$$

When considering the fluorescence emission as a second order contribution compared with the reflected radiance, the terms L$_{boa}$ and L$_{adj}$ are given by the next equations:

$$L_{boa} = L_{boa}^{0} + F + \frac{F_d S R_{do}}{1 - S R_{dd}} \tag{B.9}$$

$$L_{adj} = L_{adj}^{0} + \frac{F_d}{1 - S R_{dd}} \tag{B.10}$$

being F and F$_d$ respectively the direct and hemispheric fluorescence emission.

Bibliography

[1] National Aeronautics and Space Administration (NASA). NASA Systems Engineering Handbook, NASA/SP-2007-6105 Rev 1. Available from `http://www.acq.osd.mil/se/docs/NASA-SP-2007-6105-Rev-1-Final-31Dec2007.pdf`, March 2007.

[2] European Cooperation for Space Standardization (ECSS). Space engineering: Systems engineering general requirements, ECSS-E-ST-10C. Available from `http://www.ecss.nl/`, March 2009.

[3] ESA. NASA's EOSDIS Data Processing Levels. `http://science.nasa.gov/earth-science/earth-science-data/data-processing-levels-for-eosdis-data-products/`, 2010. [accessed 15/06/2016].

[4] H. Worden, R. Beer, K.W. Bowman, B. Fisher, M. Luo, D. Rider, E. Sarkissian, D. Tremblay, and J. Zong. TES level 1 algorithms: Interferogram processing, geolocation, radiometric, and spectral calibration. *IEEE Transactions on Geoscience and Remote Sensing*, 44(5):1288–1295, May 2006.

[5] A. Kuze, D.M. O'Brien, T.E. Taylor, J.O. Day, C.W. O'Dell, F. Kataoka, M. Yoshida, Y. Mitomi, C.J. Bruegge, H. Pollock, R. Basilio, M. Helmlinger, T. Matsunaga, S. Kawakami, K. Shiomi, T. Urabe, and H. Suto. Vicarious calibration of the GOSAT sensors using the Railroad Valley desert playa. *IEEE Transactions on Geoscience and Remote Sensing*, 49(5):1781–1795, May 2011.

[6] B.-C. Gao, R.-R. Li, R.L. Lucke, C.O. Davis, R.M. Bevilacqua, D.R. Korwan, M.J. Montes, J.H. Bowles, and M.R. Corson. Vicarious calibrations of HICO data acquired from the International Space Station. *Applied Optics*, 51(14):2559–2567, May 2012.

[7] J.A. Barsi, J.R. Schott, S.J. Hook, N.G. Raqueno, B.L. Markham, and R.G. Radocinski. Landsat-8 thermal infrared sensor (TIRS) vicarious radiometric calibration. *Remote Sensing*, 6(11):11607–11626, 2014.

[8] K. Segl, R. Richter, T. Küster, and H. Kaufmann. End-to-end sensor simulation for spectral band selection and optimization with application to the Sentinel-2 mission. *Applied Optics*, 51(4):439–449, 2012.

[9] K. Segl, L. Guanter, and H. Kaufmann. Simulation-based case studies for optimization of sensor design and image-based parameter retrieval using the EnMAP scene simulator. *Proc. of Hyperspectral Workshop*, 2010.

[10] Verstraete. M.M, D.J. Diner, and J.-L. Bézy. Planning for a spaceborne Earth Observation mission: From user expectations to measurement requirements. *Environmental Science & Policy*, 54:419 – 427, 2015.

[11] J. Verrelst, E. Romijn, and L. Kooistra. Mapping vegetation density in a heterogeneous river floodplain ecosystem using pointable CHRIS/PROBA data. *Remote Sensing*, 4(9):2866–2889, 2012.

[12] J. Verrelst, G. Camps-Valls, J. Muñoz Marí, J.P. Rivera, F. Veroustraete, J.G.P.W. Clevers, and J. Moreno. Optical remote sensing and the retrieval of terrestrial vegetation bio-geophysical properties - A review. *ISPRS Journal of Photogrammetry and Remote Sensing*, 108:273–290, 2015.

[13] J.P. Kerekes and D.A. Landgrebe. Simulation of optical remote sensing systems. *IEEE Transactions on Geoscience and Remote Sensing*, 27(6):762–771, 1989.

[14] J.P. Kerekes and J.E. Baum. Full-spectrum spectral imaging system analytical model. *IEEE Transactions on Geoscience and Remote Sensing*, 43(3):571–580, 2005.

[15] J.P. Kerekes and J.E. Baum. Spectral imaging system analytical model for subpixel object detection. *IEEE Transactions on Geoscience and Remote Sensing*, 40(5):1088–1101, 2002.

[16] A. Berk, G.P. Anderson, P.K. Acharya, L.S. Bernstein, L. Muratov, J. Lee, M. Fox, S.M. Adler-Golden, J.H. Chetwynd, M.L. Hoke, R.B. Lockwood, J.A. Gardner, T.W. Cooley, C.C. Borel, P.E. Lewis, and E.P. Shettle. MODTRAN^{TM}5: 2006 update. *Proceedings of SPIE - The International Society for Optical Engineering*, 6233 II, 2006.

[17] A. Börner, L. Wiest, P. Keller, R. Reulke, R. Richter, M. Schaepman, and D. Schläpfer. SENSOR: A tool for the simulation of hyperspectral remote sensing systems. *ISPRS Journal of Photogrammetry and Remote Sensing*, 55(5-6):299–312, 2001.

[18] S.A. Cota, J.T. Bell, R.H. Boucher, T.E. Dutton, C.J. Florio, G.A. Franz, T.J. Grycewicz, L.S. Kalman, R.A. Keller, T.S. Lomheim, D. Paulson, and T.S. Wilkinson. PICASSO: An end-to-end image simulation tool for space and airborne imaging systems. *Journal of Applied Remote Sensing*, 4(1), 2010.

[19] S.A. Cota, T.S. Lomheim, C.J. Florio, J.M. Harbold, B.M. Muto, R.B. Schoolar, D.T. Wintz, and R.A. Kellerb. PICASSO - An end-to-end Image Simulation tool for space and airborne imaging systems: II. Extension to the Thermal Infrared - Equations and methods. *Proceedings of SPIE - The International Society for Optical Engineering*, 8158, 2011.

[20] P. Coppo, L. Chiarantini, and L. Alparone. End-to-End Image Simulator for Optical Imaging Systems: Equations and Simulation Examples. *Advances in Optical Technologies*, (3):23, 2013.

[21] R. Sundberg, S. Richtsmeier, and R. Harem. Monte carlo based hyperspectral scene simulation. *Proc. of 2nd Workshop on Hyperspectral Image and Signal Processing: Evolution in Remote Sensing (WHISPERS)*, 2010.

[22] L. Guanter, K. Segl, and H. Kaufmann. Simulation of optical remote-sensing scenes with application to the EnMAP hyperspectral mission. *IEEE Transactions on Geoscience and Remote Sensing*, 47(7):2340–2351, 2009.

[23] K. Segl, L. Guanter, C. Rogass, T. Kuester, S. Roessner, H. Kaufmann, B. Sang, V. Mogulsky, and S. Hofer. EeteS - the EnMAP end-to-end simulation tool. *IEEE Journal of Selected Topics in Applied Earth Observations and Remote Sensing*, 5(2):522–530, 2012.

[24] K. Segl, L. Guanter, F. Gascon, T. Kuester, C. Rogass, and C. Mielke. S2eteS: An End-to-End Modeling Tool for the Simulation of Sentinel-2 Image Products. *IEEE Transactions on Geoscience and Remote Sensing*, 53(10):5560–5571, 2015.

[25] A. Barducci, D. Guzzi, C. Lastri, P. Marcoionni, V. Nardino, and I. Pippi. Simulating the performance of the hyperspectral payload of the PRISMA mission. *International Geoscience and Remote Sensing Symposium (IGARSS)*, pages 5013–5016, 2012.

[26] M. Parente, J.T. Clark, A.J. Brown, and J.L. Bishop. End-to-end simulation and analytical model of remote-sensing systems: Application to CRISM. *IEEE Transactions on Geoscience and Remote Sensing*, 48(11):3877–3888, Nov 2010.

[27] R. Voors, D. Donovan, J. Acarreta, M. Eisinger, R. Franco, D. Lajas, R. Moyano, F. Pirondini, J. Ramos, and T. Wehr. CSIM: The simulator framework for EarthCARE. *Proceedings of SPIE - The International Society for Optical Engineering*, 6744, 2007.

[28] M. Scagliola, D. Giudici, J.R. Acarreta, E. Del Pozo, and C. Buck. The CoReH2O end to end simulator: Architecture and simulation results analysis. *International Geoscience and Remote Sensing Symposium (IGARSS)*, pages 4541–4544, 2012.

[29] P. Lopez-Dekker, J.A. Garcia, F. De Zan, T. Borner, M. Younis, K. Papathanassiou, T. Guardabrazo, V. Bourlon, S. Ramongassie, N. Taveneau, L. Ulander, D. Murdin, N. Rogers, S. Quegan, and R. Franco. Biomass end-to-end mission performance assessment. *International Geoscience and Remote Sensing Symposium (IGARSS)*, pages 1602–1605, 2012.

[30] A. Camps, I. Corbella, M. Vall-Llossera, N. Duffo, F. Marcos, F. Martínez-Fadrique, and M. Greiner. The SMOS End-to-end Performance Simulator: Description and Scientific Applications. *International Geoscience and Remote Sensing Symposium (IGARSS)*, 1:13–15, 2003.

[31] S. Dangel, M. Schaepman, J. Brazile, F. Petitcolin, B. Su., X. Briottet, M. Gloor, J. Moreno, and K.I. Itten.

System architecture and design for a SPECTRA mission end-to-end simulator. *Proc. of 2nd SPECTRA workshop*, 1, 2003.

[32] ESA. Report for Mission Selection: PREMIER, 2012. ESA SP-1324/3 (3 volume series), European Space Agency, Noordwijk, The Netherlands.

[33] ESA (2015). Report for Mission Selection: CarbonSat. ESA SP-1330/1 (2 volume series), European Space Agency, Noordwijk, The Netherlands.

[34] S.J. Baillarin, A. Meygret, C. Dechoz, B. Petrucci, S. Lacherade, T. Tremas, C. Isola, P. Martimort, and F. Spoto. Sentinel-2 Level 1 products and image processing performances. *International Archives of the Photogrammetry, Remote Sensing and Spatial Information Sciences - ISPRS Archives*, 39:197–202, 2012.

[35] ESA. ESA Sentinel-3 Simulator for optical OLCI and SLSTR instruments, 2012. Statement of Work S3-SW-TAF-SY-00766, European Space Agency, Noordwijk, The Netherlands.

[36] C. de Negueruela, M. Scagliola, D. Guidici, J. Moreno, J. Vicent, A. Camps, H. Park, P. Flamant, and R. Franco. ARCHEO-E2E: A reference architecture for earth observation end-to-end mission performance simulators. *SESP, Simulation and EGSE facilities*, 2012.

[37] S. Centouri, C. de Negueruela, K. Ergenzinger, L. Iess, M. Gregnanin, R. Cole, S. Baker, and R. Franco. SS-E2E: Mission performance simulators for space science missions. *SESP, Simulation and EGSE facilities*, 2015.

[38] L. Soto, C. de Negueruela, A. Kobylkiewicz, A. Orych, and R. Franco. EOMODEL: A model library for earth observation end-to-end simulators. *SESP, Simulation and EGSE facilities*, 2015.

[39] ESA. Open simulation framework (openSF) official webpage. `http://eop-cfi.esa.int/index.php/opensf`, 2016. [accessed 15/06/2016].

[40] A. Porcar-Castell, E. Tyystjärvi, J. Atherton, C. van der Tol, J. Flexas, E.E. Pfündel, J. Moreno, C. Frankenberg, and J.A. Berry. Linking chlorophyll a fluorescence to photosynthesis for remote sensing applications: mechanisms and challenges. *Journal of experimental botany*, pages 4065–4095, 2014.

[41] L.A. Corp, J. E.McMurtrey, E. M.Middleton, C. L.Mulchi, E. W.Chappelle, and C. S.T.Daughtry. Fluorescence sensing systems: In vivo detection of biophysical variations in field corn due to nitrogen supply. *Remote Sensing of Environment*, 86(4):470 – 479, 2003.

[42] U. Rascher, G. Agati, L. Alonso, G. Cecchi, S. Champagne, R. Colombo, A. Damm, F. Daumard, E. de Miguel, G. Fernandez, B. Franch, J. Franke, C. Gerbig, B. Gioli, J. A. Gómez, Y. Goulas, L. Guanter, Ó. Gutiérrez-de-la Cámara, K. Hamdi, P. Hostert, M. Jiménez, M. Kosvancova, D. Lognoli, M. Meroni, F. Miglietta, A. Moersch, J. Moreno, I. Moya, B. Neininger, A. Okujeni, A. Ounis, L. Palombi, V. Raimondi, A. Schickling, J. A. Sobrino, M. Stellmes, G. Toci, P. Toscano, T. Udelhoven, S. van der Linden, and A. Zaldei. CEFLES2: the remote sensing component to quantify photosynthetic efficiency from the leaf to the region by measuring sun-induced fluorescence in the oxygen absorption bands. *Biogeosciences*, 6(7):1181–1198, 2009.

[43] F. Daumard, S. Champagne, A. Fournier, Y. Goulas, A. Ounis, J.-F. Hanocq, and I. Moya. A field platform for continuous measurement of canopy fluorescence. *IEEE Transactions on Geoscience and Remote Sensing*, 48(9):3358–3368, 2010.

[44] C. Frankenberg, J.B. Fisher, J. Worden, G. Badgley, S.S. Saatchi, J.-E. Lee, G.C. Toon, A. Butz, M. Jung, A. Kuze, and T. Yokota. New global observations of the terrestrial carbon cycle from GOSAT: Patterns of plant fluorescence with gross primary productivity. *Geophysical Research Letters*, 38(17), 2011.

[45] M. Meroni, L. Busetto, R. Colombo, L. Guanter, J. Moreno, and W. Verhoef. Performance of spectral fitting methods for vegetation fluorescence quantification. *Remote Sensing of Environment*, 114(2):363–374, 2010.

[46] M. Meroni, M. Rossini, L. Guanter, L. Alonso, U. Rascher, R. Colombo, and J. Moreno. Remote sensing of solar-induced chlorophyll fluorescence: Review of methods and applications . *Remote Sensing of Environment*, 113(10):2037 – 2051, 2009.

[47] J. Joiner, Y. Yoshida, A. P. Vasilkov, Y. Yoshida, L. A. Corp, and E. M. Middleton. First observations of global and seasonal terrestrial chlorophyll fluorescence from space. *Biogeosciences*, 8(3):637–651, 2011.

[48] C. Frankenberg, C. O'Dell, J. Berry, L. Guanter, J. Joiner, P. Köhler, R. Pollock, and T." E. Taylor. Prosects for chlorophyll fluorescence remote sensing from the Orbiting Carbon Observatory-2. *Remote Sensing of Environment*, 147:1 – 12, 2014.

[49] P. Köhler, L. Guanter, and J. Joiner. A linear method for the retrieval of sun-induced chlorophyll fluorescence from GOME-2 and SCIAMACHY data. *Atmospheric Measurement Techniques*, 8(6):2589–2608, 2015.

[50] J. Joiner, Y. Yoshida, A. P. Vasilkov, E. M. Middleton, P. K. E. Campbell, Y. Yoshida, A. Kuze, and L. A. Corp. Filling-in of near-infrared solar lines by terrestrial fluorescence and other geophysical effects: simulations and space-based observations from SCIAMACHY and GOSAT. *Atmospheric Measurement Techniques*, 5(4):809–829, 2012.

[51] ESA. Report for Mission Selection: FLEX, 2015. ESA SP-1330/2 (2 volume series), European Space Agency, Noordwijk, The Netherlands.

[52] C. Donlon, B. Berruti, A. Buongiorno, M.-H. Ferreira, P. Féménias, J. Frerick, P. Goryl, U. Klein, H. Laur, C. Mavrocordatos, J. Nieke, H. Rebhan, B. Seitz, J. Stroede, and R. Sciarra. The Global Monitoring for Environment and Security (GMES) Sentinel-3 mission. *Remote Sensing of Environment*, 120:37–57, 2012.

[53] S. Cogliati, W. Verhoef, S. Kraft, N. Sabater, L. Alonso, J. Vicent, J. Moreno, M. Drusch, and R. Colombo. Retrieval of sun-induced fluorescence using advanced spectral fitting methods. *Remote Sensing of Environment*, 169:344–357, 2015.

[54] S. Kraft, J.-L. Bézy, U. Del Bello, R. Berlich, M. Drusch, R. Franco, A. Gabriele, B. Harnisch, R. Meynart, and P. Silvestrin. FLORIS: Phase A status of the fluorescence imaging spectrometer of the earth explorer mission candidate FLEX. *Proceedings of SPIE - The International Society for Optical Engineering*, 8889, 2013.

[55] ESA (Sep. 2013). Sentinel-3 User Handbook. ESA GMES-S3OP-EOPG-TN-13-0001, Issue 1.0.

[56] CEOS. CEOS Earth Observation Satellite Database. `http://database.eohandbook.com/`, 2016. [accessed 15/06/2016].

[57] ESA. Earth Observation Portal Directory. Satellite Mission Database. `https://directory.eoportal.org/`, 2015. [accessed 15/06/2016].

[58] ESA. Earth Observation Science Strategy for ESA: A New Era for Scientific Advances and Societal Benefits, 2015. ESA SP-1329/1 (2 volumes), European Space Agency, Noordwijk, The Netherlands.

[59] J. Aschbacher and M.P. Milagro-Pérez. The European Earth monitoring (GMES) programme: Status and perspectives. *Remote Sensing of Environment*, 120:3–8, 2012.

[60] CEOS. Applications of Satellite Earth Observations: Serving society, Science & Industry. `http://ceos.org/home-2/dar-summary/`, 2015. [accessed 15/06/2016].

[61] A.F.H. Goetz. Three decades of hyperspectral remote sensing of the Earth: A personal view. *Remote Sensing of Environment*, 113(SUPPL. 1):S5–S16, 2009.

[62] H.J. Kramer. *Observation of the Earth and Its Environment: Survey of Missions and Sensors*. Springer-Verlag, Berlin (Germany), 4 edition, 2002.

[63] ESA. ESA's Earth Online website: European Remote Sensing (ERS) satellites. `https://earth.esa.int/web/guest/missions/esa-operational-eo-missions/ers`, 2016. [accessed 15/06/2016].

[64] D. Llewellyn-Jones, M.C. Edwards, C.T. Mutlow, A.R. Birks, I.J. Barton, and H. Tait. AATSR: Global-Change and Surface Temperature Measurements from Envisat. *ESA Bulletin*, 105:11–21, 2001.

[65] T. Paulsen, A.F. Popescu, G. Ratier, G. Uguen, and C. Lemercier. The Global Ozone Monitoring by Occultation of Stars (GOMOS) instrument on ENVISAT. *International Geoscience and Remote Sensing Symposium (IGARSS)*, 2:1438–1440, 1999.

[66] J.-L. Bézy, S. Delwart, and M. Rast. MERIS - A New Generation of Ocean-Color Sensor onboard ENVISAT. *ESA Bulletin*, 103:48–56, 2000.

[67] J.-L. Bézy, G. Gourmelon, R. Bessudo, G. Baudin, H. Sontag, and S. Weiss. The ENVISAT Medium Resolution Imaging Spectrometer (MERIS). *International Geoscience and Remote Sensing Symposium (IGARSS)*, 2:1432–1434, 1999.

[68] M. Endemann, P. Gare, D.J. Smith, and R. Gessuer. The ENVISAT Michelson Interferometer for Passive Atmospheric Sounding (MIPAS). *International Geoscience and Remote Sensing Symposium (IGARSS)*, 2:1435–1437, 1999.

[69] A.P.H. Goede and H. Schrijver. SCIAMACHY: an atmospheric chemistry instrument on ENVISAT. *International Geoscience and Remote Sensing Symposium (IGARSS)*, 3:1609–1611, 1999.

[70] European Comission. Copernicus. Europe eye's on Earth. `http://www.copernicus.eu/`. [accessed 15/06/2016].

[71] ESA. ESA Sentinel Online. `https://sentinel.esa.int`.

[72] ESA (24/07/2015). Sentinel-2 User Handbook. ESAStandard document, Issue 1.2.

[73] ESA. eoPortal directory: Copernicus: Sentinel-4 GEO Component Mission. `https://directory.eoportal.org/web/eoportal/satellite-missions/c-missions/copernicus-sentinel-4`, 2000-2016. [accessed 15/06/2016].

[74] ESA. eoPortal directory: Copernicus: Sentinel-5 (Atmospheric Monitoring Mission) in LEO. `https://directory.eoportal.org/web/eoportal/satellite-missions/c-missions/copernicus-sentinel-5`, 2000-2016. [accessed 15/06/2016].

[75] ESA. eoPortal directory: Copernicus: Sentinel-5P (Precursor - Atmospheric Monitoring Mission). `https://directory.eoportal.org/web/eoportal/satellite-missions/c-missions/copernicus-sentinel-5p`, 2000-2016. [accessed 15/06/2016].

[76] ESA. Meteosat Second Generation: The satellite development, ESA BR-153, 1999. ESA SP-1329/1 (2 volumes), European Space Agency, Noordwijk, The Netherlands.

[77] P. Bensi, D. Aminou, J.-L. Bézy, R. Stuhlmann, A. Rodriguez, and S. Tjemkes. Overview of Meteosat Third Generation (MTG) Activities. *Proc. of the Second MSG RAO Workshop (ESA SP-582)*, 2004.

[78] Edwards, P. G. and Pawlak, D. MetOp: The Space Segment for EUMETSAT's Polar System. `http://www.esa.int/esapub/bulletin/bullet102/Edwards102.pdf`, 2000. ESA Bulleting, No. 102, pp. 7-18, European Space Agency, Noordwijk, The Netherlands.

[79] P.A. Albiñana, R. Gelsthorpe, A. Lefebvre, M. Sauer, E. Weih, K-W Kruse, R. Münzenmayer, G. Baister, and M. Chang. The multi-spectral imager on board the EarthCARE spacecraft. *Proceedings of SPIE - The International Society for Optical Engineering*, 7808:780815–780815–10, 2010.

[80] Wright N. G. Spilling, D.A.V., M. Caldwell, and A. K. Ward. The Broadband Radiometer on the EarthCARE Spacecraft. *Proceedings of the 59th IAC (International Astronautical Congress)*, 2009.

[81] M.A. Cutter. A small satellite hyperspectral mission. *Proc. of the 4S Symposium: Small Satellites, Systems and Services*, 2004. La Rochelle, France.

[82] J.-P. Gleyzes, A. Meygret, C. Fratter, C. Panem, S. Ballaring, and C. Valorge. SPOT5: System overview and image ground segment. *International Geoscience and Remote Sensing Symposium (IGARSS)*, 2003.

[83] Special issue on EOS AM-1 Platform, Instruments, And Scientific Data. *Geoscience and Remote Sensing, IEEE Transactions on*, 36(4), Jul 1998.

[84] H.H. Aumann, M.T. Chahine, C. Gautier, M.D. Goldberg, E. Kalnay, L.M. McMillin, H. Revercomb, P.W. Rosenkranz, W.L. Smith, D.H. Staelin, L.L. Strow, and J. Susskind. AIRS/AMSU/HSB on the Aqua mission: design, science objectives, data products, and processing systems. *IEEE Transactions on Geoscience and Remote Sensing*, 41(2):253–264, Feb 2003.

[85] Y. Yamaguchi, A.B. Kahle, H. Tsu, T. Kawakami, and M. Pniel. Overview of Advanced Spaceborne Thermal Emission and Reflection Radiometer (ASTER). *IEEE Transactions on Geoscience and Remote Sensing*, 36(4):1062–1071, Jul 1998.

[86] NASA. NASA's CERES official webpage. `http://ceres.larc.nasa.gov/terra_ceres.php`, 2016. [accessed 15/06/2016].

[87] NASA. NASA's MISR official webpage. `http://misr.jpl.nasa.gov/Mission/`, 2016. [accessed 15/06/2016].

[88] NASA. NASA's MODIS official webpage. `http://modis.gsfc.nasa.gov/about/`, 2016. [accessed 15/06/2016].

[89] G.S. Drummon, J.R. an Mand. The Measurements of Pollution in the Troposphere (MOPITT) instrument: overall performance and calibration requirements. *Journal of atmospherci and oceanic technology*, 13:314–320, 1996.

[90] USGS. USGS' Landsat 9 official webpage. `http://landsat.gsfc.nasa.gov/?p=10391`, 2016. [accessed 15/06/2016].

[91] NOAA. NOAA's Geostationary Operational Environmental Satellites – R series (GOES-R) official webpage. `http://www.goes-r.gov/`, 2016. [accessed 15/06/2016].

[92] NASA. NASA Polar Operational Environmental Satellites (POES) official webpage. `http://poes.gsfc.nasa.gov/`, 2016. [accessed 15/06/2016].

[93] NASA. NASA's Earth System Science Pathfinder official webpage. `http://science.nasa.gov/about-us/smd-programs/earth-system-science-pathfinder/`, 2016. [accessed 15/06/2016].

[94] NASA. NASA's Aquarius/SAC-D official webpage. `http://aquarius.umaine.edu/cgi/index.htm`, 2015. [accessed 15/06/2016].

[95] NASA. NASA's Calipso official webpage. `http://www-calipso.larc.nasa.gov/`, 2015. [accessed 15/06/2016].

[96] R. Pollock, R.E. Haring, J.R. Holden, D.L. Johnson, A. Kapitanoff, D. Mohlman, C. Phillips, D. Randall, D. Rechsteiner, J. Rivera, J.I. Rodriguez, M.A. Schwochert, and B.M. Sutin. The Orbiting Carbon Observatory instrument: performance of the OCO instrument and plans for the OCO-2 instrument. *Proceedings of SPIE - The International Society for Optical Engineering*, 7826:78260W–78260W–13, 2010.

[97] NASA. NASA's A-Train official webpage. `http://atrain.nasa.gov/`, 2012. [accessed 15/06/2016].

[98] NASA. Aura Earth Science Reference Handbook. `http://eospso.nasa.gov/sites/default/files/mission_handbooks/Aura.pdf`. [accessed 15/06/2016].

[99] M.R. Schoeberl, A.R. Douglass, E. Hilsenrath, and M. Luce. The EOS Aura Mission. *International Geoscience and Remote Sensing Symposium (IGARSS)*, 1:227–232, 2001.

[100] CNES. CNES' Parasol official webpage. `https://parasol.cnes.fr/en/PARASOL/index.htm`, 2012. [accessed 15/06/2016].

[101] NASA. NASA's EO-1 official webpage. `https://eo1.gsfc.nasa.gov/`. [accessed 15/06/2016].

[102] NASA. HyspIRI Comprehensive Development Report. `http://hyspiri.jpl.nasa.gov/comprehensive-development-report`, 2015. [accessed 15/06/2016].

[103] P. F. Bernath, C. T. McElroy, M. C. Abrams, C. D. Boone, M. Butler, C. Camy-Peyret, M. Carleer, C. Clerbaux, P.-F. Coheur, R. Colin, P. DeCola, M. DeMazère, J. R. Drummond, D. Dufour, W. F. J. Evans, H. Fast, D. Fussen, K. Gilbert, D. E. Jennings, E. J. Llewellyn, R. P. Lowe, E. Mahieu, J. C. McConnell, M. McHugh, S. D. McLeod, R. Michaud, C. Midwinter, R. Nassar, F. Nichitiu, C. Nowlan, C. P. Rinsland, Y. J. Rochon, N. Rowlands, K. Semeniuk, P. Simon, R. Skelton, J. J. Sloan, M.-A. Soucy, K. Strong, P. Tremblay, D. Turnbull, K. A. Walker, I. Walkty, D. A. Wardle, V. Wehrle, R. Zander, and J. Zou. Atmospheric Chemistry Experiment (ACE): Mission overview. *Geophysical Research Letters*, 32(15), 2005. L15S01.

[104] ESA. eoPortal directory: Resurs-P (Resurs-Prospective) Remote Sensing Mission Constellation. `https://directory.eoportal.org/web/eoportal/satellite-missions/r/resurs-p`, 2000-2016. [accessed 15/06/2016].

[105] ESA. eoPortal directory: SPOT-5. `https://directory.eoportal.org/web/eoportal/satellite-missions/s/spot-5`, 2000-2016. [accessed 15/06/2016].

[106] ESA. eoPortal directory: SPOT-6 and SPOT-7 Commercial Imaging Constellation. `https://directory.eoportal.org/web/eoportal/satellite-missions/s/spot-6-7`, 2000-2016. [accessed 15/06/2016].

[107] A. Marini, F. J. Reina-Barragan, G. Crippa, B. Harnisch, I. Fuente, M. Lopez, I. Cabeza, and D. Zorita. SEOSAT/Ingenio - A Spanish high-spatial-resolution optical mission. *Proc. of ICSO (International Conference on Space Optics)*, 2014.

[108] T. Stuffler, C. Kaufmann, S. Hofer, K.P. Förster, G. Schreier, A. Mueller, A. Eckardt, H. Bach, B. Penné, U. Benz, and R. Haydn. The EnMAP hyperspectral imager - an advanced optical payload for future applications in earth observation programmes. *AIAA 57th International Astronautical Congress, IAC 2006*, 3:2049–2053, 2006.

[109] DLR. EnMAP's official webpage. `http://www.enmap.org/`, 2012-2015. [accessed 15/06/2016].

[110] C. Galeazzi, A. Sacchetti, A. Cisbani, and G. Babini. The prisma program. *International Geoscience and Remote Sensing Symposium (IGARSS)*, 4(1):IV105–IV108, 2008.

[111] D. Murtagh, U. Frisk, F. Merino, M. Ridal, A. Jonsson, J. Stegman, G. Witt, P. Eriksson, C. Jimenez, G. Mégie, J. de La Noëë, P. Ricaud, P. Baron, J.-R. Pardo, A. Hauchecorne, E.J. Llewellyn, D.A. Degenstein, R.L. Gattinger, N.D. Lloyd, W.F.J. Evans, I.C. McDade, C. Haley, C. Sioris, C. von Savigny, B.H. Solheim, J.C. McConnell, K. Strong, E.H. Richardson, G.W. Leppelmeier, E. Kyröä, H. Auvinen, and L. Oikarinen. An overview of the Odin atmospheric mission. *Canadian Journal of Physics*, 80(4):309–319, 2002.

[112] ESA. eoPortal directory: Ikonos-2. `https://directory.eoportal.org/web/eoportal/satellite-missions/i/ikonos-2`, 2000-2016. [accessed 15/06/2016].

[113] ESA. eoPortal directory: DMC-1G (Disaster Monitoring Constellation- First Generation) Missions). `https://directory.eoportal.org/web/eoportal/satellite-missions/d/dmc`, 2000-2016. [accessed 15/06/2016].

[114] ESA. eoPortal directory: DMC-3 (Disaster Monitoring Constellation-3). `https://directory.eoportal.org/web/eoportal/satellite-missions/d/dmc-3`, 2000-2016. [accessed 15/06/2016].

[115] ESA. eoPortal directory: Deimos-2 Minisatellite Mission. `https://directory.eoportal.org/web/eoportal/satellite-missions/d/deimos-2`, 2000-2016. [accessed 15/06/2016].

[116] Terma A/S. ASIM's official webpage. `http://asim.dk/index.php`, 2016. [accessed 15/06/2016].

[117] Jet Propulsion Laboratory - NASA. ECOSTRESS' official webpage. `http://ecostress.jpl.nasa.gov/`, 2016. [accessed 15/06/2016].

[118] Oregon State University. HICO's official webpage. `http://hico.coas.oregonstate.edu/`, 2009. [accessed 15/06/2016].

[119] Univ. of North Dakota. ISSAC's webpage. `http://www.umac.org/sensors/issac/index.html`, 2006-2011. [accessed 15/06/2016].

[120] ESA. eoPortal directory: ISS Utilization: SAGE-III (Stratospheric Aerosol and Gas Experiment-III). `https://directory.eoportal.org/web/eoportal/satellite-missions/i/iss-sage-3`, 2000-2016. [accessed 15/06/2016].

[121] P. Coppo, C. Mastrandrea, M. Stagi, L. Calamai, and J. Nieke. Sea and land surface temperature radiometer detection assembly design and performance. *Journal of Applied Remote Sensing*, 8(1):084979, 2014.

[122] B. Pfeiffer, B. Gardini, and J. Cendral. Envisat and the Polar Platform: the concept and its history. *ESA Bulletin*, 76:8–13, 1993.

[123] J.-L. Bézy, D. Aminou, P. Bensi, R. Stuhlman, S. Tjemkes, and A. Rodriguez. Meteosat Third Generation - The Future European Geostationary Meteorological Satellite. *ESA Bulletin*, 123:28–32, 2005.

[124] D. Crisp. Measuring CO2 from space: The nasa Orbiting Carbon Observatory-2. *61st International Astronautical Congress 2010, IAC 2010*, 7:5719–5726, 2010.

[125] M. Drusch, F. Gascon, and M. Berger. GMES Sentinel-2 Mission Requirements Document, EOP-SM/1163/MR-dr. Mrd, ESA/ESTEC, 2010.

[126] P. North, C. Brockmann, J. Fischer, L. Gomez-Chova, W. Grey, A. Heckel, J. Moreno, R. Preusker, and P. Regner. MERIS/AATSR synergy algorithms for cloud screening, aerosol retrieval and atmospheric correction. *European Space Agency, (Special Publication) ESA SP*, (666 SP), 2008.

[127] J. Verrelst, J.P. Rivera, L. Alonso, R. Lindstrot, and J. Moreno. Potential retrieval of biophysical parameters from FLORIS, S3-OLCI and its synergy. *International Geoscience and Remote Sensing Symposium (IGARSS)*, pages 7121–7124, 2012.

[128] J. Amorós-López, L. Gómez-Chova, L. Alonso, L. Guanter, R. Zurita-Milla, J. Moreno, and G. Camps-Valls. Multitemporal fusion of Landsat/TM and ENVISAT/MERIS for crop monitoring. *International Journal of Applied Earth Observation and Geoinformation*, 23:132–141, 2013.

[129] S. Plummer. The ESA Climate Change Initiative. Description, EOP-SEP/TN/0030-09/SP. Tn, ESA/ESTEC, 2009.

[130] ESA. eoPortal directory: DSCOVR (Deep Space Climate Observatory)). `https://directory.eoportal.org/web/eoportal/satellite-missions/d/dscovr`, 2000-2016. [accessed 15/06/2016].

[131] C.R. McInnes, M. Ceriotti, C. Colombo, J.-P. Sanchez, R. Bewick, J. Heiligers, and C. Lücking. Micro-to-Macro: Astrodynamics at Extremes of Length-scale. *Acta Futura*, 4:81–97, 2011.

[132] J. Gebbie, M. Pollard, H. Kadhem, L. Boand, A. da Silva, P. Davies, P. Palmer, J. Steyn, and G. Tyc. Spacecraft constellation deployment for the EapirEye Earth Observation system. *Proc. of the 60th IAC (International Astronautical Congress)*, 2009.

[133] J.R. Jensen. *Remote Sensing of the environment: An Earth Resource Perspective*. Prentice Hall, 2 edition, 2007.

[134] S. Sandmeier and K.I. Itten. A physically-based model to correct atmospheric and illumination effects in optical satellite data of rugged terrain. *IEEE Transactions on Geoscience and Remote Sensing*, 35(3):708–717, 1997.

[135] W. Verhoef and H. Bach. Simulation of Sentinel-3 images by four-stream surface-atmosphere radiative transfer modeling in the optical and thermal domains. *Remote Sens. Environ.*, 120:197–207, 2012.

[136] L. Guanter, R. Richter, and H. Kaufmann. On the application of the MODTRAN4 atmospheric radiative transfer code to optical remote sensing. *International Journal of Remote Sensing*, 30(6):1407–1424, 2009.

[137] EEA (European Environmental Agency). CORINE Land Cover, EEA Report. `http://www.eea.europa.eu/publications/COR0-landcover`, 1995. [accessed 15/06/2016].

[138] ESA. Climate Change Initiative. Land Cover (official webpage). `http://www.esa-landcover-cci.org/`, 2011. [accessed 15/06/2016].

[139] GCOS. GCOS Essential Climate Variables. `https://www.wmo.int/pages/prog/gcos/index.php?name=EssentialClimateVariables`. [accessed 15/06/2016].

[140] A. Inness, F. Baier, A. Benedetti, I. Bouarar, S. Chabrillat, H. Clark, C. Clerbaux, P. Coheur, R.J. Engelen, Q. Errera, J. Flemming, M. George, C. Granier, J. Hadji-Lazaro, V. Huijnen, D. Hurtmans, L. Jones, J.W. Kaiser, J. Kapsomenakis, K. Lefever, J. Leitão, M. Razinger, A. Richter, M.G. Schultz, A.J. Simmons, M. Suttie, O. Stein, J.-N. Thépaut, V. Thouret, M. Vrekoussis, and C. Zerefos. The MACC reanalysis: An 8 yr data set of atmospheric composition. *Atmospheric Chemistry and Physics*, 13(8):4073–4109, 2013.

[141] University of Wyoming - Dpt. of Atmospheric Science. Atmospheric soundings)). `http://weather.uwyo.edu/upperair/sounding.html`, 2016. [accessed 15/06/2016].

[142] NASA. AERONET - Atmospheric Robotic Network. `http://aeronet.gsfc.nasa.gov/`, 2016. [accessed 15/06/2016].

[143] European Comission. Radiation transfer Model Intercomparison (RAMI) official webpage. `http://rami-benchmark.jrc.ec.europa.eu`. [accessed 15/06/2016].

[144] B. Pinty, J.-L. Widlowski, M. Taberner, N. Gobron, M.M. Verstraete, M. Disney, F. Gascon, J.-P. Gastellu, L. Jiang, A. Kuusk, P. Lewis, X. Li, W. Ni-Meister, T. Nilson, P. North, W. Qin, L. Su, S. Tang, R. Thompson, W. Verhoef, H. Wang, J. Wang, G Yan, and H. Zang. Radiation transfer model intercomparison (RAMI)

exercise: Results from the second phase. *Journal of Geophysical Research Atmospheres*, 109(D6), Mar 2004.

[145] J.-L. Widlowski, M. Taberner, B. Pinty, V. Bruniquel-Pinel, M. Disney, R. Fernandes, J.-P. Gastellu-Etchegorry, N. Gobron, A. Kuusk, T. Lavergne, S. Leblanc, P.E. Lewis, E. Martin, M. Mõttus, P.R.J. North, W. Qin, M. Robustelli, N. Rochdi, R. Ruiloba, C. Soler, R. Thompson, W. Verhoef, M.M. Verstraete, and D. Xie. Third radiation transfer model intercomparison (RAMI) exercise: Documenting progress in canopy reflectance models. *Journal of Geophysical Research Atmospheres*, 112(9), May 2007.

[146] J.-L. Widlowski, C. Mio, M. Disney, J. Adams, I. Andredakis, C. Atzberger, J. Brennan, L. Busetto, M. Chelle, G. Ceccherini, R. Colombo, J.-F. Coté, A. Eenmäe, R. Essery, J.-P. Gastellu-Etchegorry, N. Gobron, E. Grau, V. Haverd, L. Homolová, H. Huang, L. Hunt, H. Kobayashi, B. Koetz, A. Kuusk, J. Kuusk, M. Lang, P.E. Lewis, J.L. Lovell, Z. Malenovsky, M. Meroni, F. Morsdorf, M. Mõttus, W. Ni-Meister, B. Pinty, M. Rautiainen, M. Schlerf, B. Somers, J. Stuckens, M.M. Verstraete, W. Yang, F. Zhao, and T. Zenone. The fourth phase of the radiative transfer model intercomparison (RAMI) exercise: Actual canopy scenarios and conformity testing. *Remote Sensing of Environment*, 169:418–437, Nov 2015.

[147] S.Y. Kotchenova, E.F. Vermote, R. Levy, and A. Lyapustin. Radiative transfer codes for atmospheric correction and aerosol retrieval: Intercomparison study. *Applied Optics*, 47(13):2215–2226, 2008.

[148] Emde, C. and Büll, R. and Buras, R. and Faure, F. and Hamann, U. and Kylling, A. and Mayer, B. and Meerkötter, R. Towards a Generic Radiative Transfer Model for the Earth's Surface-Atmosphere System: ESAS-Light. WP1100: Literature survey Radiative transfer tools, 2015. ESA-ESTEC Contract No AO/1-5433/07/NL/HE, Noordwijk, The Netherlands.

[149] USGS. USGS Lunar Calibration. Robotic Lunar Observatory (ROLO). `http://www.moon-cal.org/`. [accessed 15/06/2016].

[150] R.A. Schowengerdt. *Remote Sensing: Models and Methods for Image Processing*. Elsevier, Burlington, MA, 3 edition, 2007.

[151] K. Segl, L. Guanter, H. Kaufmann, J. Schubert, S. Kaiser, B. Sang, and S. Hofer. Simulation of spatial sensor characteristics in the context of the EnMAP hyperspectral mission. *IEEE Transactions on Geoscience and Remote Sensing*, 48(7):3046–3054, 2010.

[152] R.A. Neville, L. Sun, and K. Staenz. Detection of spectral line curvature in imaging spectrometer data. *Proceedings of SPIE - The International Society for Optical Engineering*, 5093:144–154, 2003.

[153] F. Kataoka, R.O. Knuteson, A. Kuze, H. Suto, K. Shiomi, M. Harada, E.M. Garms, J.A. Roman, D.C. Tobin, J.K. Taylor, H.E. Revercomb, N. Sekio, R. Higuchi, and Y. Mitomi. TIR spectral radiance calibration of the GOSAT satellite borne TANSO-FTS with the aircraft-based S-HIS and the ground-based S-AERI at the railroad valley desert playa. *IEEE Transactions on Geoscience and Remote Sensing*, 52(1):89–105, 2014.

[154] A. Kuze, H. Suto, K. Shiomi, T. Urabe, M. Nakajima, J. Yoshida, T. Kawashima, Y. Yamamoto, F. Kataoka, and H. Buijs. Level 1 algorithms for TANSO on GOSAT: Processing and on-orbit calibrations. *Atmospheric Measurement Techniques*, 5(10):2447–2467, 2012.

[155] ESA. eoPortal Directory: Terra Mission. `https://directory.eoportal.org/web/eoportal/satellite-missions/t/terra`, 2015. [accessed 15/06/2016].

[156] D.R. Hearn. Characterization of instrument spectral resolution by the spectral modulation transfer function. *Proceedings of SPIE - The International Society for Optical Engineering*, 3439:400–407, Jul 1998.

[157] R.A. Neville, L. Sun, and K. Staenz. Detection of keystone in imaging spectrometer data. *Proceedings of SPIE - The International Society for Optical Engineering*, 5425:208–217, 2004.

[158] D. Schläpfer, J. Nieke, and K.I. Itten. Spatial PSF Nonuniformity Effects in Airborne Pushbroom Imaging Spectrometry Data. *Geoscience and Remote Sensing, IEEE Transactions on*, 45(2):458–468, Feb 2007.

[159] B. Aiazzi, L. Alparone, A. Barducci, S. Baronti, and I. Pippi. Estimating noise and information of multispectral imagery. *Optical Engineering*, 41(3):656–668, 2002.

[160] G. Lichtenberg, Q. Kleipool, J.M. Krijger, G. Van Soest, R. Van Hees, L.G. Tilstra, J.R. Acarreta, I. Aben, B. Ahlers, H. Bovensmann, K. Chance, A.M.S. Gloudemans, R.W.M. Hoogeveen, R.T.N. Jongma, S. Noël, A. Piters, H. Schrijver, C. Schrijvers, C.E. Sioris, J. Skupin, S. Slijkhuis, P. Stammes, and M. Wuttke.

SCIAMACHY Level 1 data: Calibration concept and in-flight calibration. *Atmospheric Chemistry and Physics*, 6(12):5347–5367, Nov 2006.

[161] A. Barducci and I. Pippi. Analysis and rejection of systematic disturbances in hyperspectral remotely sensed images of the earth. *Applied Optics*, 40(9):1464–1477, 2001.

[162] D. Schläpfer, J. Nieke, and K.I. Itten. Spatial PSF nonuniformity effects in airborne pushbroom imaging spectrometry data. *IEEE Transactions on Geoscience and Remote Sensing*, 45(2):458–468, 2007.

[163] L. Gomez-Chova, L. Alonso, L. Guanter, G. Camps-Valls, J. Calpe, and J. Moreno. Correction of systematic spatial noise in push-broom hyperspectral sensors: application to CHRIS/PROBA images. *Applied Optics*, 47(28):46–60, Oct 2008.

[164] H. Fujisada. ASTER level-1 data processing algorithm. *IEEE Transactions on Geoscience and Remote Sensing*, 36(4):1101–1112, Jul 1998.

[165] A. Hassini, F. Benabdelouahed, N. Benabadji, and A.H. Belbachir. Active fire monitoring with level 1.5 MSG satellite images. *American Journal of Applied Sciences*, 6(1):157–166, 2009.

[166] S. Eichstädt, F. Schmähling, G. Wübbeler, K. Anhalt, L. Bünger, U. Krger, and C. Elster. Comparison of the Richardson-Lucy method and a classical approach for spectrometer bandpass correction. *Metrologia*, 50(2):107–118, 2013.

[167] D.R. Korwan, R.L. Lucke, N.R. McGlothlin, S.D. Butcher, D.L. Wood, J.H. Bowles, M. Corson, W.A. Snyder, C.O. Davis, and D.T. Chen. Laboratory characterization of the Hyperspectral Imager for the Coastal Ocean (HICO). *International Geoscience and Remote Sensing Symposium (IGARSS)*, 2:II69–II72, 2009.

[168] G. Lichtenberg. SCIAMACHY Channel 1-5 Memory Effect I: Key data implementation and in-flight measurements. Final Report, v1.1. Technical report, SRON (Netherlands), Sep 2003. (`https://personal.sron.nl/~sciadc/update_sronserver/docs/memory_effect_sronrpI.pdf`).

[169] L.G. Tilstra, J.R. Acarreta, J.M. Krijger, and P. Stammes. Verification of SCIAMACHY's Polarization Correction over the Sahara desert. *Proc. of Envisat Validation Workshop*, Dec 2002.

[170] Y. Dutil, S. Lantagne, S. Dubé, and R. Poulin. ACE-FTS level 0 to 1 data processing. *Proceedings of SPIE - The International Society for Optical Engineering*, 4814:102–110, Sep 2002.

[171] ESA. OLCI Ocean Quality and Science Flags. `https://sentinel.esa.int/web/sentinel/technical-guides/sentinel-3-olci/level-2/quality-and-science-flags-op`, 2000-2016. [accessed 15/06/2016].

[172] NASA. High Resolution Dynamics Limb Sounder (Aura). Algorithm Theoretical Basis Document, 1999. ATBD-HIR-01.

[173] K.V. Khlopenkov and A.P. Trishchenko. Implementation and evaluation of concurrent gradient search method for reprojection of MODIS level 1B imagery. *IEEE Transactions on Geoscience and Remote Sensing*, 46(7):2016–2027, Aug 2008.

[174] L. Busetto, M. Meroni, G.F. Crosta, L. Guanter, and R. Colombo. SpecCal: Novel software for in-field spectral characterization of high-resolution spectrometers. *Computers and Geosciences*, 37(10):1685–1691, 2011.

[175] R. Behling, S. Roessner, K. Segl, B. Kleinschmit, and H. Kaufmann. Robust automated image co-registration of optical multi-sensor time series data: Database generation for multi-temporal landslide detection. *Remote Sensing*, 6(3):2572–2600, 2014.

[176] Y. Lou, A.P. Trishchenko, and K.V. Khlopenkov. Developing clear-sky, cloud and cloud shadow mask for producing clear-sky composites at 250-meter spatial resolution for the seven {MODIS} land bands over Canada and North America. *Remote Sensing of Environment*, 112(12):4167 – 4185, 2008.

[177] Z. Zhu and C.E. Woodcock. Object-based cloud and cloud shadow detection in Landsat imagery. *Remote Sensing of Environment*, 118:83–94, 2012.

[178] L. Gómez-Chova, J. Amorós-López, J. Muñoz Marí, and G. Camps-Valls. Cloud masking of multitemporal remote sensing images. volume 9244, 2014.

[179] L. Gomez-Chova, G. Camps-Valls, J. Amoros-Lopez, L. Guanter, L. Alonso, J. Calpe, and J. Moreno. New Cloud Detection Algorithm for Multispectral and Hyperspectral Images: Application to ENVISAT/MERIS and PROBA/CHRIS Sensors. pages 2757–2760, Aug 2006.

[180] L. Gomez-Chova, G. Camps-Valls, J. Calpe-Maravilla, L. Guanter, and J. Moreno. Cloud-Screening Algorithm for ENVISAT/MERIS Multispectral Images. *IEEE Transactions on Geoscience and Remote Sensing*, 45(12):4105–4118, Dec 2007.

[181] G. de Leeuw, T. Holzer-Popp, S. Bevan, W.H. Davies, J. Descloitres, R.G. Grainger, J. Griesfeller, A. Heckel, S. Kinne, L. Klüser, P. Kolmonen, P. Litvinov, D. Martynenko, P. North, B. Ovigneur, N. Pascal, C. Poulsen, D. Ramon, M. Schulz, R. Siddans, L. Sogacheva, D. Tanré, G.E. Thomas, T.H. Virtanen, W. von Hoyningen Huene, M. Vountas, and S. Pinnock. Evaluation of seven european aerosol optical depth retrieval algorithms for climate analysis. *Remote Sensing of Environment*, 162:295–315, 2015.

[182] L. Guanter, L. Gomez-Chova, and J. Moreno. Coupled retrieval of aerosol optical thickness, columnar water vapor and surface reflectance maps from ENVISAT/MERIS data over land. *Remote Sensing of Environment*, 112(6):2898–2913, Feb 2008.

[183] L. Guanter, L. Alonso, and J. Moreno. A method for the surface reflectance retrieval from PROBA/CHRIS data over land: application to ESA SPARC campaigns. *Geoscience and Remote Sensing, IEEE Transactions on*, 43(12):2908–2917, Dec 2005.

[184] ESA. MERIS/AATSR Synergy Algorithms for Cloud Screening, Aerosol Retrieval, and Atmospheric Correction – Land Aerosol and Surface Reflectance ATBD, 2009. ESRIN Contract No. 21090/07/I-LG, Version 3.1.

[185] D.S. Tkacik, Y. Luna-Cruz, N. Clinton, S. Spak, and J. Ryan. Atmospheric correction for MASTER image data using localized modelled and observed meteorology and trace gases. *Remote Sensing Letters*, 3(3):201–209, 2012.

[186] J. Zhou, J. Wang, J. Li, and D. Hu. Atmospheric correction of PROBA/CHRIS data in an urban environment. *International Journal of Remote Sensing*, 32(9):2591–2604, Apr 2011.

[187] P.S. Chavez Jr. An improved dark-object subtraction technique for atmospheric scattering correction of multispectral data. *Remote Sensing of Environment*, 24(3):459–479, Apr 1988.

[188] P.S. Chavez Jr. Image-based atmospheric correction: revised and improved. *Photogrammetric Engineering and Remote Sensing*, 62(9):1025–1036, Sep 1996.

[189] X. Zhao, S.L. Liang, S.H. Liu, J.D. Wang, J. Qin, Q. Li, and X.W. Li. Improvement of dark object method in atmospheric correction of hyperspectral remotely sensed data. *Science in China, Series D: Earth Sciences*, 51(3):349–356, Mar 2008.

[190] L.S. Bernstein, X. Jin, B. Gregor, and S.M. Adler-Golden. Quick atmospheric correction code: Algorithm description and recent upgrades. *Optical Engineering*, 51(11), 2012.

[191] Y. Mekler and Y.J. Kaufman. Contrast reduction by the atmosphere and retrieval of nonuniform surface reflectance. *Applied Optics*, 21(2):310–316, 1982.

[192] Y.J. Kaufman. Atmospheric effect on spatial resolution of surface imagery. *Applied Optics*, 23(19):3400–3401, 1984.

[193] C.W. O'Dell, B. Connor, H. Bösch, D. O'Brien, C. Frankenberg, R. Castano, M. Christi, D. Eldering, B. Fisher, M. Gunson, J. McDuffie, C.E. Miller, V. Natraj, F. Oyafuso, I. Polonsky, M. Smyth, T. Taylor, G.C. Toon, P.O. Wennberg, and D. Wunch. The ACOS CO2 retrieval algorithm-Part 1: Description and validation against synthetic observations. *Atmospheric Measurement Techniques*, 5(1):99–121, 2012.

[194] D. Odermatt, A. Gitelson, V.E. Brando, and M. Schaepman. Review of constituent retrieval in optically deep and complex waters from satellite imagery. *Remote Sensing of Environment*, 118:116–126, 2012.

[195] D. Schläpfer, C.C. Borel, J. Keller, and K.I. Itten. Atmospheric precorrected differential absorption technique to retrieve columnar water vapor. *Remote Sensing of Environment*, 65(3):353–366, 1998.

[196] ESA. CEOS Cal/Val portal (official webpage). `http://calvalportal.ceos.org/`, 2016. [accessed 15/06/2016].

[197] Y. Du, C.-I. Chang, H. Ren, C.-C. Chang, J.O. Jensen, and F.M. D'Amico. New hyperspectral discrimination measure for spectral characterization. *Optical Engineering*, 43(8):1777–1785, 2004.

[198] G.M. Foody. Thematic map comparison: Evaluating the statistical significance of differences in classification accuracy. *Photogrammetric Engineering and Remote Sensing*, 70(5):627–633, 2004.

[199] I. Avcbas, B. Sankur, and K. Sayood. Statistical evaluation of image quality measures. *Journal of Electronic Imaging*, 11(2):206–223, Apr 2002.

[200] J. Moreno et al. FLEX/S3 Tandem Mission Performance Analysis and Requirements Consolitdation Study (PARCS). Final Report, v1.1. Technical report, University of Valencia (Spain), Nov 2014. (`http://ipl.uv.es/flex-parcs/`).

[201] Gina Mohammed et al. FLEX/S3 Tandem Mission Photosynthesis Study. Final Report. Technical report, P&M Technologies (Canada), Nov 2014. (`http://www.flex-photosyn.ca/`).

[202] Gina Mohammed et al. FLEX/Sentinel-3 Tandem Mission – FLEX Brigde Study. Final Report. Technical report, P&M Technologies (Canada), January 2016. ESA ESTEC Contract No. 4000112341/14/NL/FF/gp (`http://www.flex-photosyn.ca/FB_HOME.htm`).

[203] European Space Agency. Earth Observation CFI software official webpage. `http://eop-cfi.esa.int/index.php/mission-cfi-software/eocfi-software`. [accessed 15/06/2016].

[204] J.P. Rivera, N. Sabater, C. Tenjo, J. Vicent, and J. Moreno. Synthetic scene simulator for hyperspectral spaceborne passive optical sensors. application to ESA's FLEX/Sentinel-3 tandem mission. *Proc. of 4th Workshop on Hyperspectral Image and Signal Processing: Evolution in Remote Sensing (WHISPERS)*, 2014.

[205] ASTER GDEM Validation Team. ASTER Global Digital Elevation Model, version 2, Summary of Validation Results. Technical report, NASA & Ministry of Economy, Trade and Industry (METI), 08 2011.

[206] I. Reda and A. Andreas. Solar Position Algorithm for Solar Radiation Applications. Technical Report NREL/TP-560-34302, NREL - National Renewable Energy Laboratory, 2003.

[207] C. Van Der Tol, W. Verhoef, J. Timmermans, A. Verhoef, and Z. Su. An integrated model of soil-canopy spectral radiances, photosynthesis, fluorescence, temperature and energy balance. *Biogeosciences*, 6(12):3109–3129, 2009.

[208] W. Verhoef and H. Bach. Simulation of Sentinel-3 images by four-stream surface-atmosphere radiative transfer modeling in the optical and thermal domains. *Remote Sensing of Environment*, 120:197–207, 2012.

[209] U. Rascher, L. Alonso, A. Burkart, C. Cilia, S. Cogliati, R. Colombo, A. Damm, M. Drusch, L. Guanter, J. Hanus, T. Hyvärinen, T. Julitta, J. Jussila, K. Kataja, P. Kokkalis, S. Kraft, T. Kraska, M. Matveeva, J. Moreno, O. Muller, C. Panigada, M. Pikl, F. Pinto, L. Prey, R. Pude, M. Rossini, A. Schickling, U. Schurr, D. Schüttemeyer, J. Verrelst, and F. Zemek. Sun-induced fluorescence a new probe of photosynthesis: First maps from the imaging spectrometer hyplant. *Global Change Biology*, 2015.

[210] J. Vicent, L. Alonso, N. Sabater, C. Miesch, S. Kraft, and J. Moreno. Propagation of spectral characterization errors of imaging spectrometers at Level-1 and its correction within a Level-2 recalibration scheme. *Proceedings of SPIE - The International Society for Optical Engineering*, 9611:96110T–96110T–12, 2015.

[211] N. Sabater, J. Vicent, L. Alonso, J. Verreslst, and J. Moreno. An atmospheric correction algorithm for FLEX/S3 tandem mission. *Proc. of the 5th International Workshop on Remote Sensing of Vegetation Fluorescence*, 2014. [http://www.congrexprojects.com/2014-events/14c04/proceedings].

[212] N. Sabater, J. Vicent, L. Alonso, J. Verreslst, and J. Moreno. An atmospheric correction algorithm for FLuorescence EXplorer/Sentinel-3 tandem mission. 2016. (Submitted).

[213] FLEX MAG and Matthias Drusch. FLEX Mission Requirements Document (MRD), v1.0. Technical report, European Space Agency (ESA), 05 2011.

[214] A. Verger, I. Filella, F. Baret, and J. Peñuelas. Vegetation baseline phenology from kilometric global LAI satellite products. *Remote Sensing of Environment*, 178:1 – 14, 2016.

[215] V.K. Arora and G.J. Boer. A parameterization of leaf phenology for the terrestrial ecosystem component of climate models. *Global Change Biology*, 11(1):39–59, 2005.

[216] W. Verhoef and H. Bach. Simulation of hyperspectral and directional radiance images using coupled biophysical and atmospheric radiative transfer models. *Remote Sensing of Environment*, 87(1):23 – 41, Sep 2003.

[217] S.G. Leblanc and J.M. Chen. A windows graphic user interface (GUI) for the five scale model for fast BRDF simulations. *Remote Sensing Reviews*, 19(1-4):293–305, Oct 2000.

[218] A. Kuusk. A two-layer canopy reflectance model. *Journal of Quantitative Spectroscopy and Radiative Transfer*, 71(1):1 – 9, Oct 2001.

[219] J.P. Gastellu-Etchegorry, V. Demarez, V. Pinel, and F. Zagolski. Modeling radiative transfer in heterogeneous 3-D vegetation canopies. *Remote Sensing of Environment*, 58(2):131–156, Nov 1996.

[220] J.P. Gastellu-Etchegorry. 3D modeling of satellite spectral images, radiation budget and energy budget of urban landscapes. *Meteorology and Atmospheric Physics*, 102(3-4):187–207, Dec 2008.

[221] J. Stuckens, W.W. Verstraeten, S. Delalieux, R. Swennen, and P. Coppin. A dorsiventral leaf radiative transfer model: Development, validation and improved model inversion techniques. *Remote Sensing of Environment*, 113(12):2560–2573, 2009.

[222] P. North. Three-dimensional forest light interaction model using a Monte Carlo method. *IEEE Transactions on Geoscience and Remote Sensing*, 34(4):946–956, Jul 1996.

[223] P.J. Zarco-Tejada, J.R. Miller, R. Pedrós, W. Verhoef, and M. Berger. FluorMODgui V3.0: A graphic user interface for the spectral simulation of leaf and canopy chlorophyll fluorescence. *Computers and Geosciences*, 32(5):577–591, 2006.

[224] C.D. Mobley. *Light and Water: Radiative Transfer in Natural Waters*. Academic Press, 1994.

[225] J. Helbert, B. Berthelot, and C. Soler. Hyemalis: An image simulator of complex three dimensional landscapes. *Revue Française de Photogrammétrie et de Télédétection*, (173-174):27–35, 2004.

[226] W. Qin and Y. Xiang. An analytical model for bidirectional reflectance factor of multicomponent vegetation canopies. *Science in China, Series C: Life Sciences*, 40(3):305–315, Jun 1997.

[227] J. Cheng, S. Liang, F. Weng, J. Wang, and X. Li. Comparison of radiative transfer models for simulating snow surface thermal infrared emissivity. *IEEE Journal of Selected Topics in Applied Earth Observations and Remote Sensing*, 3(3):323–336, Sep 2010.

[228] T. Kajiyama, D. D'Alimonte, and J. Cunha. Performance prediction of ocean color Monte Carlo simulations using multi-layer perceptron neural networks. *Procedia Computer Science*, 4:2186 – 2195, Jun 2011.

[229] J.S. Sanders et al. Ground target infrared signature modeling with the Multi-Servide Electro-optic Signature (MuSES) code. *Proceedings of SPIE - The International Society for Optical Engineering*, 4029, Jul 2000.

[230] T. Poglio, S. Mathieu-Marni, T. Ranchin, E. Savaria, and L. Wald. OSIrIS: a physically based simulation tool to improve training in thermal infrared remote sensing over urban areas at high spatial resolution. *Remote Sensing of Environment*, 104(2):238–246, Sep 2006.

[231] S. Jacquemoud, W. Verhoef, F. Baret, C. Bacour, P.J. Zarco-Tejada, G.P. Asne, C. Francois, and S.L. Ustin. PROSPECT + SAIL models: A review of use for vegetation characterization. *Remote Sensing of Environment*, 113, Supplement 1:S56 – S66, Sep 2009. Imaging Spectroscopy Special Issue.

[232] J.-B. Feret, C. Francois, G.P. Asner, A.A. Gitelson, R.E. Martin, L.P.R. Bidel, S.L. Ustin, G. le Maire, and S. Jacquemoud. PROSPECT-4 and 5: Advances in the leaf optical properties model separating photosynthetic pigments. *Remote Sensing of Environment*, 112(6):3030–3043, 2008.

[233] S. Jacquemoud and F. Baret. PROSPECT: A model of leaf optical properties spectra. *Remote Sensing of Environment*, 34(2):75 – 91, 1990.

[234] Y.M. Govaerts and M.M. Verstraete. Raytran: a monte carlo raytracing model to compute light scattering in threedimensional heterogeneous media. *IEEE Transactions on Geoscience and Remote Sensing*, 36(2):493505, Mar 1998.

[235] W. Qin and S.A.W. Gerstl. 3-D scene modeling of semidesert vegetation cover and its radiation regime. *Remote Sensing of Environment*, 74(1):145–162, Oct 2000.

[236] W. Verhoef. Light scattering by leaf layers with application to canopy reflectance modeling: The SAIL model. *Remote Sensing of Environment*, 16(2):125–141, 1984.

[237] C. Van Der Tol, W. Verhoef, J. Timmermans, A. Verhoef, and Z. Su. An integrated model of soil-canopy spectral radiances, photosynthesis, fluorescence, temperature and energy balance. *Biogeosciences*, 6(12):3109–3129, 2009.

[238] W. Verhoef and H. Bach. Coupled soil-leaf-canopy and atmosphere radiative transfer modeling to simulate hyperspectral multi-angular surface reflectance and TOA radiance data. *Remote Sensing of Environment*, 109(2):166–182, 2007.

[239] J.-P. Lagouarde, A. Hénon, B. Kurz, P. Moreau, M. Irvine, J. Voogt, and P. Mestayer. Modelling daytime thermal infrared directional anisotropy over Toulouse city centre. *Remote Sensing of Environment*, 114(1):87–105, Jan 2010.

[240] S.P.I.Rou: un outil de Synthèse de Paysages en InfraRouge par modélisation des échanges à la surface. *International Symposium Optronics & Defense*, 1996.

[241] P. Gege. The water color simulator WASI: An integrating software tool for analysis and simulation of optical in situ spectra. *Computers and Geosciences*, 30(5):523–532, Jun 2004.

[242] E.F. Vermote, D. Tanre, J.L. Deuze, M. Herman, and J.-J. Morcette. Second Simulation of the Satellite Signal in the Solar Spectrum, 6S: an overview. *IEEE Transactions on Geoscience and Remote Sensing*, 35(3):675–686, May 1997.

[243] S.Y. Kotehenova and E.F. Vermote. Validation of a vector version of the 6S radiative transfer code for atmospheric correction of satellite data. Part II. Homogeneous Lambertian and anisotropic surfaces. *Applied Optics*, 46(20):4455–4464, 2007.

[244] B. Mayer and A. Kylling. Technical note: The libRadtran software package for radiative transfer calculations - description and examples of use. *Atmospheric Chemistry and Physics*, 5(7):1855–1877, 2005.

[245] C. Emde, R. Buras-Schnell, A. Kylling, B. Mayer, J. Gasteiger, U. Hamann, J. Kylling, B. Richter, C. Pause, T. Dowling, and L. Bugliaro. The libRadtran software package for radiative transfer calculations (Version 2.0). *Geoscientific Model Development Discussions*, 8(12):10237–10303, 2015.

[246] F. Fell and J. Fischer. Numerical simulation of the light field in the atmosphere-ocean system using the matrix-operator method. *Journal of Quantitative Spectroscopy and Radiative Transfer*, 69(3):351–388, 2001.

[247] William M. Cornette, Prabhat K. Acharya, and Gail P. Anderson. Using the MOSART code for atmospheric correction. volume 1, pages 215–219, 1994.

[248] Radiative transfer through terrestrial atmosphere and ocean: Software package SCIATRAN.

[249] F.C. Seidel, A.A. Kokhanovsky, and M.E. Schaepman. Fast and simple model for atmospheric radiative transfer. *Atmospheric Measurement Techniques*, 3(4):1129–1141, 2010.

[250] A.M. Baldridge, S.J. Hook, C.I. Grove, and G. Rivera. The ASTER spectral library version 2.0. *Remote Sensing of Environment*, 113(4):711–715, 2009.

[251] R.N. Clark, G.A. Swayze, R. Wise, E. Livo, T. Hoefen, R. Kokaly, and S.J. Sutley. USGS digital spectral library splib06a: U.S. Geological Survey. `http://speclab.cr.usgs.gov/spectral.lib06`. (2007) Digital Data Series 231.

[252] W. Verhoef and H. Bach. Coupled soil-leaf-canopy and atmosphere radiative transfer modeling to simulate hyperspectral multi-angular surface reflectance and toa radiance data. *Remote Sensing of Environment*, 109(2):166–182, July 2007.

VNIVERSITAT
DE VALÈNCIA